

## **ABSTRACT**

FANG, GANG. Development of Instrumental Techniques for Color Assessment of Camouflage Patterns. (Under the Supervision of Dr. Renzo Shamey, Dr. David Hinks, Dr. Joel Trussell and Dr. Larry Norris).

Camouflage fabrics are produced on a large scale for use in the US military and other applications. One of the highest volume camouflage fabrics is known as the Universal Camouflage Pattern (UCP) which is produced for the US Department of Defense. At present, no standard measurement-based color quality control method exists for camouflage substrates. All assessments are performed visually under standard daylight simulation at a correlated color temperature of 7500K. Visual pass/fail decisions involve myriad factors that affect accuracy and repeatability. In the case of camouflage material, visual assessment decisions are far more complex than those of solid colors. The variability in the visual assessments is currently unknown for Universal Camouflage Pattern substrates. This can cause problems in color quality control in the supply chain and production of the finished fabric.

Hence, a system is required that can accurately, repeatedly and rapidly predict pass or fail decisions objectively according to a defined tolerance, and this is the primary objective of this work.

The research goals include:

1. Development of a spectrophotometric and a non-contact based standard instrumental method for assessment of Universal Camouflage Pattern;

2. Verification the performance of the instrumental methods against the visual pass/fail data.

A calibrated digital camera system was developed using a calibrated light box for illumination of the samples. A key goal was to develop an integrated system that allows colorimetric measurement. Dedicated software was developed to control devices and obtain pass / fail ratings.

The key criterion was the repeatability and accuracy of digital measurements such that they were well within the visual pass/fail tolerances of the camouflage substrates.

© Copyright 2012 by Gang Fang

All Rights Reserved

Development of Instrumental Techniques for Color Assessment of Camouflage Patterns

by  
Gang Fang

A dissertation submitted to the Graduate Faculty of  
North Carolina State University  
in partial fulfillment of the  
requirements for the degree of  
Doctor of Philosophy

Fiber and Polymer Science

Raleigh, North Carolina

2012

APPROVED BY:

---

Dr Renzo Shamey  
Committee Chair

---

Dr David Hinks  
Committee Co-Chair

---

Dr Joel Trussell

---

Dr Larry Norris

## **BIOGRAPHY**

Gang Fang was born on June 16<sup>th</sup>, 1974 in Huhehaote, P.R. China. He received his Bachelor's degree from Tsinghua University in 1998 and his Masters degree from Hunan University in 2001. He then served in the IT industry as a software engineer for 7.5 years, including 4 years as a color algorithm engineer. In spring 2008, he came to NC State to pursue a PhD in color science.

## ACKNOWLEDGMENTS

The author would like to thank Dr. Renzo Shamey, chairman of his advisory committee, for his advice, support, and guidance throughout this study.

Dr. David Hinks, co-chairman of his advisory committee, contributed to the overall design of the hardware & software system.

Appreciation is also extended to Dr. Joel Trussell and Dr. Larry Norris, members of the advisory committee, for their valuable advice, suggestions, and encouragement.

The author would also like to thank Dr. Lina M. Cárdenas for her help in color measurement of the camouflage samples, and Ms. Weethima Sawatwarakul for her contribution in the creation of the calibration tools.

Special thanks are extended to the Natick Soldier Division Center for the financial support of the project and providing the camouflage samples.

Finally, the author wishes to express thanks to his parents and his girlfriend for their encouragement and motivation.

# TABLE OF CONTENTS

LIST OF TABLES .....	xi
LIST OF FIGURES.....	xiii
Chapter I. Literature Review .....	1
1. The Human Eye.....	1
1.1 Eye, Brain and the Color Vision.....	3
2. Essential Requirements for Color Vision .....	3
2.1 Light Sources.....	4
2.2 Interaction between Materials and Light.....	7
2.2.1 Reflection .....	7
2.2.2 Transmission.....	8
2.2.3 Absorption .....	9
2.2.4 Scattering .....	10
2.2.5 Determination of Object Color .....	11
3. Colorimetry .....	11
3.1 CIE System.....	12
3.2 CIE 1976 (L*u*v*) Color Space .....	14

3.3 CIE 1976 (L*a*b*) Color Space .....	15
4. Estimation of Color Difference .....	17
4.1 CIELAB color difference .....	17
4.2 CMC.....	19
4.3 BFD.....	21
4.4 CIE94 .....	22
4.5 DIN99.....	23
4.6 CIEDE2000 .....	24
4.7 CIECAM02 .....	25
4.8 Performance of Various Color Difference Formulas.....	27
5. Color Appearance Models .....	28
5.1 Color Appearance Phenomena .....	28
5.2 Chromatic Adaptation Transforms .....	29
5.3 Color Appearance Models.....	32
5.3.1 ‘Wrong’ von Kries Transform .....	32
5.3.2 CIECAM02.....	33
6. ICC Color Management.....	37
6.1 PCS .....	37

6.2 ICC Profile .....	38
7. Various Color Input Devices.....	41
7.1 Scanners .....	41
7.2 Digital Cameras .....	42
7.3 Hyperspectral Camera.....	44
7.4 Colorimeter.....	46
7.5 Spectrophotometer .....	47
7.6 Measurement Variability.....	50
8. Device Calibration.....	50
8.1 Display Monitor.....	50
8.1.1 Structure of Monitors based on the Liquid Crystal Display (LCD).....	51
8.1.2 Calibration of the LCD Monitor .....	52
8.1.3 Corrected Calibration Model .....	54
8.2 Digital Camera.....	55
8.2.1 Structure of Digital Camera (DC).....	55
8.2.2 Calibration of the DC .....	57
8.2.2.1 Regression Method.....	58
8.2.2.2 Look-Up-Table Method.....	59

8.2.2.3 PCA Method .....	61
8.2.2.4 SVD Method .....	63
8.2.3 Other Factors Improving the Accuracy of the Camera Calibration .....	63
8.2.3.1 Illumination.....	64
8.2.3.2 Training Set.....	65
8.2.3.3 Image Acquisition .....	66
8.2.3.4 Spatial Variation.....	68
Chapter II. Quality Control of Universal Camouflage Samples .....	70
1. Universal Camouflage Pattern .....	70
2. Color Measurement and Data Analysis .....	71
2.1 Tristimulus Values .....	71
2.2 Chromatic Adaptation.....	76
2.3 Color Difference Evaluation .....	77
2.4 Variations in the Color of the Samples .....	80
3. Conclusion .....	82
Chapter III. Variations due to the Measurements with Spectrophotometer .....	83
1. BCRA Tiles and Color Measurement.....	83
2. Endeavor to Correct the Spectrum .....	90

3. Data Analysis, Results and Discussion.....	92
4. Conclusion .....	98
Chapter IV. DigiEye System .....	99
1. Introduction of the DigiEye System.....	99
2. Variability within the DigiEye System and Correction.....	102
2.1 Spatial Non-Uniformity of Nikon D90.....	102
2.2 Spatial Non-Uniformity of DigiEye Illumination Chamber .....	104
2.3 Time Difference Variance.....	117
3. Conclusion .....	126
Chapter V. Calibration of the LCD Monitor.....	126
1. Variations in the LCD Color Management.....	126
1.1 Variation of the Spectrophotometer.....	127
1.2 Non-Uniformity in the Display Surface.....	128
1.3 Variation caused by Eye One Orientation.....	133
2. LCD Calibration Method .....	134
3. Conclusion .....	140
Chapter VI. Calibration of the Digital Camera.....	140
1. Calibration via the ICC Profile.....	141

1.1 Color Measurement of the Test Chart.....	141
1.2 Algorithm Design .....	145
1.3 Results and Analysis .....	152
2. Calibration based on Other Methods .....	161
2.1 Simulation of the Camera Output .....	161
2.2 PCA.....	163
2.3 Regression .....	166
2.4 Two Illuminants.....	167
2.5 Calibration based on the Camouflage Samples .....	168
2.6 Data Analysis.....	169
2.7 Calibration Tool Using Camouflage Samples .....	173
3. Pass/Fail Judgment .....	176
3.1 Pass/Fail Judgment in the Device Space.....	176
3.2 Data Analysis and Discussion .....	182
3.3 Comparison of Judgment .....	188
4. Conclusion .....	189
Chapter VII. Software Design.....	190
1. Introduction .....	190

2. User Interface .....	193
3. Introduction of the Modules.....	198
3.1 Control of Gretag Eye One.....	198
3.2 Control of the Nikon D90 .....	199
3.3 Accessing the Raw Image of Nikon D90.....	204
3.4 Image Segmentation for Camouflage Pattern .....	209
3.5 Digital Color Management.....	217
3. Conclusion .....	217
Chapter VIII. Conclusions and Future Work.....	217
References.....	223
Appendices.....	232

## LIST OF TABLES

Table 1. $k_L$ , $c_1$ and $c_2$ Parameters used in the CIECAM02 Color Difference Models.....	26
Table 2. Viewing Condition Parameters for Different Surrounds .....	33
Table 3. Boundaries between the samples rated as ‘Pass’ and ‘Fail’ in CIELAB space .....	72
Table 4. Boundaries between the samples rated as ‘Pass’ and ‘Fail’ in CIELCH space Based on Response from One Expert Assessor at Natick Soldier Center .....	73
Table 5. Boundary between the ‘pass’ and the ‘fail’ from wrong von – Kries results .....	77
Table 6. Boundary from the max $\Delta E$ and Correct Ratio from ‘Fail’ Samples .....	79
Table 7. Boundary from Compressed $\Delta E$ and Correct Ratio from All Samples .....	79
Table 8. Boundary from the max $\Delta E$ with optimized $k_L$ and Correct Ratio from ‘Fail’ Samples .....	80
Table 9. $dL^*$ , $da^*$ and $db^*$ between SF600X and SF500 .....	86
Table 10. Intra - Variance of BCRA $L^*a^*b^*$ from SF400 .....	87
Table 11. Intra - Variance of BCRA $L^*a^*b^*$ from SF600 .....	87
Table 12. Intra - Variance of BCRA $L^*a^*b^*$ from SF600X .....	88
Table 13. Intra - Variance of BCRA $L^*a^*b^*$ from SF650 .....	88
Table 14. Inter - Variance of BCRA $L^*a^*b^*$ .....	89
Table 15. Inter - Variance of ColorChecker before Correction.....	92
Table 16. Inter - Variance of ColorChecker after Correction.....	93
Table 17. Inter-Variance of ColorChecker $L^*a^*b^*$ under Specular-Excluded Mode.....	95
Table 18. Inter-Variance of ColorChecker $L^*a^*b^*$ under Specular-Included Mode.....	96
Table 19. Inter-Variations of the CIEXYZ Tristimulus Values for Tiles S5, S6, S8 and S9 from Test 2 under Specular Excluded Mode and Specular Included Mode .....	97
Table 20. RGB from Nikon Image SDK before Spatial Correction .....	113
Table 21. RGB from Nikon Image SDK after Spatial Correction .....	114
Table 22. RGB from LibRaw before Spatial Correction.....	115
Table 23. RGB from LibRaw after Spatial Correction .....	116
Table 24. RGB values from Nikon D90 that indicate the variation of the camera .....	121
Table 25. RGB values from the video camera.....	125
Table 26. Color Differences from the Dataset to Calibrate the Monitor.....	139
Table 27. Comparison of Two Color Patches.....	144
Table 28. Average and Maximum Color Difference from Various Combination of Training and Testing Dataset Employed .....	154
Table 29. Average and Maximum Color Difference from Various Combinations of Training and Testing Data Set using Xrite <sup>®</sup> ProfileMaker 4 .....	155
Table 30. Original and Converted CIELAB Value for 5 Camouflage Samples.....	159
Table 31. Converted CIELAB of the Standard Sample with Noise.....	160
Table 32. Relationship between $\Delta L^*$ , $\Delta a^*$ and $\Delta b^*$ and the number of Eigenvectors used....	166
Table 33. $\Delta L^*$ , $\Delta a^*$ and $\Delta b^*$ of Samples when Calibrated using the Digitizer Chart .....	169

Table 34. $\Delta L^*$ , $\Delta a^*$ and $\Delta b^*$ of Samples when Calibrated using the Colorchecker Chart .....	170
Table 35. $\Delta L^*$ , $\Delta a^*$ and $\Delta b^*$ of the color patches in the two test charts .....	171
Table 36. $\Delta L^*$ , $\Delta a^*$ and $\Delta b^*$ of Samples for Calibration based on the Camouflage Samples .....	172
Table 37. $\Delta E_{00}^*$ from Various Methods for Calibrations using the Camouflage Samples .....	172
Table 38. Converted CIELAB of the Standard Sample with Noise .....	177
Table 39. Results of the Pass / Fail Judgments in the Device Space .....	183
Table 40. Comparison of the Convex Hull Volume .....	184
Table 41. Comparison of the Average and Standard Deviation .....	185
Table 42. Relation between $\alpha$ and Number of the Mistakenly Judged ‘Fail’ Samples .....	186
Table 43. Difference between Max and Min after Image Segmentation .....	214
Appendix Table A. CIELAB* Values of All Samples .....	233
Appendix Table B. CIELAB* based on the Wrong Von – Kries Adaptation .....	236
Appendix Table C. Variances in the Repeated Color Measurement of UCP Samples .....	240
Appendix Table D. Original and Converted Tristimulus of the 22 Training Samples Colors in the Calibration Tool .....	243
Appendix Table E. Average RGB values of the Samples after Image Segmentation .....	245
Appendix Table 1. Boundaries between the Samples Rated as ‘Pass’ and ‘Fail’ in CIELAB Space from PFJDO Result .....	249
Appendix Table 2. Boundaries between the Samples Rated as ‘Pass’ and ‘Fail’ in CIELCH Space from PFJDO Result .....	249
Appendix Table 3. Boundaries between the Samples Rated as ‘Pass’ and ‘Fail’ in CIELAB Space from PFJND Result .....	249
Appendix Table 4. Boundaries between the Samples Rated as ‘Pass’ and ‘Fail’ in CIELCH Space from PFJND Result .....	250
Appendix Table 5. Relation between $\alpha$ and Number of the Mistakes from PFJDO and PFJND .....	255
Appendix Table 6. Comparison of the Correct Ratio under Different Methods .....	255

# LIST OF FIGURES

Figure 1. Schematic Structure of the Eye .....	1
Figure 2. Cross Section of the Retina .....	4
Figure 3. The Spectral Energy Distribution for Average Daylight of D65 .....	5
Figure 4. The Color versus Temperature of an Ideal Black Body .....	6
Figure 5. Specular Reflection (left) and Diffuse Reflection (right) .....	8
Figure 6. Change of Refractive Index at a Boundary .....	9
Figure 7. Scattering of the Incident Light .....	10
Figure 8. Determination of the Object Color .....	11
Figure 9. Measurement of Trichromatic Coordinates of a Light Source .....	12
Figure 10. Color Matching Functions $x$ , $y$ , $z$ of the CIE 1931 Observer vs. Color Matching Function $x_{10}$ , $y_{10}$ , $z_{10}$ of the CIE 1964 Standard Colorimetric Observer .....	14
Figure 11. Coordinates of CIELAB* Space .....	16
Figure 12. Unit Color Discrimination Ellipses in the CIELAB's $a^*b^*$ Plane .....	19
Figure 13. Components of the Viewing Field .....	29
Figure 14. Profile Connection Space (PCS) .....	38
Figure 15. ICC Profile Structure .....	40
Figure 16. Matrix based Profile .....	40
Figure 17. Look-Up-Table based Profile .....	41
Figure 18. Structure of the Flatbed CCD Scanner .....	42
Figure 19. Schematic Representation of a Colorimeter .....	46
Figure 20. Structure of DataColor SF500 .....	48
Figure 21. The effect of the Surface Texture on the Appearance of an Object .....	49
Figure 22. Diffuse Sphere Reflectance Modes .....	49
Figure 23. Schematic Representation of LCD Monitors .....	52
Figure 24. Graphical Representation of the Forward Calibration Model .....	52
Figure 25. Typical Block Diagram of a Digital Still Camera .....	56
Figure 26. Typical Arrangement of a Point-and-shoot Digital Still Camera .....	57
Figure 27. Trilinear Interpolation .....	59
Figure 28. Tetrahedron Division .....	61
Figure 29. Recommended Illumination / Viewing Geometries for the Measurement of Object Color .....	65
Figure 30. Gretag ColorChecker DC Chart .....	66
Figure 31. Spectra of the RGB filters in Nikon D90 .....	67
Figure 32. Factors related with the Image Illumination .....	69
Figure 33. Universal Camouflage Sample with 'Key' Pattern .....	71
Figure 34. Convex Hulls from the "Pass" Samples of Three Colors in CIELAB .....	74

Figure 35(a-c). Convex Hulls from the Samples Rated as “Pass” of Three Colors in the CIEXYZ Space - Foliage Green (a), Urban Gray (b), Desert Sand (c).....	75
Figure 36. Variances vs. Absolute Average CIELAB values for Camouflage Samples (Left) and Variances vs. Absolute of Average CIELAB values for BCRA Tiles (Right).....	81
Figure 37. BCRA Tiles.....	84
Figure 38. Reflectance Spectra of BCRA Tiles based on SF500 under Specular-Excluded Mode (Dash Line) and Reflectance Spectra of BCRA Tiles under Specular-Included Mode (Solid Line).....	85
Figure 39. Snapshot of the Software Application.....	91
Figure 40. Spectra of S9 from four Datacolor Spectrophotometers.....	94
Figure 41. Spectra of BCRA yellow tile from Four Datacolor Spectrophotometers.....	95
Figure 42. DigiEye System.....	99
Figure 43. Possible Applications of the DigiEye System in the Food Industry.....	100
Figure 44. a. Schematic Representation of the d/0 °Illumination / Viewing Setting Employed inside the DigiEye Illumination Chamber b. Schematic Representation of the 45 °Illumination / Viewing Setting Employed inside the DigiEye Illumination Chamber.....	101
Figure 45. Field Size of Nikon D90 when it is on top of DigiEye Illumination Chamber....	103
Figure 46. Distribution of the Green Channel of the Illumination Board Used Outdoor.....	104
Figure 47. Distribution of the RGB Channels for the Uniformity Board at 1/3s and F11 Red Channel (a), Green Channel (b) and Blue Channel (c).....	106
Figure 48. Distribution of the Green Channel for the Uniformity Board with 1/2s and F13.....	107
Figure 49. Distribution of the Green Channel for the Uniformity Board with 1/5s and F9..	108
Figure 50. Distribution of the Green Channel when the Minimal Focal Length is Used.....	109
Figure 51. Distribution of the Green Channel when the Maximal Focal Length is Used.....	109
Figure 52. Distribution of the Green Channel when Nikon Image SDK is Used.....	111
Figure 53. Images of Digitizer Test Chart at Different Position in the DigiEye.....	112
Figure 54. PR670 for the Measurement of Illumination inside DigiEye.....	118
Figure 55. Variation of the Illumination of DigiEye Illumination Chamber.....	119
Figure 56. Change of the Spectra when LEDs are Used.....	120
Figure 57. Paper and the Selected Positions to Sample the Average of RGB Values.....	120
Figure 58. RGB values from the top left corner.....	123
Figure 59. GretagMacbeth Eye One and its Cradle.....	127
Figure 60. Snapshot of the Software Application to Verify the Spatial Variation.....	129
Figure 61(a-f). Temporal Variation of Y Channel Distribution.....	133
Figure 62. Relationship between CIEXYZ values and the Eye One Orientation.....	133
Figure 63. Snapshot of the Monitor Calibration UI.....	134
Figure 64. Red Tone Reproduction Curve of the Eizo ColorEdge CG211.....	137
Figure 65. GretagMacbeth Colorchecker (top) and Verivide Digitizer (bottom).....	142

Figure 66. Captured Image of Selected Set of Color Patches on the Colorchecker Testchart of DigiEye without Mirror Reflection Boards (left) and with Mirror Reflection Boards (right).....	144
Figure 67. RG Projection of Division of the Device Space into Regions .....	150
Figure 68. Comparison between the Color Differences based on the Three-Component-Matrix and LUT .....	153
Figure 69. Distribution of the Color Differences under Different Conditions .....	156
Figure 70. Difference in the Distribution of Colors in Two Test Charts in the Low Lightness .....	157
Figure 71. Difference in the Distribution of Colors in Two Test Charts in the Blue Region .....	157
Figure 72. Unsmooth Surface of Gamut Boundary based on Local Polynomial Regression .....	158
Figure 73. Spectral Power Distribution of D75 and U30 after Normalization .....	163
Figure 74. Image of the Calibration Tool based on the Camouflage Samples .....	173
Figure 75. Distribution of Absolute $\Delta L^*$ , $\Delta a^*$ and $\Delta b^*$ for the Calibration Tool.....	175
Figure 76. Convex Hulls from the Simulated RGB Values of the ‘Pass’ Samples Foliage Green (a), Urban Gray (b), Desert Sand (c).....	178
Figure 77. Image of the Calibration Tool used for P/F Ratings based on the Device Space	180
Figure 78. Snapshot of the Sample used in the Computation of Variation .....	185
Figure 79. Convex Hull of Urban Gray before (Top) and after (Bottom) Expansion .....	187
Figure 80. C# and .Net Framework.....	191
Figure 81. Snapshot of the Main UI.....	193
Figure 82. Snapshot of the Camera Setup UI .....	195
Figure 83. Snapshot of the Camera Calibration UI.....	196
Figure 84. Snapshot of the UI to Setup the Options.....	197
Figure 85. Snapshot of the Sample Capturing UI .....	197
Figure 86. Flowchart of the Process on Nikon D90.....	200
Figure 87. Schematic Representation of MAID .....	201
Figure 88. Layers inside MAID .....	201
Figure 89. Bayer Pattern of the CFA of D90 Image Sensor from Nikon Document .....	205
Figure 90. CCD output of the Top Left Corner .....	205
Figure 91. Structure of D90 Raw File .....	206
Figure 92. Relation between the Raw Pixel Value and the Pixel Value after Conversion....	209
Figure 93. Output from Transfer Curve (Left) vs. that from the Linear Conversion (Right) .	209
Figure 94. Histogram of Average Green Values of Macroblocks with Initial and Final Positions of Three Colors .....	211
Figure 95. Macro-block to be Removed .....	212
Figure 96. Original Image and its Reconstruction without Step 11 .....	213
Figure 97. Original Image and its Reconstruction with Step 11.....	213
Appendix Figure 1. Convex Hulls from the “Pass” Samples of Three Colors in CIELAB based on PFJND.....	251

Appendix Figure 2(a-c). Convex Hulls from the Samples Rated as “Pass” of Three Colors in the CIEXYZ Space based on PFJND - Foliage Green (a), Urban Gray (b), Desert Sand (c).....252

Appendix Figure 3. Convex Hulls from the “Pass” Samples of Three Colors in CIELAB based on PFJDO.....253

Appendix Figure 4(a-c). Convex Hulls from the Samples Rated as “Pass” of Three Colors in the CIEXYZ Space based on PFJDO - Foliage Green (a), Urban Gray (b), Desert Sand (c).....254

# Chapter I. Literature Review

## 1. The Human Eye

Human eyes can detect the light from the outside world and transform the light signal into the nerve impulse. Figure 1 shows the schematic structure of the eye. The main components of the eye include sclera, cornea, lens, iris, vitreous humor, retina, macula, and fovea. [1, 2]

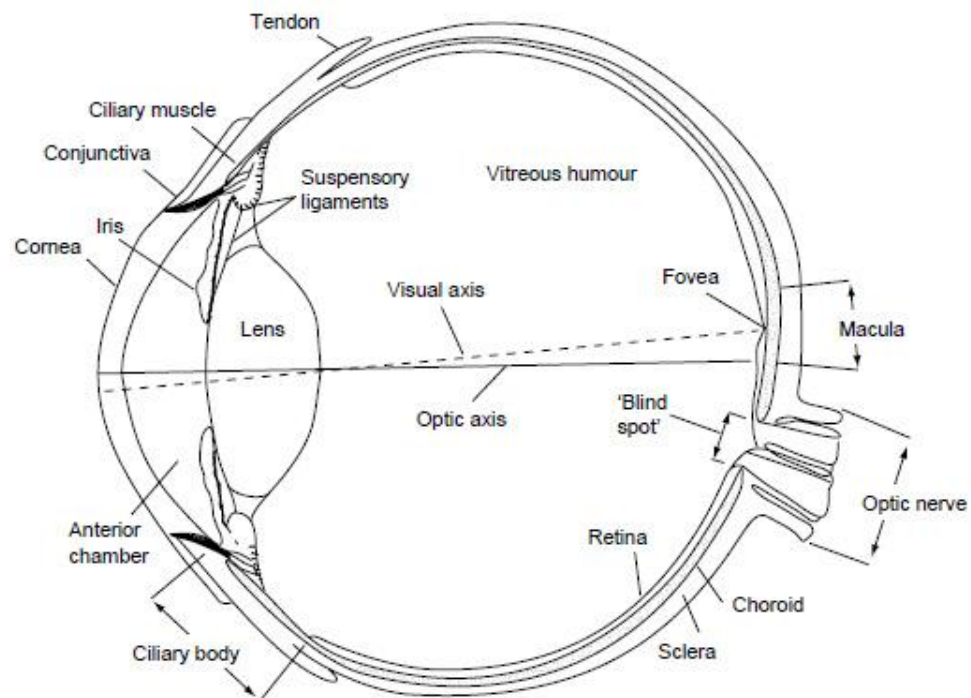


Figure 1. Schematic Structure of the Eye [2]

The sclera, also known as the white of the eye, is the opaque, fibrous, protective outer layer of the eye. The cornea is the transparent front part of the eye that covers the iris, pupil, and anterior chamber. The lens is a transparent biconvex structure in the eye. Both the cornea and

the lens refract light and focus the image on the retina. The iris is a thin and circular structure in the eye, responsible for controlling the diameter and size of the pupils and the amount of the light entering the eye. The vitreous humor is the clear gel, filling the space between the lens and the retina. The retina is a light-sensitive tissue lining the inner surface of the eye, which transforms the light signal on the retina into the nerve impulses. There are two types of photosensitive receptors in the retina, i.e., cones and rods. The macula is an oval-shaped highly pigmented yellow spot near the center of the retina, with a diameter of around 5mm. The fovea, which is located in the center of the macula region of the retina, is responsible for sharp central vision [1, 2].

There are roughly seven million cones located in the fovea of the eyes [2]. The rods gradually appear when moving away from the fovea, which is approximately at an angle subtended to the retina of five degrees, and there are no rod cells in the fovea. The macula, which subtends approximately 20 degrees away from the visual axis, is a larger region of the retina [2].

Rods are responsible for vision at low levels of illumination (less than 0.1 lux), while the cones do not respond on such low illumination levels. At higher illumination (above about 500 lux), the cones start to function and provide us with both color vision and the ability to see fine detail, and the rods terminate their functions. Between these two illumination levels, human vision involves a mixture of rod and cone functions [3].

## **1.1 Eye, Brain and the Color Vision**

Color is the result of a physiological-based visual perception requiring the eye-brain combination. The interaction of visible light with rods/cones is the first stage that leads to a perception of what we call color. Rods/cones translate the visual image into the neural impulses. The passage of the nerve impulse through the retinal tissue involves a series of complex interactions between adjacent neurons which improve the signal-to-noise ratio. Figure 2 shows the schematic cross section of the retina. Retinal horizontal cells integrate and regulate the input from the cones/rods. Ganglion cells receive the visual information from the cones/rods via the intermediate neuron cells: horizontal cells, bipolar cells and amacrine cells, although in some cases the pathway from rods and cones to ganglion cells may vary. Ganglion cells transmit the visual information from retina to the brain.

## **2. Essential Requirements for Color Vision**

Visible light rays may be modified in a number of ways by objects. The most common is via selective absorption or scattering of light. This modified light may then enter the human eye and be transformed into electrical signals that are then interpreted by the brain. So, the production of color requires a source of light, an object to be illuminated (not required for a self luminous bodies) and the eye and the brain to perceive the color. [4, 5]

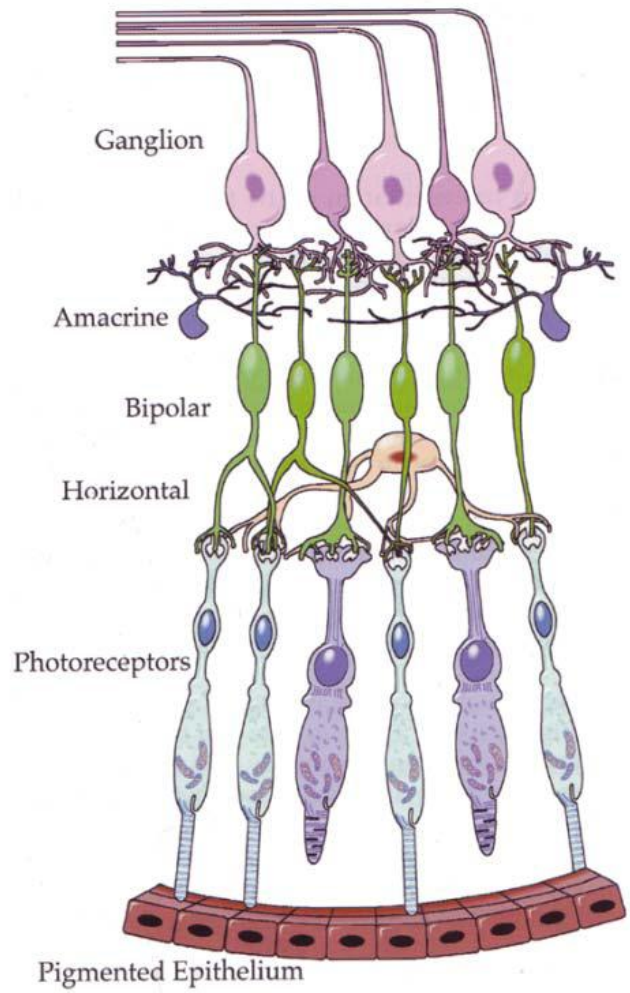


Figure 2. Cross Section of the Retina [3]

## 2.1 Light Sources

The visible spectrum is a range of electromagnetic energies with wavelengths ranging from 380nm to 750nm. The light that is ranged between 200nm and 380nm is called the ultraviolet and the light with the wavelength between 750nm and 1mm is denoted as the near infrared.

Both the ultraviolet and the infrared rays are invisible to the human eyes because humans' lack receptors that are sensitive outside approximately 380-750nm. [4, 5, 6]

A number of different types of light sources emit light that is white or close to white, for example, the sun, incandescent light bulbs, fluorescent lamps, etc. Light sources can be described in terms of their relative energy emitted at each wavelength. Figure 3 shows the spectral power distribution of the average daylight at noon.

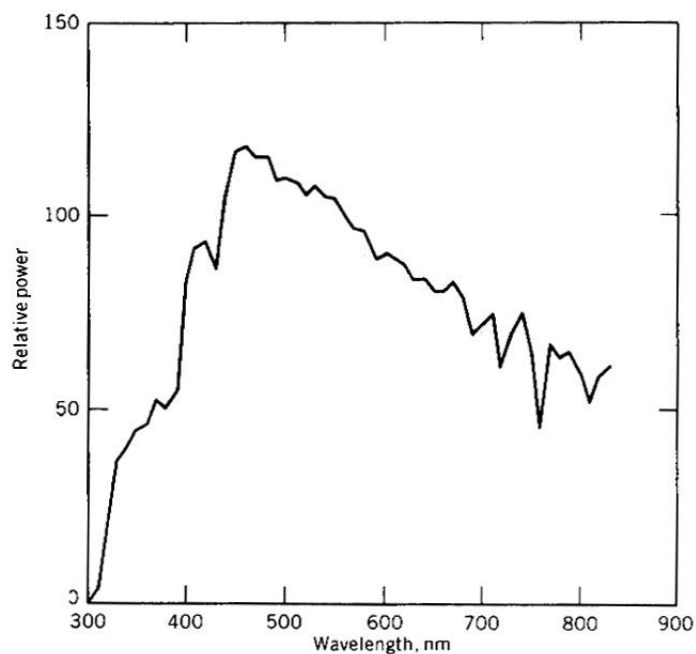


Figure 3. The Spectral Energy Distribution for Average Daylight of D65 [4]

Black-bodies are a special group of light sources. They look black only when they are cold. When they are heated, they glow like the metals. Black bodies are important because their spectral energy distribution, i.e., their color, is not related to their composition and only

depend on their temperature. The temperature of the black body is called their correlated color temperature (CCT). Figure 4 shows the relation between the color and the temperature of the black body radiator.

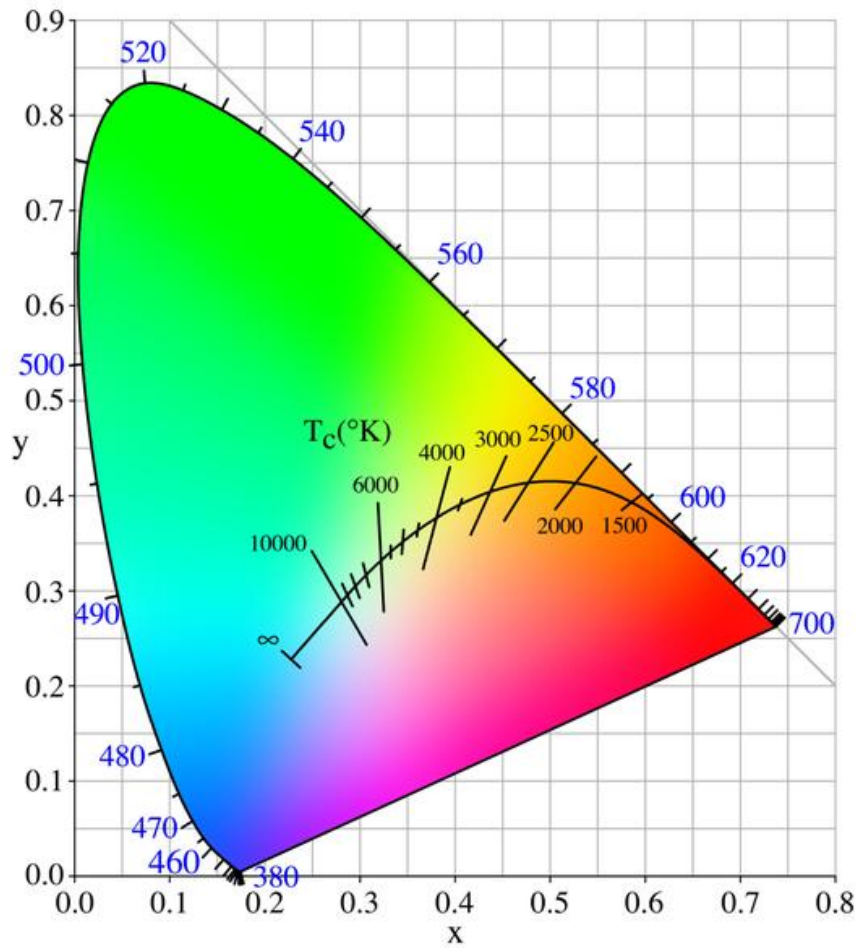


Figure 4. The Color versus Temperature of an Ideal Black Body [3]

Non-black body light sources can be approximated by the CCT of an idealized black body.

Several standard illuminants have been defined for use in describing color by the

Commission internationale de l'éclairage (CIE). For example, CIE illuminant A, is simulated with a tungsten filament lamp operating at a color temperature of 2854K; CIE illuminant B, with a color temperature of about 4874K, is an approximation of noon sunlight; CIE illuminant C, with a color temperature of about 6774K, is an approximation of average daylight; CIE D65, with a color temperature of about 6504K, is an approximation of noon daylight; and CIE D75, with a color temperature of about 7504K, is an approximation of north sky daylight. [1]

## **2.2 Interaction between Materials and Light**

### **2.2.1 Reflection**

Reflection is the change in direction of a light beam at the boundary of two different media, where the direction of the beam changes in relation to the direction of the beam originating from the source. There are two kinds of light reflection: specular reflection and diffuse reflection. [1, 4]

In specular reflection, the light from a single incoming direction is reflected into a single outgoing direction. The direction of the incoming light and that of the outgoing light are identical in regards of the surface normal, as shown in Figure 5a.

In diffuse reflection, the reflection of the light from a surface is such that an incident ray is reflected at many angles rather than just one angle, as shown in Figure 5b.

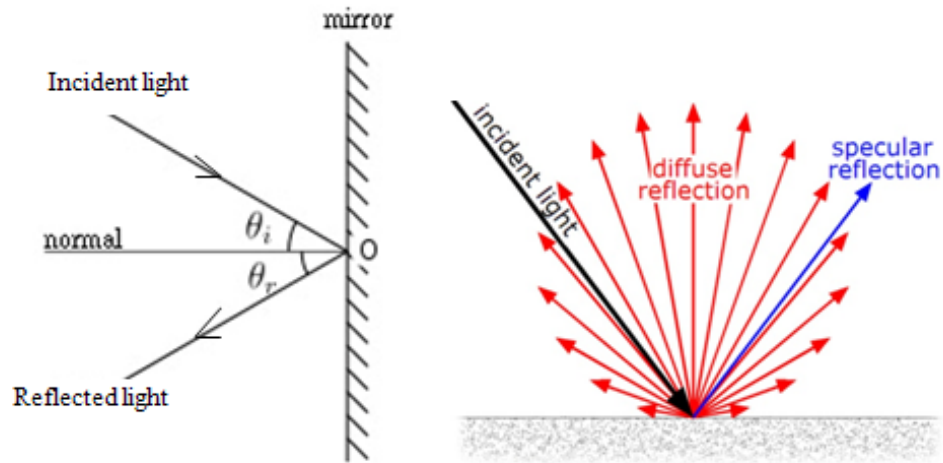


Figure 5. Specular Reflection (left) and Diffuse Reflection (right)

### 2.2.2 Transmission

Light can be transmitted unchanged through a transparent material. If the material is colorless and non-scattering, all the light is transmitted except for a small amount which is reflected at the boundary of two media. The reflection occurs whenever there is a change in refractive index when the light travels from one media into another media. At every boundary between two different media, light changes speed. As a result, a small fraction of the light is reflected and the direction of the light is changed if the incident light is not normal to the plane of the material, as shown in Figure 6.

The Snell's law, shown in equation (1) can be used to determine the refractive index or the angle of refraction in various media.

$$\frac{\sin\theta_1}{\sin\theta_2} = \frac{v_1}{v_2} = \frac{n_2}{n_1} \quad (1)$$

Here  $\theta_1$  is the angle of incidence,  $\theta_2$  is the angle of refraction;

$v_1$  and  $v_2$  are the speed of incident and refracted light;

$n_1$  and  $n_2$  are the refractive indices of the two media. [6]

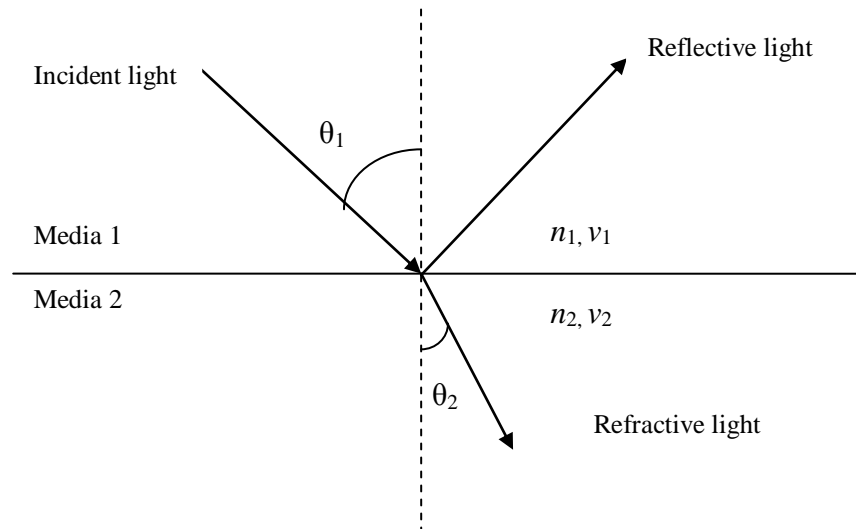


Figure 6. Change of Refractive Index at a Boundary

### 2.2.3 Absorption

Light may be absorbed in a media in addition to being reflected or transmitted. If the material absorbs part of the light and the remaining light is transmitted, it appears colored and is called translucent; if the entire incident light is completely absorbed, the material appears black; if no light is allowed to transmit through the material, it is considered to be opaque. [6]

According to the Beer's law, when light travels through a substance, the logarithm of the transmission,  $T$ , is proportional to the distance that the light travels through the material,  $l$ , as shown in equation (2).

$$T = e^{-kl} \quad (2)$$

Here  $k$  is the absorption coefficient, and is dependent on the material.

### 2.2.4 Scattering

Light may be absorbed, reemitted and scattered when it passes through the matte, some of the light travels in one direction and some travels in another direction, until ultimately the light travels in many different directions. This is known as scattering. Scattering is caused by light falling on small particles, whose refractive index is different from that of their surrounding material. This is schematically shown in Figure 7 [4, 5].

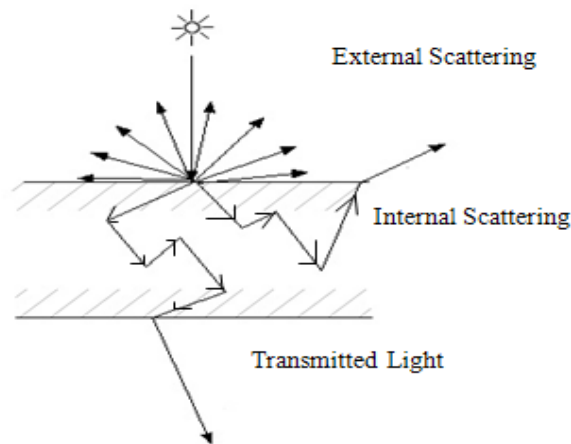


Figure 7. Scattering of the Incident Light

## 2.2.5 Determination of Object Color

The effect of an object on light can be described by its spectral transmittance or reflectance curve. Figure 8 schematically shows the methodology employed to determine the object color. If the spectral power distribution (SPD) of the illumination and the object's reflectance are given, the object color can be obtained via the multiplication on a wavelength - by - wavelength basis of these functions. [4, 5]

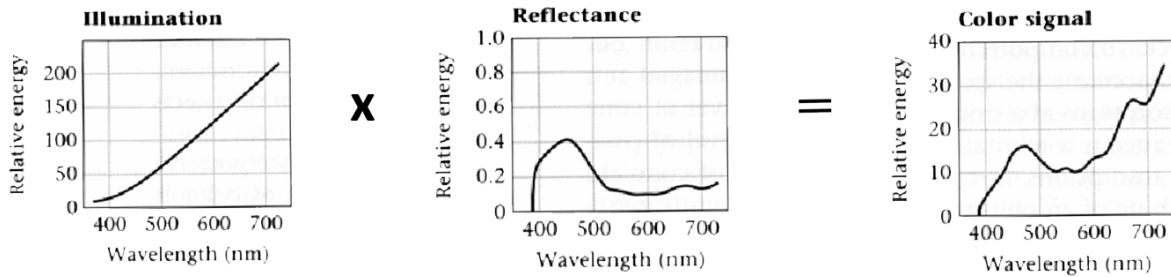


Figure 8. Determination of the Object Color [4]

## 3. Colorimetry

Colorimetry is the science and technology used to quantify and describe physically the human color perception, with specifying, numerically, the color of a physically defined visual stimulus in a way that:

- (a) When viewed by an observer with normal color vision, under the fixed viewing conditions, stimuli with the same specification are similar;
- (b) Stimuli that are similar have the same specification;

(c) The numbers comprising the specification are continuous functions of the physical parameters defining the spectral radiant power distribution of the stimulus [1].

### 3.1 CIE System

The CIEXYZ system is developed from the concept of additive color mixing, based on separate experiments by Wright and Guild in which colors were matched by mixing colored lights [7].

Figure 9 schematically shows the experimental setup employed to determine the trichromatic coordinates of a colored light source. A 2° visual field was used so that the light was only incident on the fovea. Primary colors were chosen to be monochromatic. The observation field was divided into two sections; one of them was illuminated by a monochromatic source, and the other was illuminated under the combination of the three primary colored sources. The observer could tune the amount of each primary source until the two colors matched [4].

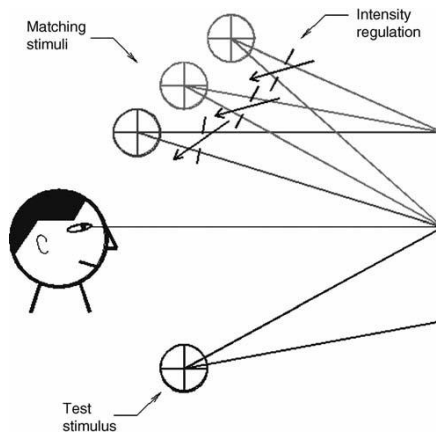


Figure 9. Measurement of Trichromatic Coordinates of a Light Source [8]

The results of these experiments, after suitable normalization, were adopted by the CIE and are known as the CIE 1931 standard observer, defined by the color matching functions  $\bar{x}(\lambda)$ ,  $\bar{y}(\lambda)$ ,  $\bar{z}(\lambda)$ , in the range of  $\lambda = 380$  to  $780$  nm at wavelength intervals of  $\Delta\lambda = 5$  nm as depicted in Figure 10 [4]. In 1964, the CIE recommended an alternative set of standard color-matching functions, using a  $10^\circ$  field of view, denoted by  $\bar{x}_{10}(\lambda)$ ,  $\bar{y}_{10}(\lambda)$ ,  $\bar{z}_{10}(\lambda)$ , as a supplement to those of the 1931 standard observer for use whenever more accurate correlation with visual color-matching in fields of large angular subtense is desired. Figure 10 also shows the comparison between color matching functions of the CIE 1931 observer and color matching functions of the CIE 1964 standard colorimetric observer [4].

Given the spectral power distribution of the light source  $S(\lambda)$ , the color matching conditions for two objects with different spectral reflectance properties  $\beta_1(\lambda)$  and  $\beta_2(\lambda)$ , can be shown in equation (3),  $\lambda$  stands for the wavelength:

$$\begin{cases} \int_{\lambda} \beta_1(\lambda)S(\lambda)\bar{x}(\lambda)d\lambda = \int_{\lambda} \beta_2(\lambda)S(\lambda)\bar{x}(\lambda)d\lambda \\ \int_{\lambda} \beta_1(\lambda)S(\lambda)\bar{y}(\lambda)d\lambda = \int_{\lambda} \beta_2(\lambda)S(\lambda)\bar{y}(\lambda)d\lambda \\ \int_{\lambda} \beta_1(\lambda)S(\lambda)\bar{z}(\lambda)d\lambda = \int_{\lambda} \beta_2(\lambda)S(\lambda)\bar{z}(\lambda)d\lambda \end{cases} \quad (3)$$

The coordinates of the 1931 CIE system are known as the CIE tristimulus values, denoted X, Y and Z, which are defined in equation (4): [4]

$$\begin{cases} X = k \int_{\lambda} \beta(\lambda)S(\lambda)\bar{x}(\lambda)d\lambda \\ Y = k \int_{\lambda} \beta(\lambda)S(\lambda)\bar{y}(\lambda)d\lambda \\ Z = k \int_{\lambda} \beta(\lambda)S(\lambda)\bar{z}(\lambda)d\lambda \end{cases} \quad (4)$$

Here  $k$  is the normalization factor which is defined as  $k = \frac{100}{\int_{\lambda} S(\lambda)\bar{y}(\lambda)d\lambda}$

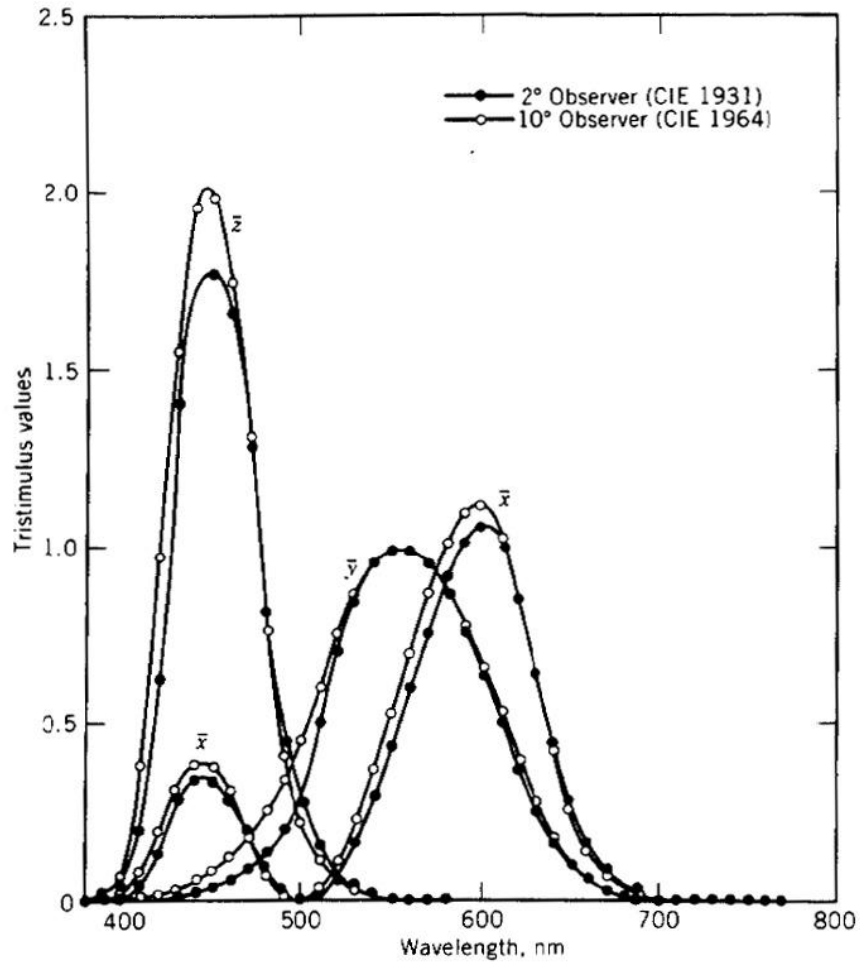


Figure 10. Color Matching Functions  $\bar{x}$ ,  $\bar{y}$ ,  $\bar{z}$  of the CIE 1931 Observer vs. Color Matching Function  $\bar{x}_{10}$ ,  $\bar{y}_{10}$ ,  $\bar{z}_{10}$  of the CIE 1964 Standard Colorimetric Observer [5]

### 3.2 CIE 1976 ( $L^*u^*v^*$ ) Color Space

CIE1976  $L^*u^*v^*$  is an approximately uniform color space, with parameters  $L^*$ ,  $u^*$  and  $v^*$  defined in equation (5). The uniform color space means that a change of the same amount in the color value should lead to a change of the same visual experience.

$$\begin{cases} L^* = 116f\left(\frac{Y}{Y_n}\right) - 16 \\ u^* = 13L^*(u' - u'_n) \\ v^* = 13L^*(v' - v'_n) \end{cases} \quad (5)$$

$$\text{Where } f\left(\frac{Y}{Y_n}\right) = \begin{cases} \left(\frac{Y}{Y_n}\right)^{1/3} & \frac{Y}{Y_n} > 0.008856 \\ 903.3\left(\frac{Y}{Y_n}\right) & \frac{Y}{Y_n} \leq 0.008856 \end{cases}$$

$$u' = \frac{4X}{X+15Y+3Z} \quad v' = \frac{9X}{X+15Y+3Z}$$

$$u'_n = \frac{4X_n}{X_n+15Y_n+3Z_n} \quad v'_n = \frac{9X_n}{X_n+15Y_n+3Z_n}$$

Here  $L^*$  represents the lightness of the object color. The tristimulus values  $X$ ,  $Y$ ,  $Z$  are the color stimuli of the object. The tristimulus values  $X_n$ ,  $Y_n$ ,  $Z_n$  are the color stimuli of the nominally white object. Usually, the white object-color stimulus is given by the spectral radiant power of one of the CIE standard illuminants, for example D65, reflected into the observer's eye by the perfect reflecting diffuser. Under these conditions,  $X_n$ ,  $Y_n$ ,  $Z_n$  are the tristimulus values of the standard illuminant with  $Y_n$  arbitrarily set to 100. [1, 4, 5, 9]

### 3.3 CIE 1976 ( $L^*a^*b^*$ ) Color Space

The CIE1976  $L^*a^*b^*$  color space, schematically shown in Figure 11, is a color-opponent space with dimension  $L^*$  representing lightness ( $L^* = 0$  denotes perfect black and  $L^* = 100$  indicates a perfect diffuser),  $a^*$  represents redness-greenness (negative values indicate greenness while positive values indicate magenta) and  $b^*$  represents yellowness-blueness (negative values indicate blueness and positive values indicate yellowness), all parameters being based on a nonlinear compression of CIE XYZ color space coordinates. This color

space is also an approximately uniform color space.

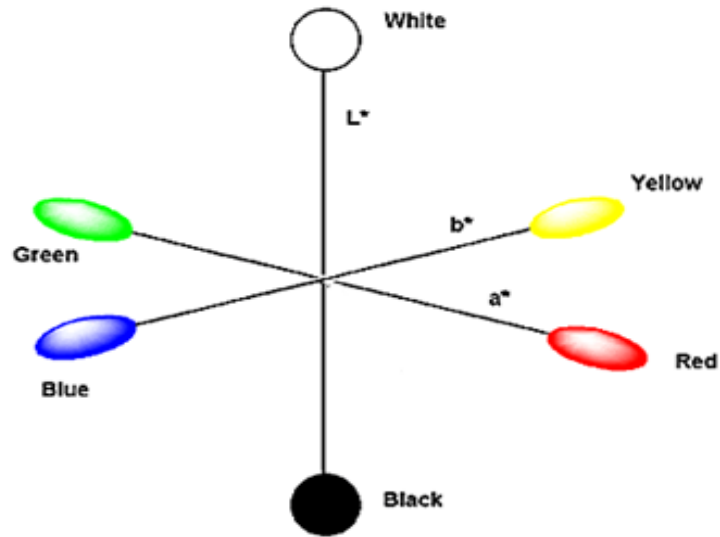


Figure 11. Coordinates of CIELAB\* Space [5]

The colorimetric parameters in the CIE 1976 ( $L^*a^*b^*$ ) color space are defined in equation

(6):

$$\begin{cases} L^* = 116f\left(\frac{Y}{Y_n}\right) - 16 \\ a^* = 500\left(f\left(\frac{X}{X_n}\right) - f\left(\frac{Y}{Y_n}\right)\right) \\ b^* = 200\left(f\left(\frac{Y}{Y_n}\right) - f\left(\frac{Z}{Z_n}\right)\right) \end{cases} \quad (6)$$

Here

$$f\left(\frac{X}{X_n}\right) = \begin{cases} \left(\frac{X}{X_n}\right)^{1/3} & \frac{X}{X_n} > 0.008856 \\ 7.787\left(\frac{X}{X_n}\right) + \frac{16}{116} & \frac{X}{X_n} \leq 0.008856 \end{cases}$$

$$f\left(\frac{Y}{Y_n}\right) = \begin{cases} \left(\frac{Y}{Y_n}\right)^{1/3} & \frac{Y}{Y_n} > 0.008856 \\ 7.787\left(\frac{Y}{Y_n}\right) + \frac{16}{116} & \frac{Y}{Y_n} \leq 0.008856 \end{cases}$$

$$f\left(\frac{Z}{Z_n}\right) = \begin{cases} \left(\frac{Z}{Z_n}\right)^{1/3} & \frac{Z}{Z_n} > 0.008856 \\ 7.787\left(\frac{Z}{Z_n}\right) + \frac{16}{116} & \frac{Z}{Z_n} \leq 0.008856 \end{cases}$$

The tristimulus values  $X, Y, Z$  are the color stimuli of the object. The tristimulus values  $X_n, Y_n, Z_n$  are the color stimuli of the nominally white object. Usually,  $X_n, Y_n, Z_n$  are the tristimulus values of the standard illuminant with  $Y_n$  set to 100. [1, 4, 9, 10]

## 4. Estimation of Color Difference

If the perceptual difference between two colors can be represented as the Euclidean distance between their coordinates in the color space and the dimensions of the color space are orthogonal, that color space is a perceptually uniform space. The generation of a perceptually uniform color space is a key object in the scientific color research. In absence of a completely uniform color space, various color difference equations have been proposed over the last several decades [9] and some of the main equations are briefly described here.

### 4.1 CIELAB color difference

In the CIELAB color space, the basic  $\Delta E_{ab}^*$  color difference model is defined as that shown in equation (7). [1, 5, 11]

$$\Delta E_{ab}^* = \sqrt{\Delta L^{*2} + \Delta a^{*2} + \Delta b^{*2}} \quad (7)$$

$$\text{Here } \Delta L^* = L_b^* - L_s^*$$

$$\Delta a^* = a_b^* - a_s^*$$

$$\Delta b^* = b_b^* - b_s^*$$

The Subscript 's' refers to the standard sample, and subscript 'b' denotes the batch color.

Figure 12 shows the unit difference volumes in the  $a^*b^*$  surface, and these volumes are ellipses. The visual difference between any point in each ellipse boundary and the center of that ellipse is the same. The ellipses, however are of different volumes and have various orientations. If the CIELAB space is a perceptually uniform color space, these would be circles of the same size instead of ellipses with different volumes. This figure demonstrates that the CIELAB is not a perceptually uniform space and the CIELAB color difference equation is not accurate enough to describe the color difference through the whole color space. Likewise, CIELUV is not a perceptually uniform space either.

In terms of psychophysical percepts, chroma, hue and lightness, the following observations could be made based on Figure 12:

- Chroma: it can be seen that for highly chromatic colors, i.e., regions far away from the point of origin, the ellipsoids are usually larger than those which are near the central point;
- Hue: the ellipsoids change their sizes and directions at different hue angles. For example, the ellipsoids at the negative region of  $b^*$  do not point to the point of origin;

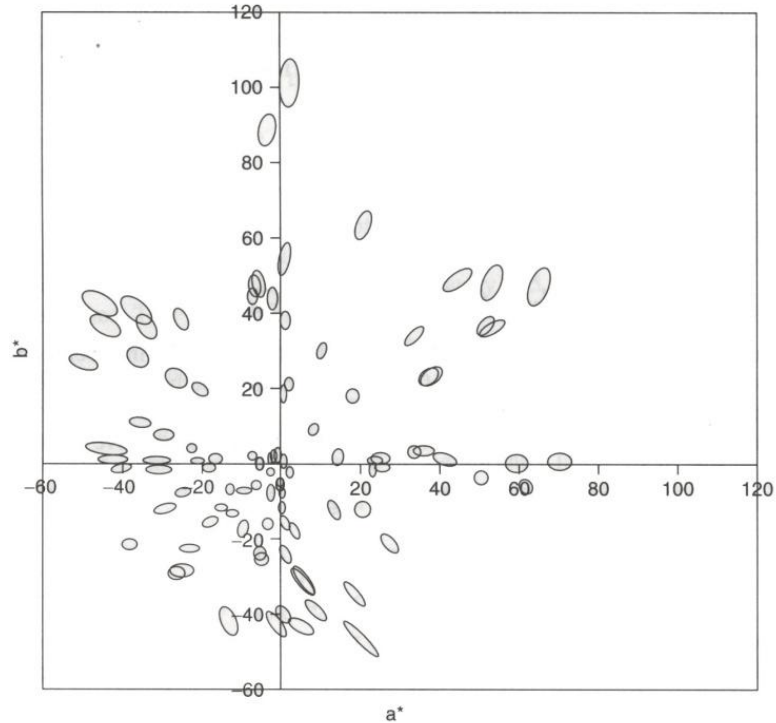


Figure 12. Unit Color Discrimination Ellipses in the CIELAB's  $a^*b^*$  Plane [9]

Owing to these issues, a number of additional color difference equations were proposed to improve the performance of the CIELAB based color differences.

## 4.2 CMC

The CMC ( $l:c$ ) equation was developed from the JPC79 colour-difference formula which was based on the visual assessment of 600 polyester samples around 55 color standards from 8 observers and 8000 pairs around 600 centers assessed by a single observer. In 1984, the CMC ( $l:c$ ) equation, shown in equation (8), was adopted by the Colour Measurement Committee of the Society of Dyers and Colourists (SDC).

$$\Delta E_{CMC} = \sqrt{\left(\frac{\Delta L^*}{lS_L}\right)^2 + \left(\frac{\Delta C_{ab}^*}{cS_C}\right)^2 + \left(\frac{\Delta H_{ab}^*}{S_H}\right)^2} \quad (8)$$

Here

$$S_L = \begin{cases} \frac{0.040975L^*}{1 + 0.01765L^*} & L^* \geq 16 \\ 0.511 & L^* < 16 \end{cases}$$

$$S_C = \frac{0.0638C_{ab}^*}{1 + 0.0131C_{ab}^*} + 0.638$$

$$S_H = S_C(fT + 1 - f)$$

$$f = \sqrt{(C_{ab}^*)^4 / ((C_{ab}^*)^4 + 1099)}$$

$$T = \begin{cases} 0.36 + |0.4 \cos(h_{ab} + 35)| & h_{ab} \in [164^\circ, 345^\circ] \\ 0.56 + |0.2 \cos(h_{ab} + 168)| & h_{ab} \notin [164^\circ, 345^\circ] \end{cases}$$

The weighting functions  $S_L$ ,  $S_C$ ,  $S_H$  adjust the sizes of the semi-axes of the ellipsoids defining the tolerance volume in CIELAB [1, 2, 5, 11].

$l$  and  $c$  are parametric factors which can be set to adjust the formula for application to flat surfaces where  $l:c$  is 1:1 or texture material where  $l:c$  is 2:1.

The shortcoming of CMC is that the calculation of  $S_L$ ,  $S_C$ ,  $S_H$  is based on the tristimulus values of the standard sample. If the standard sample is swapped with the batch sample, the magnitude of the color difference will change [12]. Furthermore, in the computation of  $T$ , it is not continuous when  $h_{ab} = 164^\circ$  or  $345^\circ$ .

### 4.3 BFD

Luo and Rigg [12] developed two datasets – BFD (Bradford) perceptibility (4000 color pairs) and BFD acceptability (2000 color pairs) and used these datasets to develop the BFD (l:c) color difference equation, which was suggested in 1987 as a refinement of CMC. The formula is shown in equation (9).

$$\Delta E_{BFD} = \sqrt{\left(\frac{\Delta L_{BFD}}{l}\right)^2 + \left(\frac{\Delta C_{ab}^*}{D_C}\right)^2 + \left(\frac{\Delta H_{ab}^*}{D_H}\right)^2 + R_T \frac{\Delta C_{ab}^*}{D_C} \frac{\Delta H_{ab}^*}{D_H}} \quad (9)$$

Where

$$D_C = \frac{0.035C_m^*}{1 + 0.00365C_m^*} + 0.521$$

$$D_H = D_C(GT' + 1 - G)$$

$$G = \sqrt{(C_m^*)^4 / ((C_m^*)^4 + 14000)}$$

$$T' = 0.627 + 0.055 \cos(h_m - 254) - 0.04 \cos(2h_m - 136) + 0.07 \cos(3h_m - 32) - \\ - 0.049 \cos(4h_m + 114) - 0.015 \cos(5h_m - 103)$$

$$R_T = R_H R_C$$

$$R_H = -0.26 \cos(h_m - 308) - 0.379 \cos(2h_m - 160) - 0.636 \cos(3h_m + 254) + \\ + 0.226 \cos(4h_m + 140) - 0.194 \cos(5h_m + 280)$$

$$R_C = \sqrt{(C_m^*)^6 / ((C_m^*)^6 + 70000000)}$$

$C_m^*$  and  $h_m$  are the mean CIELAB  $C_{ab}^*$  and  $h_{ab}$  values for the standard sample and the batch sample. [1, 5, 11]

$l$  and  $c$  are adjustment weights, for flat and textured surfaces.

In this equation, a new term  $R_T \frac{\Delta C_{ab}^*}{D_C} \frac{\Delta H_{ab}^*}{D_H}$  is introduced to take into account of the tilt of the ellipsoids in the blue region as shown in Figure 12. The calculation of  $S_L, S_C, S_H$  is based on the average of the tristimulus values of the standard sample and the batch sample. Thus, the color difference is constant when the standard sample is swapped with the batch sample. Furthermore, in the computation of  $T'$  and  $R_H$ , the model is continuous.

## 4.4 CIE94

A technical committee of the CIE (TC 1-29) was set up to study industrial color difference evaluation and published its recommendations as a CIE Technical Report in 1995. The recommendations included a new equation which became known as CIE94.

This equation is similar to the CMC (1:c) equation in structure, but its weighting functions are largely based on the RIT/DuPont tolerance data [1, 2, 5, 11] and the calculation of the coefficients is simplified.

The CIE94 equation is shown in equation (10):

$$\Delta E_{94}^* = \sqrt{\left(\frac{\Delta L^*}{k_L S_L}\right)^2 + \left(\frac{\Delta C_{ab}^*}{k_C S_C}\right)^2 + \left(\frac{\Delta H^*}{k_H S_H}\right)^2} \quad (10)$$

$$S_L = 1$$

$$S_C = 1 + 0.045 C_{ab}^*$$

$$S_H = 1 + 0.015 C_{ab}^*$$

$k_L, k_C$  and  $k_H$  are parameter factors which can be set by the users to adjust the formula for use on flat surface or textured material.

Similarly, like CMC, the calculation of  $S_C$  and  $S_H$  is still based on the standard sample. The color difference thus varies when the standard is exchanged with the batch.

## 4.5 DIN99

The DIN99 formula was developed in 1999 and accepted as a German standard. The DIN99 is also based on the CIELAB equation but aims to improve the correlation with the visual assessments of small color differences. The DIN99 formula is based on a nonlinear transformation of the color coordinates in the CIELAB color space. The color differences in the DIN99 color space are smaller for high chroma color pairs and thus correlate better with the visual assessments. The DIN99 formula is shown in equation (11) [13, 14].

$$\begin{cases} \Delta E_{99} = \frac{1}{k_E} \sqrt{\Delta L_{99}^2 + \Delta a_{99}^2 + \Delta b_{99}^2} \\ L_{99} = 105.51 \ln(1 + 0.0158L^*) \\ h_{99} = \arctan \frac{f}{e} \\ C_{99} = \frac{\ln(1+0.045G)}{0.045} \\ a_{99} = C_{99} \cos(h_{99}) \\ b_{99} = C_{99} \sin(h_{99}) \end{cases} \quad (11)$$

Here,  $h_{99}$  and  $C_{99}$ , denote DIN99 correlates of hue, and chroma and  $a_{99}$  and  $b_{99}$ , represent DIN99's  $a$  and  $b$  parameters. Here,

$$e = a^* \cos 16^\circ + b^* \sin 16^\circ$$

$$f = -0.7a^* \sin 16^\circ + 0.7b^* \cos 16^\circ$$

$$G = \sqrt{e^2 + f^2}$$

$k_E$  is a parameter which can be set by the user to adjust the magnitude of the color difference.

## 4.6 CIEDE2000

The CIE Technical Committee 1-47 proposed the first major revision to CIE94 in 2001, where a hue-chroma interaction term similar to that of BFD equation was introduced and adjustments were made to the weighting functions  $S_L$  and  $S_H$ . This revision was based on experimental data accumulated through a number of different studies, including the datasets from RIT-DuPont [1, 2, 5, 11], Witt [11, 15, 16], Kim and Nobbs [12] and BFD perceptibility [12]. The CIEDE2000 formula is shown in equation (12) [11, 15, 16].

$$\Delta E_{00}^* = \sqrt{\left(\frac{\Delta L'}{k_L S_L}\right)^2 + \left(\frac{\Delta C'_{ab}}{k_C S_C}\right)^2 + \left(\frac{\Delta H'}{k_H S_H}\right)^2 + R_T \left(\frac{\Delta C'_{ab}}{k_C S_C}\right) \left(\frac{\Delta H'}{k_H S_H}\right)} \quad (12)$$

Where,

$$L' = L^*$$

$$a' = (1 + G)a^*$$

$$b' = b^*$$

$$C'_{ab} = \sqrt{a'^2 + b'^2}$$

$$h'_{ab} = \tan^{-1}\left(\frac{b'}{a'}\right)$$

$$G = 0.5\left(1 - \sqrt{\frac{C_{ab}^{*-7}}{C_{ab}^{*-7} + 25^7}}\right)$$

$$\Delta L' = L'_b - L'_s$$

$$\Delta C'_{ab} = C'_{ab,b} - C'_{ab,s}$$

$$\Delta H'_{ab} = 2\sqrt{C'_{ab,b}C'_{ab,s}} \sin\left(\frac{\Delta h'_{ab}}{2}\right)$$

$$\Delta h'_{ab} = h'_{ab,b} - h'_{ab,s}$$

$$S_L = 1 + \frac{0.015(\overline{L'} - 50)^2}{\sqrt{20 + (\overline{L'} - 50)^2}}$$

$$S_C = 1 + 0.045\overline{C'_{ab}}$$

$$S_H = 1 + 0.015\overline{C'_{ab}T}$$

$$T = 1 - 0.17 \cos(\overline{h'_{ab}} - 30^\circ) + 0.24 \cos(2\overline{h'_{ab}}) + 0.32 \cos(3\overline{h'_{ab}} + 6^\circ) - 0.20 \cos(4\overline{h'_{ab}} - 63^\circ)$$

$$\overline{h'_{ab}} = \begin{cases} \frac{h'_{ab,s} + h'_{ab,b}}{2}, & \overline{h'_{ab}} \leq 180 \\ \frac{h'_{ab,s} + h'_{ab,b}}{2} - 180, & \overline{h'_{ab}} > 180 \end{cases}$$

$$R_T = -\sin(2\Delta\theta) R_C$$

$$\Delta\theta = 30 \exp \{ -[(\overline{h'_{ab}} - 275^\circ)/25]^2 \}$$

$$R_C = 2 \sqrt{\frac{\overline{C_{ab}^*}{}^7}{\overline{C_{ab}^*}{}^7 + 25^7}}$$

Here the subscript 's' refers to the standard color, and the subscript 'b' denotes the batch color.

CIEDE2000 still employs the simplified weighting functions in CIEDE94, but it applies the average of the tristimulus values of the standard and the batch in the computation. The computation of  $T$  is continuous and similar to the computation of  $T'$  in BFD.

## 4.7 CIECAM02

Luo, et al., proposed a uniform color space based on the CIECAM02 color appearance model [17]. The color difference formula in such a space is given in the form of equation (13).

$$\Delta E' = \sqrt{\left(\frac{\Delta J'}{k_L}\right)^2 + \Delta a'^2 + \Delta b'^2} \quad (13)$$

Here  $J' = \frac{(1+100c_1)J}{1+c_1J}$

$$M' = \frac{1}{c_2} \ln(1 + c_2 M)$$

$$a' = M' \cos(h)$$

$$b' = M' \sin(h)$$

$J, M, h$  are the perceptual parameters defined in the CIECAM02 model which is described in Section 5.

$k_L, c_1$  and  $c_2$  are coefficients which vary for various applications, e.g. Large Color Differences (LCD), Small Color Differences (SCD) and Uniform Color Space (UCS) as shown in Table 1.

Table 1.  $k_L, c_1$  and  $c_2$  Parameters used in the CIECAM02 Color Difference Models

Versions	CAM02-LCD	CAM02-SCD	CAM02-UCS
$k_L$	0.77	1.24	1.00
$c_1$	0.007	0.007	0.007
$c_2$	0.0053	0.0363	0.0228

## 4.8 Performance of Various Color Difference Formulas

A number of authors have attempted to describe the difference in performance of various color difference equations over the last several years. Gibert, et al [18, 19] examined the performance

of various color difference equations and showed that CMC(2:1) provides a better prediction of the color difference for textile samples than CIEDE2000. In a different study, Shen, et al [20] discussed the performance of CIELAB, CIEDE94 and CIEDE2000 and found that both CIEDE94 and CIEDE2000 performed better than CIELAB. Melgosa, et al, [21], analyzed the performance of CIE94 and CIEDE2000 and found that CIE2000 provides good results with better correlation compared to other models. Shamey, et al, [22] reviewed the performance of various color difference formulas on two experimental datasets developed at North Carolina State University and determined DIN99 performed better than other color difference formulas including CMC, CIE94 and CIEDE2000, and that CIELAB performed the worst among the color difference formulas examined.

## 5. Color Appearance Models

### 5.1 Color Appearance Phenomena

Two color stimuli, with different tristimuli values, might match to a person with a normal color vision under different viewing conditions, changes in the surround, background, size, shape, surface characters, illumination geometry, etc. A color appearance model predicts whether two stimuli match for a given observer under different viewing conditions. The color phenomena listed below are the typical phenomena included in general color appearance models:

1. Simultaneous contrast[23];
2. Hue changes with luminance[23];
3. Hue changes with chroma [24];
4. Brightness changes with luminance and chromaticity [23];
5. Colorfulness depends on luminance [25];
6. Contrast variation with luminance [26];
7. Contrast changes with surround [27];

The perception of a color stimulus is not only related to the stimulus itself, but also depends on other adjacent spatial or temporal stimuli. Typical color appearance models do not deal with the temporal effects as the observers are supposed to have enough time to adapt to the viewing environment.

The viewing field is consisted of three components: stimulus, which extends from the viewing axis of about 2°, background, which extends from the edge of the stimulus for 10° and surround – the environment outside of the background, as shown in Figure 13 [23].

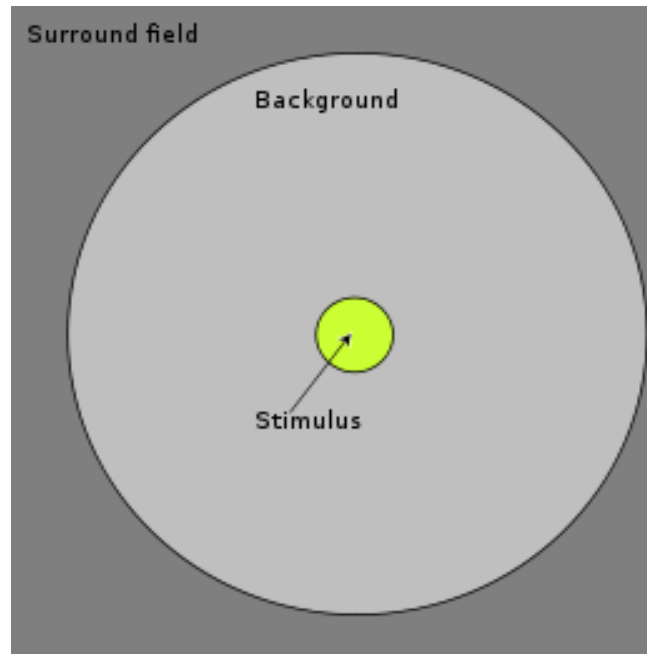


Figure 13. Components of the Viewing Field [23]

## 5.2 Chromatic Adaptation Transforms

The chromatic adaptation models normally use the cone responses instead of the tristimulus values. First, the tristimulus values are converted to the cone responses, then the adapted cone responses are calculated, finally the relative cone response are converted back to the tristimulus values.

The von Kries model is a chromatic adaptation technique which can be illustrated using equation (14) [23].

$$\begin{bmatrix} X_2 \\ Y_2 \\ Z_2 \end{bmatrix} = M^{-1} \begin{bmatrix} L_{max2} & 0 & 0 \\ 0 & M_{max2} & 0 \\ 0 & 0 & S_{max2} \end{bmatrix} \begin{bmatrix} 1/L_{max1} & 0 & 0 \\ 0 & 1/M_{max1} & 0 \\ 0 & 0 & 1/S_{max1} \end{bmatrix} M \begin{bmatrix} X_1 \\ Y_1 \\ Z_1 \end{bmatrix} \quad (14)$$

$M$  is the transformation matrix from CIE tristimulus values to the relative cone responses;

$X_1, Y_1, Z_1$  are the tristimulus values under the source illumination;

$X_2, Y_2, Z_2$  are the tristimulus values under the destination illumination;

$L_{max1}, M_{max1}, S_{max1}$  are the cone responses for the source white point; and

$L_{max2}, M_{max2}, S_{max2}$  are the cone responses for the white point to be adapted to.

The Nayatani model is a nonlinear alternation of the von Kries model, consisting of a gain adjustment and a power function with a variable exponent, as shown in equation (15) [23].

$$\begin{bmatrix} X_2 \\ Y_2 \\ Z_2 \end{bmatrix} = M^{-1} \begin{bmatrix} L_a & 0 & 0 \\ 0 & M_a & 0 \\ 0 & 0 & S_a \end{bmatrix} M \begin{bmatrix} X_1 \\ Y_1 \\ Z_1 \end{bmatrix} \quad (15)$$

Here  $L_a = a_L \left( \frac{L+L_n}{L_0+L_n} \right)^{\beta_L}$ ,  $M_a = a_M \left( \frac{M+M_n}{M_0+M_n} \right)^{\beta_M}$ ,  $S_a = a_S \left( \frac{S+S_n}{S_0+S_n} \right)^{\beta_S}$

$M$  is the transformation matrix from CIE tristimulus values to the relative cone responses;

$L_a, M_a, S_a$  are the adapted cone signals;

$L, M, S$  are the original cone signals;

$L_n, M_n, S_n$  are the noise signals;

$L_0, M_0, S_0$  are the cone excitations for the adapting field;

$\beta_L, \beta_M, \beta_S$  are the exponents and are monotonically increasing functions of the respective cone excitations for the adapting field;

$a_L, a_M, a_S$  are the coefficients determined by the principle that exact color constancy holds for a nonselective sample of the same Y in the tristimulus as the adapting background.

The Fairchild model is another modification of the von Kries model, and it includes the ability to predict the degree of the adaptation based on the adapting stimulus. The whole model can be written as the matrix multiplication, shown in equation (16) [23].

$$\begin{bmatrix} X_2 \\ Y_2 \\ Z_2 \end{bmatrix} = M^{-1} A_2^{-1} C_2^{-1} C_1 A_1 M \begin{bmatrix} X_1 \\ Y_1 \\ Z_1 \end{bmatrix} \quad (16)$$

$M$  is the transformation matrix converting CIE tristimulus values to the relative cone responses;

$A_1, A_2$  are the modified form of the von Kries chromatic adaptation transform;

$C_1, C_2$  are matrixes that account for the luminance dependency which shift the overall lightness with luminance level.

In this model, the first step is to transform the tristimulus values into the relative cone response via the matrix  $M$ ; the cone response is incompletely chromatically adapted via the matrix  $A_1$  and after that is transformed via the matrix  $C_1$  which allows the luminance-dependant interaction among the cone responses. The transformed cone response is finally converted back to the tristimulus under the desired illumination via  $C_2, A_2$  and  $M$ .

The prediction of the Fairchild chromatic adaptation model can match the Breneman corresponding colors data [23].

## 5.3 Color Appearance Models

A color appearance model is any model that includes predictors of at least the relative color-appearance attributes of lightness, chroma, hue, brightness, saturation and colorfulness [23].

The first step in the development of a color appearance model is the application of some form of chromatic adaptation transform from the tristimulus values to the cone responses. Then the post-adaptation signals are combined into higher-level signals, usually modeled after the opponent-color theory of color vision, and including threshold and/or compressive nonlinearities. These signals can be combined to predict various appearance attributes [23].

### 5.3.1 ‘Wrong’ von Kries Transform

When the von Kries type adaptation transforms are applied to the tristimulus instead of the cone responses, the transform is called the wrong von Kries transform. The wrong von Kries transform is usually used in the normalization of CIE XYZ values to those of the source [28], as shown in equation (17).

$$\begin{bmatrix} X_a \\ Y_a \\ Z_a \end{bmatrix} = \begin{bmatrix} k_x & 0 & 0 \\ 0 & k_y & 0 \\ 0 & 0 & k_z \end{bmatrix} \begin{bmatrix} X \\ Y \\ Z \end{bmatrix} \quad (17)$$

$$\text{Here } k_x = \frac{X_{dstwp}}{X_{srcwp}} \quad k_y = \frac{Y_{dstwp}}{Y_{srcwp}} \quad k_z = \frac{Z_{dstwp}}{Z_{srcwp}}$$

$X, Y, Z$  are the tristimulus values of the color;

$X_a, Y_a, Z_a$  are the tristimulus values of the color after chromatic adaptation;  
 $X_{dstwp}, Y_{dstwp}, Z_{dstwp}$  are the tristimulus values of the illuminant in the actual destination  
viewing condition; and  $X_{srcwp}, Y_{srcwp}, Z_{srcwp}$  are the tristimulus values of the illuminant in  
the reference viewing condition.

### 5.3.2 CIECAM02

The CIECAM02 was proposed by the CIE Technical Committee 8-01 in 2002, as the  
successor of CIECAM97s [29-31]. CIECAM02 is consisted of two parts, the chromatic  
adaptation transform CAT02, and the calculations of the six dimensions of color appearance:  
brightness, lightness, colorfulness, chroma, saturation and hue [29, 30].

It is convenient to start from the calculation of the viewing condition parameters. Table 2  
lists the parameters  $F$ ,  $c$  and  $N_c$ .

Table 2. Viewing Condition Parameters for Different Surrounds

Surround	F	c	$N_c$
Average	1.0	0.69	1.0
Dim	0.9	0.59	0.95
Dark	0.8	0.525	0.8

Here  $F$  is the factor determining the degree of adaptation;  $c$  is the impact of surround; and  
 $N_c$  is the chromatic induction factor.

The luminance level adaptation factor,  $F_L$ , can be computed via the equation (18) below:

$$F_L = 0.2k^4(5L_A) + 0.1(1 - k^4)^2(5L_A)^{1/3} \quad (18)$$

Where  $k = 1/(5L_A + 1)$ ,  $L_A$  is the luminance of adapting field in  $\text{cd/m}^2$ .

$$N_{bb} = N_{cb} = 0.725\left(\frac{1}{n}\right)^{0.2} \quad (19)$$

$$z = 1.48 + \sqrt{n} \quad (20)$$

Where  $n = Y_b/Y_w$  is the luminance factor of the background;

$Y_b$  is the luminance of the background and  $Y_w$  is the luminance of the white point;

$N_{bb}$  is the background brightness induction factor;

$N_{cb}$  is the chromatic brightness induction factor;

and  $z$  is the base exponential nonlinearity.

The tristimulus XYZ values can be converted to the corresponding RGB values by the

$M_{CAT02}$  transformation matrix according to equations (21, 22).

$$\begin{bmatrix} R \\ G \\ B \end{bmatrix} = M_{CAT02} \begin{bmatrix} X \\ Y \\ Z \end{bmatrix} \quad (21)$$

$$M_{CAT02} = \begin{bmatrix} 0.7328 & 0.4296 & -0.1624 \\ -0.7036 & 1.6975 & 0.0061 \\ 0.0030 & 0.0136 & 0.9834 \end{bmatrix} \quad (22)$$

Next, the corresponding color after chromatic adaptation can be obtained via equation (23),

$$\begin{bmatrix} R_c \\ G_c \\ B_c \end{bmatrix} = \begin{bmatrix} \frac{Y_w}{R_w} D + 1 - D & 0 & 0 \\ 0 & \frac{Y_w}{G_w} D + 1 - D & 0 \\ 0 & 0 & \frac{Y_w}{B_w} D + 1 - D \end{bmatrix} \begin{bmatrix} R \\ G \\ B \end{bmatrix} \quad (23)$$

$D$  is the degree of adaptation, which can be set from 0 (no adaptation) to 1 (complete

adaptation).  $D$  can be calculated by

$$D = F\left(1 - \frac{1}{3.6} e^{-\frac{L_A+42}{-92}}\right),$$

where  $L_A$  is the adapting field luminance.

After adaptation, the cone responses are converted to the Hunt-Pointer-Est évez space [32]:

$$\begin{bmatrix} R' \\ G' \\ B' \end{bmatrix} = M_H M_{CAT02}^{-1} \begin{bmatrix} R_c \\ G_c \\ B_c \end{bmatrix} \quad (24)$$

$$\text{Where } M_{CAT02}^{-1} = \begin{bmatrix} 1.096124 & -0.278869 & 0.182745 \\ 0.454369 & 0.473533 & 0.072098 \\ -0.009628 & -0.005698 & 1.015326 \end{bmatrix} \text{ and}$$

$$M_H = \begin{bmatrix} 0.38971 & 0.68898 & -0.07868 \\ -0.22981 & 1.18340 & 0.04641 \\ 0 & 0 & 1.0 \end{bmatrix}$$

Here  $\begin{bmatrix} R' \\ G' \\ B' \end{bmatrix}$  is the cone response in the Hunt-Pointer-Est évez space.

$M_H$  is the transform matrix converting the tristimulus values to the cone response in the Hunt-Pointer-Est évez space.

Finally, the  $R'$ ,  $G'$  and  $B'$  response is compressed, as shown in equation (25).

$$\begin{cases} R'_a = \frac{400 \left(\frac{F_L R'}{100}\right)^{0.42}}{27.13 + \left(\frac{F_L R'}{100}\right)^{0.42}} + 0.1 \\ G'_a = \frac{400 \left(\frac{F_L G'}{100}\right)^{0.42}}{27.13 + \left(\frac{F_L G'}{100}\right)^{0.42}} + 0.1 \\ B'_a = \frac{400 \left(\frac{F_L B'}{100}\right)^{0.42}}{27.13 + \left(\frac{F_L B'}{100}\right)^{0.42}} + 0.1 \end{cases} \quad (25)$$

$R'_a$ ,  $G'_a$  and  $B'_a$  are the cone response after compression.

The calculation of perceptual attribute correlates starts from the calculation of the preliminary Cartesian coordinates,  $a$  and  $b$  and the preliminary magnitude  $t$ .

$$\begin{cases} a = R'_a - \frac{12}{11}G'_a + \frac{B'_a}{11} \\ b = \frac{R'_a + G'_a - 2B'_a}{9} \\ h = \tan^{-1} \frac{b}{a} \end{cases} \quad (26)$$

Where  $e = \frac{1}{4} [\cos(h \frac{\pi}{180} + 2) + 3.8]$ ,  $h = \tan^{-1}(\frac{b}{a})$ ,  $h$  is the hue angle.

Lightness,  $J$ , is obtained via equation (27),

$$J = 100 \left( \frac{A}{A_w} \right)^{cz} \quad (27)$$

Here  $A = [2R'_a + G'_a + \frac{1}{20}B'_a - 0.305]N_{bb}$

$c$  can be found in Table 2,  $z$  is calculated in equation (20).

Brightness  $Q$  is given in equation (28),

$$Q = \frac{4}{c} \sqrt{\frac{J}{100}} (A_w + 4) F_L^{0.25} \quad (28)$$

Chroma,  $C$ , can be calculated via equation (29), where  $J$  is given in equation (27).

$$C = t^{0.9} \sqrt{\frac{J}{100}} (1.64 - 0.29^n)^{0.73} \quad (29)$$

Where  $t = \frac{e\sqrt{a^2+b^2}}{R'_a + G'_a + \frac{21}{20}B'_a}$

Colorfulness,  $M$ , can be obtained via equation (30),

$$M = C F_L^{0.25} \quad (30)$$

Saturation,  $s$ , can be obtained using equation (31),

$$s = 100 \sqrt{\frac{M}{Q}} \quad (31)$$

## 6. ICC Color Management

The ICC color management architecture consists of four main elements [28]:

- The color management framework enables the applications with the profiles and the color management module;
- ICC profile sets up the data mapping between the coordinates of the device space and those of the reference color space;
- The color management module links the input profile together with the output profile to set up the transformations between source and destination device / color space;
- The application can make calls to the operating system to handle color transformations.

### 6.1 PCS

Profile connection space (PCS), shown in Figure 14, is a reference color space specified by the International Color Consortium (ICC) in which every input and output device can be related. Such a reference color space must define the colorimetry of both the reference medium and its assumed viewing condition.

PCS operates as a virtual space, defining the relationship between different device spaces thus a unique transformation can be created for any pair of devices or color spaces for which profiles are available [28].

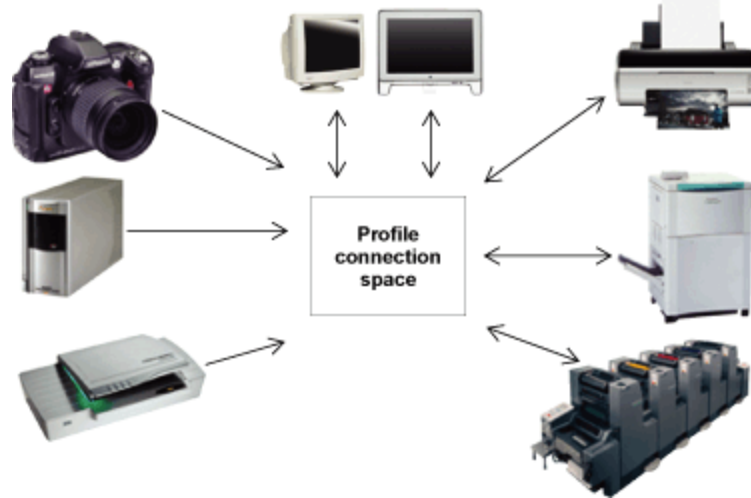


Figure 14. Profile Connection Space (PCS) [33]

## 6.2 ICC Profile

The ICC profile is a storage file which can provide the data necessary to transform the colors of an image from the color characterization of one device to those of another [11, 28]. In this research project, the calibrations of the digital camera and the monitor are based on the ICC profile, so that the image from the digital camera can be shown on the monitor.

Normally, the profile contains the following information: [11, 28]

- The company / software that created, or was used to create the profile;
- The device and its settings / media for which the profile was created;
- The color characteristics of the device;
- The data necessary to convert the color from the device color space and settings into a PCS;
- The data to convert from the PCS back to the device color space;

- Additional information to aid in printing, viewing etc;

The file format is a tag-based structure which allows a variable amount of data (tags) to be included. There is a fixed length header for each profile and a listing of the tag keywords, their byte offsets from the beginning of the profile, and their length. Following this is the actual tag data, identified by the tag identification, length, and specific data, as depicted in Figure 15.

Four rendering intents are provided as the actual device gamut may not be large enough to reproduce the desired color appearances, as listed below.

- Relative colorimetric intents preserve the in-gamut colors;
- Absolute colorimetric intents preserve the in-gamut chromatic-adapted colors;
- Perceptual intents present the details throughout the tonal range;
- Saturation intents keep the saturation of the pure colors [28].

Normally, there are two types of ICC profiles – the matrix based profile, shown in Figure 16, and the Look-Up-Table based profile, illustrated in Figure 17. The matrix based profile is usually used in the color management of displays and digital cameras. The Look-Up-Table based profile is usually used in the color management of printers and digital cameras [33].

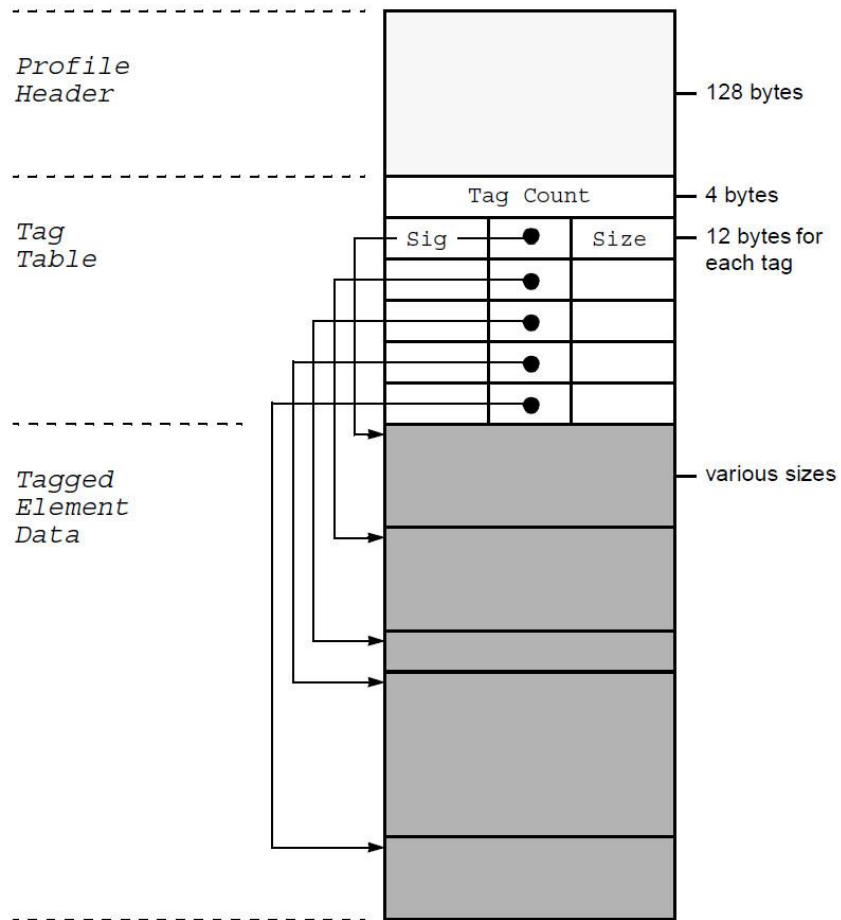


Figure 15. ICC Profile Structure [28]

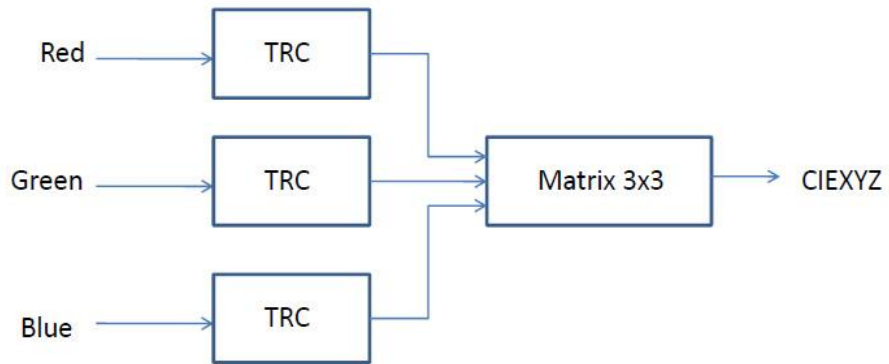


Figure 16. Matrix based Profile [33]

‘TRC’ stands for the tone response curve of the R, G or B.

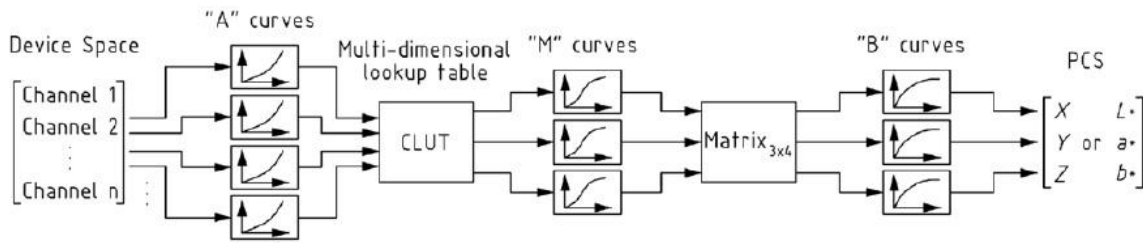


Figure 17. Look-Up-Table based Profile [33]

‘A’ curves are the prelinearized curves for the look-up-table;

CLUT is the color look-up-table;

‘M’ curves are the parametric curves for the matrix;

‘B’ curves are the postlinearized curves from the matrix.

## 7. Various Color Input Devices

Before starting the discussion on the calibration of the digital camera, which is used as the main input device in this project, several color input devices, together with their applications and calibrations are briefly described below. These include scanners, digital cameras, hyperspectral cameras, colorimeters and spectrophotometers.

### 7.1 Scanners

A scanner is an optical device which can capture images, printed text, handwriting or an object and turn it into a digital image. Nowadays the most popular scanner is the flatbed CCD scanner, as shown in Figure 18. There is a glass pane, under which there is a movable

light source that can illuminate the glass pane and a movable mirror that can reflect the image of the object to the sensor. The sensor generates the signals line by line. Normally there are three types of sensors with red, green and blue filters [34].

In 1994, Farrell, et al. [35] discussed the use of scanner as a colorimeter. Shahin, et al. [36] showed how to use a calibrated scanner to grade grains. Nateri [44] reported the use of the neural network in the color evaluation of textile fabrics. In 2007, Kuo, et al. used the scanner in the color separation of the printed fabrics.

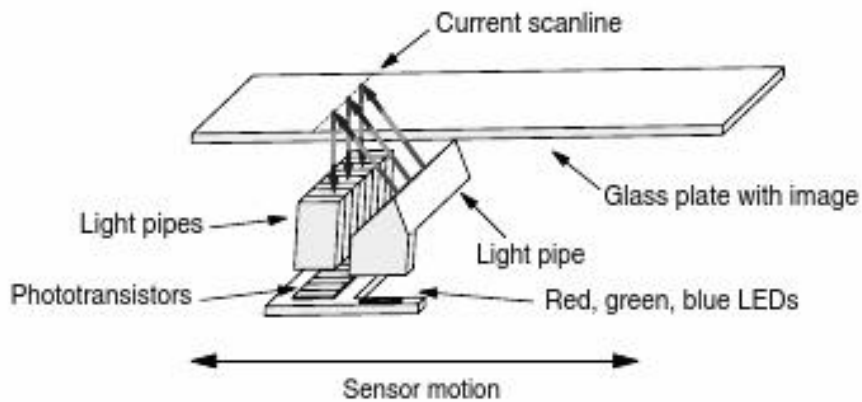


Figure 18. Structure of the Flatbed CCD Scanner [34]

## 7.2 Digital Cameras

Digital cameras are similar to scanners in that they capture the digital images. However, unlike the scanners, the digital camera has various parameters that can be set, such as the aperture, the shutter and the focal length. After the image capturing, demosaicing as well as

some post image processing such as white balancing are carried out in the digital camera.

Various applications based on the digital cameras have been reported.

In 1993, Malmqvist, et al. [37, 38] used a digital camera to measure the densities within the halftone dots of a halftone tint. Sodergard, et al. [38], used the digital camera as a densitometer to inspect color printing with what was reported as an average accuracy.

Brydges, et al. [39] discussed the use of a digital camera as a colorimeter and densitometer in the color measurements of the graphic arts.

The digital camera can be applied in other non-traditional applications. Since cameras may be employed as non-contact color measurement tools, they have found applications in several diverse fields. Marguier, et al. [40], reported the use of a digital camera for home decoration. They showed the use of the digital camera for measurement of colors in a painted sample and the selection of the optimal palette for the sample.

Wu, et al. [41], used a camera based system to measure the color of human teeth. Multiple filters were used to increase the color accuracy of the process. Ng, et al. [42] devised a method and improved the illumination of this camera based system. Kim, et al., [43] applied a digital camera to analyze the color of port wine skin. In the field of medical applications, cameras provide a means of non-contact color measurement, and are considered safe, clean and void of contamination, which are critical quality parameters in these domains. Grana, et al., [44] used a video camera based system for diagnosis in the field of dermatology.

Recently, some research has been done on the automatic colorimetric measurement of the chronic wounds to monitor how the wounds heal [45].

Digital cameras have also been used for the archival and conservation of artifacts in museums and galleries. Cupitt et al. [46] described an imaging system based on the application of the digital camera in the museum for the archival of paintings. Berns et al. [47] discussed the use of cameras for reproduction of the museum art collections, which included a multi-spectral camera. The multi-spectral camera was based on a monochromatic camera with seven channels to reconstruct spectrum and reduce metamerism. Principal component analysis was used to reconstruct the spectral curves.

Calibrated cameras can also be applied in the food industry, for example, to inspect or grade the agricultural products [48]; and to analyze the color of the food surfaces [49]. The application of the camera in the food industry has been described as a versatile, simple process which can lead to a reduction of the overall cost of the quality control process.

### **7.3 Hyperspectral Camera**

A hyperspectral camera is an optical apparatus that can collect image data simultaneously in tens or hundreds of narrow, adjacent spectral bands [50]. Hyperspectral is a term given to tens or hundreds of spectral bands with a relative spectral resolution order of 0.01 [50].

Brelstaff, et al. [51] introduced a simple hyperspectral system based on a video camera plus a set of filters. Aikio showed [52] the design of a prism-grating-prism optics, which has been adopted and used in some hyperspectral imaging systems as optical filters. Other hyperspectral imaging systems use the electronically tunable elements such as liquid crystal (LCTF) and acousto-optic tunable filters (AOTF) [53] instead of the optical filters.

The hyperspectral imaging system can be applied in the quality control of the product line and perform an accurate and real-time inspection. It has been shown [54] that such a system can be used for the online measurement of textile dyeing, inspection of quality of ceramic tiles, or the quality control of the print material.

In recent years, hyperspectral imaging systems were applied in the field of biomedicine, especially in the analysis of different types of samples, ranging from individual biochemical species observed in samples to organs of living people. Hyperspectral cameras can perform in-vivo diagnosis on tissue without the need for sample excision and processing. Dinh et al [55] discussed various methods to obtain in-vivo spectral information of organs via optical diagnostics.

The hyperspectral camera can also be used in the conservation of artifacts. The current and potential applications include the study of materials in the archaeological, artistic, cultural and historic research; monitoring and evaluation of conservation treatments; digital imaging for documentation and archiving; assessing and monitoring the state of deterioration of archaeological sites; as well as identification and sourcing of archaeological artifacts [56]. Berns et al. [47], showed the application of the hyperspectral camera in the conservation of several paintings.

## 7.4 Colorimeter

A colorimeter is a simple instrument for the measurement of color, as depicted in Figure 19. There are three photodetectors in the colorimeter that can directly measure the tristimulus values of a sample, a design similar to that present in human eyes – that contain long wavelength, L, medium wavelength, M, and short wavelength, S, filter photoreceptors. The incident light from the device's light source hits the measured sample and is then collected by the detector - which consists of colored filters [2].

The output of the colorimeter is the tristimulus values, which is dependent on the illumination and the color matching functions. The measurement might not be useful if the required illumination and color matching functions are different. There is no information about the spectra from the output of the colorimeter. Furthermore, the illumination and the color matching functions should be specified when citing a measurement [57].

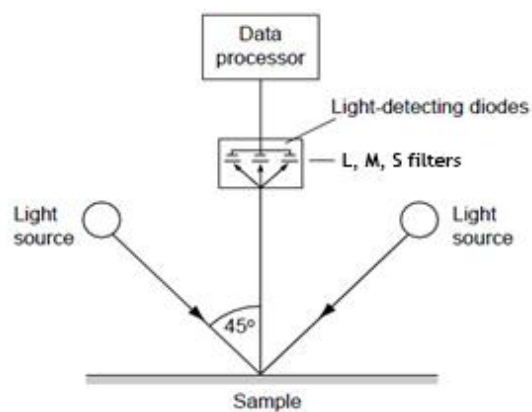


Figure 19. Schematic Representation of a Colorimeter [2]

## 7.5 Spectrophotometer

Spectrophotometers are used to measure reflectance, transmittance or absorbance of a sample at different wavelengths. Spectrophotometers are usually designed to operate in the visible range of the electromagnetic radiation from 380nm to 750nm. When measuring reflectance, spectrophotometers aim to determine the ratio of the reflectance of the light and that from a perfect diffuse white calibration tile. Figure 20 shows the schematic structure of the DataColor SF500 spectrophotometer and depicts the sample aperture, the light source, optical components to collect the light, diffraction gratings to separate the light ray and a microprocessor for data analysis [1]. The beam from the light source is split into two parts – one part illuminates the reference standard and the other part illuminates the sample. Then the beams are separated by the monochromators for processing in the microprocessor. The advantage of the dual beam system is that the variation of the system can be removed before the data is processed [58]. Monochromator is an optical device which can transmit a narrow band of wavelengths of light from a wider range wavelength available at the input [2].

When a spectrophotometer with the diffuse illuminating geometry is used to measure the reflectance of objects, two modes may be employed – specular included and specular excluded. Specular included mode is used to measure the total reflectance, which includes the specular reflectance and the diffuse reflectance, and is more related with the color content; the specular excluded mode is used to measure only the diffuse reflectance and is more closely related with the appearance [59].

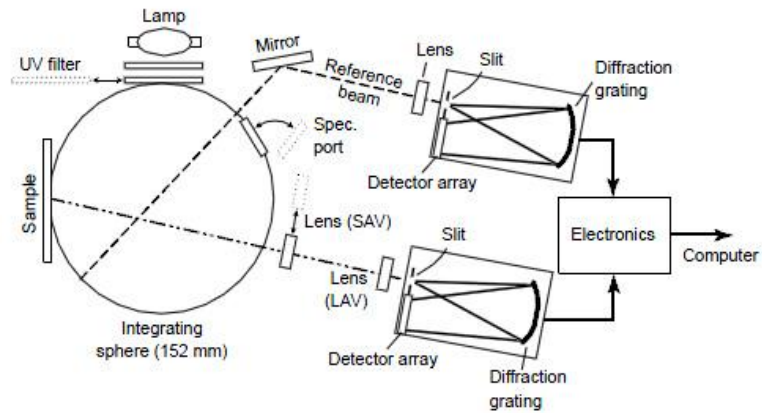


Figure 20. Structure of DataColor SF500 [2]

When a spectrophotometer with the diffuse illuminating geometry is used to measure the reflectance of objects, two modes may be employed – specular included and specular excluded. Specular included mode is used to measure the total reflectance, which includes the specular reflectance and the diffuse reflectance, and is more related with the color content; the specular excluded mode is used to measure only the diffuse reflectance and is more closely related with the appearance [59].

Figure 21 demonstrates the effect of surface texture on the appearance of objects. There are three surfaces, all of which have the same reflectance spectra. If the specular included mode is used to measure the reflectance, identical results are obtained for these surfaces which appear differently to the human eyes, for example, the glossy smooth surface looks much darker and more saturated than the other two surfaces [59].

Figure 22 shows the difference between these measurement modes. A specular exclusion port is placed on top of the integrating sphere. Under the specular included mode, the port is

closed and the specular reflected light is reflected back to the sphere and collected by the sensor. Under the specular excluded mode, the port is open and the specular reflected light is excluded [59].

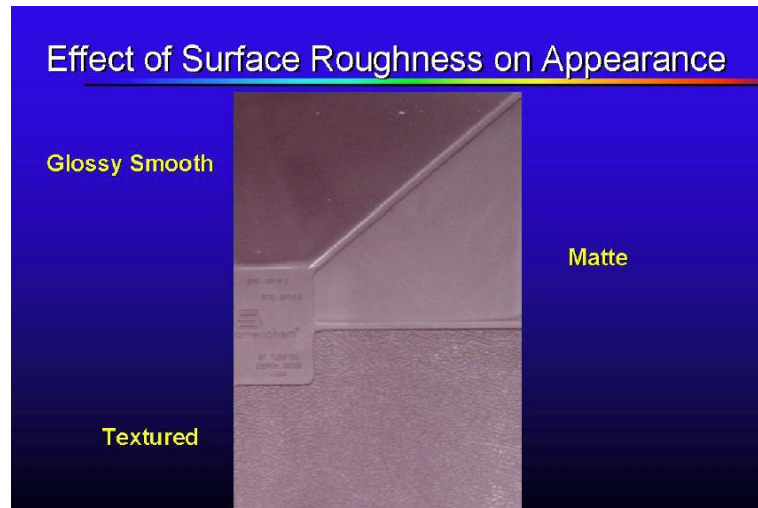


Figure 21. The effect of the Surface Texture on the Appearance of an Object [59]

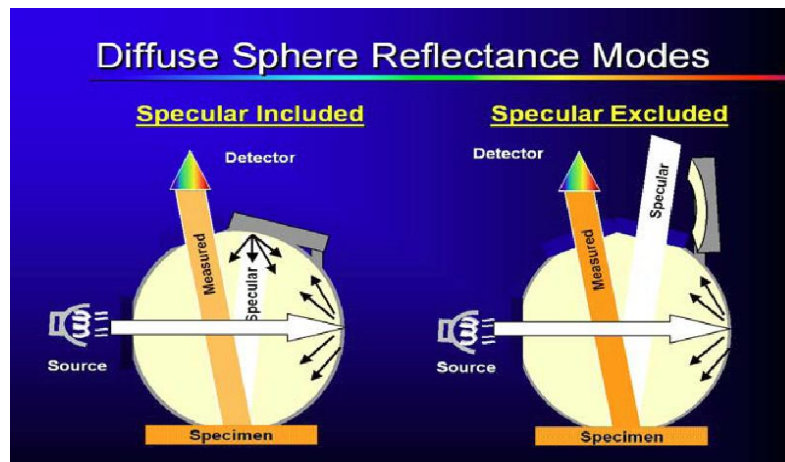


Figure 22. Diffuse Sphere Reflectance Modes [59]

## **7.6 Measurement Variability**

The research on inter- and intra- spectrophotometer variance is not a new topic, which can date back to almost 60 years ago. In 1953, Nimeroff confirmed the uncertainty of the spectrophotometric data [60]. In 1956, Shipley and Walker analyzed the propagation of random errors through spectrophotometric measurements and colorimetric calculations [61]. In 1988, Berns and Peterson applied the multiple-linear regression to diagnose and correct the spectrophotometric errors [62]. In 1991, Fairchild and Reniff analyzed the correlation between the uncertainty in the calibration chain and the random errors in colorimetric coordinates [63]. In 2005, Dolezalek proposed the application of regression techniques to correct the colorimetric calculations and another regression method to correct the spectrum [64].

To reduce inter-instrumental variability amongst spectrophotometers, X-Rite® developed a software tool as well as a process denoted NetProfiler®, which is claimed to constantly monitor instruments and detect problems before they affect quality [65].

## **8. Device Calibration**

### **8.1 Display Monitor**

Several authors [66-70] have described the calibration of the CRT monitors. Cazes et al. [71] discussed the differences in the calibration of the CRT and the LCD and presented a corrected model. Sharma [72] compared the calibrations of the CRT and the LCD and

proposed a calibration method based on the spectral response of the monitor. He pointed out the color accuracy of CRT is better than that of the LCD due to the dispersion inside liquid crystals.

As an EIZO LCD is used in this project to display the images captured from the digital camera, an accurately calibrated display was needed to help the software users to view the images of the samples that have been judged previously.

Furthermore, the distribution of the emission from the LCD also requires some investigation.

### **8.1.1 Structure of Monitors based on the Liquid Crystal Display (LCD)**

A typical LCD, which can be seen in Figure 23, is consisted of a color filter layer, a liquid crystal layer aligned between two transparent electrodes, and two polarizing layers. In most cases, the axes of transmission of the polarizing layers are perpendicular to each other [2].

When there is no electric field, the orientation of the liquid crystal molecules is dependent on the alignment of two electrode layers, which are normally perpendicular to each other, thus the liquid crystal molecules are twisted.

When a large voltage is applied, the liquid crystal molecules in the center of the layer are almost completely untwisted and the polarized incident light is not rotated as it passes through the liquid crystal layer. Thus the polarized light which passes through the first polarizer layer, will be blocked by the second polarizer layer. If the voltage applied on every pixel is controlled, light can pass through in different amounts thus constituting different levels of gray [2, 34].

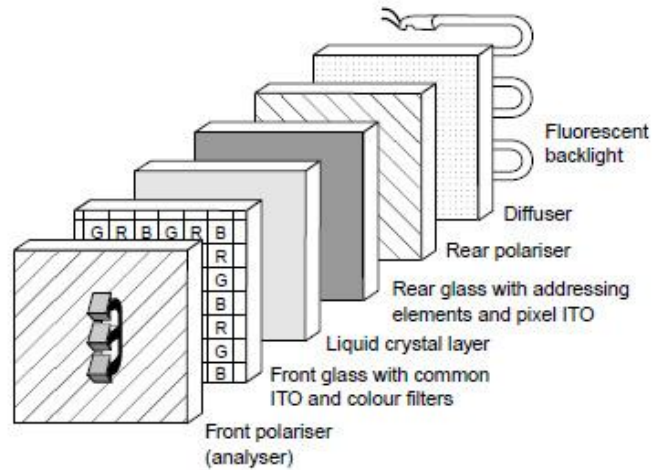


Figure 23. Schematic Representation of LCD Monitors [2]

### 8.1.2 Calibration of the LCD Monitor

The calibration of the LCD is to set up the data mapping between the color space and the display device space. A forward calibration model, which can be seen in Figure 24, is often employed [72].

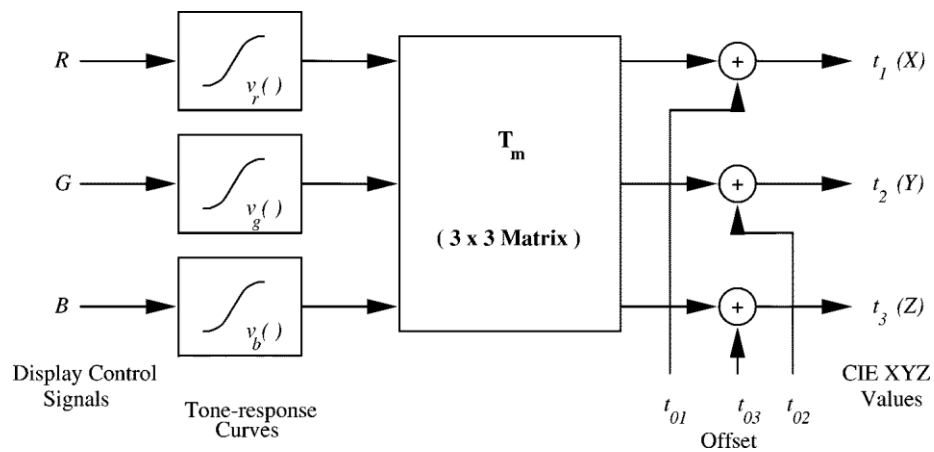


Figure 24. Graphical Representation of the Forward Calibration Model [72]

The light emitting out of every pixel is supposed to be consisted of three individual components, red light, green light and blue light [72], which can be combined together. A typical model, based on Sharma [60] is shown in equation (32).

$$\begin{bmatrix} X \\ Y \\ Z \end{bmatrix} = \begin{bmatrix} X \\ Y \\ Z \end{bmatrix}_R + \begin{bmatrix} X \\ Y \\ Z \end{bmatrix}_G + \begin{bmatrix} X \\ Y \\ Z \end{bmatrix}_B + \begin{bmatrix} X \\ Y \\ Z \end{bmatrix}_0 \quad (32)$$

$$\begin{bmatrix} X \\ Y \\ Z \end{bmatrix}_R = tr(R) \begin{bmatrix} X_R \\ Y_R \\ Z_R \end{bmatrix}$$

$$\begin{bmatrix} X \\ Y \\ Z \end{bmatrix}_G = tg(G) \begin{bmatrix} X_G \\ Y_G \\ Z_G \end{bmatrix}$$

$$\begin{bmatrix} X \\ Y \\ Z \end{bmatrix}_B = tb(B) \begin{bmatrix} X_B \\ Y_B \\ Z_B \end{bmatrix}$$

$\begin{bmatrix} X \\ Y \\ Z \end{bmatrix}_0$  is the tristimulus values when  $R = G = B = 0$ ;

$\begin{bmatrix} X \\ Y \\ Z \end{bmatrix}_R$ ,  $\begin{bmatrix} X \\ Y \\ Z \end{bmatrix}_G$ ,  $\begin{bmatrix} X \\ Y \\ Z \end{bmatrix}_B$  are the tristimulus values based on the R, G, B filters respectively;

$tr()$ ,  $tg()$ ,  $tb()$  are the tone reproduction curves for the R, G, B channels respectively;

$\begin{bmatrix} X_R \\ Y_R \\ Z_R \end{bmatrix}$ ,  $\begin{bmatrix} X_G \\ Y_G \\ Z_G \end{bmatrix}$ ,  $\begin{bmatrix} X_B \\ Y_B \\ Z_B \end{bmatrix}$  represent the tristimulus values when R, G, B channels reach their

maximum, respectively.

### 8.1.3 Corrected Calibration Model

Cazes, et al. [71], analyzed the color difference between the measured tristimulus and the calculated tristimulus and proposed a corrected model using equation (33):

$$\begin{cases} R_{mod}(i) = R(i) - g(0) - b(0) - LE_R(i) \\ G_{mod}(i) = G(i) - r(0) - b(0) - LE_G(i) \\ B_{mod}(i) = B(i) - r(0) - g(0) - LE_B(i) \end{cases} \quad (33)$$

Where  $i$  is the input RGB level, that is,  $i = R, G, B$ , ranged from 0 to 255, the maximum value of RGB channels;

$R_{mod}(i)$ ,  $G_{mod}(i)$  and  $B_{mod}(i)$  are the modified tristimulus values (XYZ) for the individual RGB values at the input level  $i$ ;

$R(i)$ ,  $G(i)$  and  $B(i)$  are the measured tristimulus values (XYZ) for the individual RGB values at the input level  $i$ ;

$W(i)$  is the tristimulus for the  $i$ th gray level and  $W(0)$  is the tristimulus for the black point;

$r(0)$ ,  $g(0)$  and  $b(0)$  are the tristimulus values (XYZ) for the black subpixels, which are constant as shown in equation (34).

$$r(0) = \alpha \begin{bmatrix} X_R(255) \\ Y_R(255) \\ Z_R(255) \end{bmatrix}, g(0) = \beta \begin{bmatrix} X_G(255) \\ Y_G(255) \\ Z_G(255) \end{bmatrix}, b(0) = \gamma \begin{bmatrix} X_B(255) \\ Y_B(255) \\ Z_B(255) \end{bmatrix} \quad (34)$$

$$\begin{bmatrix} \alpha \\ \beta \\ \gamma \end{bmatrix} \text{ can be determined using } \begin{bmatrix} X_R(255) & X_G(255) & X_B(255) \\ Y_R(255) & Y_G(255) & Y_B(255) \\ Z_R(255) & Z_G(255) & Z_B(255) \end{bmatrix} \begin{bmatrix} \alpha \\ \beta \\ \gamma \end{bmatrix} = \begin{bmatrix} X_{W(0)} \\ Y_{W(0)} \\ Z_{W(0)} \end{bmatrix};$$

$LE_R(i)$ ,  $LE_G(i)$ ,  $LE_B(i)$  are the tristimulus values related with the color leakage and can be approximated via equation (35-38):

$$LE_R(i) + LE_G(i) + LE_B(i) = R(i) + G(i) + B(i) - W(i) - 2W(0) \quad (35)$$

$$X_{LE_R(i)}:X_{LE_G(i)}:X_{LE_B(i)} = X_R(255):X_G(255):X_B(255) \quad (36)$$

$$Y_{LE_R(i)}:Y_{LE_G(i)}:Y_{LE_B(i)} = Y_R(255):Y_G(255):Y_B(255) \quad (37)$$

$$Z_{LE_R(i)}:Z_{LE_G(i)}:Z_{LE_B(i)} = Z_R(255):Z_G(255):Z_B(255) \quad (38)$$

Here 255 is the maximum of the *RGB* values.

## **8.2 Digital Camera**

In this project, a digital camera is used as the input device. The structure and calibration of digital cameras is reviewed in the following sections.

### **8.2.1 Structure of Digital Camera (DC)**

Figure 25 shows a typical block diagram of a digital still camera. Usually, a digital camera includes an optical and a mechanical subsystem, an image sensor and an electronic subsystem. Fundamental optics of digital still cameras is equivalent to those of silver halide cameras. The output analog signals of the image sensor are processed by an analog preprocessor, where sample-and-hold, color separation, automatic gain control, tone adjustment, and other signal processing are carried out. These signals are then converted to digital signals via an A/D converter. The digital signals are processed by the digital signal processor and/or the microprocessor. The process includes tone adjustment, white balance and image compression. Image signals used for automatic exposure control, auto focus and automatic white balance are also generated here [73].

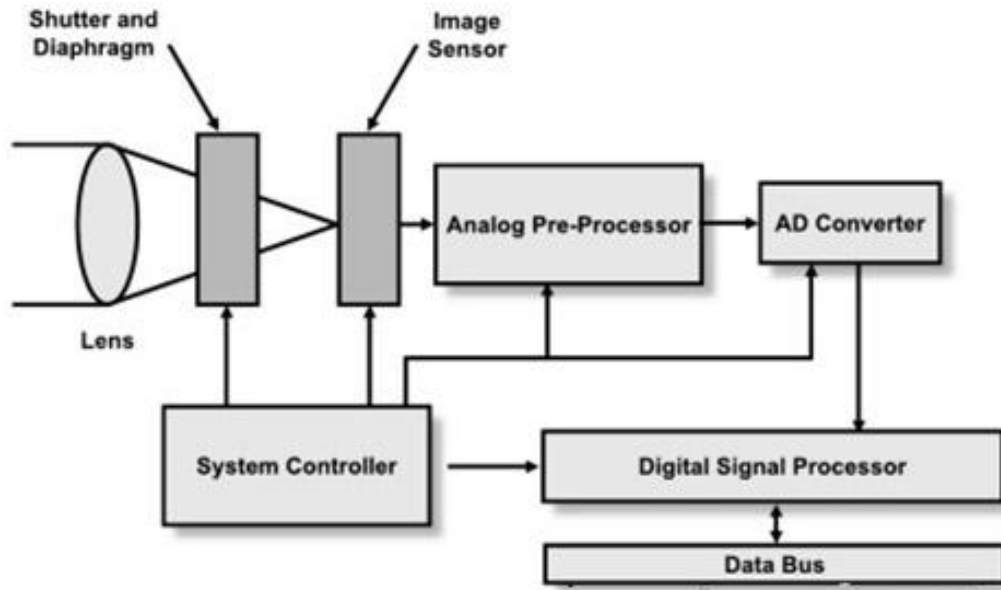


Figure 25. Typical Block Diagram of a Digital Still Camera [73]

The system's control circuits control the sequence of the camera's operation: automatic exposure control (AE), and auto focus (AF), etc. Before taking a picture, the control circuit quickly reads sequential image signals from the image sensor and adjusts the focus and the exposure parameters [73].

Figure 26 shows the typical arrangement of a point-and-shoot digital still camera. Charge-Coupled Devices (CCDs) and Complementary Metal–Oxide–Semiconductor (CMOS) are the popular image sensors used in digital cameras. The infrared cut filter can filter out the mid-infrared wavelength and let in the visible light because the infrared light affects the image quality. The color filter array filters the incident light in different wavelength regions, and the microlens array condenses the incident light on each pixel. All these filters are arranged on the image receiving surface of the imaging devices.

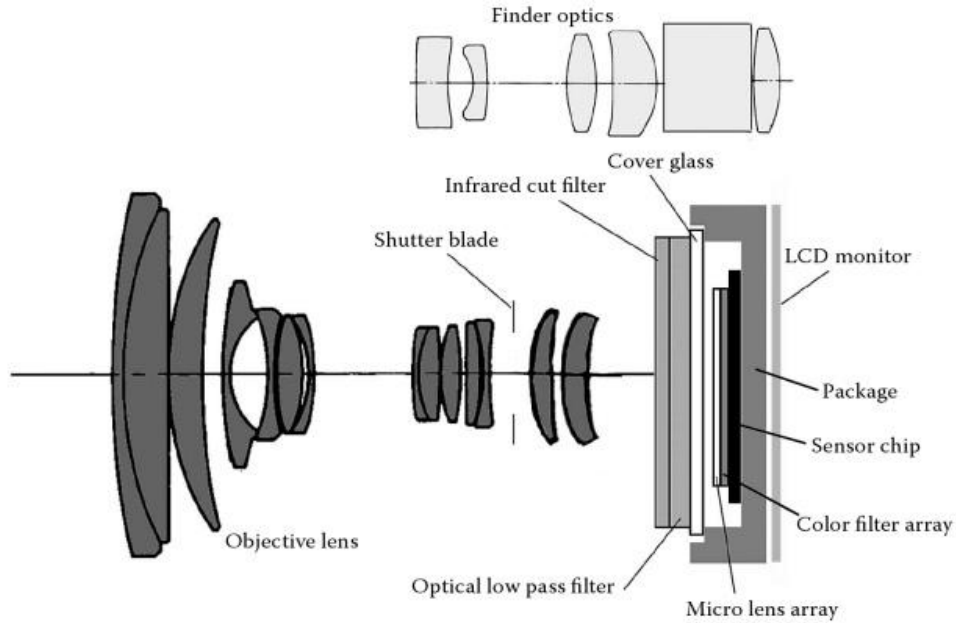


Figure 26. Typical Arrangement of a Point-and-shoot Digital Still Camera [73]

### 8.2.2 Calibration of the DC

The calibration of the DC is carried out to set up the data mapping between the color space and the camera device space. Usually, the DC calibration methods can be classified into two categories: colorimetric estimation and spectral reconstruction [74].

The colorimetric estimation is to acquire the colorimetric attributes via the regression model [75] or via the Look-Up-Table [76]. In the spectral reconstruction method, the spectrum is obtained via the regression method or the Principle Component Analysis (PCA) or Singular Value Decomposition (SVD) method [41, 42, 77].

### 8.2.2.1 Regression Method

Regression method is a technique used for modeling and analyzing the variables to set up the relationship between a dependant variable and one or more independent variables. In 1992, Kang, et al. proposed the scanner calibration based on polynomial regression [78], and found that lower order polynomials fit both training and test dataset well. Shen et al. [79] used a local polynomial regression in the colorimetric calculation, and showed that this technique outperformed the linear regression model. Least square method is often used to approximate the solution of over-determined systems, which means that the overall solution minimizes the sum of squares of the errors made in solving every single equation. This is shown in equation (39) [75].

$$\begin{aligned} [X_i, Y_i, Z_i]_{N \times 3} &= [f(R_i, G_i, B_i)]_{N \times P} [M]_{P \times 3} \\ [f(R_i, G_i, B_i)]_{N \times P}^T [X_i, Y_i, Z_i]_{N \times 3} &= [f(R_i, G_i, B_i)]_{N \times P}^T [f(R_i, G_i, B_i)]_{N \times P} [M]_{P \times 3} \quad (39) \\ [M]_{P \times 3} &= ([f(R_i, G_i, B_i)]_{N \times P}^T [f(R_i, G_i, B_i)]_{N \times P})^{-1} [f(R_i, G_i, B_i)]_{N \times P}^T [X_i, Y_i, Z_i]_{N \times 3} \end{aligned}$$

Here,  $i$  is the index of the color patch,

$[X_i, Y_i, Z_i]_{N \times 3}$  is the matrix consisting of the tristimulus values of all the color patches,

$[f(R_i, G_i, B_i)]_{N \times P}$  is the matrix of the polynomials with order P from the RGB signals,

$[M]_{P \times 3}$  is the transform matrix,

$[\ ]^T$  is the transpose of the matrix.

### 8.2.2.2 Look-Up-Table Method

A Look-Up-Table is a data structure, usually an array which pairs the coordinates in different domains, such as device values and their associated values in a CIE color space. In 1991, Hung, et al. [76] reported the use of polynomial regression and 3D Look-Up-Table (LUT) for the calibration of a scanner, and showed that the 3D LUT generated reduced error when compared with the polynomial regression method. The application of the neural network was proposed in the calculation of the 3D LUT by Vrhel and Trussell [80]. Look-Up-Tables can be employed where the relation between two domains cannot be well defined by a closed formula and to locate the values faster than applying a complex function [11].

Normally, there are two interpolations that are popularly used in the Look-Up-Table calculation, trilinear interpolation, as shown in Figure 27, and the tetrahedron interpolation, as shown in Figure 28.

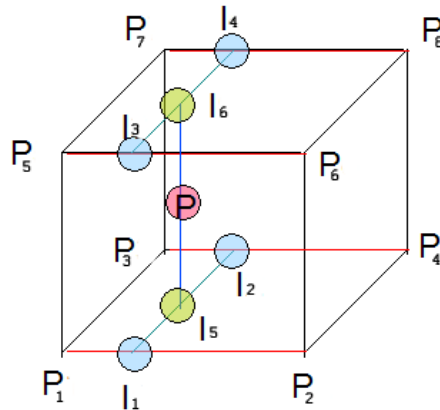


Figure 27. Trilinear Interpolation

The process of the trilinear interpolation is described in equation (40). [11, 81]

$$\begin{aligned}
x(l_1) &= rx(P_1) + (1 - r)x(P_2) & x(l_2) &= rx(P_3) + (1 - r)x(P_4) \\
x(l_3) &= rx(P_5) + (1 - r)x(P_6) & x(l_4) &= rx(P_7) + (1 - r)x(P_8) \\
x(l_5) &= gx(l_1) + (1 - g)x(l_2) \\
x(l_6) &= gx(l_3) + (1 - g)x(l_4) \\
x(P) &= bx(l_5) + (1 - b)x(l_6) \\
x(P) &= rgbx(P_1) + (1 - r)gbx(P_2) + r(1 - g)bx(P_3) + (1 - r)(1 - g)bx(P_4) + \\
&rg(1 - b)x(P_5) + (1 - r)g(1 - b)x(P_6) + r(1 - g)(1 - b)x(P_7) + (1 - r)(1 - \\
&g1 - bx(P_8) \tag{40}
\end{aligned}$$

Here  $P_1, P_2, P_3, P_4, P_5, P_6, P_7, P_8$  are the known tristimulus values at the 8 vertices of a unit cube,  $l_1$  is in the line  $\overline{P_1P_2}$ ,  $l_2$  is in the line  $\overline{P_3P_4}$ ,  $l_3$  is in the line  $\overline{P_5P_6}$ ,  $l_4$  is in the line  $\overline{P_7P_8}$ ,  $l_5$  is in the line  $\overline{l_1l_2}$ ,  $l_6$  is in the line  $\overline{l_3l_4}$ , and  $P$  is in the line  $\overline{l_5l_6}$ .

$x()$  is the variable (e.g. the tristimulus values) at a given position.  $r, g, b$  can be defined below.

$$\begin{aligned}
r &= \frac{\overline{l_1P_2}}{\overline{P_1P_2}} = \frac{\overline{l_2P_4}}{\overline{P_3P_4}} = \frac{\overline{l_3P_6}}{\overline{P_5P_6}} = \frac{\overline{l_4P_8}}{\overline{P_7P_8}} \\
g &= \frac{\overline{l_5l_2}}{\overline{l_1l_2}} = \frac{\overline{l_6l_4}}{\overline{l_3l_4}} \\
b &= \frac{\overline{Pl_6}}{\overline{l_5l_6}}
\end{aligned}$$

In a tetrahedron interpolation, a unitary cube is divided into 6 tetrahedrons, as depicted in Figure 28, and any point  $(r, g, b)$  inside the cube must lie within one tetrahedron [81, 82], for example  $((0, 0, 0), (0, 1, 0), (1, 1, 0), (1, 1, 1))$ , as shown in equation (41).

$$(r, g, b) = (1 - r)x(0, 0, 0) + (1 - g)rx(0, 1, 0) + rg(1 - b)x(1, 1, 0) + rgbx(1, 1, 1) \quad (41)$$

Where  $x(, , )$  is the variable (e.g. the tristimulus value) at the given position.

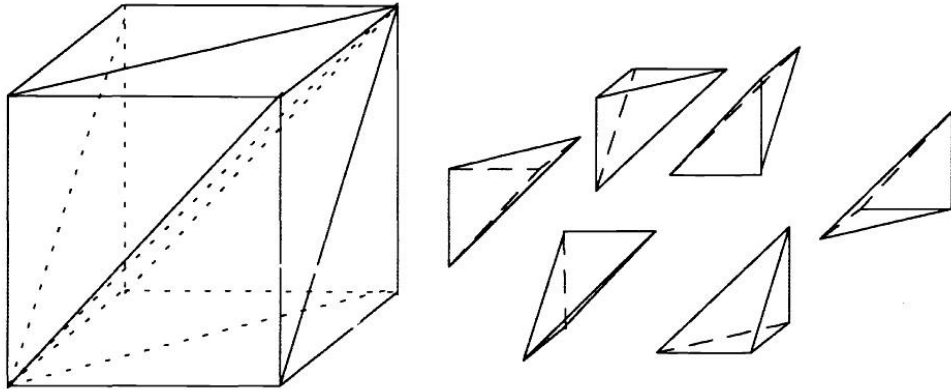


Figure 28. Tetrahedron Division [82]

When the tetrahedron interpolation is compared with the trilinear interpolation, it can be seen that the tetrahedron interpolation requires only 4 points in the calculation while the trilinear interpolation requires 8 points in the calculation. So the tetrahedron interpolation is faster than the trilinear interpolation.

### 8.2.2.3 PCA Method

The visible spectrum detected by the human eye ranges from 380nm to 750nm. If a sampling width of 10nm is used, the entire visible spectrum can be represented by 31 wavelength bands. PCA method can be used to determine the patterns within the data set, and express the

data in a way to highlight their similarities and differences [77]. Once the patterns are determined, it is possible to reduce the number of the dimensions of the data set and represent the data set with fewer dimensions [77]. Trussell and Vrhel discussed [77] the application of Principal Component Analysis (PCA) in the color correction of the scanner. PCA involves a mathematical procedure that transforms a number of possibly correlated variables into a number of uncorrelated variables called principal components [77, 83]. Given  $X_{m \times n} = [X_1 \ \dots \ X_m]^T$ , the spectra of the  $m$  colors in the training dataset with  $n$  wavelengths, mean  $\mu$  and covariance matrix  $\Sigma$ , where  $\Sigma$  is a symmetric matrix,

$$\Sigma = [a_1 \ \dots \ a_n]^T \begin{bmatrix} \delta_1 & \dots & 0 \\ \vdots & \ddots & \vdots \\ 0 & \dots & \delta_n \end{bmatrix} [a_1 \ \dots \ a_n] \quad (42)$$

Here  $\delta_1 \ \dots \ \delta_n$  are the eigenvalues of  $\Sigma$  that are ranked from the highest value to the lowest value, and

$a_1 \ \dots \ a_n$  are the associated eigenvectors of  $\Sigma$ .

$a_1 \ \dots \ a_n$  can be used as the principal components, and  $X$  can be approximated by the linear combination of the principal components plus the mean  $\mu$ .

Normally, in order to simplify the computation, only the eigenvectors related with a few highest eigenvalues are used in the computation, as shown in equation (43).

$$P_{m \times k} = [X_1 - \mu \ \dots \ X_m - \mu]^T_{m \times n} [a_1 \ \dots \ a_k]_{n \times k} \quad (43)$$

Here  $P_{m \times k}$  is the weight matrix, which by multiplying  $[a_1 \ \dots \ a_k]_{n \times k}$  can be used to reconstruct  $[X_1 - \mu \ \dots \ X_m - \mu]^T$ . The relationship between  $P_{m \times k}$  and the device values can be approximated via the regression.

### 8.2.2.4 SVD Method

Another method to reduce the dimensions of the data set is the SVD method [82]. Given  $X_{m \times n} = [X_1 \ \dots \ X_m]^T$ , the spectra of the  $m$  colors in the training dataset, there exists a factorization form of  $X$  shown in equation (43).

$$X = URV^T \quad (43)$$

Where,

$U$  is a  $m \times m$  unitary matrix,

$R$  is a diagonal matrix with  $r$  non-zero entries ( $r$  is equal to the rank of  $X$ ),

$V$  is a  $n \times n$  unitary matrix.

$$X^T X = (URV^T)^T URV^T = V(R^T R)V^T$$

Here  $R^T R$  is a diagonal matrix;

So,  $V$  is composed of the eigenvectors of  $X^T X$  and the diagonal entries of the  $R$  is composed of the square roots the eigenvalues of  $X^T X$ . Likewise,  $X$  can be approximated via the linear combination of the eigenvectors related with a few biggest eigenvalues, and the weight matrix can be computed via the regression based on the RGB values.

### 8.2.3 Other Factors Improving the Accuracy of the Camera Calibration

In addition to the calibration algorithm, other factors also affect the accuracy of the camera calibration, which include illumination, training set, image acquisition as well as spatial variation. These are briefly described in the following sections.

### 8.2.3.1 Illumination

A well-defined, spatially and temporally uniform and constant illumination would help minimize variability during image capture and analysis. The illumination and viewing geometry of the camera-based system should be similar to that used in the color measurement. The CIE has recommended 4 types of illumination and viewing geometries for measurement of the object color: (a) normal/diffuse (0/d), (b) diffuse/normal (d/0), (c) 45°normal (45/0) and (d) normal/45° (0/45), as shown in Figure 29. Thus the illumination and viewing geometry of a camera-based system should be selected from one of the recommended geometries [2].

Ng et al. [42] reported an experimental apparatus which simulated the illumination viewing geometry of d/0. Pointer et al. [74] used two directional light sources at 45° to simulate the 45/0 illumination viewing geometry. In this work, the illuminating/viewing geometry inside the DigiEye® system, developed by Verivide, approximates d/0.

### 8.2.3.2 Training Set

A training set is required to set up the data mapping between the camera device dependent space and the independent color space. The color patches inside the training set are measured and their spectral values or tristimulus values are obtained. Usually, a standard test chart is used as the training data. Figure 30 shows the Gretag ColorChecker DC chart which contains 240 color patches.

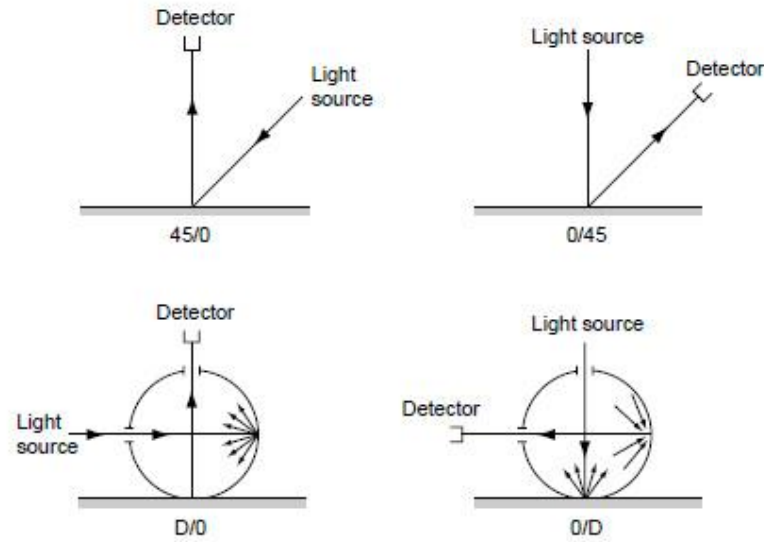


Figure 29. Recommended Illumination / Viewing Geometries for the Measurement of Object Color [2]

The distribution and number of colors in a training set are crucial for accurate training of a colorimetric system. Pointer, et al. [74] concluded that when a larger number of color patches were used in the training set, the mean of the color differences do not change, while the distribution is narrowed. Lasarte, et al. [84] pointed out that the color accuracy was independent of the training set, when the number of color patches in the training set exceeds 120 if the color samples in the training set are uniformly distributed in the color space.

Several researches have suggested the use of color patches that span the colors of interest in the calibration of a digital camera to improve the color accuracy [40, 41].



Figure 30. Gretag ColorChecker DC Chart

### 8.2.3.3 Image Acquisition

In most cases, a camera based system uses only three channels, i.e., R, G and B. More channels can provide additional information or constraints into the calculation when higher color accuracy is desired. A multi-spectral system based on a monochrome camera plus 7 filters has been used [47, 84] for close approximation of the reflected spectral curves. Wu, et al. [41], and Trussell and Vrhel [85, 86] discussed the optimization of the color filters to improve the accuracy of data acquisition. Sharma et al. [87] used set theoretic estimations to consider the effect of the physical constraints, such as the smooth and nonnegative filter

spectra, on the scanner characterization. Wu et al. [41, 42, 88] applied a RGB camera with 2 filters to obtain the data from 6 channels. Other researchers determined how to add additional filters to the scanner to increase its accuracy [35]. Hewlett-Packard developed a novel six-channel scanner, which is claimed to improve the accuracy of the color correction algorithm [89].

Figure 31 shows the spectral response of the RGB channels in Nikon D90.

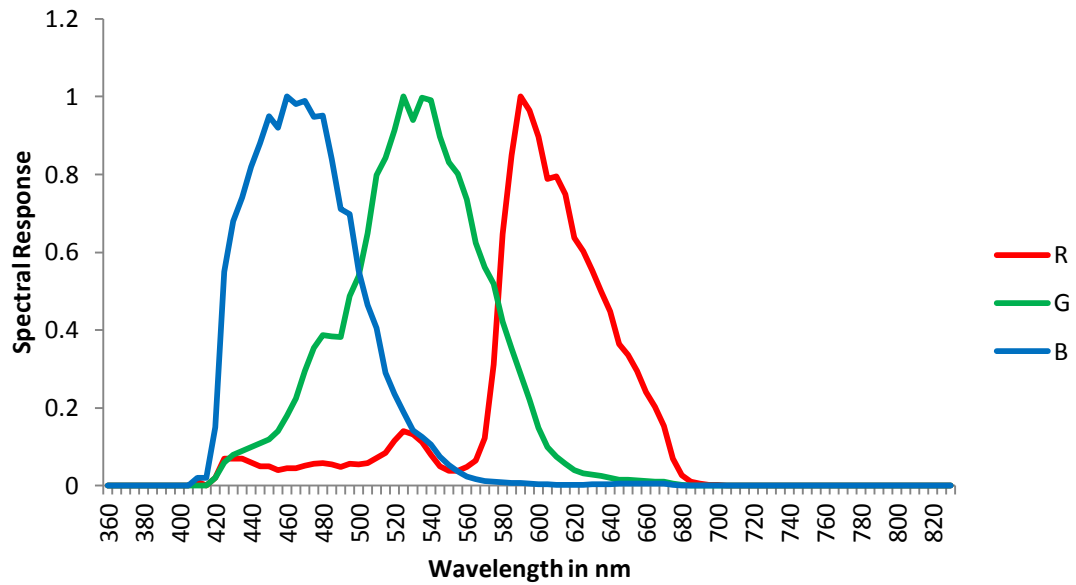


Figure 31. Spectra of the RGB filters in Nikon D90

### 8.2.3.4 Spatial Variation

When camera is used to capture the image, there is spatial variation in the image illumination. Luo, et.al, pointed out that the RGB values of the center pixels were 25% higher than the RGB values of the corner pixels when a uniform gray matte surface was digitized [75]. The derivation below can be used to estimate the spatial variation of the image illumination.

When light is transmitted through the camera lens, there are light losses and the illumination becomes smaller. Figure 32 shows the factors related with the loss of the image illumination.  $S$  is an area at the distance of  $u$  from the lens, with the luminance of  $L$ . The solid angle subtended by the lens at  $S$  is  $\omega$ , which can be described with equation (44).

$$\omega = \frac{A \cos \theta}{\left(\frac{u}{\cos \theta}\right)^2} \quad (44)$$

The flux which leaves  $S$  and travels through the center of the cone is  $LS \cos \theta$ . So the flux that enters the cone is expressed in equation (45).

$$K = (LS \cos \theta) \frac{A \cos \theta^3}{u^2} \quad (45)$$

The flux that reaches  $S'$  is  $K'$  which equals  $KT$ . Here  $T$  is the transmittance of the lens.

The illumination at  $S'$  can be defined via equation (46). Thus  $E$  is proportional to  $\cos^4 \theta$  [90].

$$E = \frac{K'}{S'} = \frac{TL S A \cos^4 \theta}{u^2 S'} = \frac{TL A \cos^4 \theta}{v^2} \quad (46)$$

$$\text{Here } \frac{S}{S'} = \frac{u^2}{v^2}$$

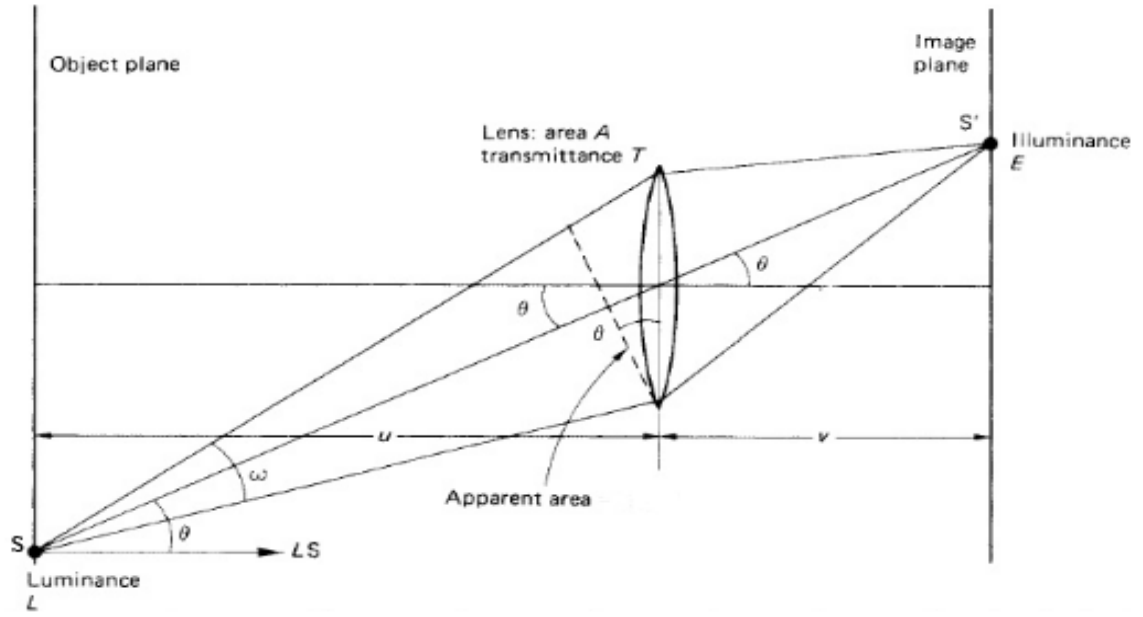


Figure 32. Factors related with the Image Illumination [90]

## **Chapter II. Quality Control of Universal Camouflage Samples**

### **1. Universal Camouflage Pattern**

The Universal camouflage pattern (UCP), also referred to as ACUPAT (Army Combat Uniform PATtern) or Digital Camouflage (“digicam”), is a military camouflage pattern used in the United States Army. Its pattern is developed from some field and laboratory experiments that were carried out between 2003 and 2004, and is a modification of the United States Marine Corps’ MARPAT camouflage and research into Dual Texture (Dual-Tex) Camouflage conducted in the 1970s. The color scheme of the universal camouflage pattern is composed of three colors - Desert Sand, Urban Gray and Foliage Green. The pattern is noticeable for its elimination of the color black because black is a color that cannot be commonly seen in nature. Pure black appears excessively dark and creates an undesirable high-contrast image when viewed through night vision goggles [91, 92].

The pattern contains a section known as the ‘key’ as it resembles the shape of a key. In visual assessments, the ‘key’ pattern, which is shown in Figure 33, is used as a common area for comparison. When a batch sample is compared against the standard sample, the comparison is based on colors around the ‘key’. In the visual comparison of complicated patterns, the use of the same region can help decrease the effects of the background on judgments. At the Natick soldier center, a batch sample is failed if any of the three colors is failed in the visual assessment.

One hundred and six samples were obtained from the Natick soldier center and employed in this research. Each sample contains an ID number and was assessed by the visual assessor at

the Natick soldier center as 'pass' or 'fail'. These samples include 1 standard sample, 41 'pass' samples and 64 'fail' samples.

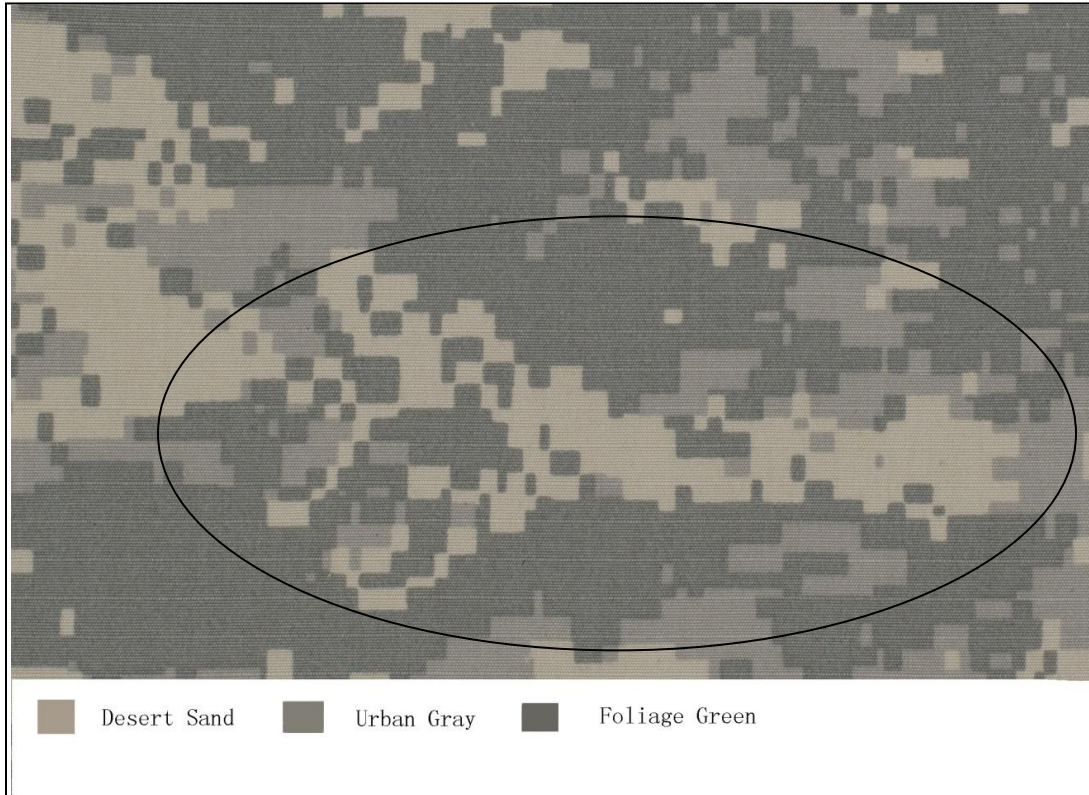


Figure 33. Universal Camouflage Sample with 'Key' Pattern

## 2. Color Measurement and Data Analysis

### 2.1 Tristimulus Values

All the samples were previously measured with a Datacolor SF600X spectrophotometer by L.M. Cardenas[93]. The conditions employed for the measurement included a 9mm sample

measurement aperture and specular included. Colorimetric data were calculated using the CIE illuminant D75 and 10 °Supplemental Standard Observer. It was decided to measure each color on every fabric in six different regions and these regions were selected randomly by the operator. In every region, the area of the color of interest was sufficient to cover the 9mm measurement aperture. Each color in each region was measured four times, and an average of the four readings was obtained. Samples were folded two times to ensure opacity during measurements.

Table A in Appendix shows the CIELAB values of the three colors for all samples. From these data, the maximal and minimal CIELAB values for ‘pass’ samples were determined to form definite borders separating the ‘pass’ samples from the ‘fail’ samples and only 1 fail sample is recognized as ‘pass’. This is shown in Table 3. When the difference between the maximal value and the minimal value is smaller than unity, the numbers are marked in red. The small tolerance will likely be affected by the variation and error in the experiment. When all data are converted to CIELCH, similar boundaries can be determined to divide the ‘pass’ samples from the ‘fail’ samples except for one ‘fail’ sample as shown in Table 4. It can be seen that the difference between the max and the min C\* for Foliage Green is less than 1.

Table 3. Boundaries between the samples rated as ‘Pass’ and ‘Fail’ in CIELAB space based on responses from one expert assessor at Natick Soldier Center

	Desert Sand			Urban Gray			Foliage Green		
	L*	a*	b*	L*	a*	b*	L*	a*	b*
Max	66.13	2.39	11.09	54.60	-0.34	6.27	45.17	-1.58	3.39
Min	63.71	1.85	9.61	51.63	-1.00	5.23	41.26	-1.97	2.69

Table 4. Boundaries between the samples rated as ‘Pass’ and ‘Fail’ in CIELCH space based on response from one expert assessor at Natick Soldier Center

	Desert Sand			Urban Gray			Foliage Green		
	L*	C*	h°	L*	C*	h°	L*	C*	h°
Max	66.13	11.27	80.47	54.60	6.35	99.04	45.17	3.91	123.34
Min	63.71	9.84	76.79	51.63	5.25	93.59	41.26	3.14	115.21

For each color, all ‘pass’ samples are within a rectangular cube in the CIELAB space ( $L_{min}^* < L^* < L_{max}^*$ ,  $a_{min}^* < a^* < a_{max}^*$ ,  $b_{min}^* < b^* < b_{max}^*$ ), and this rectangular cube covers the convex hull developed from the ‘pass’ samples for that color. So, there are three convex hulls developed from the ‘pass’ samples in the CIELAB color space for the three colors, and they may also be used as the boundary for pass / fail judgments. From the results in Table A in Appendix, and Figure 34 is shown that the ‘pass’ samples are within three small convex hulls in the CIELAB space. A batch sample is rated as pass when all its three colors are within these convex hulls. Similarly, such convex hulls can also be formed in the CIEXYZ color space, which separate the samples rated as pass from those rated as ‘fail’ completely, as shown in Figure 35(a-c). Likewise, a batch sample can be regarded as ‘pass’ when all its three colors are within these convex hulls in the CIEXYZ color space, which is equivalent to that in the CIELAB color space.

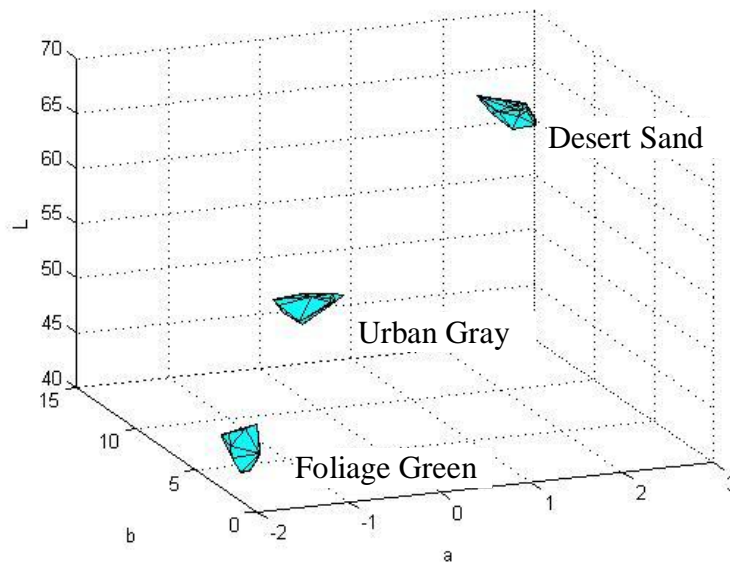
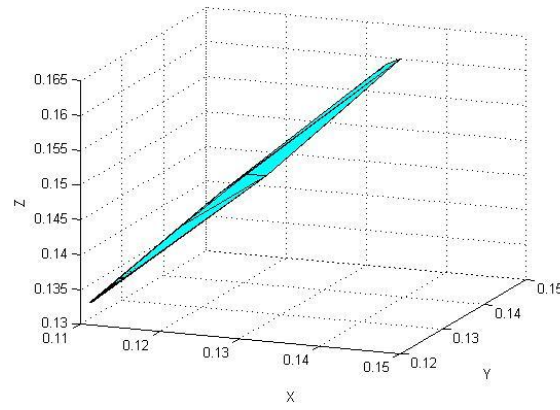


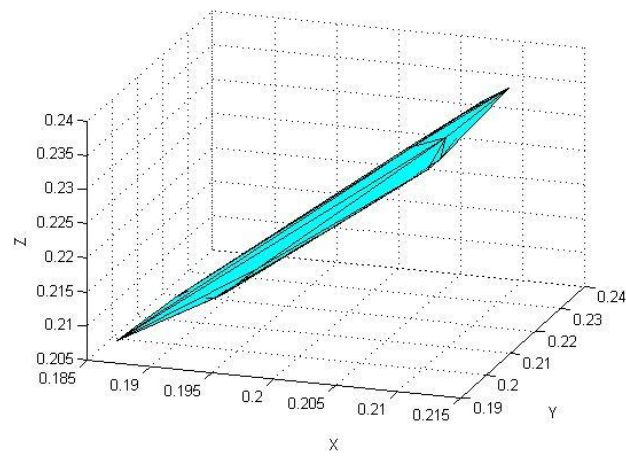
Figure 34. Convex Hulls from the “Pass” Samples of Three Colors in CIELAB

Given the tolerance boundary in the CIELAB space shown in Table 3, if the information pertaining to lightness is removed, and only  $a^*$  and  $b^*$  are used for judgments, 1 ‘fail’ sample will be included in the ‘pass’ volume; if  $a^*$  is removed, and only  $L^*$  and  $b^*$  are used in the judgment, 12 ‘fail’ samples will be included in the ‘pass’ volume; if  $b^*$  is removed, and only  $L^*$  and  $a^*$  are used in the judgment, 2 ‘fail’ samples will be included in the ‘pass’ volume. Similarly, with the boundary of the CIELCH space shown in Table 4, if  $L^*$  is removed, and only  $C^*$  and  $h^\circ$  are used for judgments, 1 ‘fail’ sample will be included in the ‘pass’ volume; if  $C^*$  is removed, and only  $L^*$  and  $h^\circ$  are used in the judgment, 8 ‘fail’ samples will be categorized as the ‘pass’ samples; if  $h^\circ$  is removed, and only  $L^*$  and  $C^*$  are used in the judgment, 17 ‘fail’ samples will be mistakenly passed.

(a)



(b)



(c)

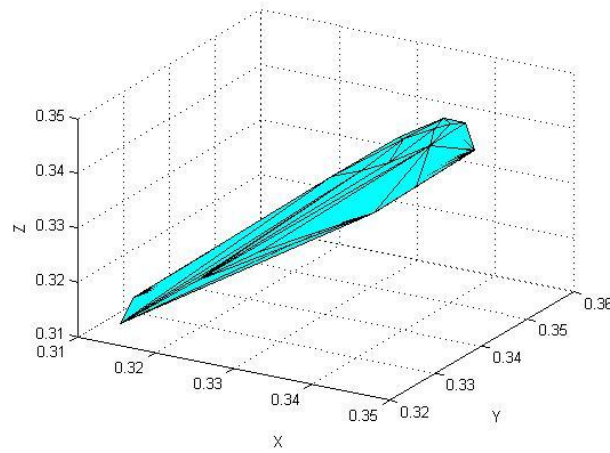


Figure 35(a-c). Convex Hulls from the Samples Rated as “Pass” for the Three Colors in the CIEXYZ Space- Foliage Green (a), Urban Gray (b), Desert Sand (c)

The operations above do not introduce error into the judgment of ‘pass’ samples. From the analysis, hue is the most indispensable attribute in the judgments.

## **2.2 Chromatic Adaptation**

In the manufacture of the universal camouflage fabric, Desert Sand is dyed on the substrates at first, and then Urban Gray and Foliage Green are printed on top of the dyed fabric. So, Desert Sand can be regarded as the ‘white point’ of the fabric, and it is possible to compute the adapted Urban Gray and Foliage Green via the chromatic adaptation. Likewise, chromatic adaptation can be also applied on Foliage Green when Urban Gray is assumed as the ‘white point’.

Three two-color combinations, e.g., Desert Sand / Foliage Green, Urban Gray / Foliage Green and Desert Sand / Urban Gray, exist for the camouflage pattern used. In each combination, the lighter color is used as the “white point” and the darker color is used as the foreground color. Chromatic adaptation was used to shift the foreground color when the background color was shifted to D65. Table B in Appendix shows the results of the application of the wrong von-Kries adaptation. Table 5 shows the boundary developed from Table B in Appendix and with this boundary, 4 ‘fail’ samples have been mistakenly recognized as ‘pass’ samples and all ‘pass’ samples are recognized correctly. If Table 5 is compared with Table 3, it can be noticed that the difference between max and min is expanded in Table 5. But, there are still some differences between the max and the min that are less than 1.

Table 5. Boundary between the ‘pass’ and the ‘fail’ from wrong von – Kries results

	Urban Gray / Foliage Green			Desert Sand / Foliage Green			Desert Sand / Urban Gray		
	L*	a*	b*	L*	a*	b*	L*	a*	b*
Max	86.58	-1.84	-2.58	70.67	-4.68	-6.03	84.73	-3.18	-3.60
Min	79.85	-2.42	-4.34	65.15	-5.64	-7.84	81.01	-4.24	-5.25

However, the chromatic adaptation might also exaggerate the variation or error from the color measurement. Here is an example. The CIELAB values for Desert Sand of the standard sample are (66.17, 2.96, 10.93), and the CIELAB values for Urban Gray of the standard sample are (53.02, -0.41, 5.78). Some noise error  $\delta$  is added to the CIELAB values of Urban Gray while the CIELAB values for Desert Sand are kept constant.  $\delta$  can be one of (-0.1, 0, 0.1). The chromatic adaptation is then applied on ‘Urban Gray / Desert Sand’. In the result, L\* is within (81.29, 81.58), a\* is within (-3.91, -4.20) and b\* is within (-5.03, -5.38); while L\* without  $\delta$  is 81.44, a\* without  $\delta$  is -4.05 and b\* without  $\delta$  is -5.20. The difference between L\*a\*b\* without  $\delta$  and the value after adding the noise is roughly within (-0.15, 0.15). Yet the noise error  $\delta$  is just between -0.1 and 0.1. From another perspective, when the noise  $\delta$  changes the boundary in Table 3 by 0.1, it changes the boundary in Table 5 by 0.15. So, while chromatic adaptation can enlarge the difference between the max and the min the variation will also become larger.

## 2.3 Color Difference Evaluation

Table 6 shows the application of color difference equations for the determination of pass or fail judgments. For each color, the color difference (DE) between the color from the standard

sample and that from the batch sample is calculated using five color difference equations – namely, CIEDE76, CIEDE94, CMC(1:1), CIEDE2000(1:1:1) and CIEDE2000(2:1:1). The maximal  $\Delta E$  from all the ‘pass’ samples are used as the boundary. As three colors are used in the camouflage pattern, it was decided to pass a batch sample only when all three  $\Delta E$ s from its three colors are below the three maximal  $\Delta E$ s. This method was used on all the ‘fail’ samples, and the column ‘Correct Ratio’ is based on the number of the correctly categorized ‘fail’ samples over the number of all the ‘fail’ samples. It can be seen that the majority of the ‘fail’ samples are not correctly clarified. CIEDE2000(2:1:1) performs the best overall, where 15 ‘fail’ samples out of 64 are classified as fail. It might not be a good strategy to apply the maximal  $\Delta E$ s from ‘pass’ samples for the determination of pass / fail judgments.

One possible improvement is to compress the tolerance boundary. Likewise, the maximal DE from all the ‘pass’ samples are used as the boundary. A batch sample is passed when all its three  $\Delta E$ s are smaller than the three maximal  $\Delta E$ s. This would lead to failing some ‘pass’ samples, but would correctly fail more ‘fail’ samples. A program was thus developed to dynamically adjust the values of three  $\Delta E$ s and the most optimized values are shown in Table 7. It can be seen that CIEDE2000 (2:1:1) performs better than other methods with the correct assessment ratio of 75% for the 106 samples.

One possible improvement is to optimize the parameter  $k_L$  in CIEDE94 ( $k_L:1:1$ ), CMC(1:1) and CIEDE2000( $k_L:1:1$ ) color difference formulae. The maximal DE from all the ‘pass’ samples were used as the boundary. A batch sample was passed when all its three  $\Delta E$ s were below the associated three maximal  $\Delta E$ s. This was achieved by using a range of  $k_L$  values

between 0.2-10.0 with an interval of 0.1 initially to determine the locally minimum value. Then around that value a new iteration was set up for  $k_L$  with a decreasing interval. The above step was repeated, until the interval reached 0.0001. The result is shown in Table 8. It can be noticed that with the optimization of  $k_L$ , the correct ratio for the ‘fail’ samples increases. CMC(1:1) performs the best when  $l$  is 3.4. But even for this case, the correct ratio is still less than 50%.

Therefore the overall performance of the color difference equations was not as good as the application of the tristimulus values for the determination of pass / fail results.

Table 6. Boundary from the max  $\Delta E$  and Correct Ratio from ‘Fail’ Samples

	Desert Sand	Urban Gray	Foliage Green	Correct Ratio
CIEDE76	2.84	1.67	2.64	31.82%
CIEDE94	2.84	1.64	2.55	28.79%
CMC(1:1)	2.83	1.51	2.16	25.76%
CIEDE2000(1:1:1)	2.61	1.59	2.19	28.79%
CIEDE2000(2:1:1)	1.39	0.94	1.50	63.64%

Table 7. Boundary from Compressed  $\Delta E$  and Correct Ratio from All Samples

	Desert Sand	Urban Gray	Foliage Green	Correct Ratio
CIEDE76	1.52	1.03	2.72	75.93%
CIEDE94	1.52	0.82	2.57	69.44%
CMC(1:1:1)	1.42	1.06	1.98	79.63%
CIEDE2000(1:1:1)	1.31	0.99	1.99	74.07%
CIEDE2000(2:1:1)	0.70	0.77	1.55	70.37%

Table 8. Boundary from the max  $\Delta E$  with optimized  $k_L$  and Correct Ratio from 'Fail' Samples

	Desert Sand	Urban Gray	Foliage	$k_L$	Correct Ratio
CMC(l:1)	1.5996	0.9550	1.6734	1.9	72.73%
CIEDE94( $k_L$ :1:1)	1.0601	0.6913	1.1695	3	74.24%
CIEDE2000( $k_L$ :1:1)	1.4544	0.9492	1.4992	1.9	72.73%

## 2.4 Variations in the Color of the Samples

Variations among the average color measurements at 6 different locations were calculated and shown in Table C in Appendix. Figure 36 shows the relationship between the absolute of the CIELAB average values and the variances of these CIELAB values for the camouflage samples. The BCRA tiles were also used to test the repeatability of the readings from the Datacolor SF600X spectrophotometer under the same conditions. The relationship between the absolute of the CIELAB average values and the variances of the CIELAB values is also shown in Figure 36. The variances in the CIELAB values of the camouflage samples are apparently larger than those for the BCRA tiles. The standard BCRA tiles are made of ceramic with a smooth, glossy surface. So, the main variance from the BCRA tiles may be regarded as the variation due to spectrophotometer itself, and the larger variances in the camouflage sample might be related with variability in the manufacture of the camouflage samples. According to the analysis above,  $a^*$  and  $b^*$  are more important in the visual assessment and  $L^*$  could be ignored. There are 127  $a^*$  and  $b^*$  variances in Table C in Appendix which are between 0.01 and 0.04, 55  $a^*$  and  $b^*$  variances in Table C in Appendix

which are larger than 0.04 and the maximal  $a^*$  and  $b^*$  variance is 0.2. There are totally 642  $a^*$  and  $b^*$  variances. Thus, the variances of the color measurements at different regions may only affect the final ratings of some samples.

In the visual assessments at the Natick soldier center, the ‘key’ region was used for comparison. Likewise, it would be better that the color measurements are also based on regions around the ‘key’. When the Datacolor bench top spectrophotometers are used for the color measurement, a fixed-sized sample aperture is used. Thus the Datacolor bench top spectrophotometers cannot be used to measure the average CIELAB values around the ‘key’ region directly. Some other spectral devices such as the hyperspectral camera may be applied on the ‘key’ region to avoid this variance.

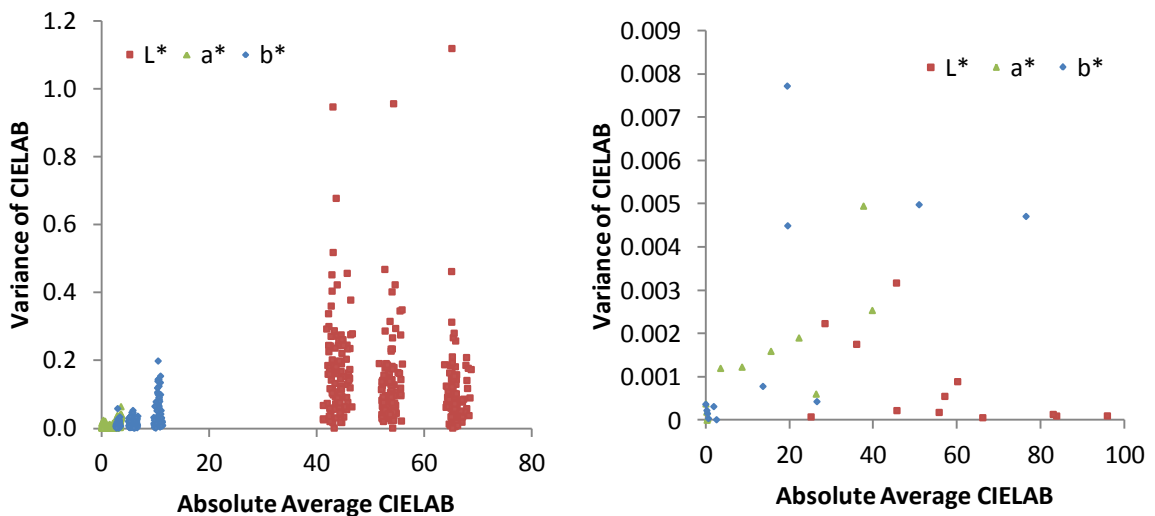


Figure 36. Variances vs. Absolute Average CIELAB values for Camouflage Samples (Left) and Variances vs. Absolute of Average CIELAB values for BCRA Tiles (Right)

### 3. Conclusion

Based on the analysis described, the conclusions below may be drawn:

- The 'pass' samples are distributed in three narrow acceptability volumes in the CIEXYZ and the CIELAB color spaces;
- Hue is the most indispensable color attribute in the visual judgments;
- The use of chromatic adaptation transform to improve results does not significantly change the performance of the system compared to the use of tristimulus values and results in the exaggeration of error;
- Color difference equations do not demonstrate the full complexity of visual judgments as the tristimulus values;
- Variances in the color measurement of the camouflage samples are larger than the variances for the BCRA tiles as expected and the larger variances are likely due to variations in the sample production;
- Other devices such as hyperspectral camera may be used on the 'key' region to decrease the variation in the production.

## **Chapter III. Variations due to the Measurements with Spectrophotometer**

A target of the research project was to determine the threshold between the samples judged as 'pass' and those judged as 'fail' in the color space. In chapter III, it was demonstrated that a boundary in the CIELAB color space or the CIELCH color space can be established to separate the 'pass' samples from the 'fail' samples. The color measurement of samples was carried out on a Datacolor SF600X spectrophotometer which in comparison to a master device such as Datacolor SF500 is more variable. Readings from a master spectrophotometer are more constant, and the inter- and intra- variances for repeated measurements of the same sample over time or in different positions are relatively small. Furthermore, in this study, the 'pass' samples are distributed in three narrow regions of the color space. Therefore, it was decided to determine the level of agreement between the results from Datacolor SF600X and those from Datacolor SF500. Since the acceptability boundary was established based on the SF600X readings, it is important to determine if results are accurate enough and can be used for modeling, or whether a transformation would be needed to convert the results from Datacolor SF600X to those based on Datacolor SF500. The following sections describe the methodology employed to examine this question.

### **1. BCRA Tiles and Color Measurement**

The British Ceramic Research Association (BCRA) tiles are commonly used as the reference standards in colorimetry and spectrophotometry. The ceramic tiles are maintained under the

controlled conditions. The BCRA tiles do not experience significant changes in their physical properties over time and their colors remain relatively unchanged. The set consists of 12 tiles, five of which are of neutral colors and the rest are of saturated colors, as shown in Figure 37. These tiles are measured with the Datacolor SF500 under two modes – specular-included and specular-excluded and the data is supplied with tiles. This information can be used to determine variability among instruments or drifts over time. Figure 38 shows the spectra based on SF500 measurements. It can be seen that the reflectance spectra under specular-included mode are a little higher than those under specular-excluded mode, which was expected since mirror reflected light is leaked when the specular exclusion port is open under the specular-excluded mode.



Figure 37. BCRA Tiles

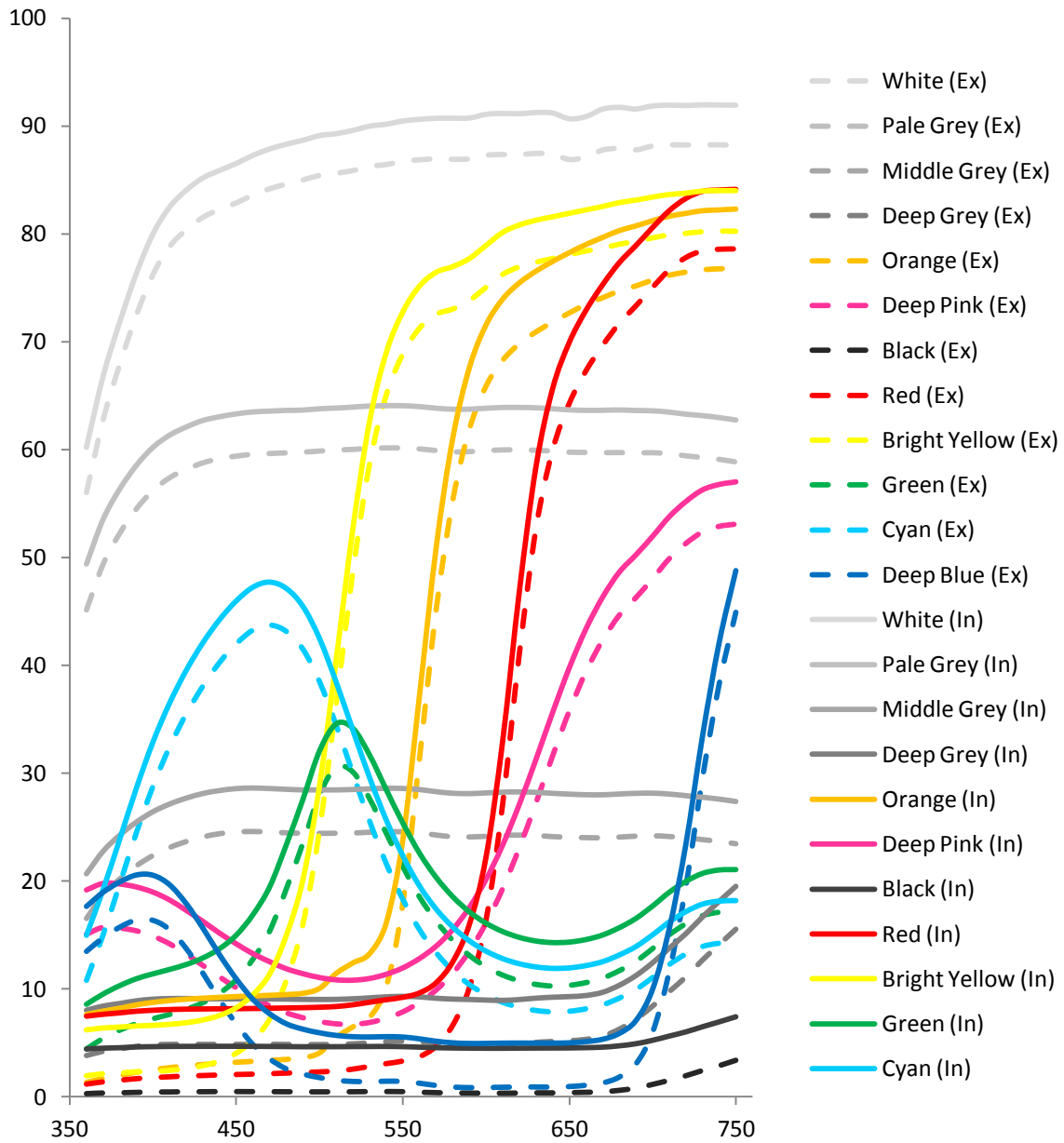


Figure 38. Reflectance Spectra of BCRA Tiles based on SF500 under Specular-Excluded Mode (Dash Line) and Reflectance Spectra of BCRA Tiles under Specular-Included Mode (Solid Line)

Four Datacolor spectrophotometers, namely – SF400, SF600, SF600X and SF650, were used to measure the BCRA tiles repeatedly under both modes – specular-included and-specular excluded. Table 9 shows the  $dL^*$ ,  $da^*$  and  $db^*$  between the average readings from SF600X and the readings from SF500. A noticeable difference in some color titles is observed which due to small differences between colors examined in this research cannot be ignored. The intra-variances of colorimetric values between these devices are shown in Table 10-13 and the inter-variances are shown in Table 14.

Table 9.  $dL^*$ ,  $da^*$  and  $db^*$  between SF600X and SF500

	Specular Excluded			Specular Included		
	$dL^*$	$da^*$	$db^*$	$dL^*$	$da^*$	$db^*$
White	-0.0617	-0.0415	0.061	-0.1091	-0.0261	0.002
Pale Grey	-0.0615	-0.1151	0.0116	-0.0725	-0.0784	0.0124
Mid Grey	0.0235	-0.0649	-0.0684	-0.0659	-0.0105	-0.0425
Deep Grey	-0.1935	0.0190	-0.0193	-0.1877	0.1276	0.2426
Orange	-0.3306	0.3313	-0.1665	-0.2651	0.1195	-0.3727
Pink	-0.1017	-0.1739	-0.0751	-0.1485	-0.0672	-0.1526
Black	0.0375	0.0506	0.1629	-0.3492	0.1217	0.0816
Red	-0.2433	-0.3214	-0.3568	-0.2253	-0.5241	-0.3769
Yellow	-0.1794	0.1455	-0.0046	-0.1771	0.1937	-0.0821
Green	-0.0350	0.1000	0.0632	-0.1467	0.0971	0.1693
Cyan	-0.0584	-0.0017	0.0045	-0.1274	0.0633	0.0182
Blue	-0.0468	-0.1048	0.0888	-0.0693	0.0638	0.2612
Avg of Abs Values	0.114408	0.122475	0.090225	0.161983	0.124417	0.151175

Table 10. Intra - Variance of BCRA L\*a\*b\* from SF400

	Specular Excluded			Specular Included		
	Var(L*)	Var(a*)	Var(b*)	Var(L*)	Var(a*)	Var(b*)
White	0.000190	0.000247	0.000476	2.76E-06	8.3E-05	0.000147
Pale Grey	0.000449	0.000153	0.000802	0.000726	0.000171	6.37E-06
Mid Grey	0.000385	0.000424	0.002183	0.003792	0.000279	0.001231
Deep Grey	0.006977	0.000900	0.001051	3.97E-05	0.000113	0.000723
Orange	0.018688	0.021194	0.052291	0.010019	0.018486	0.012434
Pink	0.004361	0.003798	0.002782	0.000205	0.000584	2.91E-05
Black	0.005733	0.001564	0.010712	1.64E-05	0.000336	0.000239
Red	0.002239	0.009428	0.045876	0.000244	0.005512	0.002255
Yellow	0.004080	0.012230	0.002313	0.000354	0.000323	0.014581
Green	0.000948	0.008593	0.005999	0.000501	0.000653	0.000465
Cyan	0.001183	0.001902	0.001334	0.000136	0.001486	0.000784
Blue	0.001816	0.002895	0.002428	0.000155	0.001490	0.001918
Average	0.003921	0.005277	0.010687	0.001349	0.002460	0.002901

Table 11. Intra - Variance of BCRA L\*a\*b\* from SF600

	Specular Excluded			Specular Included		
	Var(L*)	Var(a*)	Var(b*)	Var(L*)	Var(a*)	Var(b*)
White	0.012993	0.000428	0.050323	0.000346	3.47E-05	3.54E-05
Pale Grey	0.008736	0.000275	0.040629	0.001402	6E-05	0.000562
Mid Grey	0.007575	0.000193	0.018757	0.010096	6.8E-05	0.000598
Deep Grey	0.019246	0.001823	0.013796	0.002513	0.000156	0.003169
Orange	0.008088	0.005865	0.012108	0.016278	0.004878	0.020983
Pink	0.005734	0.003203	0.021212	0.002894	0.000202	0.000138
Black	0.041064	0.010957	0.018386	0.000159	4.3E-05	0.000572
Red	0.001495	0.003832	0.031908	0.003000	0.011950	0.004373
Yellow	0.009783	0.010364	0.006476	0.001300	0.000946	0.013295
Green	0.007014	0.005440	0.010107	4.65E-05	0.001580	0.001533
Cyan	0.007488	0.005065	0.058513	0.002686	0.002621	0.000403
Blue	0.003903	0.024307	0.038224	0.000668	0.000417	0.002930
Average	0.011093	0.005979	0.026703	0.003449	0.001913	0.004049

Table 12. Intra - Variance of BCRA L\*a\*b\* from SF600X

	Specular Excluded			Specular Included		
	Var(L*)	Var(a*)	Var(b*)	Var(L*)	Var(a*)	Var(b*)
White	0.014169	0.000276	0.040160	0.000101	1.21E-06	1.2E-05
Pale Grey	0.007046	0.000132	0.033968	9.81E-05	4.26E-05	4.01E-05
Mid Grey	0.006895	0.000216	0.019483	0.000892	3.5E-05	0.000369
Deep Grey	0.005800	0.000530	0.007302	0.001755	0.000378	0.000155
Orange	0.007932	0.005282	0.107059	5.89E-05	0.002537	0.004981
Pink	0.006923	0.002634	0.013615	0.003171	0.001902	0.000316
Black	0.001097	0.004042	0.009800	7.74E-05	0.000188	0.000225
Red	0.002432	0.005407	0.014599	0.000223	0.004948	0.004493
Yellow	0.006995	0.008452	0.001625	0.000135	0.001199	0.004710
Green	0.005274	0.008107	0.005944	0.000181	0.000604	0.000782
Cyan	0.006655	0.001808	0.025247	0.000552	0.001592	0.000431
Blue	0.002851	0.021199	0.027315	0.002233	0.001228	0.007722
Average	0.006172	0.004840	0.025510	0.000790	0.001221	0.002020

Table 13. Intra - Variance of BCRA L\*a\*b\* from SF650

	Specular Excluded			Specular Included		
	Var(L*)	Var(a*)	Var(b*)	Var(L*)	Var(a*)	Var(b*)
White	4.63E-05	0.000197	4.69E-05	8.38E-05	0.000137	0.000107
Pale Grey	0.000197	9.44E-05	6.27E-05	0.000186	6.09E-05	4.32E-05
Mid Grey	0.000798	0.000212	0.000275	0.003399	0.000424	1.43E-05
Deep Grey	0.004286	0.000890	0.000831	0.000794	0.000630	0.000339
Orange	0.004836	0.004551	0.038203	0.000572	0.002469	1.73E-05
Pink	0.001002	0.003161	0.001025	0.000955	3.43E-05	0.000110
Black	0.005619	0.001901	0.005533	0.000469	0.000373	0.000145
Red	0.002986	0.019848	0.083015	0.000147	0.002180	0.000832
Yellow	0.000787	0.003452	0.002663	9.63E-05	7.84E-06	0.001284
Green	0.000270	0.004212	0.001395	0.000103	2.36E-05	0.000184
Cyan	0.001935	0.000953	0.001809	0.000425	0.001126	0.000308
Blue	0.003744	0.012323	0.011124	0.002361	0.001354	0.004317
Average	0.002209	0.004316	0.012165	0.000799	0.000735	0.000642

Table 14. Inter - Variance of BCRA L\*a\*b\*

	Specular Excluded			Specular Included		
	Var(L*)	Var(a*)	Var(b*)	Var(L*)	Var(a*)	Var(b*)
White	0.019387	0.009883	0.055729	0.004693	2.16E-06	0.000152
Pale Grey	0.008013	0.011090	0.030319	0.012564	0.000261	0.001226
Mid Grey	0.010903	0.007584	0.013262	0.001290	0.000878	0.001362
Deep Grey	0.001804	0.001877	0.000649	0.005651	0.000385	0.006033
Orange	0.005073	0.001733	0.005458	0.005105	0.000320	0.003144
Pink	0.002856	0.000755	0.012335	0.003520	1.93E-05	0.002189
Black	0.000688	0.001651	0.041340	0.014459	0.000686	0.018670
Red	0.001449	0.000242	0.014602	0.012089	0.000369	0.003956
Yellow	0.010833	0.007609	0.015388	0.006063	0.002477	0.001897
Green	0.008424	0.024474	0.000276	0.001747	0.001889	0.007283
Cyan	0.010758	0.007116	0.023989	0.001963	0.000576	0.004465
Blue	9.17E-05	0.014229	0.008397	0.008195	0.000374	0.002984
Average	0.006690	0.007354	0.018479	0.006445	0.000686	0.004447

It can be noted that both inter- and intra- variances are larger under specular-excluded mode than those under specular-included mode. Furthermore, the intra-variances from Table 10-13 under specular-excluded mode are within 4.63E-05 and 0.107, the intra-variances from Table 10-13 under specular-included mode are within 1.21E-06 and 0.021; the inter-variances from Table 14 under specular-excluded mode are within 9.17E-05 and 0.0557, the inter-variances from Table 14 under specular-included mode are within 2.16E-06 and 0.01867. Thus, the inter-variances and the intra-variances are at the same magnitude level. The method described below was examined to determine whether the inter-variance could be decreased from the mixture of the intra-variance and the inter-variance.

## 2. Endeavor to Correct the Spectrum

A software application was developed to modify the spectrum. The spectra of BCRA tiles based on SF500 readings were known and those from other Datacolor spectrophotometers were acquired. Thus, it was possible to set up a data mapping from each spectrophotometer to SF500 at any given wavelength, as shown in equation (47):

$$r_{SF500} = f_{SFXXX}(r_{SFXXX}) \quad (47)$$

Here  $r_{SFXXX}$  is the spectral reading at a given wavelength from a given spectrophotometer;

$r_{SF500}$  is the spectral reading at a given wavelength from SF500;

$f_{SFXXX}$  stands for the data mapping for the device  $SFXXX$ . Here  $SFXXX$  can be one of the SF400, SF600, SF600X and SF650.

At any given wavelength, 12 reflectance factors from the SF500 readings and the associated 12 reflectance factors from a given spectrophotometer under the same measurement mode are presented. Catmull-Rom spline interpolation [94] is employed to set up the data mapping,  $f_{SFXXX}$ , in every wavelength.  $f_{SFXXX}$  can be used to transform any given spectra from a given spectrophotometer into the spectral reading from SF500. In our experiments, the effective wavelength range in the spectrophotometers was from 400nm to 700nm with the interval of 10nm; so 31  $f_{SFXXX}$ s were calculated and applied in the correction.

Figure 39 shows the snapshot of the software application developed. The spectra from SF500 can be preset into the data file as the reference standard. As there are two sets of spectra for the specular – included mode and the specular – excluded mode, two sets of reference standard are obtained from SF500. The operator can choose the reference standard based on

the settings used in the color measurement. The color spectra and the BCRA spectra of the experimental results can be copied into the text box. When the conversion is completed, the converted color spectra are copied back into the system clipboard for analysis.

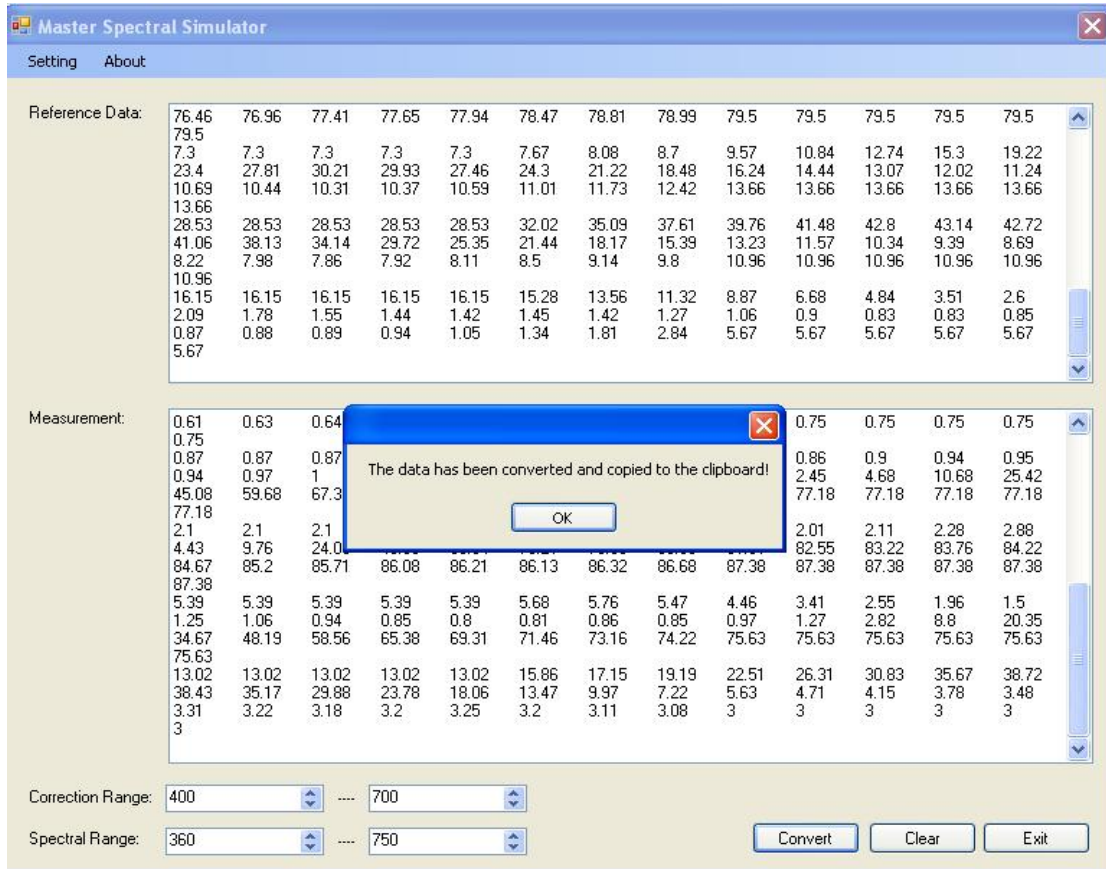


Figure 39. Snapshot of the Software Application

### 3. Data Analysis, Results and Discussion

In order to check the performance of the software, 17 color patches from GretagMacbeth ColorChecker were measured using the four spectrophotometers. Samples included 9 matte surface patches and 8 glossy surface patches. Three tests were run. In every test, 12 BCRA tiles were measured first and then 17 color patches were measured in each spectrophotometer. Finally, the software was used to correct the spectra of the ColorChecker tiles. The inter-variance before correction is listed in Table 15. The inter-variance after correction is listed in Table 16.

Table 15. Inter - Variance of ColorChecker before Correction

	Specular Excluded			Specular Included		
	Var(L*)	Var(a*)	Var(b*)	Var(L*)	Var(a*)	Var(b*)
A1	0.007424	0.005954	0.001452	0.006559	0.010030	0.003244
B1	0.006877	0.003399	0.002281	0.003292	0.004345	0.002487
C1	0.022205	0.005253	0.003917	0.008986	0.001199	0.021307
S4	0.025329	0.003116	0.002605	0.008099	0.005418	0.011024
S5	0.072992	0.334041	0.297593	0.012980	0.051149	0.034334
S6	0.039087	0.144097	1.107628	0.025238	0.017359	0.012827
S7	0.010346	0.004335	0.000642	0.009871	0.009045	0.000620
S8	0.124569	0.000115	0.040887	0.008451	0.000850	0.013979
S9	0.033649	0.006958	2.555459	0.006770	0.004234	0.031769
S10	0.006614	0.040537	0.018262	0.009165	0.000772	0.005286
S11	0.020384	0.035228	0.004906	0.007415	0.003175	0.001317
D2	0.013330	0.005697	0.007058	0.007346	0.003537	0.002881
M5	0.013528	0.007288	0.002388	0.013205	0.003959	0.008846
M7	0.008376	0.010736	0.011209	0.003998	0.026783	0.003322
K9	0.009702	0.003461	0.003275	0.007887	0.006779	0.005010
E10	0.008110	0.014628	0.000691	0.005181	0.015197	0.004623
F11	0.005650	0.002770	0.003084	0.005722	0.003869	0.001369
Average	0.025187	0.036918	0.239020	0.008833	0.009865	0.009661

It can be noted that both inter- variance and intra- variance are larger under specular- excluded mode than those under specular- included mode. For specular- excluded mode, the glossy surface patches – S4 to S11 are the major source of the large variation.

It should be pointed out that the variance of b\* for sample S9 (a yellow tile), is caused by a difference of 0.5 unit in the spectral range of 400nm and 500nm between SF650 and the other three spectrophotometers, as shown in Figure 40.

Table 16. Inter - Variance of ColorChecker after Correction

	Specular Excluded			Specular Included		
	Var(L*)	Var(a*)	Var(b*)	Var(L*)	Var(a*)	Var(b*)
A1	0.000488	0.003425	0.004127	0.004185	0.002632	0.00135
B1	0.002358	0.000503	0.001270	0.001204	0.004378	0.002975
C1	0.019996	0.019363	0.026850	0.000000	0.000000	0.000000
S4	0.022814	0.003997	0.009447	0.000904	0.001672	0.009694
S5	0.069955	0.381798	0.356359	0.001952	0.019100	0.007236
S6	0.039030	0.174693	1.512893	0.010453	0.020008	0.029159
S7	1.67E-08	3.24E-05	0.000107	4.22E-08	6.67E-05	0.000219
S8	0.195041	0.022320	0.035973	0.000220	3.28E-06	0.000362
S9	0.015400	0.010742	2.959082	0.001190	0.002588	0.008386
S10	0.008194	0.053130	0.034542	0.000766	0.001404	0.001485
S11	0.012233	0.066229	0.003118	0.003902	0.001648	0.001096
D2	0.006027	0.004690	0.006327	0.004086	0.004509	0.028838
M5	0.005124	0.023502	0.001852	0.002810	0.000293	0.011556
M7	0.007290	0.009907	0.014073	0.002281	0.017086	0.004423
K9	0.006556	0.000700	0.003082	0.004097	0.002365	0.000235
E10	0.005381	0.013032	0.001078	0.004081	0.007612	0.006196
F11	0.002118	0.003646	0.003061	0.000607	0.004714	0.000898
Average	0.024589	0.046571	0.292544	0.002514	0.005299	0.006712

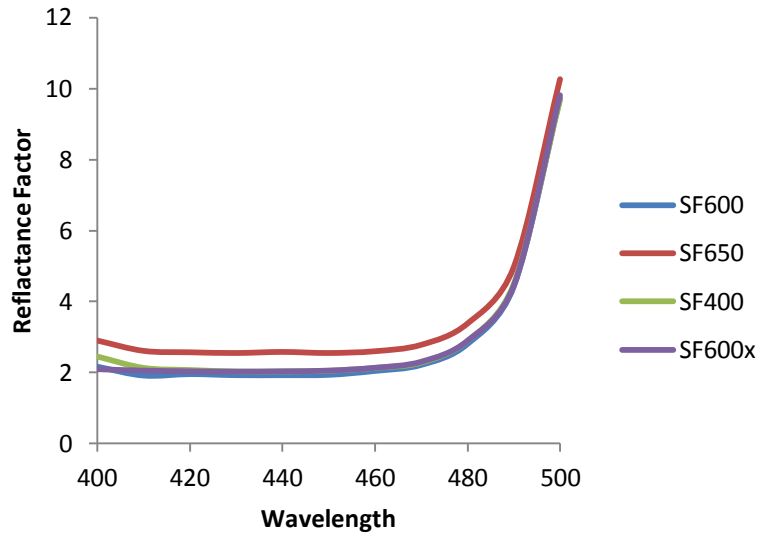


Figure 40. Spectra of S9 from four Datacolor Spectrophotometers

The BCRA tiles include a yellow tile, but no such difference was observed on the measurements of that tile, as shown in Figure 41. Thus, the software application fails to correct for this difference.

As no information regarding sample S9 is available for measurements based on the SF500 under specular-excluded mode, it was not possible to determine whether SF650 performs better than the other three or worse for this color tile.

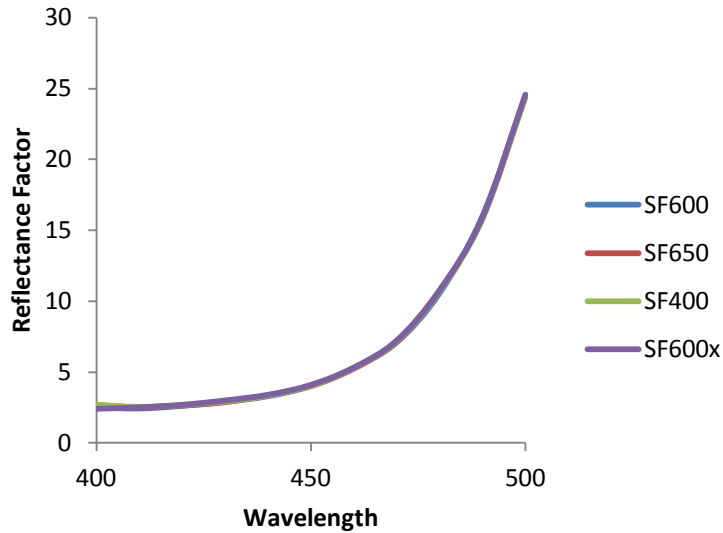


Figure 41. Spectra of BCRA yellow tile from Four Datacolor Spectrophotometers

Table 17 shows the average inter-variance before and after correction for the spectrum, XYZ and L\*a\*b\* under specular-excluded mode. Table 18 shows the average of the inter-variance before and after correction for the spectrum, XYZ and L\*a\*b\* under specular-included mode. It is clear that readings based on the specular-included mode show less variance than those based on the specular-excluded mode.

Table 17. Inter-Variance of ColorChecker L\*a\*b\* under Specular-Excluded Mode

	Variance Before Correction			Variance After Correction		
	Spectrum	XYZ( $\times 10^6$ )	L*a*b*	Spectrum	XYZ( $\times 10^6$ )	L*a*b*
Test 1	2.041	16.538	0.366	0.803	4.456	0.361
Test 2	2.027	10.120	0.292	1.208	3.897	0.386
Test 3	1.430	6.053	0.312	1.028	2.785	0.400

Table 18. Inter-Variance of ColorChecker L\*a\*b\* under Specular-Included Mode

	Variance Before Correction			Variance After Correction		
	Spectrum	XYZ( $\times 10^6$ )	L*a*b*	Spectrum	XYZ( $\times 10^6$ )	L*a*b*
Test 1	1.126	4.721	0.034	0.748	1.728	0.024
Test 2	1.184	4.766	0.034	0.719	1.859	0.020
Test 3	0.958	3.861	0.400	0.665	1.808	0.025

From Tables 17-18, it can be seen that the software can successfully reduce the variances among the spectrum and CIEXYZ, but in some cases it fails to reduce the variances for the L\*a\*b\* in some cases under the specular-excluded mode. This is related with the high glossy color patches. If tiles S5, S6, S8 and S9 are not used in the computation of variance, the average inter-variances of CIELAB after correction are lower than those average variances before correction. S5, S6, S8 and S9 are all high glossy color patches. Table 19 shows the inter-variances of the CIEXYZ tristimulus values for S5, S6, S8 and S9 from test 3 under specular-excluded mode and specular-included mode, and both the values before and after correction are shown. It can be noted that for the specular-excluded mode, more variances of CIEXYZ of S5, S6, S8 and S9 increase rather than drop after correction. According to the CIE definition, L\* is only dependent on Y, a\* is dependent on X and Y and b\* is dependent on Y and Z. Thus, the larger variances in X, Y and Z after correction lead to the increased variance in L\*, a\* and b\*. For the specular-included mode, there is only a slight increase for the variance of X for tile S8. This also supports the conclusion that the high glossy media under specular excluded mode is the major source of the large variation.

As the spectra for the ColorChecker color patches based on the SF500 measurements were not available, it is unknown whether this correction can result in improving results compared to those from SF500.

Table 19. Inter-Variations of the CIEXYZ Tristimulus Values for Tiles S5, S6, S8 and S9 from Test 2 under Specular Excluded Mode and Specular Included Mode

		$\text{Var}(X) \times 10^6$	$\text{Var}(Y) \times 10^6$	$\text{Var}(Z) \times 10^6$	$\text{Var}(L^*)$	$\text{Var}(a^*)$	$\text{Var}(b^*)$
Specular Excluded Before Correction	S5	1.009	1.503	1.549	0.048	0.379	0.387
	S6	0.937	0.190	0.209	0.009	0.089	0.396
	S8	0.197	0.220	0.327	0.169	0.005	0.040
	S9	9.903	12.537	8.209	0.034	0.013	2.595
Specular Excluded After Correction	S5	1.317	1.987	1.909	0.061	0.614	0.489
	S6	0.609	0.217	0.556	0.011	0.105	1.028
	S8	0.383	0.409	0.449	0.330	0.066	0.076
	S9	3.409	4.540	8.576	0.012	0.007	3.009
Specular Included Before Correction	S5	0.197	0.336	0.600	0.007	0.046	0.046
	S6	2.596	0.747	0.176	0.022	0.032	0.019
	S8	0.060	0.056	0.169	0.004	0.001	0.012
	S9	5.303	5.709	0.543	0.015	0.004	0.023
Specular Included After Correction	S5	0.007	0.017	0.033	0.000	0.009	0.006
	S6	1.593	0.383	0.000	0.011	0.036	0.034
	S8	0.100	0.056	0.109	0.005	0.001	0.004
	S9	0.880	0.603	0.047	0.002	0.004	0.005

## 4. Conclusion

From the data analysis above, the conclusions below can be drawn:

- The software application can reduce the variances in the spectra, as well as the XYZ values. This proves the validation of the algorithm developed. However, sometimes the variances in the  $L^*a^*b^*$  values under the specular-excluded mode could not be reduced;
- Under the specular-excluded mode, high glossy media were the main source of the large variances;
- Under the specular-included mode, the variances were much smaller;
- A noticeable difference in the measurements between SF500 and four other spectrophotometers used in the research was found;
- Since the intra- and inter- variances were found to be of the same magnitude, it was not possible to apply this software to eliminate the inter-variance from the mixture of both variances;
- Information regarding the spectra of the color patches or standard color tiles from SF500 are needed to test the accuracy and precision of the spectrophotometers used.

## Chapter IV. DigiEye System

### 1. Introduction of the DigiEye System

A DigiEye illumination chamber was used in this research. This illumination chamber, as shown in Figure 42, is manufactured by Verivide Company in the United Kingdom. There are two fluorescent lamps inside the illumination chamber, along the sliding drawer, to provide the simulated illumination conditions. The object is placed on the surface of the sliding drawer. On top of the illumination chamber, a white balanced digital camera is placed in the direction normal to the sliding drawer. The camera is controlled by the computer to capture the image of the object.



Figure 42. DigiEye System

The captured image can be transferred to the computer and analyzed by the software, and the RGB values of every pixel in the image are then converted to tristimulus values, such as CIEXYZ and CIELAB. Unlike the traditional colorimeter or spectrophotometer, the DigiEye system is used for the non-contact color measurement where traditional colorimeters or spectrophotometers cannot be used, such as for the irregular surfaces and non-solid colors. Figure 43 shows the possible applications of DigiEye system in the food industry. One shortcoming of the non-contact color measurement system is the error in the conversion from the device space to the color space.



Figure 43. Possible Applications of the DigiEye System in the Food Industry [95]

The DigiEye illumination chamber can be used to simulate two of these recommended settings, i.e.,  $d/0^\circ$  and  $45^\circ$ , as shown in Figure 44. The arched roof inside the DigiEye illumination chamber can effectively diffuse the light; when two mirror reflection boards are installed, the light source hits the object at an angle of  $45^\circ$ . In this research, the  $d/0^\circ$  setting

was used, which is identical to the illuminating/viewing geometry of the Datacolor spectrophotometer used for the contact measurement of camouflage substrates.

In the DigiEye illumination chamber, there is no specular exclusion port. This structure is similar to the specular-included color measurement mode.

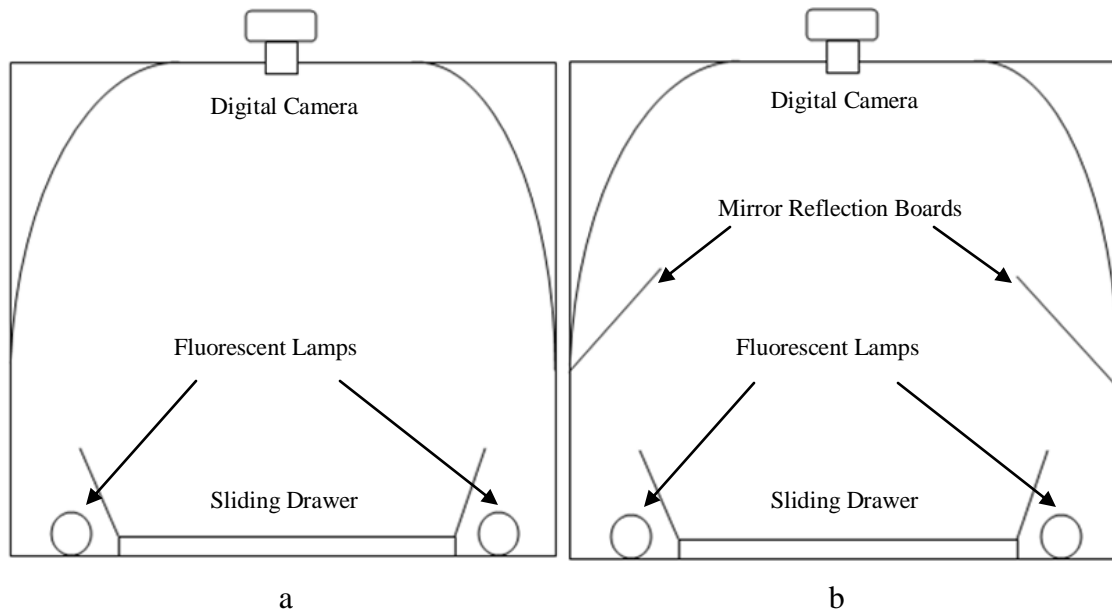


Figure 44. a. Schematic Representation of the  $d/0^\circ$  Illumination / Viewing Setting Employed inside the DigiEye Illumination Chamber  
b. Schematic Representation of the  $45^\circ/90^\circ$  Illumination / Viewing Setting Employed inside the DigiEye Illumination Chamber

Two Verivide D75 ‘Artificial Daylight’ fluorescent lamps [96] were used as the light source, with a recommended lifetime of 2000 hours. The illumination from the lamps is relatively stable in the recommended lifetime. In the recent versions of DigiEye system, LED bulbs are employed. This is designed to improve the simulated spectra of the standard light source.

Furthermore, some LEDs can serve to provide the required UV illumination.

## 2. Variability within the DigiEye System and Correction

### 2.1 Spatial Non-Uniformity of Nikon D90

Figure 45 shows the estimation of the field size of Nikon D90 with Nikkor f2D lens under focal length of 2 feet when it is placed on top of DigiEye illumination chamber, which is roughly 9 inches by 13.5 inches. The distance from the camera lens to the table surface in DigiEye illumination chamber is roughly 22 inches. The  $\theta$  of the four corners of the field in equation (46) can be computed by  $\arctan \frac{\sqrt{9^2+13.5^2}}{22 \times 2} = 20.24^\circ$ . According to equation (46), the ratio between the image illumination of the four corners and the image illumination of the center should be  $\cos^4 \theta = 0.77$ . Thus the difference is 23%.

In order to determine the spatial non-uniformity of the Nikon D90, a uniformity board is used. This is a precisely manufactured gray board with a uniform coating.

Nikon D90 was used outdoor to capture the image of the uniformity board as the sun light outdoor was considered to be uniform. This was done in a sunny day, and the uniformity board was placed in the open field. There was no shadow on the uniformity board. The focal length of the camera was the same as that used on top of the DigiEye illumination chamber. The camera was held at the height of 22 inches, identical to that in the DigiEye illumination chamber. Manual focus was used. Exposure mode was switched to the auto mode. The shutter speed was 1/640s and the aperture was F14. The captured image was converted to dng file format and opened in the Matlab via libtiff. In order to eliminate the random noise, the

whole image was divided into the combination of the macro-blocks of  $16 \times 16$  pixels. In each macro block, the average of RGB is used to represent the RGB values of every pixel in that macro block, and its distribution is shown in Figure 46. It can be noted that the illumination at the center is the highest and the illumination drops from the center to the corners radically. This distribution is similar to the above analysis, although the RGB values were found to be between 378 and 408. The difference between the minimal and the maximal value was 8%, which is less than the estimated value – 23%.



Figure 45. Field Size of Nikon D90 when it is on top of DigiEye Illumination Chamber

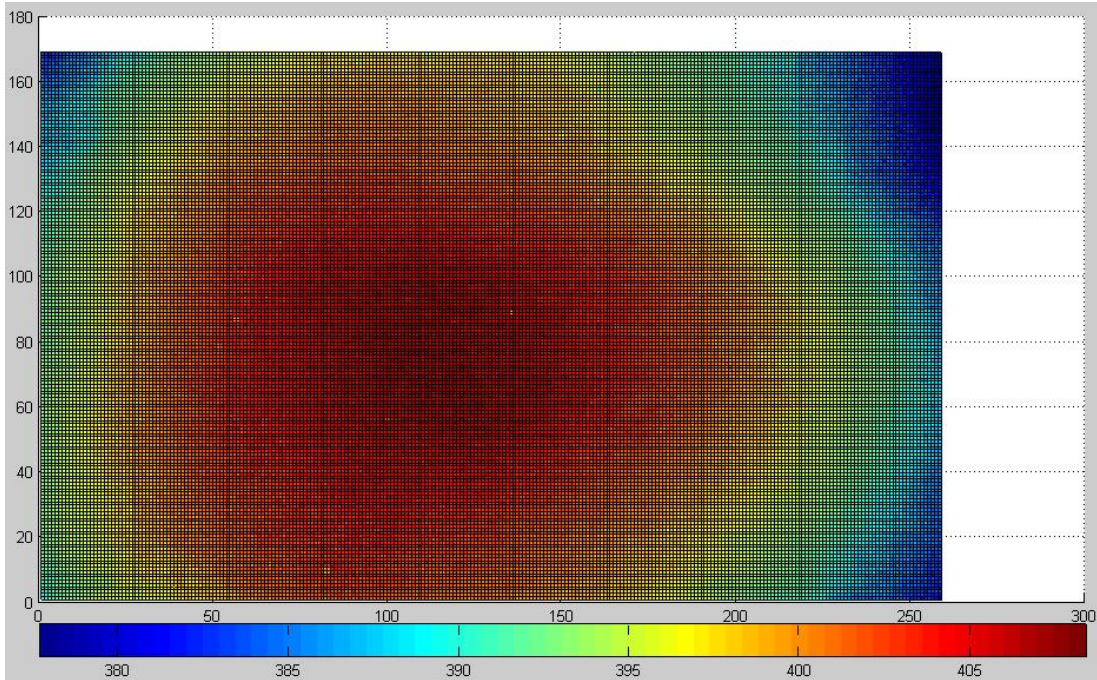


Figure 46. Distribution of the Green Channel of the Illumination Board Used Outdoor

## 2.2 Spatial Non-Uniformity of DigiEye Illumination Chamber

Although the semicylindrical roof inside the DigiEye illumination chamber is designed to provide the diffused illumination, it is unknown whether the distribution of the illumination is uniform throughout the chamber. To determine the variation of the DigiEye illumination chamber, the uniformity board was placed inside the DigiEye illumination chamber, and the camera was set to the manual focus. Then the image of the uniformity board was captured. The whole image was still processed according to the steps above. Figure 47 shows the spatial distribution of the RGB channels after implementing this process. From the color bar below, it can be seen that the red values are ranged between 328 and 358 – the difference is

9.14%; the green values are ranged between 478 and 518 – the difference is 8.36% and the blue values are ranged between 454 and 489 – the difference is 7.71%. The shutter speed was 1/3s and the aperture used was F11 when the image was taken. An algorithm was used to compensate for this difference, as shown in equation (48).

$$\begin{cases} r'(x, y) = r(x, y) \frac{r_{min}}{r_{unif}(x, y)} \\ g'(x, y) = g(x, y) \frac{g_{min}}{g_{unif}(x, y)} \\ b'(x, y) = b(x, y) \frac{b_{min}}{b_{unif}(x, y)} \end{cases} \quad (48)$$

Here,  $r_{unif}(x, y)$ ,  $g_{unif}(x, y)$ ,  $b_{unif}(x, y)$  are the RGB values of the uniformity board at a position  $(x, y)$ ;

$r_{min}$ ,  $g_{min}$ ,  $b_{min}$  are the minimal RGB values of the uniformity board;

$r(x, y)$ ,  $g(x, y)$ ,  $b(x, y)$  are the RGB values at a position  $(x, y)$  before correction;

$r'(x, y)$ ,  $g'(x, y)$ ,  $b'(x, y)$  are the RGB values at a position  $(x, y)$  after correction;

Because  $\frac{r_{min}}{r_{unif}(x, y)} < 1$ ,  $\frac{g_{min}}{g_{unif}(x, y)} < 1$ ,  $\frac{b_{min}}{b_{unif}(x, y)} < 1$ , it can be seen that  $0 < r'(x, y) <$

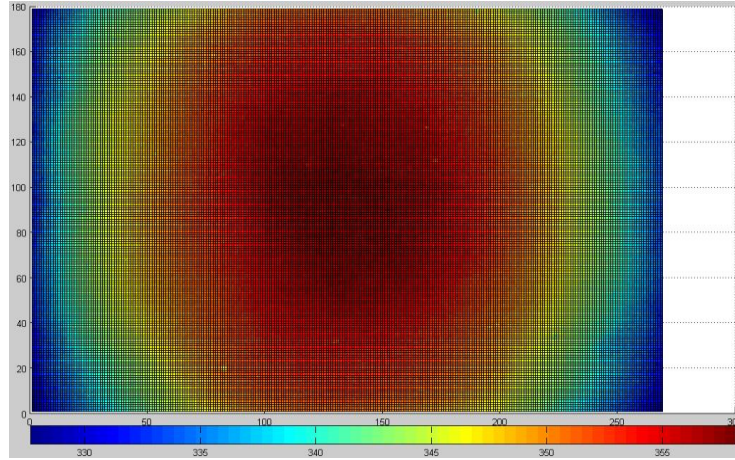
$r(x, y) < r_{max}$ ,  $0 < g'(x, y) < g(x, y) < g_{max}$ ,  $0 < b'(x, y) < b(x, y) < b_{max}$ .

$\frac{r_{min}}{r_{unif}(x, y)}$ ,  $\frac{g_{min}}{g_{unif}(x, y)}$ ,  $\frac{b_{min}}{b_{unif}(x, y)}$  for all the  $16 \times 16$  blocks are saved in a data file for the spatial

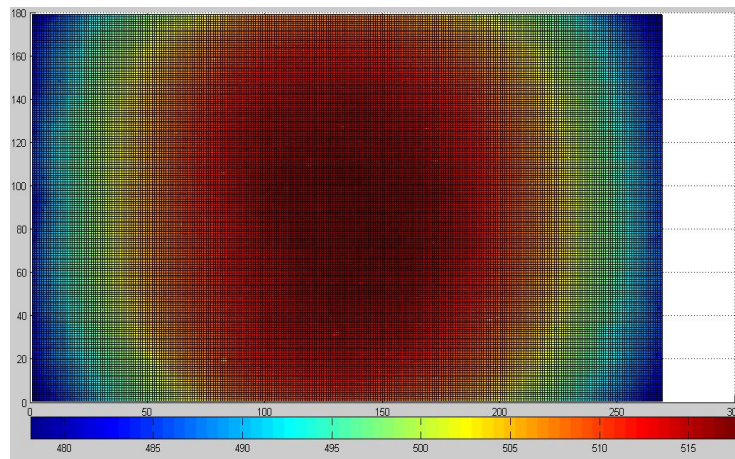
correction in the future.

After such a correction, the difference between the maximal and the minimal average green channels of the  $16 \times 16$  blocks is 1. Thus, the spatial variation of the uniformity board in the DigiEye after correction is close to 0.

(a)



(b)



(c)

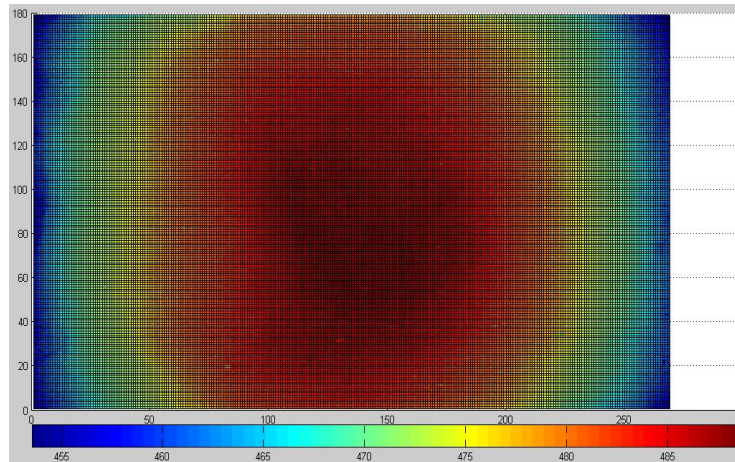


Figure 47. Distribution of the RGB Channels for the Uniformity Board at 1/3s and F11Red Channel (a), Green Channel (b) and Blue Channel (c)

In order to test the effect of the camera parameters, different shutter speeds and apertures were used to verify the change in the distribution of the green channel while the focal length of the camera lens remained unchanged, as shown in Figure 48 and Figure 49. In Figure 48, the shutter speed was 1/2s and the aperture was F13, the green values are ranged between 482 and 522, with the difference of 8.3%; and in Figure 49, the shutter speed was 1/5s and the aperture was F9, the green values are ranged between 490 and 530, with the difference of 8.16%. The distributions in Figure 48 and Figure 49 are different from those in Figure 47. It would be better to apply the same camera parameters to capture the images of the uniformity board and the images of the samples.

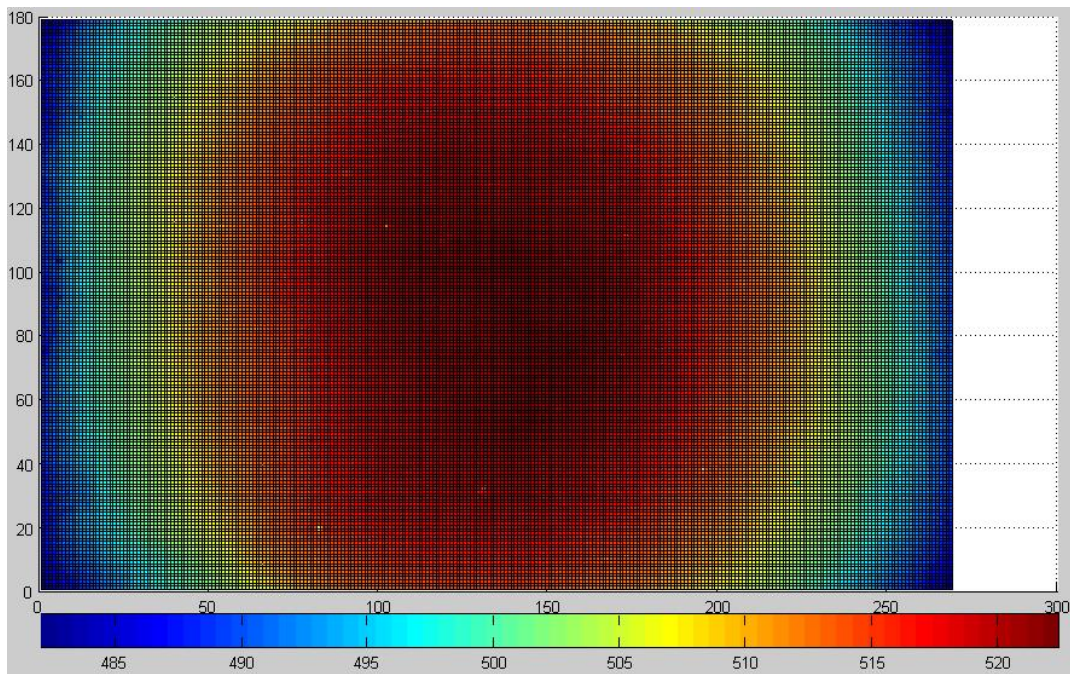


Figure 48. Distribution of the Green Channel for the Uniformity Board with 1/2s and F13

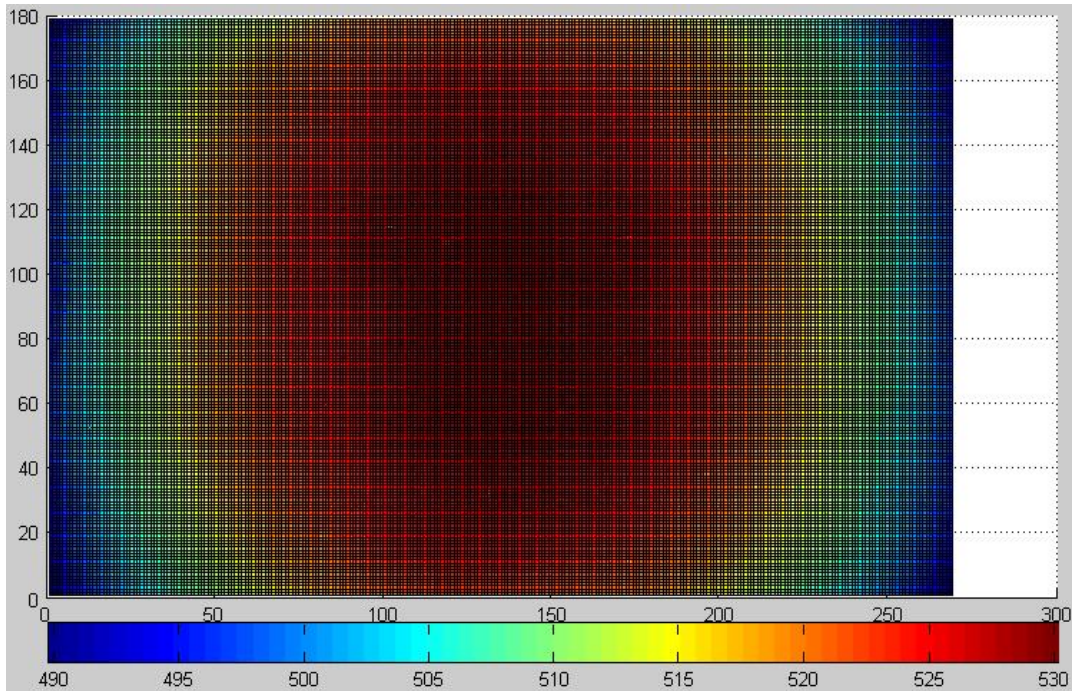


Figure 49. Distribution of the Green Channel for the Uniformity Board with 1/5s and F9

It should be noticed here that the image of the uniformity board changes when the focal length is variable. Figure 50 shows the distribution of the green channel based on the uniformity board when the minimal focal length of 10 inches was used. The green values are in the range of 451 and 479, with the difference of 6.2%. Figure 51 shows the distribution of the green channel based on the uniformity board when the maximal focal length was applied. The green values are in the range of 494 and 544, with the difference of 10.1%. Both of these distributions are different from those given in Figure 47. As the manual focus was used in taking pictures, the focal length should be identical to the focal length when auto focus is enabled to capture the images.

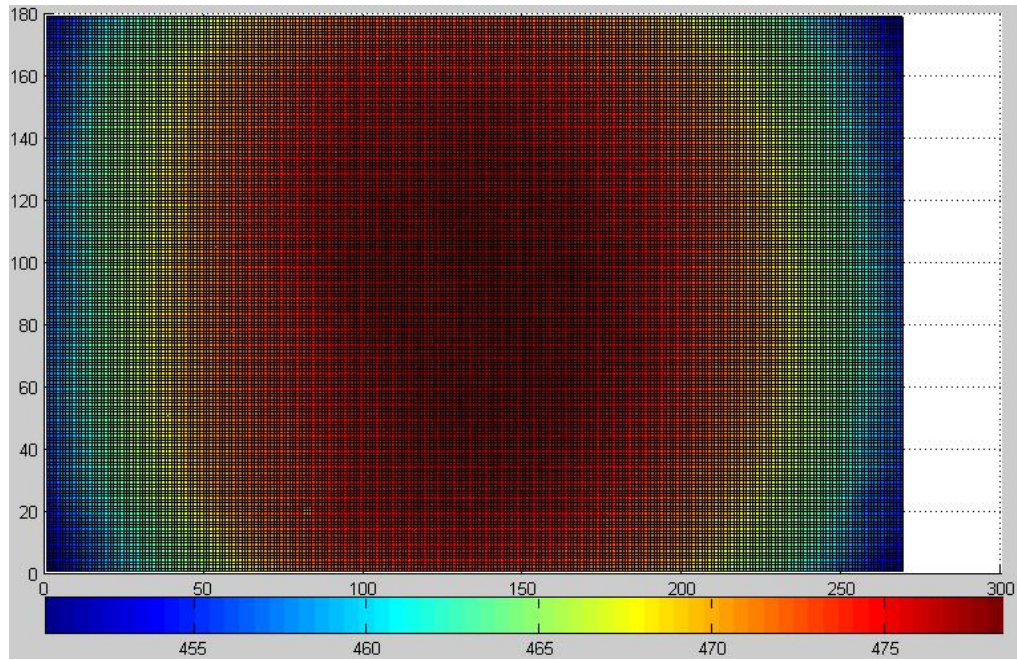


Figure 50. Distribution of the Green Channel when the Minimal Focal Length is Used

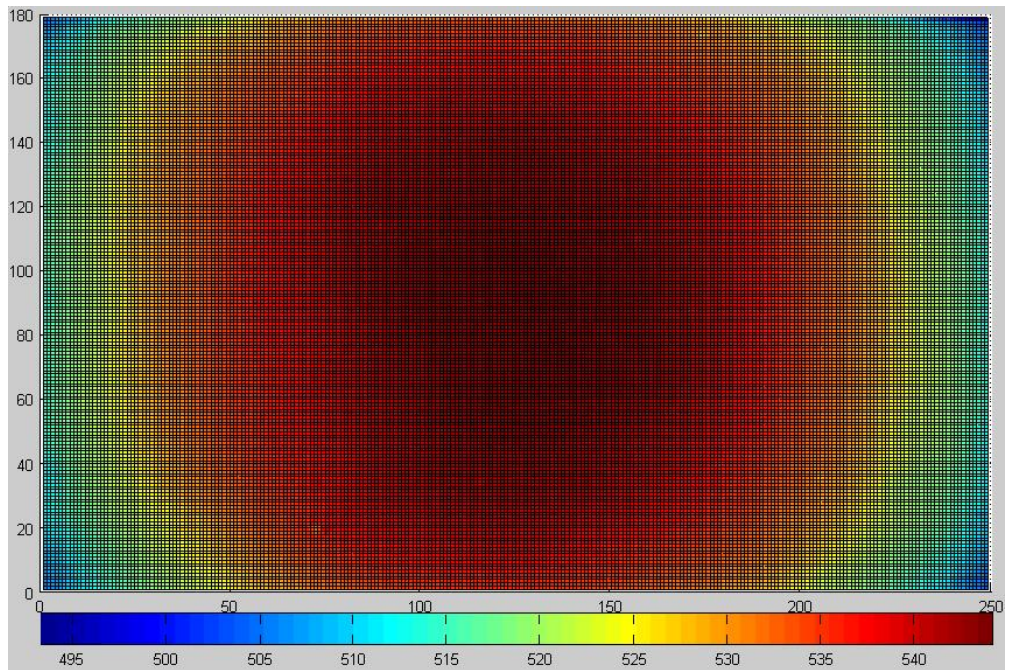


Figure 51. Distribution of the Green Channel when the Maximal Focal Length is Used

All these results are based on the conversion of the raw image to dng file format and then opening images in the Matlab via libtiff.

In the software developed there are two ways to read the values out of the raw file. One way is through LibRaw, which outputs raw values and is identical to the method used above. The other method is through the Nikon Image SDK, which outputs the RGB values after image processing. As there is some image processing inside Nikon Image SDK, the output and the distribution is different from that of the first method. Figure 52 shows the distribution of the green channel from the image used in Figure 47, which shows a different distribution from that in Figure 47. Thus,  $\frac{r_{min}}{r_{unif}(x,y)}$ ,  $\frac{g_{min}}{g_{unif}(x,y)}$ ,  $\frac{b_{min}}{b_{unif}(x,y)}$  for all the  $16 \times 16$  blocks that are generated under one method cannot be used in the spatial correction for the image processed under the other method.

An experiment was done to check the effectiveness of the spatial uniformity correction, as shown in Figure 53.

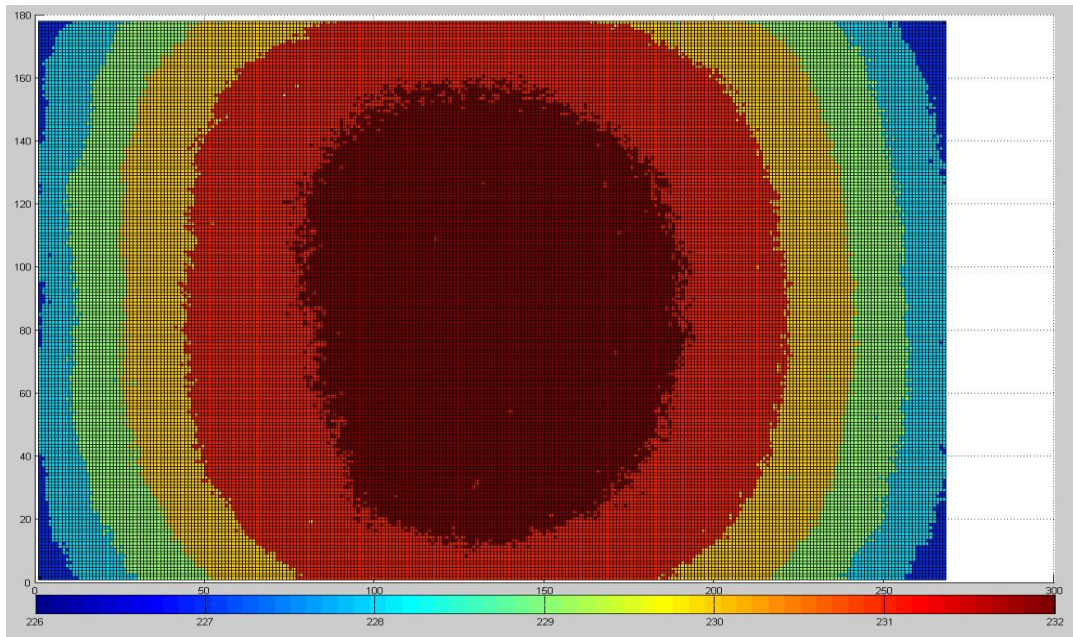


Figure 52. Distribution of the Green Channel when Nikon Image SDK is Used

The Verivide Digitizer test chart was placed inside the DigiEye table surface at 8 different positions. These images are indexed from (a) to (h) in Figure 53. In each position, an image was captured and the RGB values from 8 color tiles around the center, H4, M4, M9, H9, I5, L5, I8, L8, were analyzed. The camera parameters remained constant in the experiment. Table 20 shows the RGB values without the spatial uniformity correction; and Table 21 shows the RGB values after the spatial uniformity correction. It can be seen that the spatial uniformity correction successfully decreased the standard deviations in all cases. However, more than half of the variances after the correction are larger than 1. The maximum is the variance for the R channel of H4, which is 3.4.

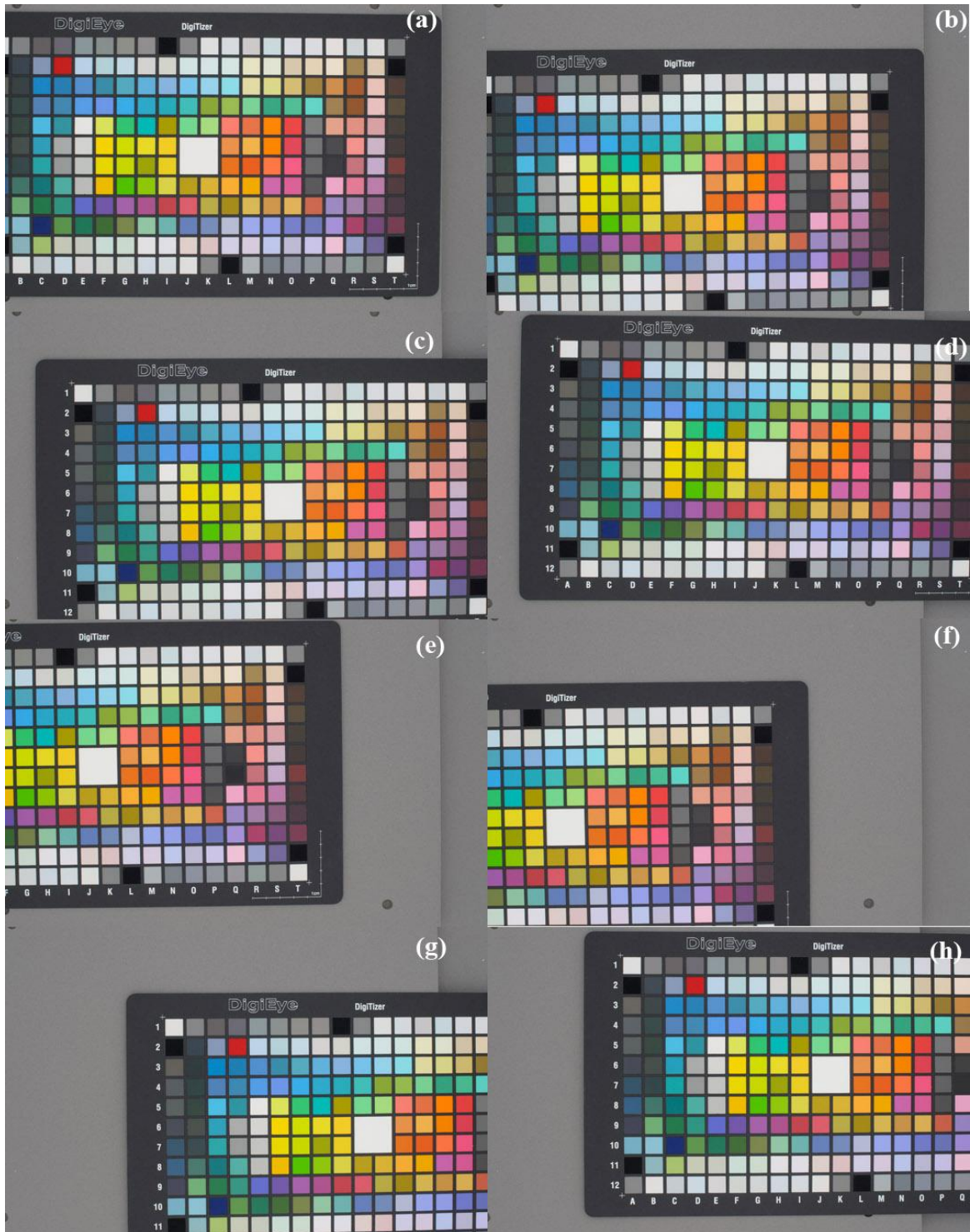


Figure 53. Images of Digitizer Test Chart at Different Position in the DigiEye

Table 20. RGB from Nikon Image SDK before Spatial Correction

	R	G	B	R	G	B	R	G	B	R	G	B
ID	H4			M4			M9			H9		
(a)	52	164	197	118	207	148	211	182	88	169	83	137
(b)	51	164	197	117	207	148	211	182	89	170	84	137
(c)	43	163	197	119	207	149	209	181	88	171	85	138
(d)	51	165	198	119	207	148	210	182	88	170	83	137
(e)	49	160	193	118	206	147	210	182	87	164	80	134
(f)	48	159	192	118	206	147	209	181	88	163	78	133
(g)	54	165	198	116	204	145	205	178	85	170	84	137
(h)	54	165	198	116	205	147	207	179	86	170	84	137
avg	50	163	196	118	206	147	209	181	87	168	83	136
dev	3.62	2.36	2.37	1.19	1.13	1.19	2.07	1.55	1.30	3.07	2.39	1.75
ID	I5			L5			L8			I8		
(a)	163	153	16	247	128	110	245	173	60	213	207	78
(b)	163	153	16	247	127	109	245	173	61	213	207	79
(c)	163	153	17	247	130	112	245	173	61	214	208	80
(d)	164	154	20	247	130	112	245	173	62	214	207	78
(e)	160	151	15	245	129	109	244	172	59	209	204	76
(f)	159	150	16	244	129	109	243	172	60	209	203	77
(g)	163	54	23	242	127	109	240	170	59	212	206	78
(h)	164	154	23	243	128	110	243	171	61	213	207	79
avg	162	140	18	245	129	110	244	172	60	212	206	78
dev	1.85	1.49	3.28	2.05	1.20	1.31	1.75	1.13	1.06	2.03	1.73	1.24

Table 21. RGB from Nikon Image SDK after Spatial Correction

ID	R	G	B	R	G	B	R	G	B	R	G	B
	H4			M4			M9			H9		
(a)	50	160	193	114	201	145	204	178	86	164	82	134
(b)	50	160	193	113	200	144	204	178	87	165	82	135
(c)	42	159	193	116	202	146	203	177	86	166	83	136
(d)	49	160	194	116	202	145	204	178	86	165	81	134
(e)	48	158	190	115	201	144	203	178	85	161	79	132
(f)	47	157	190	115	201	144	204	177	86	161	77	132
(g)	53	161	194	113	200	143	202	174	84	165	82	135
(h)	52	161	194	114	200	144	203	176	85	165	82	135
avg	49	160	193	115	201	144	203	177	86	164	81	134
dev	3.40	1.41	1.69	1.20	0.84	0.92	0.74	1.41	0.92	1.93	2.00	1.46
ID	I5			L5			L8			I8		
(a)	159	149	17	239	124	107	237	168	59	207	202	77
(b)	159	149	16	239	124	107	237	169	60	207	202	78
(c)	158	149	18	239	127	109	238	169	60	207	202	78
(d)	158	150	20	240	127	109	237	169	60	206	201	76
(e)	157	148	15	238	126	107	237	168	59	205	200	75
(f)	156	148	17	238	126	107	237	168	59	204	200	76
(g)	159	150	23	237	125	107	236	167	58	206	201	77
(h)	160	150	23	237	125	108	236	168	60	207	202	77
avg	158	149	19	238	126	108	237	168	59	206	201	77
dev	1.28	0.84	3.07	1.06	1.20	0.92	0.64	0.71	0.74	1.13	0.89	1.03

The above results are from the output of Nikon Image SDK. The output of the LibRaw is also examined. Table 22 shows the RGB values before spatial correction, and Table 23 shows the RGB values after spatial correction. Similarly, spatial correction can reduce the variances for RGB channels of these color patches. It can be noted that the variances from LibRaw before spatial correction are even larger than those from the Nikon Image SDK before spatial correction, as shown in Table 20. After spatial correction, the variances become smaller, and

the average value of the variances is even smaller than that from Nikon Image SDK after spatial correction, as shown in Table 21. Half of the variances after correction from LibRaw are still larger than 1 and the maximal variance is for G channel for L5, which is 2.17.

Table 22. RGB from LibRaw before Spatial Correction

ID	R	G	B	R	G	B	R	G	B	R	G	B
	H4			M4			M9			H9		
(a)	120	281	296	196	369	289	254	319	216	150	156	189
(b)	120	281	296	194	367	287	255	319	217	151	157	190
(c)	117	279	296	196	368	289	252	317	216	153	159	192
(d)	119	282	298	196	368	289	253	318	216	151	156	189
(e)	117	273	288	195	366	286	253	318	215	144	149	183
(f)	116	271	287	194	365	286	251	316	215	141	147	181
(g)	121	283	299	190	359	281	243	307	209	151	158	190
(h)	121	283	299	192	361	284	248	311	212	152	158	191
avg	119	279	295	194	365	286	251	316	215	149	155	188
dev	1.96	4.61	4.73	2.17	3.58	2.82	3.91	4.34	2.67	4.26	4.47	3.94
ID	I5			L5			L8			I8		
(a)	180	245	135	260	224	195	287	298	186	275	375	236
(b)	180	245	134	259	222	194	288	299	188	275	376	238
(c)	180	245	135	261	228	199	286	298	188	276	376	238
(d)	181	246	136	260	228	198	287	299	188	276	375	237
(e)	175	240	132	257	225	195	284	296	185	268	366	231
(f)	174	238	132	256	225	196	283	295	185	266	363	230
(g)	181	246	137	253	222	194	279	291	182	273	373	235
(h)	181	247	137	255	224	195	282	295	185	275	376	238
avg	179	244	135	258	225	196	285	296	186	273	373	235
dev	2.83	3.21	1.98	2.82	2.32	1.83	3.07	2.72	2.10	3.85	5.10	3.20

Above all, spatial correction can reduce the variances of the results from both the Nikon Image SDK and LibRaw.

The Nikon DSLR is a complicated machine. Some of the variance might be originated from the image processing inside the camera, which cannot be corrected with the spatial uniformity board.

Table 23. RGB from LibRaw after Spatial Correction

ID	R	G	B	R	G	B	R	G	B	R	G	B
	H4			M4			M9			H9		
(a)	108	260	276	175	338	266	228	293	200	135	145	176
(b)	108	260	276	173	336	265	228	294	202	136	145	177
(c)	104	256	273	176	340	268	228	294	202	137	146	178
(d)	107	259	276	176	340	268	228	294	201	135	143	175
(e)	108	261	276	176	339	267	227	293	200	133	142	175
(f)	108	261	276	176	339	267	229	295	202	133	142	174
(g)	108	260	276	176	339	267	227	293	200	137	146	177
(h)	108	259	276	176	339	267	227	293	200	136	145	176
avg	107	260	276	176	339	267	228	294	201	135	144	176
dev	1.41	1.60	1.06	1.07	1.28	0.99	0.71	0.74	0.99	1.58	1.67	1.31
ID	I5			L5			L8			I8		
(a)	162	226	125	232	205	180	256	273	172	246	345	220
(b)	161	226	124	231	204	179	257	275	174	247	347	221
(c)	161	225	125	234	209	184	257	276	175	247	346	221
(d)	161	226	125	234	210	184	257	275	174	246	344	219
(e)	162	227	125	233	209	183	257	275	173	247	346	219
(f)	161	227	126	233	209	183	257	275	174	247	346	219
(g)	163	228	127	232	208	183	257	275	173	247	346	220
(h)	163	227	127	232	209	183	256	274	173	247	346	220
avg	162	227	126	233	208	182	257	275	174	247	346	220
dev	0.89	0.93	1.07	1.06	2.17	1.85	0.46	0.89	0.93	0.46	0.89	0.84

## 2.3 Time Difference Variance

If post image processing of the camera were not considered, the variation of the pixel output at a position could be expressed via equation (49).

$$\mathbf{c} = \mathbf{S} \times \mathbf{O} \times \mathbf{I}$$

$$\mathbf{Var}(\mathbf{c}) = \mathbf{Var}(\mathbf{S}) \times \mathbf{O} \times \mathbf{I} + \mathbf{S} \times \mathbf{O} \times \mathbf{Var}(\mathbf{I}) \quad (49)$$

Here  $\mathbf{c}$  is the raw value of a pixel,  $\mathbf{S}$  is a  $\mathbf{1} \times \mathbf{n}$  matrix standing for the spectral transmittance of the camera at that position,  $\mathbf{O}$  is a  $\mathbf{n} \times \mathbf{n}$  diagonal matrix for the color spectra of the position in the image and  $\mathbf{I}$  is an  $\mathbf{n} \times \mathbf{1}$  matrix showing the spectral power distribution of the illumination at the position. It can be noted from equation (49) that the variation of the color output of the camera is the sum of the variation of the spectral transmittance of the camera and the variation of the illumination.

SpectroScan PR670 [97] from Photo Research was placed on top of the DigiEye unit and used to measure the illumination of the DigiEye illumination chamber, as shown in Figure 54. The device provides spectra in the range of 380nm to 780nm, with an interval of 8nm. The diffusing accessory CR670 serves to capture the incident light. Each time, an average of three readings was acquired [98]. As the exposure time is adaptive, it takes 40 seconds to make three readings for an average. The readings were taken every 90 seconds repeatedly, and a total of 40 results were acquired for analysis.

The results are shown in Figure 55. It can be noted that the illumination increases rapidly in the initial 10 minutes. Then it reaches the maximal value. After that, it drops slowly, i.e., it drops 0.4% in 30 minutes. The illumination is automatically switched off after 40 minutes. When it is turned on again, the illumination is still relatively stable.

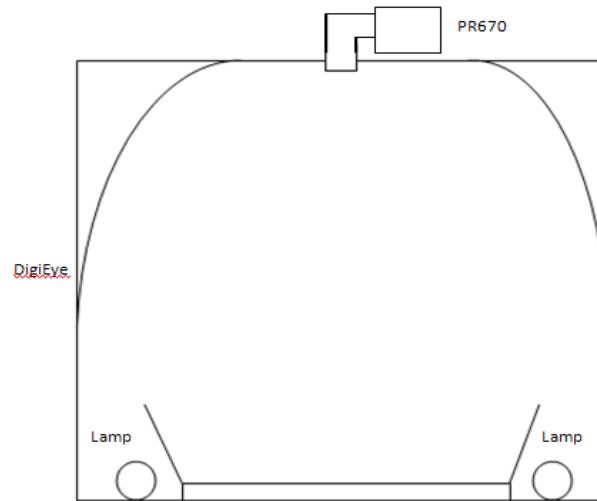


Figure 54. PR670 for the Measurement of Illumination inside DigiEye

Verivide requires a warming up period of 10 minutes for the illumination chamber, when the illumination changes rapidly. After that, the illumination becomes stable. So, in this research project, the variation from the illumination, which is smaller than 1%, can be ignored. In the DigiEye illumination chamber, LEDs are used to provide UV illumination and improve the color temperature of the fluorescent lamps. Figure 56 shows the change of the spectra when LED bulbs are used. It can be noted that the power increases in the whole spectrum. When no LEDs are used, the color temperature is 7646K, and it becomes 7363K when LEDs are

turned on. In this DigiEye illumination chamber, the application of the LED does not help in improving the color temperature.

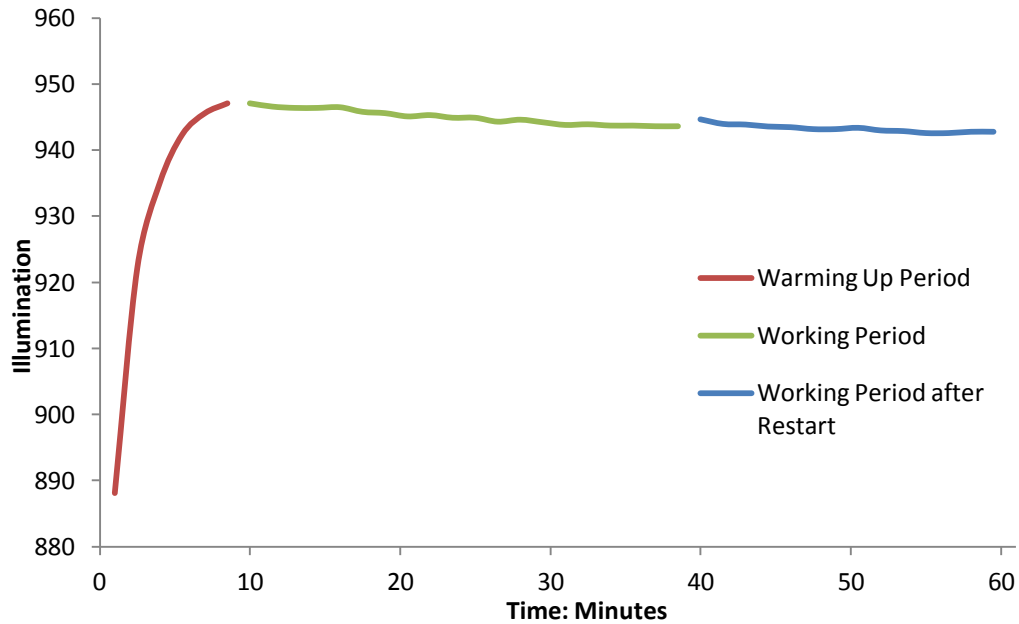


Figure 55. Variation of the Illumination of DigiEye Illumination Chamber

In order to determine whether the image capturing were temporally dependant, a piece of white paper was placed inside the DigiEye illumination chamber and its image was captured over an extended period of time. It would be ideal to conduct this experiment using a Uniformity Board. However, at the time of the experiment this was not available. Four 10 × 10 pixel squares were chosen from the images of the paper, and the average RGB values of these squares were calculated, as shown in Figure 57.

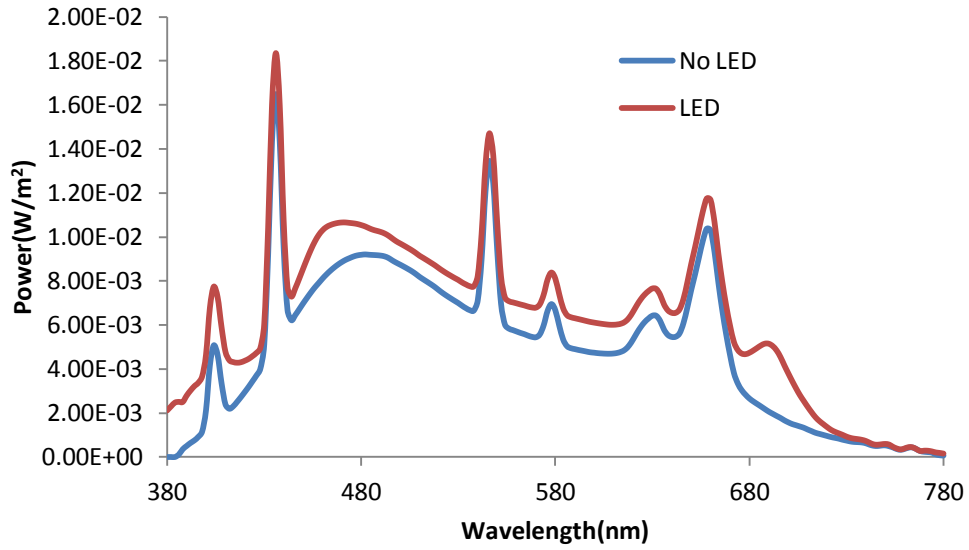


Figure 56. Change of the spectra when LEDs are used

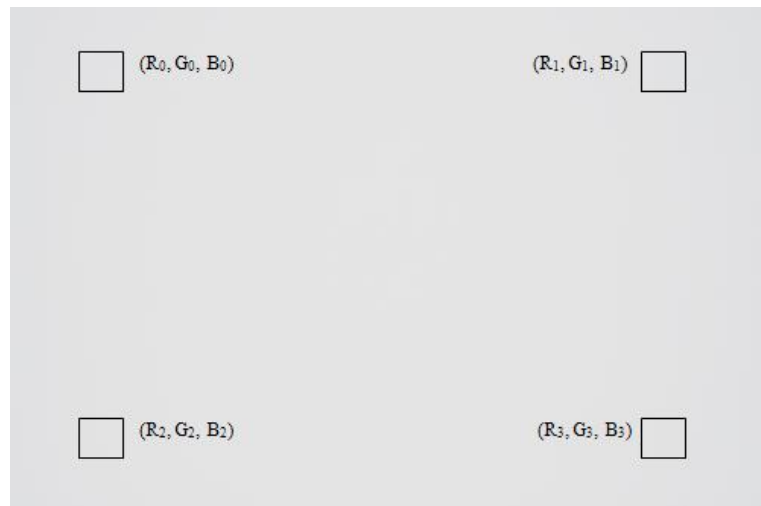


Figure 57. Paper and the Selected Positions to Sample the Average of RGB Values

According to the results, there is some variation related with the digital camera, as shown in Table 24. On the one hand, it can be seen that strong correlations among the RGB values

from all the four spots exist with a coefficient of correlation exceeding 0.95. On the other hand, the difference between the minimal value and the maximal value is significant (more than 5%). Since the illumination is relatively constant, as shown in Figure 55, this variation (for DNG) should be due to the camera. Figure 58 shows the RGB values from the top left corner in Table 24. It can be noticed that the variation becomes larger with time.

Two Nikon D90 cameras with two exchangeable lenses were examined, and the camera driver was updated, as recommended by Nikon. However this issue was not eliminated. One possible cause of the variability may be due to the camera lens.

Table 24. RGB values from Nikon D90 that indicate the variation of the camera

Time	Top Left			Bottom Left			Top Right			Bottom Right		
	R <sub>0</sub>	G <sub>0</sub>	B <sub>0</sub>	R <sub>2</sub>	G <sub>2</sub>	B <sub>2</sub>	R <sub>1</sub>	G <sub>1</sub>	B <sub>1</sub>	R <sub>3</sub>	G <sub>3</sub>	B <sub>3</sub>
10:29	171	173	170	172	174	170	186	186	182	187	184	180
10:30	170	173	171	172	174	170	187	186	182	186	184	180
10:31	171	173	170	172	174	171	187	185	182	186	184	181
10:32	170	173	171	172	174	171	186	186	182	185	185	180
10:32	171	173	170	173	174	171	186	186	182	186	185	180
10:33	171	173	169	172	174	171	186	185	182	186	184	180
10:34	172	173	170	173	174	171	187	186	182	186	185	180
10:35	170	173	170	172	173	170	187	185	181	186	184	180
10:35	170	173	170	172	174	169	186	185	181	185	184	180
10:36	171	172	170	172	173	170	186	185	181	186	184	180
10:37	171	173	169	171	174	170	186	185	182	186	185	181
10:38	171	173	169	172	174	170	186	185	182	186	184	180
10:39	171	172	170	172	173	169	186	185	181	186	183	180
10:43	170	172	169	171	173	169	186	185	181	186	184	179
10:47	170	172	169	172	173	170	186	185	181	186	184	179
10:50	171	172	169	172	173	170	186	185	181	185	184	179
10:52	170	172	169	171	173	170	186	185	180	186	184	179
10:53	171	172	169	172	173	169	186	185	181	186	184	179
10:57	172	173	171	173	174	172	187	185	184	187	185	182

Table 24. Continued

Time	Top Left			Bottom Left			Top Right			Bottom Right		
	R <sub>0</sub>	G <sub>0</sub>	B <sub>0</sub>	R <sub>2</sub>	G <sub>2</sub>	B <sub>2</sub>	R <sub>1</sub>	G <sub>1</sub>	B <sub>1</sub>	R <sub>3</sub>	G <sub>3</sub>	B <sub>3</sub>
10:59	170	173	170	172	174	170	187	185	182	186	184	179
11:00	172	173	170	173	174	171	187	185	182	187	185	180
11:00	177	178	175	178	179	175	191	191	187	191	189	186
11:00	171	173	170	173	174	170	187	186	182	187	184	181
11:01	171	173	169	172	173	171	186	185	182	186	184	180
11:01	172	172	170	172	173	169	186	185	181	186	184	180
11:02	177	178	175	177	179	176	192	190	186	192	189	185
11:03	176	178	175	178	179	175	192	190	186	191	189	185
11:08	170	172	169	172	173	170	186	185	181	186	184	178
11:15	170	173	169	171	174	169	186	185	181	186	184	179
11:15	172	173	169	172	174	170	186	185	181	186	184	180
11:16	171	172	169	173	173	170	186	185	181	186	184	179
11:16	176	178	174	177	179	175	191	191	187	191	190	185
11:17	177	177	173	177	178	174	190	190	186	191	189	184
11:19	177	177	174	177	179	175	192	190	186	191	189	185
11:20	177	177	173	177	178	174	191	190	185	190	189	184
11:23	177	177	174	176	179	174	192	190	186	190	189	185
11:27	176	178	174	177	179	174	192	190	186	191	189	184
11:28	180	181	178	182	182	178	196	194	190	195	193	188
11:28	177	178	175	177	179	175	193	191	186	192	190	185
11:28	177	178	174	176	179	175	191	191	186	191	189	185
11:29	176	177	173	177	178	174	191	190	185	191	189	184
11:29	180	181	177	181	182	178	195	194	189	195	193	188
11:31	172	173	170	173	174	169	187	186	182	186	185	180
11:33	177	178	174	177	179	175	192	191	186	191	190	184
11:34	180	181	177	180	182	177	195	194	189	195	193	187
Correlation	0.97	0.97	0.97	0.97	0.97	0.96	0.98	0.97	0.97	0.98	0.96	0.97
Min	170	172	169	171	173	169	186	185	180	185	183	178
Max	180	181	178	182	182	178	196	194	190	195	193	188

A CMOS camera, DCC1645C from Thorlabs, was also examined. Likewise, a piece of paper was placed inside the DigiEye illumination chamber and its image was captured over an extended period of time; and still, four  $10 \times 10$  pixels squares were chosen from the images.

The average RGB values of these squares were calculated. Results showed significantly smoother output, as shown in Table 25.

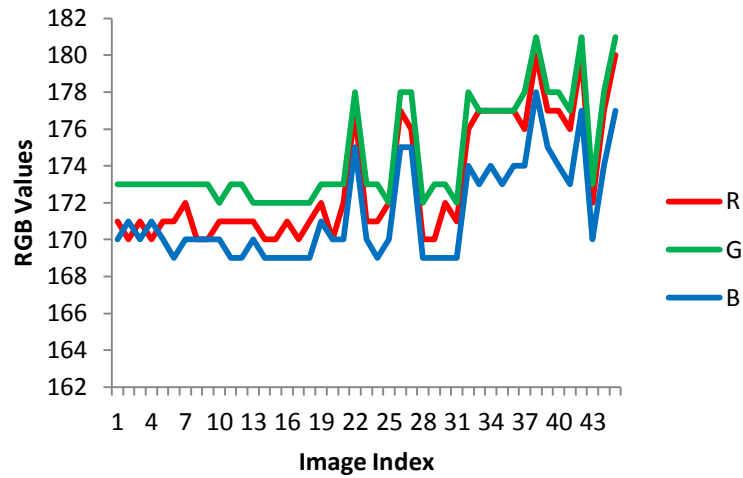


Figure 58. RGB values from the top left corner

The standard deviation of most columns is below 1, which is much lower than the average of these values. It may be useful to examine alternative camera systems with digital shutters and aperture control or lock the shutter and aperture of Nikon camera and reassess this source of variability to elucidate the source of the issue.

### 3. Conclusion

From the analysis above, the following conclusions below can be drawn:

- The spatial variance of the Nikon D90 on the uniformity board when exposed outdoor is roughly 8%;
- In the DigiEye illumination chamber, the spatial variance of the Nikon D90 is different from that when exposed outdoor.
- The spatial variance is dependent on the camera parameters, the focal length as well as the image processing;
- A spatial correction was developed to decrease the spatial variations and the spatial variation of the uniformity board after correction was close to 0;
- When the Digitizer test chart is used to examine the spatial variation inside the DigiEye illumination chamber, it was noted that all the RGB values were decreased after correction for both outputs from Nikon Image SDK and LibRaw. The spatial variances from LibRaw after correction were lower than those from Nikon Image SDK, although there were still some large variances from LibRaw after correction. What LibRaw outputs is the raw values and the Nikon Image SDK outputs the RGB values which develop from the raw values via the image processing. The image processing can enlarge the variation;
- The illumination inside the DigiEye illumination chamber was found to be relatively constant after 10 minutes' warming up period;

- The application of the LEDs increased the spectral power distribution but slightly dropped the color temperature, which makes the color temperature farther away from the required 7500K;
- The variation of Nikon D90 output become larger with time;
- It is recommended to replace Nikon D90 camera with an alternative device.

Table 25. RGB values from the video camera

Time	Top Left			Bottom Left			Top Right			Bottom Right		
	R <sub>0</sub>	G <sub>0</sub>	B <sub>0</sub>	R <sub>2</sub>	G <sub>2</sub>	B <sub>2</sub>	R <sub>1</sub>	G <sub>1</sub>	B <sub>1</sub>	R <sub>3</sub>	G <sub>3</sub>	B <sub>3</sub>
11:22	205	192	197	208	193	201	251	232	237	250	230	238
11:23	206	193	197	208	195	202	252	234	238	251	232	238
11:23	205	192	196	207	193	201	250	233	237	249	232	236
11:24	206	193	198	209	194	202	252	233	239	250	232	238
11:26	206	193	198	208	194	202	251	233	238	251	231	238
11:26	206	193	196	207	193	201	251	232	237	250	232	236
11:27	204	191	198	206	193	200	251	231	235	249	231	235
11:28	204	193	196	205	193	201	251	231	236	250	231	236
11:29	205	194	197	206	195	201	252	232	236	251	232	237
11:30	205	194	198	207	194	201	252	233	237	249	233	237
12:39	204	193	198	208	193	203	252	232	237	251	232	237
12:39	205	192	197	207	193	201	250	231	238	249	231	237
12:40	204	192	197	207	193	201	250	231	235	249	231	235
12:41	204	192	197	205	192	202	250	231	237	249	230	236
12:42	206	193	197	207	194	201	251	232	237	251	231	238
12:45	205	193	196	208	194	202	251	232	237	250	231	237
12:49	206	192	196	207	194	200	251	232	237	250	231	237
12:49	205	193	197	206	194	201	250	232	236	249	231	236
12:51	205	192	196	207	192	200	251	232	236	250	231	235
12:53	204	194	196	206	194	201	252	232	237	251	231	236
Std Dev	0.79	0.80	0.79	1.05	0.83	0.77	0.76	0.83	0.99	0.83	0.73	1.04

## **Chapter V. Calibration of the LCD Monitor**

An Eizo monitor – ColorEdge CG211 was used in this research. The calibration of the ColorEdge CG211 was carried out to set up the data mapping from the device space to the color space and enable the color management.

Eizo Corp., Japan, is a global reputable manufacturer of display monitors. Eizo LCD monitor is a well-known brand and the ColorEdge series are widely used in the photography, broadcasting, pre-press and post-production to provide consistent and predictable colors. In 2007, ColorEdge CG211 received the European Photo & Imaging Awards for its high brilliance, precise calibration and color stability [99]. The color temperature of the LCD is important in the soft proofing, and on the ColorEdge series, the color temperature can be controlled via a USB cable. There are two CCT options in the attached Color Navigator software, 5000K and 6500K, and for this project the color temperature of the monitor was tuned to 6500K.

### **1. Variations in the LCD Color Management**

There are several kinds of variations in the LCD display which might affect its color management. These variations might be related with non-uniformity of the display surface, time dependant variation of the display, the polarization of the LCD, as well as potential variations due to spectrophotometric determination of color characteristics of the display. These are briefly described below.

## 1.1 Variation of the Spectrophotometer

A GretagMacbeth Eye One was used to measure the spectra of the display. This is a portable spectrophotometer, capable of measuring colors in three modes – spot reflectance measurement, spot emission measurement and scan reflectance measurement. It supports measurements in the spectral range of 380nm to 730nm, with 10nm intervals. A calibration is required before the color measurement. The Eye One is placed in its cradle with the aperture on top of the white reference, as shown in Figure 59. This is the black point calibration as there is no illumination on the reference white. Each measurement mode requires a related calibration method and these calibration modes are different. For the calibration of the emission measurement, only the black point calibration is employed. It is difficult to predict the accuracy of the spectrophotometer sensors after a period of usage. Thus, the simple calibration method used for emission is likely not sufficient for an accurate color measurement of the emission for displays over an extended period of time.



Figure 59. GretagMacbeth Eye One and its Cradle

## 1.2 Non-Uniformity in the Display Surface

In order to determine the time dependant variation of the display, the screen is divided into 35 (7×5) blocks in the software, as shown in Figure 60. The horizontal index is from C1 to C7 and the vertical index is from R1 to R5. The size of each block is 216 pixels in width by 226 pixels in height. The width of the spacing is 5% of the white blocks lengths in both the horizontal and the vertical directions.

This software supports the measurement of light emission from the screen for each square via GretagMacbeth Eye One. The Eye One was used to measure the emissions from the 35 squares covering the display area. Several measurements were taken, and their distributions are shown in Figure 61 (a-f).

It can be noted that the distributions vary with time. The Y values at the top two rows are always higher than the Y values at the bottom two rows. In these distributions, the maximal Y value is always at the top two rows and the minimal Y value is always at the bottom two rows, and their positions are variable. The difference between the maximum and the minimum is from 9% to 16%.

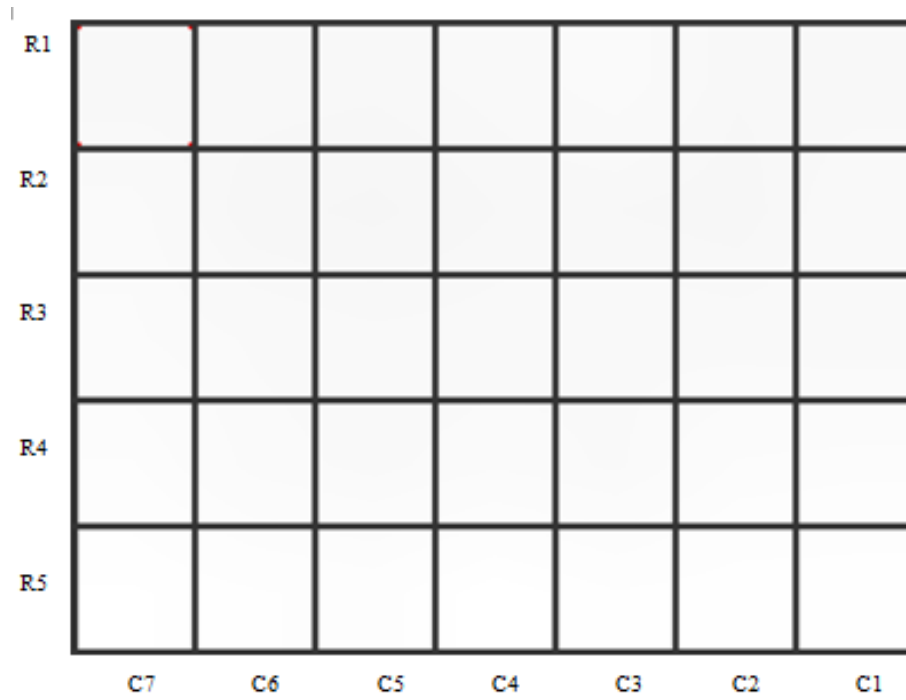
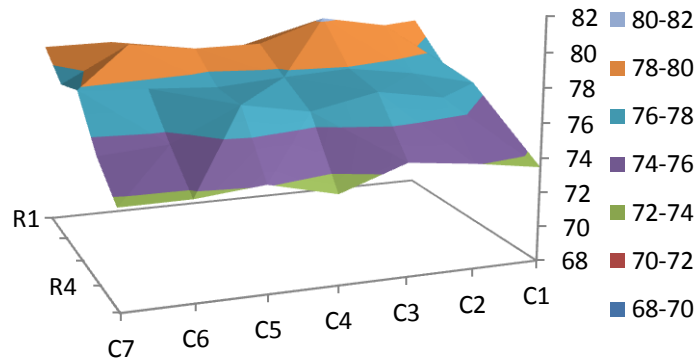


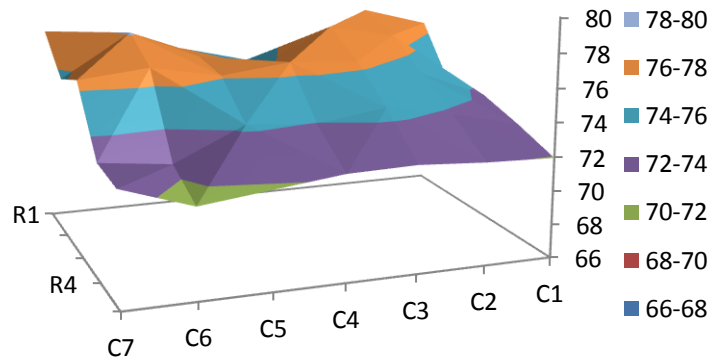
Figure 60. Snapshot of the Software Application to Verify the Spatial Variation

Figure 61(a-f). Temporal Variation of Y Channel Distribution

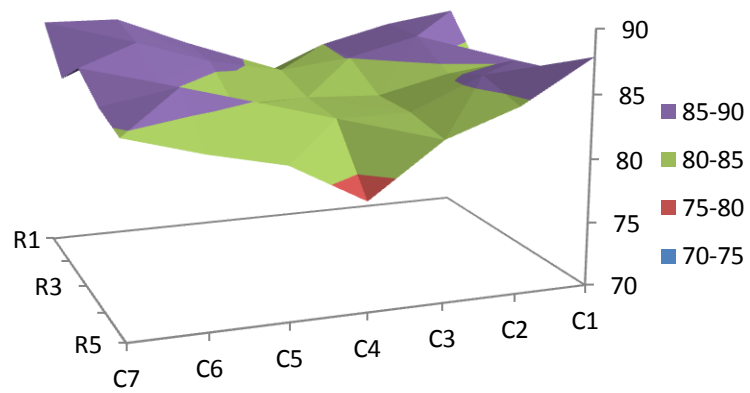
(a)

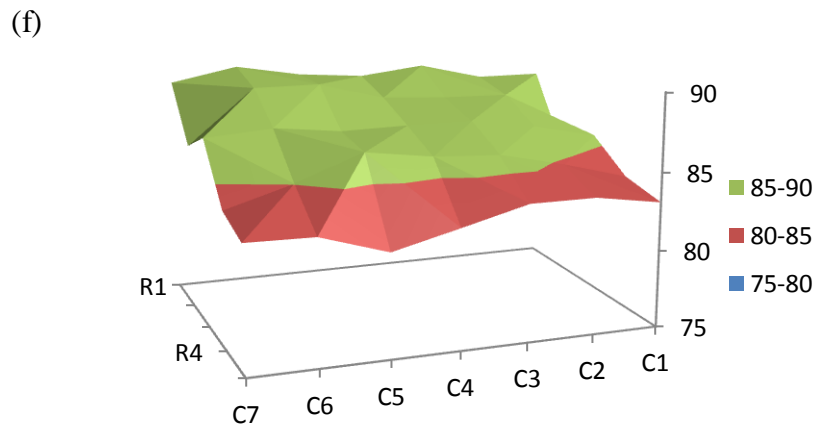
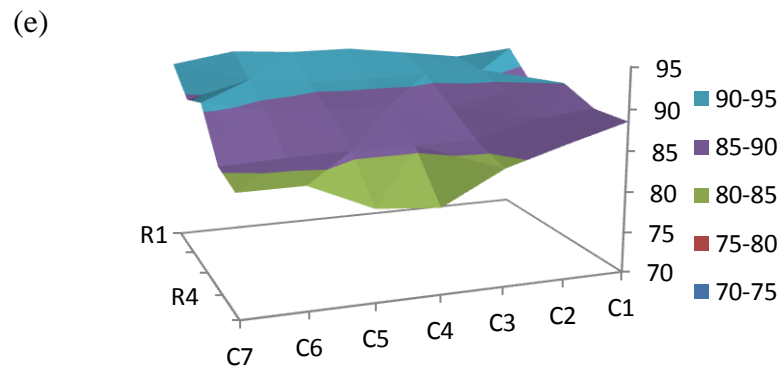
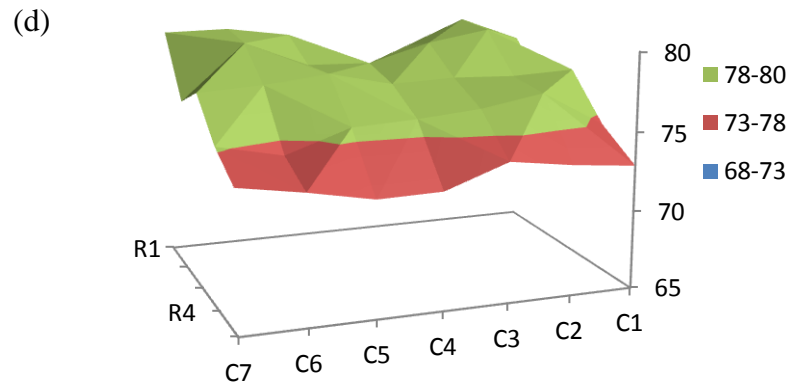


(b)



(c)





### 1.3 Variation caused by Eye One Orientation

There are two polarizing filters on the front and back side of the LCD panel. The emission from the LCD is polarized and the light intensity changes according to the orientation of the emitted light. The color measurement readings therefore change when Eye One is oriented differently at the same position. Figure 62 shows the relation between the orientation of Eye One and the CIEXYZ values for a constant background illumination at the center of the display. It can be seen that the Eye One reading reaches the minimum at 135 °and 315 °; and reaches the maximum at 45 °and 225 °. The difference between the maximum and the minimum is roughly 10%. So, it is necessary to keep the spectrometer at a fixed angle during the color measurement. In this study, for simplicity, the Eye One was always placed at 270 °

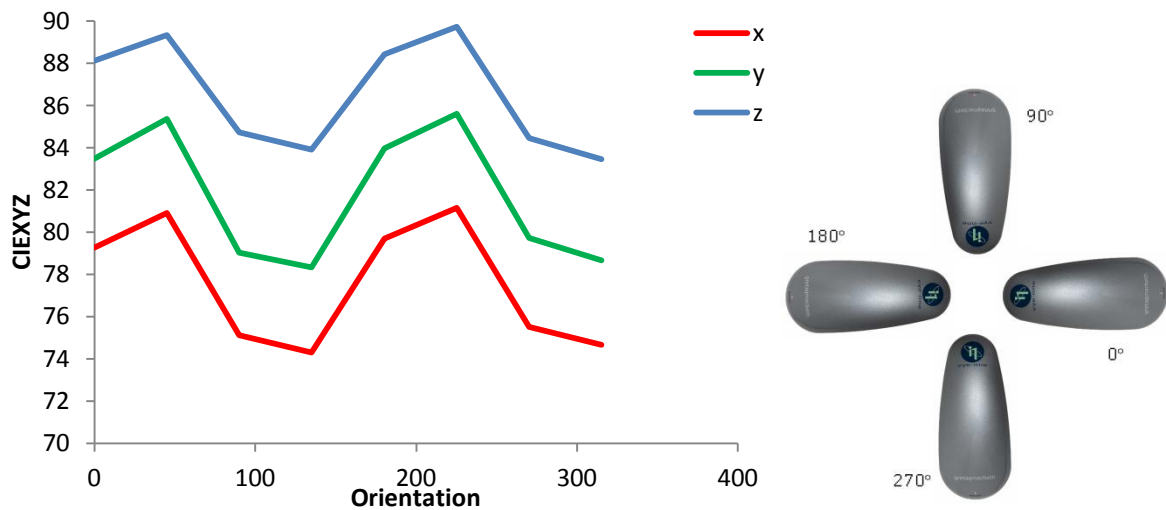


Figure 62. Relationship between CIEXYZ values and the Eye One Orientation

## 2. LCD Calibration Method

Before the LCD calibration, the software checks the USB connection with the Eye One and prompts a message to place Eye One in its cradle for the calibration process. If the calibration of Eye One is successful, the dialog shown in Figure 63 pops up at the center of the screen. Then the operator is prompted to place Eye One in the center of the black square in the dialog manually and click 'start' to begin the measurement. The color displayed in the square changes after one measurement is carried out and the Eye One readings are sent back to the computer. All the readings form a dataset of the tristimulus values. This dataset is combined with the associated device values and used for the profile computation.

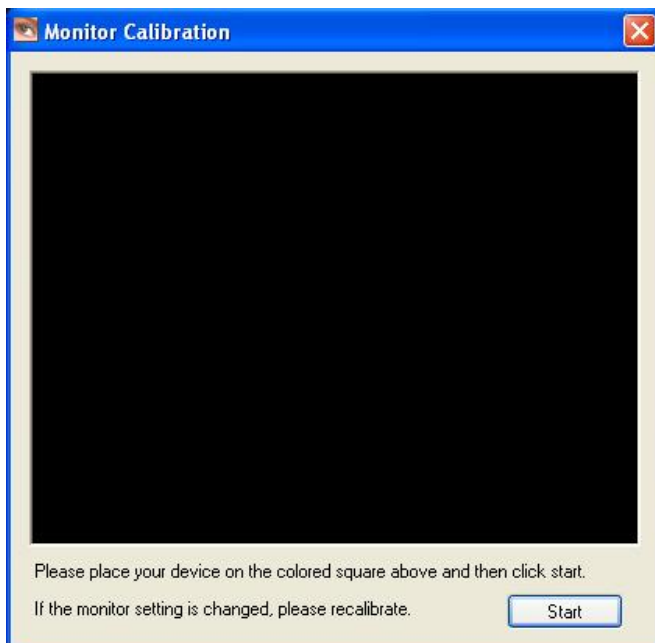


Figure 63. Snapshot of the Monitor Calibration UI

The calibration of the LCD is based on the three-component-matrix model. Below is the work flow used to calibrate the LCD:

1. Determine the black point  $X_k Y_k Z_k$  for the screen, i.e., the tristimulus values when the RGB values are 0;
2.  $X_k Y_k Z_k$  are subtracted for each set of tristimulus values in the dataset as the offset for the black point;
3. Determine the white point  $X_w Y_w Z_w$  of the screen, i.e., the tristimulus values when the RGB values all reach the maximum;
4. Calculate the chromaticity matrix using equations (50-52) [33]. The Bradford Chromatic Adaptation transform is used here to shift the white point of the display to D50, which is the default white point for ICC profiles [28]:

$$M_{adapt} = M_{BFD}^{-1} \begin{bmatrix} \rho_{pcs}/\rho_{src} & 0 & 0 \\ 0 & \gamma_{pcs}/\gamma_{src} & 0 \\ 0 & 0 & \beta_{pcs}/\beta_{src} \end{bmatrix} M_{BFD} \quad (50)$$

$$\begin{bmatrix} \rho_{pcs} \\ \gamma_{pcs} \\ \beta_{pcs} \end{bmatrix} = M_{BFD} \begin{bmatrix} X_{D50} \\ Y_{D50} \\ Z_{D50} \end{bmatrix} \quad (51)$$

$$\begin{bmatrix} \rho_{src} \\ \gamma_{src} \\ \beta_{src} \end{bmatrix} = M_{BFD} \begin{bmatrix} X_w \\ Y_w \\ Z_w \end{bmatrix} \quad (52)$$

Here  $M_{BFD} = \begin{bmatrix} 0.8951 & 0.2664 & -0.1614 \\ -0.7502 & 1.7135 & 0.0367 \\ 0.0389 & -0.0685 & 1.0296 \end{bmatrix}$ , which is the Bradford Chromatic

Adaptation Transformation matrix.

5. Multiply the chromaticity matrix from equation (50) on all the tristimuli in the dataset so that all the tristimuli are mapped to the new tristimuli under the illumination of D50;
6. Determine the red point  $X_R Y_R Z_R$  of the screen, i.e., the tristimulus when the R value reaches the maximum and the B and G values are 0;
7. Similarly, determine the blue point  $X_B Y_B Z_B$  and the green point  $X_G Y_G Z_G$  of the screen;
8. Determine the red tone reproduction curve of the screen. First find out all the points from the dataset with B and G values equal to 0, then sort these points from 0 to maximum based on their R values, finally construct the spline curve via the Catmull Rom interpolation [94] between R of the device space and X of the color space from these points. The curve is shown in Figure 64;
9. Similar to step 8, determine the green and blue tone reproduction curves of the screen;
10. Save all the information into the ICC profile. Note, as the Chromaticity matrix is used to map all the tristimuli under the D50 illuminant, the white point should be set to D50.

Thus the profile includes the data mapping from RGB to the CIEXYZ under D50 as well as  $M_{adapt}$ . In the color management,  $M_{adapt}$  is firstly used to convert the input CIEXYZ values which are under the white point of the display into the CIEXYZ values under D50. Then the CIEXYZ values under D50 are further converted into RGB values for the monitor via the three-component-matrix model.

One issue that should be noticed here is that the black point of the display is not considered in the color management in the ICC specification. Normally, the tristimulus values of the

black point are rather small, but not zero. For example, the tristimulus values of the black point for this Eizo ColorEdge CG211 are (0.20, 0.22, 0.32) in CIEXYZ space, and (2.0, 0.52, -2.55) in the CIELAB space. If the colors of interest are of the low lightness, the black point will affect the display results. In this research, the colors of the military camouflage are not of low lightness and ignoring the black point will not play an important role on the visualization of the displayed result. Nonetheless, the offset of the black point was added in the color management module.



Figure 64. Red Tone Reproduction Curve of the Eizo ColorEdge CG211

Table 26 lists the RGB values and the CIEXYZ values from the Eizo display. The device values were processed using the ICC profile to acquire the converted CIEXYZ values. Thus two sets of CIEXYZ values were obtained which were converted into the CIELAB values and the color differences in CIEDE2000 (1:1:1) between the CIELAB values were computed.

From Table 26, it can be noticed that the color differences are small – with the maximum of 1.87.

### **3. Conclusion**

From the analysis given above, the following conclusions can be drawn:

- GretagMacbeth Eye One spectrophotometer was used to measure the emission of the monitor, however, it lacked the white point calibration which might affect the accuracy of the measurement;
- The measured colorimetric attributes of the monitor and their distribution show a change with time;
- The orientation of the Eye One when placed on the monitor affects the spectrophotometric reading. In the case of Eizo ColorEdge CG211, the tristimulus values at 270 °were smaller than the tristimulus values at 315 °and greater than the tristimulus values at 225 °;
- The three- component- matrix model performed well for the calibration of the Eizo display in this research project;
- The black point should be compensated in the color management module to improve the color accuracy.

Table 26. Color Differences from the Dataset to Calibrate the Monitor

R	G	B	X	Y	Z	$\Delta E$
0	0	0	0.20	0.22	0.32	0.00
0	0	128	1.73	0.90	8.87	0.24
0	0	255	12.22	5.45	66.15	0.01
0	128	0	4.31	8.48	1.37	0.19
0	128	128	6.11	9.52	10.27	0.60
0	128	255	16.63	14.42	66.92	1.46
0	255	0	29.75	59.38	7.76	0.01
0	255	128	31.40	60.00	17.05	0.69
0	255	255	41.54	64.29	72.75	0.24
128	0	0	5.35	2.83	0.57	0.20
128	0	128	7.12	3.60	9.46	0.37
128	0	255	17.70	8.21	66.12	0.38
128	128	0	9.76	11.43	1.68	0.59
128	128	128	11.75	12.56	10.86	1.28
128	128	255	22.46	17.57	67.05	1.87
128	255	0	35.24	61.96	7.98	0.39
128	255	128	37.10	62.69	17.64	0.70
128	255	255	47.33	67.00	72.88	0.56
255	0	0	36.28	18.31	1.97	0.01
255	0	128	37.87	18.99	11.35	1.50
255	0	255	47.87	23.31	67.08	0.22
255	128	0	40.68	27.23	3.11	1.04
255	128	128	42.55	28.27	12.86	1.33
255	128	255	52.71	33.06	68.38	1.28
255	255	0	65.46	76.84	9.34	0.23
255	255	128	67.20	77.57	19.53	1.03
255	255	255	76.86	81.56	74.03	0.40
0	0	64	0.32	0.29	1.02	0.83
0	0	160	3.29	1.58	17.34	0.14
0	0	224	8.66	3.88	46.71	0.08
0	64	0	0.57	1.00	0.45	0.95
0	160	0	8.18	16.23	2.38	0.25
0	224	0	21.26	42.36	5.66	0.06
64	0	0	0.72	0.52	0.36	1.50
160	0	0	10.21	5.26	0.83	0.35
224	0	0	26.16	13.25	1.54	0.13

## Chapter VI. Calibration of the Digital Camera

The Nikon D90 is a digital single-lens reflex (DSLR) camera which was marketed on August 27, 2008, as a prosumer model, fitting between the company's entry-level and professional DSLR models. It is equipped with the Nikon's EXPEED image processor and 23.6mm×15.8mm Nikon CMOS sensor, which can output at the maximum resolution of 4288×2848 [100]. The Nikon D90 can support the ISO range from 200 to 3200, and the range can be extended to ISO 100-6400. In order to fit the Nikon D90 on the camera stand, a Nikkor 35mm f2D AF lens was used, which can support the aperture setting up to f 2. There are two file formats for the output of Nikon D90, jpeg and raw. The jpeg output is based on the raw output after some image processing. In order to improve the accuracy of the image pixels, raw image is recommended in this study.

Two methods can be used to access the Nikon raw image, both of which were examined in this study. This first method is based on Nikon Image SDK is used. In this method, three 8 bits of data according to the RGB channels can be acquired for every pixel. The second method is to apply the LibRaw, which is an open source solution and can be downloaded from the Internet. In this method, one original 9.5 bits of data is acquired in every pixel.

Calibration of the of digital camera can set up the data mapping from the device space to the color space which can be used to convert the RGB values to the tristimulus values.

# 1. Calibration via the ICC Profile

An ICC profile stores the data mapping between the color space and the device space for a device. Thus, the ICC profile was first examined to determine whether the tristimulus values of the samples could be acquired accurately.

## 1.1 Color Measurement of the Test Chart

Test charts are used when an ICC profile is generated. Two test charts, namely, GretagMacbeth Colorchecker test chart and Verivide Digitizer test chart, as shown in Figure 65 were used. There are 240 color patches on each test chart, arranged in 12 rows and 20 columns. The color patches under both test charts span the color space. Also, there is a range of neutral gray color patches in both test charts.

The calibration of the digital camera aims to set up the data mapping from the device space to the color space. The values in the device space can be acquired from the output of the digital camera. The values in the color space are acquired via color measurement, using a spectrophotometer prior to the calibration.

Two types of spectrophotometers, namely, Datacolor SF series spectrophotometers and GretagMacbeth Eye One were available for the measurement of color patches of standard test charts. However, it may be easier to employ Eye One because of its portability and flexibility. The Datacolor SF series spectrophotometers are bench top devices and it was found difficult to fit the test chart on these devices due to the size of the test charts and possibility of damaging color patches. However, both Eye One and Datacolor SF600X were

used to measure the test charts and results were compared.

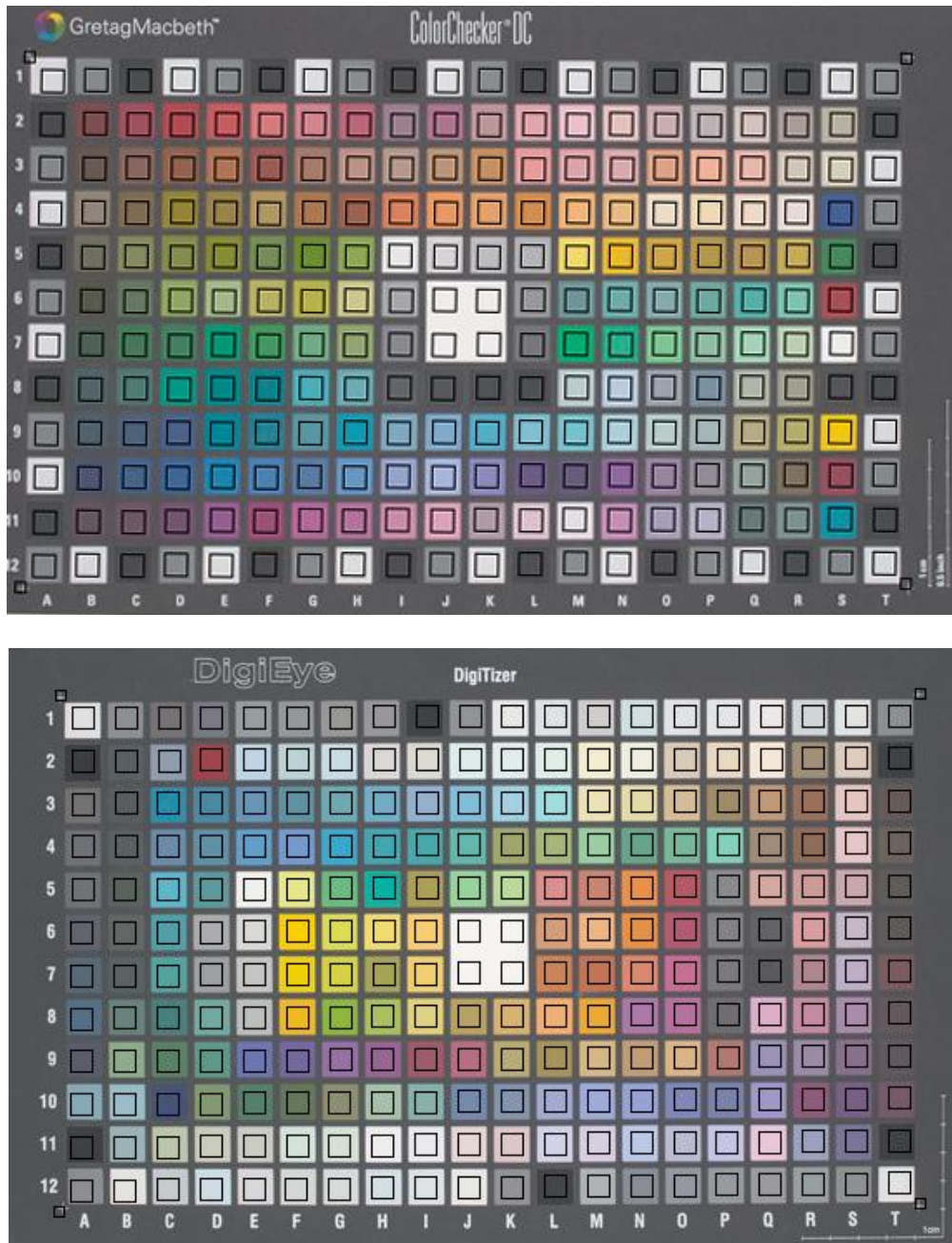


Figure 65. GretagMacbeth Colorchecker (top) and Verivide Digitizer (bottom)

In Figure 66, the image on the left (a) shows the output from the DigiEye system for the Colorchecker test chart without the mirror reflection board. The upper left patch is denoted as S8 and the upper right patch is denoted as T8. It is obvious that the lightness of S8 is higher than the lightness of T8. Using measurements based on Eye One, the  $L^*$ ,  $a^*$ ,  $b^*$  values for S8 were 0.63, 0.65, 0.54 respectively, and the CIELAB values for T8 were (2.91, 3.09, 3.63), which do not correspond to the image of the patches shown in Figure 66a. Figure 66 is qualitatively like the actual image. Measurements based on the Datacolor SF600X generated CIELAB values for S8 of (4.84, 5.1, 5.43), and CIELAB values for T8 of (3.4, 3.6, 3.97), and these corresponded to the appearance of patches in Figure 66a. Figure 66b shows the Colorchecker test chart using the DigiEye system when the mirror reflection boards were installed. These results match those obtained from Eye One. One possible explanation may be related with the illumination / viewing geometry employed. There may also be other reasons. The illumination / viewing geometry for DigiEye system without the mirror reflection board is  $d / 0^\circ$ ; while it is  $45^\circ / 0^\circ$  when the mirror reflection boards were installed. The illumination / viewing geometry for Eye One is  $45^\circ / 0^\circ$ ; but it is  $d / 8^\circ$  for Datacolor SF600X, which is close to that of DigiEye system without the mirror reflection board. The color patch S8 in the Colorchecker test chart is made of a highly glossy material, which reflects more light under the diffused illumination than under the directional illumination. On the other hand, the color patch T8 is matte.

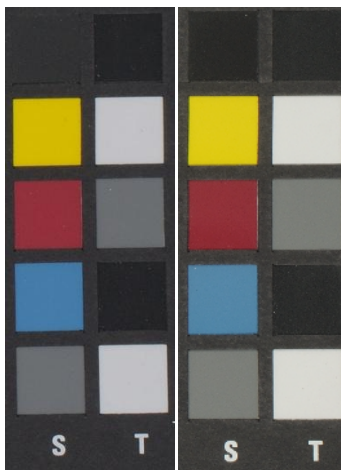


Figure 66. Captured Image of Selected Set of Color Patches on the Colorchecker Testchart of DigiEye without Mirror Reflection Boards (left) and with Mirror Reflection Boards (right)

Table 27 shows a comparison of two matte color patches. Based on DigiEye results under  $d / 0^\circ$ , the lightness of A6 in Digitizer test chart is larger than that of A2 in Colorchecker test chart. The tristimulus values based on Eye One show that they are of the same lightness, however the tristimulus values from Datacolor SF600X demonstrate that  $L^*$  of A6 in the Digitizer test chart is larger than that of A2 in the Colorchecker test chart, which matches the results based on the DigiEye system. It is apparent that Eye One is not as accurate as Datacolor SF600X.

Table 27. Comparison of Two Color Patches

Patch	RGB from DigiEye	CIELAB from SF600X	CIELAB from i1
A2 in Colorchecker	(114, 118, 122)	(51.11, -1.27, 0.09)	(50.7,-1.15,-0.43)
A6 in Digitizer	(124, 127, 129)	(53.39,-2.27, 0.81)	(50.7,-2.43,0.28)

From the data analysis above, it is clear that results using Datacolor SF600X should be incorporated in this research and the illumination / viewing geometry in this research should always be set to  $d / 0^\circ$ .

## 1.2 Algorithm Design

In the ICC specification, there are two models that can be employed for the calibration of the digital camera, the three - component - matrix model and the LUT [33]. The three - component - matrix model is simple and requires fewer parameters, the tristimulus values of the RGB points plus RGB tone reproduction curves, resulting in a fast computation. The LUT is much more complicated and can give a more accurate prediction than that of the three-component-matrix model. In this study, both models were combined together in the ICC profile. However, only LUT was used in the color management.

The first part of the algorithm was designed to estimate the parameters for the three - component - matrix model. Here the tone reproduction curves were simplified as the power equations. The exponents  $(e_r, e_g, e_b)$  must be greater than 0 as the power  $R^{(e_r)}, G^{(e_g)}, B^{(e_b)}$  are ranged from 0 to 1 when  $R, G, B$  values are normalized between (0, 1). Traditionally, these exponents are greater than 1. For example, they are in the range of 2.35 to 2.55 for the CRT, and they are in the range of (1.8, 2.2) for the video LUT in computers [11]. When they are greater than 4.5,  $R^{(e_r)}, G^{(e_g)}, B^{(e_b)}$  are close to 0 and when  $R, G, B$  are smaller than 0.3, and there is no detail. Thus, the exponents  $e_r, e_g, e_b$  were all set to the range (0.5, 4.5). At this point, the model can be expressed by 12 parameters, as shown in equation (53):

$$\begin{bmatrix} X_0 & Y_0 & Z_0 \\ X_i & Y_i & Z_i \\ X_n & Y_n & Z_n \end{bmatrix} = \begin{bmatrix} R_0^{(e_r)} & G_0^{(e_g)} & B_0^{(e_b)} \\ R_i^{(e_r)} & G_i^{(e_g)} & B_i^{(e_b)} \\ R_n^{(e_r)} & G_n^{(e_g)} & B_n^{(e_b)} \end{bmatrix} \begin{bmatrix} X_r & Y_r & Z_r \\ X_g & Y_g & Z_g \\ X_b & Y_b & Z_b \end{bmatrix} \quad (53)$$

Here  $X_i Y_i Z_i$  and  $R_i G_i B_i$  are the tristimulus and device values of one color respectively;

$X_r Y_r Z_r, X_g Y_g Z_g, X_b Y_b Z_b$  are the tristimulus values of the red point, green point and blue

point in the three - component - matrix model, which are between 0 and 1;

When  $R_i G_i B_i$  values are all 1,  $X_i Y_i Z_i$  are the tristimulus values of the default white point,

which is set to illuminant D50 according to the ICC specification [28], where;

$$\begin{cases} X_r + X_g + X_b = X_{D50} \\ Y_r + Y_g + Y_b = Y_{D50} \\ Z_r + Z_g + Z_b = Z_{D50} \end{cases} \quad (54)$$

From equation (54), the  $X_r Y_r Z_r, X_g Y_g Z_g$  and  $X_b Y_b Z_b$  can be simplified to 6 parameters

$(X_g, X_b, Y_r, Y_b, Z_r, Z_g)$  with the following constraints:

$$\begin{cases} X_r > X_g + X_b \\ Y_g > Y_r + Y_b \\ Z_b > Z_r + Z_g \end{cases} \quad (55)$$

Now there are 9 parameters, which can be divided into two groups: tristimulus parameters

$(X_g, X_b, Y_r, Y_b, Z_r, Z_g)$  and exponential parameters  $(e_r, e_g, e_b)$ . From the analysis above, the

ranges for these two groups are known and the search algorithm is applied. Because of the

huge computational complexity of the 9-nested-loop, the search was divided into a 6-nested-

loop for the tristimuli parameters and a 3-nested-loop for the exponential parameters.

For the 6-nested-loop, the exponential parameters were set as constants; initially they were

set to 1. The 6-nested-loop was set up for the tristimuli parameters from their minimum to their maximum, with  $\frac{1}{4}$  of the difference between the minimum and the maximum to be set as the intervals. If the constraint in equation (55) was not met, the associated loop was broken.

When all the tristimuli parameters were set, equation (53) was used to compute  $(X_i Y_i Z_i)'$  on all the color patches in the standard test chart. The maximal color difference between  $(X_i Y_i Z_i)'$  and  $X_i Y_i Z_i$  in CIEDE2000 (1:1:1) was recorded. When the circulation was completed,  $15^3$  maximal color differences were obtained. The smallest difference from them was determined and the associated tristimuli parameters  $(X_g^1, X_b^1, Y_r^1, Y_b^1, Z_r^1, Z_g^1)$  were obtained.

Then  $(X_g^1, X_b^1, Y_r^1, Y_b^1, Z_r^1, Z_g^1)$  were used as the center for a new search. An alternation was made on the minimal and the maximal values for the tristimuli parameters based on  $(X_g^1, X_b^1, Y_r^1, Y_b^1, Z_r^1, Z_g^1)$ . The  $(X_g^1, X_b^1, Y_r^1, Y_b^1, Z_r^1, Z_g^1)$  minus the intervals was used as the minimal values for the tristimuli parameters and the  $(X_g^1, X_b^1, Y_r^1, Y_b^1, Z_r^1, Z_g^1)$  plus the intervals was used as the maximal values for the tristimuli parameters and the 6-nested-loop above was repeated to acquire  $(X_g^2, X_b^2, Y_r^2, Y_b^2, Z_r^2, Z_g^2)$ . After 5 iterations, the intervals became  $\frac{1}{4^5}$  of the original intervals and the tristimuli parameters under the current exponential parameters were acquired.

For the 3-nested-loop, the tristimuli parameters were set to constants. The 3-nested-loop was set up for the exponential parameters from their minimum to maximum, with the intervals set

to  $\frac{1}{4}$  of the difference between the minimum and the maximum. In each iteration equation (53) was used to compute  $(X_i Y_i Z_i)'$  for all the color patches in the standard test chart. The maximum color difference between  $(X_i Y_i Z_i)'$  and  $X_i Y_i Z_i$  based on CIEDE2000 (1:1:1) was recorded. When the iteration was completed,  $5^3$  maximal color differences were obtained. The smallest color difference was determined and the associated exponential parameters  $(e_r^1, e_g^1, e_b^1)$  were obtained.

The minimal and the maximal values for the exponential parameters, based on  $(e_r^1, e_g^1, e_b^1)$ , were then changed.  $(e_r^1, e_g^1, e_b^1)$  minus the intervals was used as the minimal values for the exponential parameters and  $(e_r^1, e_g^1, e_b^1)$  plus the intervals was used as the maximal values for exponential parameters and the tri-circulation above was repeated to acquire

$(e_r^2, e_g^2, e_b^2)$ . After 5 iterations, the intervals became  $\frac{1}{4^5}$  of the original intervals and the exponential parameters under the current tristimuli parameters were acquired.

The above hex-circulation and tri-circulation were iterated, until the minimum of the maximum color difference was no longer reduced. Then the tristimuli parameters and the exponential parameters were acquired. This is a locally optimal solution.

The second part of the algorithm was designed to compute the LUT. LUT is an assorted array. If the grid points number is  $n$ , the coordinate for a RGB LUT entry is  $(\frac{i}{n-1}, \frac{j}{n-1}, \frac{k}{n-1})$ , where  $i, j, k$  are all integers and  $0 \leq i, j, k < n$ . The associated tristimulus values at the LUT entry is to be computed. The RGB values and tristimulus values of the color patches in the standard test chart are used as the input dataset.

For one LUT entry  $(R_0, G_0, B_0)$  the input data set was divided into two sub datasets  $\varepsilon$  and  $\varepsilon^c$ , as shown:

$$\begin{cases} \|(R_0, G_0, B_0) - (r, g, b)\|_2 < \mu & \forall (r, g, b) \in \varepsilon \\ \|(R_0, G_0, B_0) - (r, g, b)\|_2 > \mu & \forall (r, g, b) \in \varepsilon^c \end{cases} \quad (56)$$

Here  $\mu$  was a given constant distance.

For any point in  $\varepsilon$ , a vector  $\rho$  was developed from the camera output  $(r, g, b)$ , and a vector  $\tau$  was the corresponding tristimulus values  $(x, y, z)$ .  $\rho$  has various formats according to  $N_\varepsilon$  and the number of data in  $\varepsilon$ , as shown in equation (57).

$$\begin{cases} \rho = (r, g, b) & N_\varepsilon = 4 \\ \rho = (r, g, b, 1) & 5 \leq N_\varepsilon \leq 8 \\ \rho = (rgb, rg, gb, rb, r, g, b, 1) & 9 \leq N_\varepsilon \leq 11 \\ \rho = (rgb, r^2, g^2, b^2, rg, gb, rb, r, g, b, 1) & 12 \leq N_\varepsilon \end{cases} \quad (57)$$

Equation (58) can be used to describe the data mapping from the device space to the color space.

$$T_{3 \times n} = M_{3 \times k} P_{k \times n} \quad (58)$$

Here  $T$  is a matrix composed of CIEXYZ values of all points in  $\varepsilon$ ,  $P$  is a matrix composed of  $\rho$  of all points in  $\varepsilon$ , and  $M$  is the transformation matrix.  $n$  is the number of color patches in  $\varepsilon$  and  $k$  is the number of items in equation (57).

As  $T$  and  $P$  are not square matrices, a pseudo inverse method was applied to acquire  $M$ , as shown in equation (59).

$$M_{3 \times k} = T_{3 \times n} P_{k \times n}^T (P_{k \times n} \cdot P_{k \times n}^T)^{-1} \quad (59)$$

The color patches on the test charts only span a section of the color gamut of the digital camera used. In order to apply the technique shown in equations (56-59) to the whole gamut,

a special technique was used. The device space was divided into a combination of regions.

The projection of this division in the RG plane is shown in Figure 67.

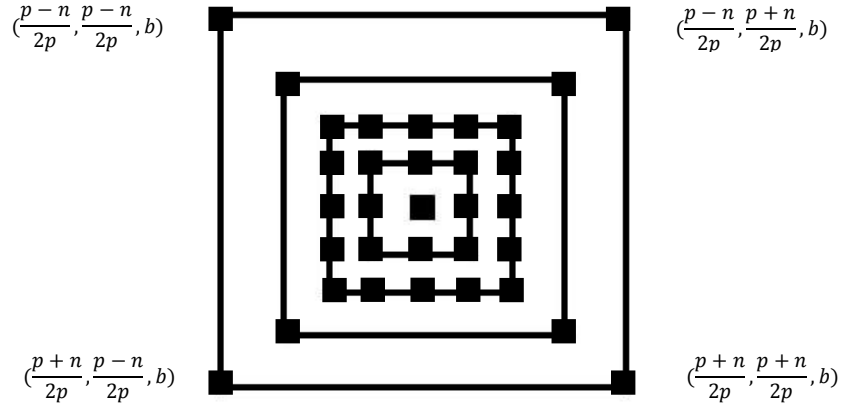


Figure 67. RG Projection of Division of the Device Space into Regions

The center of the RGB device space was set at (0.5, 0.5, 0.5). The grid points in the  $n^{\text{th}}$  layer can be expressed using equation (60).

$$(r, g, b) = \begin{cases} r = \frac{p-n}{2p} \text{ or } \frac{p+n}{2p}, g \in \left[ \frac{p-n}{2p}, \frac{p+n}{2p} \right], b \in \left[ \frac{p-n}{2p}, \frac{p+n}{2p} \right] \\ g = \frac{p-n}{2p} \text{ or } \frac{p+n}{2p}, r \in \left[ \frac{p-n}{2p}, \frac{p+n}{2p} \right], b \in \left[ \frac{p-n}{2p}, \frac{p+n}{2p} \right] \\ b = \frac{p-n}{2p} \text{ or } \frac{p+n}{2p}, r \in \left[ \frac{p-n}{2p}, \frac{p+n}{2p} \right], g \in \left[ \frac{p-n}{2p}, \frac{p+n}{2p} \right] \end{cases} \quad (60)$$

$p$  is the integer number which equals the number of the grid points divided by 2, and the number of the grid points of one side is  $2p + 1$ .

The calculation starts from the center. The standard test charts used in this study have 240 color patches which span in the color space from the central gray axis. Thus there were more than 11 points for the computation of the center.

Once the LUT entries in the  $n^{\text{th}}$  layer were calculated, they were put into the input and served as the input for the calculation of the LUT entries on the  $(n+1)^{\text{th}}$  layer.

When  $\mu$  is set to  $\frac{3}{2p}$ , for the vertices of the  $(n+1)^{\text{th}}$  layer, where  $r, g, b$  are either  $\frac{p-n-1}{2p}$  or

$\frac{p+n+1}{2p}$ , 7 points from the inner  $n$  layers were used as the input. For example, for

$(\frac{p-n-1}{2p}, \frac{p-n-1}{2p}, \frac{p-n-1}{2p})$ , there are 7 points:  $(\frac{p-n}{2p}, \frac{p-n}{2p}, \frac{p-n}{2p})$ ,  $(\frac{p-n}{2p}, \frac{p-n}{2p}, \frac{p-n+1}{2p})$ ,

$(\frac{p-n}{2p}, \frac{p-n+1}{2p}, \frac{p-n}{2p})$ ,  $(\frac{p-n+1}{2p}, \frac{p-n}{2p}, \frac{p-n}{2p})$ ,  $(\frac{p-n+1}{2p}, \frac{p-n+1}{2p}, \frac{p-n}{2p})$ ,  $(\frac{p-n+1}{2p}, \frac{p-n}{2p}, \frac{p-n+1}{2p})$ ,

$(\frac{p-n}{2p}, \frac{p-n+1}{2p}, \frac{p-n+1}{2p})$ . Their distances to  $(\frac{p-n-1}{2p}, \frac{p-n-1}{2p}, \frac{p-n-1}{2p})$  are smaller than or equal to  $\mu$ .

Thus they can be used as input for the computation of  $(\frac{p-n-1}{2p}, \frac{p-n-1}{2p}, \frac{p-n-1}{2p})$ .

Similarly, for the LUT entries at the edges of the  $(n+1)^{\text{th}}$  layer, where only two of the  $(r, g, b)$

are either  $\frac{p-n-1}{2p}$  or  $\frac{p+n+1}{2p}$ , at least 11 points from the inner  $n$  layers can serve as the input

when  $\mu = \frac{3}{2p}$ . Likewise, for the LUT entries at the surfaces of the  $(n+1)^{\text{th}}$  layer, where only

one of  $(r, g, b)$  is either  $\frac{p-n-1}{2p}$  or  $\frac{p+n+1}{2p}$ , at least 18 points from the inner  $n$  layers can be used

as the input when  $\mu = \frac{3}{2p}$ .

Thus, if  $\mu$  is set to  $\frac{3}{2p}$ , there will be no less than 7 points from the inner  $n$  layers for the local polynomial regression.

### 1.3 Results and Analysis

Firstly, a comparison is made between the three - component - matrix model and the LUT [33]. It can be noticed that the three - component - matrix model is fast, requiring only 9 multiplications and 6 additions for the color conversion of one point, as shown in equation (32) in chapter II. The transfer curves of RGB can be realized via three 1D LUTs. For the LUT method, if the trilinear interpolation is applied, at least 43 multiplications and 33 additions are required, as shown in equation (35) in chapter II.

Normally for the color correction, a device link is set up to connect the input profile and the output profile [11]. If both of them are based on the three - component - matrix model, where for example, the input profile is for the digital camera and the output profile is for the monitor, the conclusion above still holds true.

However, the accuracy of the three - component - matrix model is worse than that of the LUT method. A profile was generated using the Gretag Colorchecker. Both the three – component – matrix model and LUT in the profile were used in the conversion of the device values of the standard test chart to the tristimulus values. Figure 68 shows the average and max color differences between the original tristimuli and the converted tristimuli. It can be noted that the LUT method was more accurate than the three-component-matrix method, both for the mean as well as the max color difference.

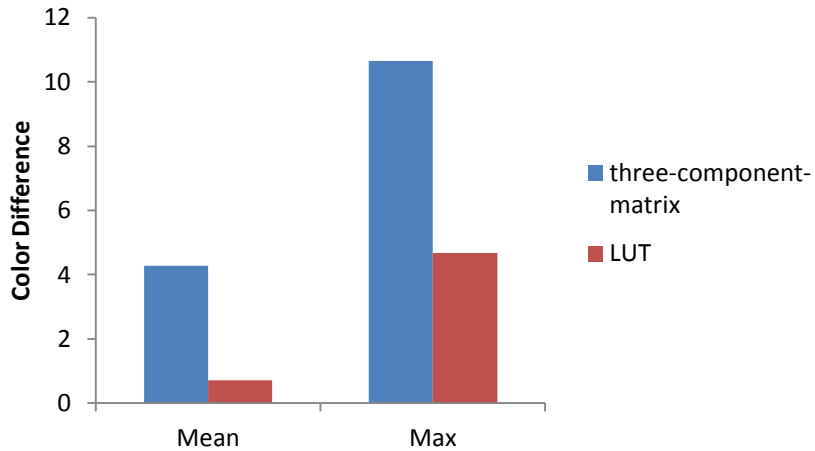


Figure 68. Comparison between the Color Differences based on the Three-Component-Matrix and LUT

As mentioned earlier, two standard test charts were used in this study, Gretag ColorChecker and Verivide DigiTizer. They were placed inside the DigiEye illumination chamber and a Nikon D90 was used to capture images. With the algorithm above, two profiles were generated from the standard test charts. The default white point in the ICC specification is D50. Chromatic adaptation was applied if the white point is not D50. The chromatic adaptation is done in the CIEXYZ space and the interpolation of the LUT is in the CIELAB space. However, the conversion between the CIEXYZ and the CIELAB is nonlinear. In order to improve the accuracy, the white point of the profile LUT is not mapped to D50 and chromatic adaptation was not applied to the LUT entries. Instead, the original tristimuli were fed into the regression directly.

The test charts were then used as the test dataset to check the accuracy of the two profiles separately. Trilinear interpolation was employed to convert the mean device values of some

color patches from the standard test charts into the color values, and the color difference between the actual color values and the converted color values were computed based on CIEDE2000(1:1:1) for further analysis.

Table 28 shows the results of the average and maximum color difference values of all the combinations, profiling based on DigiTizer and testing with DigiTizer, profiling using Colorchecker and testing with Colorchecker, profiling based on Colorchecker and testing with DigiTizer, and profiling using DigiTizer and testing with Colorchecker.

Table 28. Average and Maximum Color Difference from Various Combination of Training and Testing Dataset Employed

Profiling Chart	Testing Chart	Average	Maximum
DigiTizer	DigiTizer	0.56	1.96
ColorChecker	ColorChecker	0.77	3.98
ColorChecker	DigiTizer	1.27	5.27
DigiTizer	ColorChecker	1.71	6.71

Xrite<sup>®</sup> ProfileMaker 4 was also used for comparison. Based on the color measurements of the standard test charts, two reference files were generated and put under the reference folder of ProfileMaker 4. Two profiles based on the two reference files were generated using the images of the two standard test charts separately. In the ProfileMaker, the LUT size was set to large, that is, there are 25 grid points in one side. A2B1 LUT, which records the relative intent of the profile, was retrieved from the profile, and the trilinear interpolation was used to determine the tristimulus and wrong von Kries was applied to map the color from D50 to the camera white point. The results are shown in Table 29. It can be seen both the LUT computation in this study and Xrite<sup>®</sup> ProfileMaker 4 performed similarly.

Table 29. Average and Maximum Color Difference from Various Combinations of Training and Testing Data Set using Xrite<sup>®</sup> ProfileMaker 4

Training Chart	Testing Chart	Average	Maximum
DigiTizer	DigiTizer	0.77	7.19
ColorChecker	ColorChecker	0.69	2.09
ColorChecker	DigiTizer	1.26	7.38
DigiTizer	ColorChecker	1.39	7.53

When the profile was checked using the same test chart used to create it, most of the  $\Delta E$ s were smaller than 1.0 (Figure 69a and 69b); when the profile was checked using the different test chart, most of the  $\Delta E$ s were lower than 2.0 (Figure 69c and 69d). All combinations are shown in Figure 69.

Figure 70 shows that Digitizer test chart exhibits a larger distribution in the low lightness axis region leading to the large color differences for color patches A2, A11 and T11 in the Digitizer test chart when they were converted using the profile from Colorchecker,  $\Delta E_{A2} = 3.68$ ,  $\Delta E_{T11} = 3.72$ ,  $\Delta E_{A11} = 4.48$ .

When the profile from Digitizer test chart was employed to convert the color patches in the Colorchecker test chart, the large color differences for S4, B10, C10 and D10 in the Colorchecker test chart were attributed to the insufficient number of color patches in the blue region in the Digitizer test chart, as shown in Figure 71.  $\Delta E_{S4} = 5.90$ ,  $\Delta E_{B10} = 5.75$ ,  $\Delta E_{C10} = 6.71$ ,  $\Delta E_{D10} = 5.06$ . There is only one color patch in that region from the Digitizer test chart.

Thus, the conversion accuracy is dependent on the span of the colors used for calibration.

One shortcoming of the algorithm is that the calculation of the LUT entries in the outer layer is partly dependent on the LUT entries in the inner layers. So the error from the inner layers might be propagated to the outer layer.

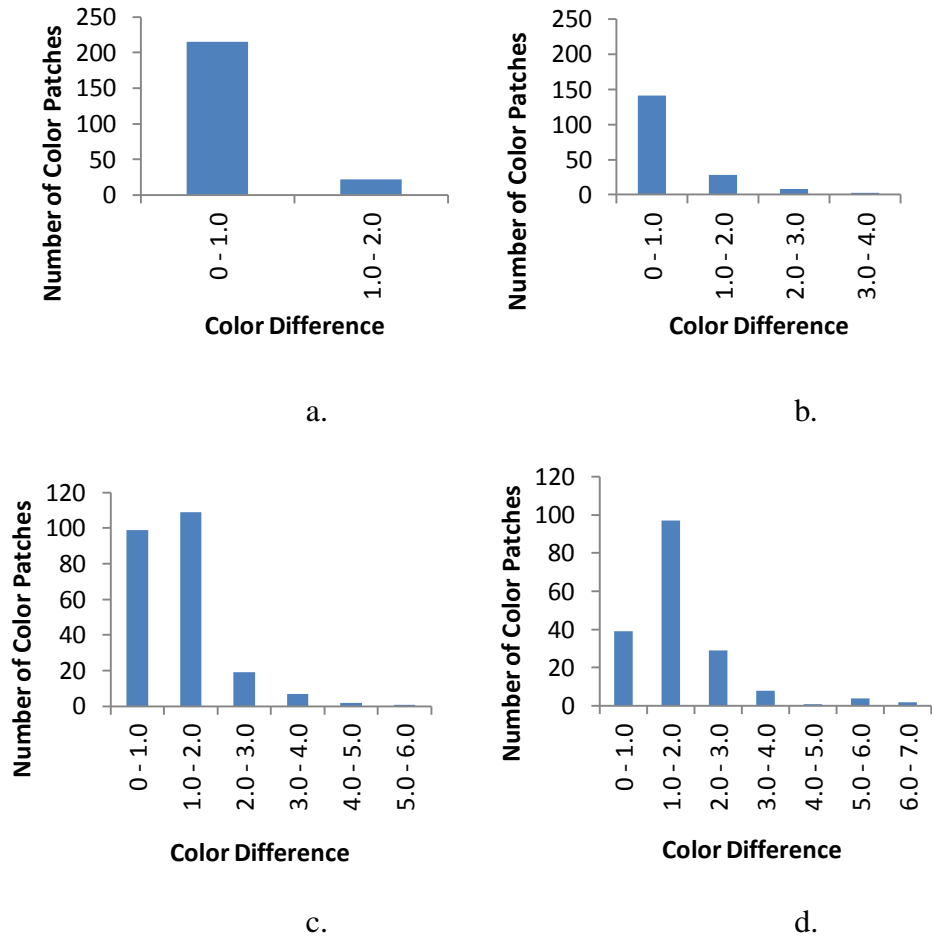


Figure 69. Distribution of the Color Differences under Different Conditions

- a. Test the Profile from Digitizer Test Chart with Digitizer Test Chart
- b. Test the Profile from Colorchecker Test Chart with Colorchecker Test Chart
- c. Test the Profile from Colorchecker Test Chart with Digitizer Test Chart
- d. Test the Profile from Digitizer Test Chart with Colorchecker Test Chart

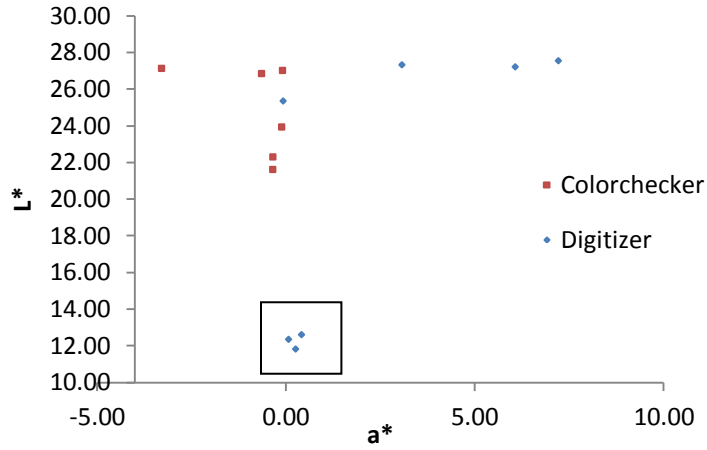


Figure 70. Difference in the Distribution of Colors in Two Test Charts in the Low Lightness

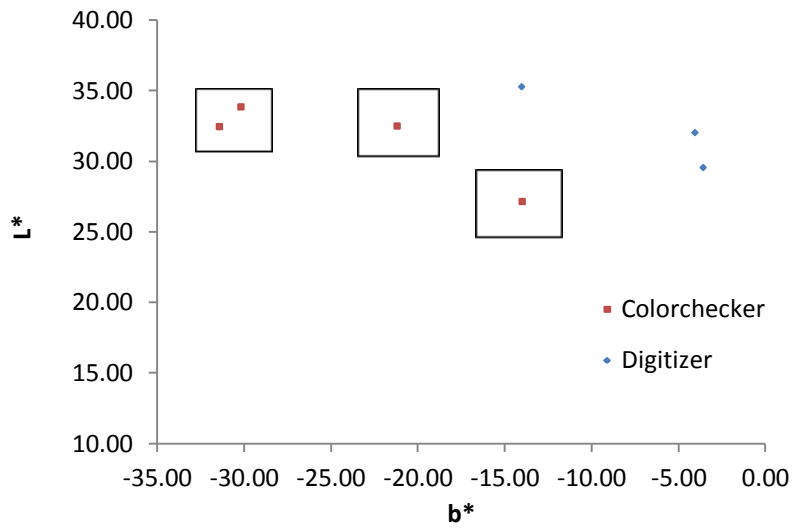


Figure 71. Difference in the Distribution of Colors in Two Test Charts in the Blue Region

Another shortcoming is that the local polynomial regression fails to generate a smooth surface of the gamut boundary, as shown in Figure 72.

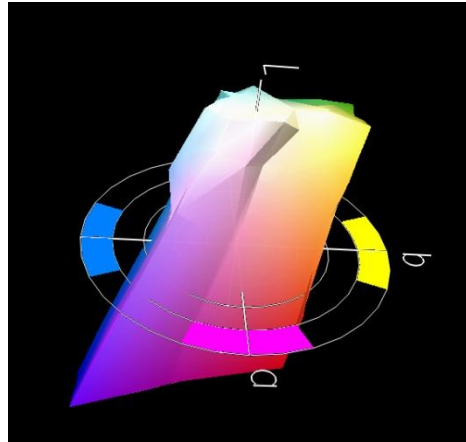


Figure 72. Unsmooth Surface of Gamut Boundary based on Local Polynomial Regression

An experiment was carried out to check the effectiveness of the color conversion based on the ICC profile. Verivide Digitizer test chart was used to generate a profile, then 5 random camouflage samples were placed inside the DigiEye illumination chamber and their images were captured for analysis. The average RGB values were converted into CIELAB values based on the profile and compared with the measured CIELAB values, as shown in Table 30. The  $\Delta L^*$ ,  $\Delta a^*$  and  $\Delta b^*$  are ranged from -3.82 to 1.18, and all these samples were judged as ‘fail’ samples. It can be seen from Table 3 in Chapter III that all the sample colors in the small regions and some of  $\Delta L^*$ ,  $\Delta a^*$  and  $\Delta b^*$  based on ICC are even larger than the difference between the max and min. Thus other techniques were therefore decided to be examined.

Table 30. Original and Converted CIELAB Value for 5 Camouflage Samples

Sample ID		Desert Sand			Urban Gray			Foliage Green		
		L*	a*	b*	L*	a*	b*	L*	a*	b*
459958	Original	68.56	3.64	10.54	54.85	-0.61	5.27	46.23	-1.21	2.87
	Converted	69.32	4.76	12.56	55.47	0.07	7.66	45.48	-0.89	3.93
	Difference	<b>-0.76</b>	<b>-1.12</b>	<b>-2.02</b>	<b>-0.62</b>	<b>-0.68</b>	<b>-2.39</b>	<b>0.75</b>	<b>-0.32</b>	<b>-1.06</b>
479354	Original	66.02	3.01	10.54	52.89	-0.72	5.25	46.04	-1.36	3.35
	Converted	66.44	3.75	13.20	52.65	-0.10	7.26	45.14	-1.04	4.70
	Difference	<b>-0.42</b>	<b>-0.74</b>	<b>-2.66</b>	<b>0.24</b>	<b>-0.62</b>	<b>-2.01</b>	<b>0.90</b>	<b>-0.32</b>	<b>-1.35</b>
236942338	Original	64.51	2.82	10.33	52.18	-0.58	5.67	43.64	-1.80	2.96
	Converted	65.74	4.14	13.43	52.47	0.44	8.21	44.00	-0.89	5.19
	Difference	<b>-1.24</b>	<b>-1.32</b>	<b>-3.10</b>	<b>-0.29</b>	<b>-1.02</b>	<b>-2.54</b>	<b>-0.36</b>	<b>-0.91</b>	<b>-2.23</b>
Standard	Original	66.17	2.96	10.93	53.02	-0.41	5.79	44.05	-1.59	3.31
	Converted	66.50	4.12	14.75	52.65	0.37	7.95	42.87	-0.81	4.99
	Difference	<b>-0.33</b>	<b>-1.16</b>	<b>-3.82</b>	<b>0.37</b>	<b>-0.78</b>	<b>-2.16</b>	<b>1.18</b>	<b>-0.78</b>	<b>-1.68</b>
462399	Original	68.24	3.53	10.73	55.66	-0.39	5.82	46.60	-1.05	3.23
	Converted	69.05	4.83	13.17	56.14	0.19	8.75	46.09	-0.72	4.59
	Difference	<b>-0.81</b>	<b>-1.30</b>	<b>-2.44</b>	<b>-0.48</b>	<b>-0.58</b>	<b>-2.93</b>	<b>0.51</b>	<b>-0.33</b>	<b>-1.36</b>

Based on the analysis in Chapter IV, it can be noted that the output of the camera is variable, and this variation inevitably affects the color conversion from the device space to the color space. In order to determine the effect of the camera output variation on results, a simulation was done. A noise error,  $\delta$ , was added to the camera output of the standard sample.  $\delta$  can be one of (-1, 0, 1). Then the RGB values with noise signal were converted into the CIELAB values, as shown in Table 31.

When CIELAB values were compared with the CIELAB values without noise  $\delta$  in the input, the differences  $\Delta L^*$ ,  $\Delta a^*$  and  $\Delta b^*$  were roughly in the range of (-0.7, 0.7), as shown in the row 'range', which are in the same magnitude to the difference between max and min in Table 3 of Chapter III.

Table 31. Converted CIELAB of the Standard Sample with Noise

Noise $\delta$	Foliage Green			Urban Gray			Desert Sand		
	L*	a*	b*	L*	a*	b*	L*	a*	b*
(1,1,1)	43.37	0.35	5.88	52.57	2.46	8.73	65.35	5.96	13.85
(1,0,1)	43.25	0.66	5.61	52.47	2.76	8.46	65.25	6.23	13.61
(1,-1,1)	43.13	0.96	5.34	52.37	3.06	8.19	65.16	6.50	13.36
(1,1,0)	43.38	0.28	6.22	52.59	2.37	9.06	65.36	5.86	14.17
(1,0,0)	43.26	0.59	5.95	52.49	2.67	8.79	65.27	6.13	13.93
(1,-1,0)	43.14	0.89	5.68	52.39	2.97	8.53	65.17	6.39	13.68
(1,1,-1)	43.39	0.21	6.56	52.60	2.28	9.40	65.38	5.75	14.49
(1,0,-1)	43.27	0.51	6.29	52.50	2.58	9.13	65.28	6.02	14.24
(1,-1,-1)	43.15	0.82	6.02	52.40	2.88	8.86	65.19	6.29	14.00
(0,1,1)	43.32	0.03	5.81	52.52	2.13	8.66	65.30	5.70	13.78
(0,0,1)	43.19	0.34	5.54	52.42	2.43	8.40	65.20	5.97	13.54
(0,-1,1)	43.07	0.64	5.27	52.31	2.73	8.13	65.11	6.24	13.30
(0,1,0)	43.33	-0.04	6.15	52.53	2.04	9.00	65.31	5.60	14.10
(0,0,0)	43.21	0.27	5.88	52.43	2.34	8.73	65.21	5.87	13.86
(0,-1,0)	43.08	0.57	5.61	52.33	2.64	8.47	65.12	6.14	13.62
(0,1,-1)	43.33	-0.04	6.15	52.53	2.04	9.00	65.31	5.60	14.10
(0,0,-1)	43.21	0.27	5.88	52.43	2.34	8.73	65.21	5.87	13.86
(0,-1,-1)	43.08	0.57	5.61	52.33	2.64	8.47	65.12	6.14	13.62
(-1,1,1)	43.26	-0.29	5.74	52.46	1.80	8.60	65.24	5.45	13.72
(-1,0,1)	43.14	0.02	5.47	52.36	2.10	8.34	65.15	5.71	13.47
(-1,-1,1)	43.02	0.33	5.19	52.26	2.40	8.07	65.05	5.98	13.23
(-1,1,0)	43.28	-0.36	6.07	52.47	1.71	8.94	65.26	5.34	14.03
(-1,0,0)	43.15	-0.05	5.80	52.37	2.01	8.67	65.16	5.61	13.79
(-1,-1,0)	43.03	0.26	5.53	52.27	2.31	8.40	65.07	5.88	13.55
(-1,1,-1)	43.17	-0.12	6.14	52.38	1.92	9.01	65.18	5.51	14.11
(-1,0,-1)	43.17	-0.12	6.14	52.38	1.92	9.01	65.18	5.51	14.11
(-1,-1,-1)	43.04	0.18	5.87	52.28	2.22	8.74	65.08	5.77	13.87
max	43.39	0.96	6.56	52.60	3.06	9.40	65.38	6.50	14.49
min	43.02	-0.36	5.19	52.26	1.71	8.07	65.05	5.34	13.23
range	0.19	0.69	0.68	0.17	0.72	0.66	0.16	0.63	0.63
	-0.19	-0.62	-0.68	-0.17	-0.63	-0.66	-0.16	-0.53	-0.63

## 2. Calibration based on Other Methods

In Chapter II, it was noted that several techniques can be employed to improve the accuracy of the calibration process other than the application of the ICC profile. These include the regression technique, PCA method, multiple illuminations and calibration based on the samples. These techniques were simulated and described below.

### 2.1 Simulation of the Camera Output

As the calibration of the camera is to setup the data mapping between the camera output and the color values, the camera output can be simulated via the spectra of the RGB channels of the digital camera.

Given the spectra of the R, G, B channels of the digital camera, as shown in Figure 31, the maximum R, G, B values under D75 illumination can be computed using equation (61).

$$\begin{aligned}R_{max} &= \sum I_{D75}(\lambda)r(\lambda) \\G_{max} &= \sum I_{D75}(\lambda)g(\lambda) \\B_{max} &= \sum I_{D75}(\lambda)b(\lambda)\end{aligned}\tag{61}$$

Here  $I_{D75}(\lambda)$  is the spectra for the D75 illumination,  $r(\lambda)$ ,  $g(\lambda)$ ,  $b(\lambda)$  are the spectra of R, G, B channels of the digital camera.

$R_{max}$ ,  $G_{max}$  and  $B_{max}$  are used to normalize responses from the R, G, B channels.

When a color spectrum is given, the R, G, B values of that color from the digital camera under illumination D75 can be calculated using equation (62).

$$\begin{aligned}
R &= \frac{\sum I_{D75}(\lambda)r(\lambda)s(\lambda)}{R_{max}} \\
G &= \frac{\sum I_{D75}(\lambda)r(\lambda)s(\lambda)}{G_{max}} \\
B &= \frac{\sum I_{D75}(\lambda)b(\lambda)s(\lambda)}{B_{max}}
\end{aligned} \tag{62}$$

Here,  $s(\lambda)$  is the spectrum of the color.

In the simulation of the color under the illumination U30, the R, G, B values of that color from the digital camera under illumination U30 can be calculated via the equation (63).

$$\begin{aligned}
R' &= k \frac{\sum I_{U30}(\lambda)r(\lambda)s(\lambda)}{R_{max}} \\
G' &= k \frac{\sum I_{U30}(\lambda)g(\lambda)s(\lambda)}{G_{max}} \\
B' &= k \frac{\sum I_{U30}(\lambda)b(\lambda)s(\lambda)}{B_{max}}
\end{aligned} \tag{63}$$

Here  $I_{U30}(\lambda)$  is the spectrum for the illumination U30, and  $k$  is a normalization factor, which equals to the maximal value in the D75 spectral power distribution over the maximal value in the U30 spectral power distribution.

The spectral power distribution of U30 and D75 is shown in Figure 73. The SPD of D75 is from [1], and the SPD of U30 is based on radiometric measurement of the source in a Gretag Macbeth SpectraLight III booth.

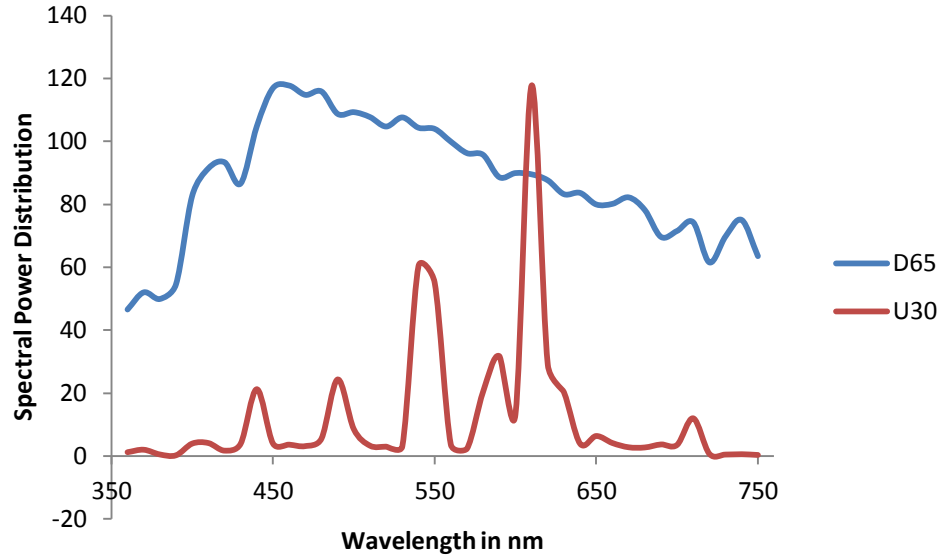


Figure 73. Spectral Power Distribution of D75 and U30 after Normalization

## 2.2 PCA

The principle components analysis (PCA) method was firstly used to estimate the reflectance spectra of the sample colors. The method shown in equation (64) is used to train the model.

$$[R]_{m \times k}^T [R]_{m \times k} = [V]_{k \times k}^T [N]_{k \times k} [V]_{k \times k} \quad (64)$$

Here,  $m$  is the number of the samples in the training set,

$k$  is the number of wavelengths to represent a spectra from 360nm to 750nm and was 40 in the calculation, with an interval of 10nm,

$R$  are the reflectance spectra (360nm-750nm) of the colors from the training data set,  $V$  is composed of the eigenvectors of  $R^T R$ , and  $N$  is a diagonal matrix composed of the eigenvalues of  $R^T R$ .

The eigenvectors related with the biggest  $n$  coefficients of  $m$  samples for the PCA were used, and equation (65) was obtained:

$$[P]_{m \times n} = [R]_{m \times k} [V']_{n \times k}^T \quad (65)$$

$n$  is the number of the eigenvectors used.

$V'$  is the matrix consisting of the eigenvectors related with the biggest  $n$  eigenvalues,

$P$  is the matrix of the parameters for the eigenvectors related with the biggest  $n$  eigenvalues.

$[\ ]^T$  is the transpose of the matrix.

$[R]_{m \times k}$  can be computed by  $[P]_{m \times n} [V']_{n \times k}$

The transformation matrix  $[M]_{8 \times n}$  is then used to set up the relationship from device value matrix  $[f]_{m \times 8}$  to  $[P]_{m \times n}$ , as shown in equations (66-68).

$$[P]_{m \times n} = [f]_{m \times 8} [M]_{8 \times n} \quad (66)$$

$$[f]_{m \times 8}^T [P]_{m \times n} = [f]_{m \times 8}^T [f]_{m \times 8} [M]_{8 \times n} \quad (67)$$

$$[M]_{8 \times n} = ([f]_{m \times 8}^T [f]_{m \times 8})^{-1} [f]_{m \times 8}^T [P]_{m \times n} \quad (68)$$

$[f]_{m \times 8}$  is the matrix of the vectors developed from the RGB signals, and the vector is in the format of equation (69) when calibration was carried out using the standard test chart.

$$f = (rgb \quad gb \quad rb \quad rg \quad r \quad g \quad b \quad 1) \quad (69)$$

Equation (70) was only applied when calibrating via the camouflage samples, in which case the average was subtracted to avoid the ill conditioning of the matrices.

$$f = \begin{pmatrix} (r - \bar{r})(g - \bar{g})(b - \bar{b}) & (g - \bar{g})(b - \bar{b}) & (r - \bar{r})(b - \bar{b}) & (r - \bar{r})(g - \bar{g}) \\ r - \bar{r} & g - \bar{g} & b - \bar{b} & 1 \end{pmatrix} \quad (70)$$

$\bar{r}$ ,  $\bar{g}$ ,  $\bar{b}$  are the average values of  $RGB$  for one color for all the samples in the training set.

When the calibration was based on the camouflage samples, three  $[M]_{8 \times n}$  were trained as there are three colors.

During the testing,  $\|Conv_1([XYZ]_{N \times 3}) - Conv_2([f]_{N \times 8}[M]_{8 \times n}[V']_{n \times 40})\|_{inf}$  was used to acquire the maximal  $\Delta L^*$ ,  $\Delta a^*$  and  $\Delta b^*$ ;

$\|Conv_1([XYZ]_{N \times 3}) - Conv_2([f]_{N \times 8}[M]_{8 \times n}[V']_{n \times 40})\|_2$  was used to acquire the  $\Delta E$  in CIEDE2000.

$Conv_1$  is the function that converts the CIE XYZ values to CIELAB values;

$Conv_2$  is the function that converts the spectra to CIELAB values.

PCA is a method that identifies patterns in data, and expresses the data in such a way that highlights their similarities and differences. The error after spectral reconstruction should be less than the threshold, as shown in the equation (71).

$$\|Conv_2([P]_{m \times n}[V']_{n \times 40}) - Conv_2([R]_{m \times 40})\|_{inf} < threshold \quad (71)$$

Here  $n$  is the number of the eigenvectors used,  $m$  is the number of the samples for training;

$V'$  is the matrix consisting of the eigenvectors related with the biggest  $n$  eigenvalues;

$P$  is the matrix of the parameters for the eigenvectors related with the biggest  $n$  eigenvalues of the colors of interest from all samples;

$R$  is the matrix composed of the reflectance spectra of the colors of interest from all the samples;

*threshold* is the maximal value of  $\Delta L^*$ ,  $\Delta a^*$ ,  $\Delta b^*$  that can be tolerated in the spectra reconstruction, here 0.2 was used, which is half of the smallest difference between max and min in Table 3 of Chapter III.

The cases when  $n = 3$ ,  $n = 5$  and  $n = 6$  were tested and it was determined that  $n = 6$  can satisfy the requirements. Results are shown in Table 32 below.

Table 32. Relationship between  $\Delta L^*$ ,  $\Delta a^*$  and  $\Delta b^*$  and the number of Eigenvectors used

		Foliage Green			Urban Gray			Desert Sand		
		$\Delta L^*$	$\Delta a^*$	$\Delta b^*$	$\Delta L^*$	$\Delta a^*$	$\Delta b^*$	$\Delta L^*$	$\Delta a^*$	$\Delta b^*$
$n = 3$	Max	0.07	0.47	0.44	0.11	0.45	0.68	0.19	0.71	0.68
	Min	-0.10	-0.34	-0.38	-0.17	-0.53	-0.88	-0.20	-0.57	-0.96
$n = 5$	Max	0.02	0.19	0.12	0.03	0.18	0.19	0.09	0.34	0.63
	Min	-0.02	-0.21	-0.10	-0.03	-0.12	-0.19	-0.06	-0.55	-0.36
$n = 6$	Max	0.01	0.10	0.04	0.01	0.07	0.04	0.03	0.09	0.06
	Min	-0.01	-0.08	-0.05	-0.01	-0.09	-0.03	-0.02	-0.14	-0.04

## 2.3 Regression

The second method examined was the regression method in which data mapping from RGB to XYZ was established. Equations (72-74), as shown below, describe the methodology employed to train the model for one color:

$$[XYZ]_{m \times 3} = [f]_{m \times 8} [M]_{8 \times 3} \quad (72)$$

$$[f]_{m \times 8}^T [XYZ]_{m \times 3} = [f]_{m \times 8}^T [f]_{m \times 8} [M]_{8 \times 3} \quad (73)$$

$$[M]_{8 \times 3} = ([f]_{m \times 8}^T [f]_{m \times 8})^{-1} [f]_{m \times 8}^T [XYZ]_{m \times 3} \quad (74)$$

Where  $m$  is the number of the samples in the training set,

$[XYZ]_{m \times 3}$  is the matrix consisting of the CIEXYZ of the colors of interest from all samples,

$[M]_{8 \times 3}$  is the transform matrix for one of the three colors,

$[f]_{m \times 8}$  is the matrix of the vectors developed from the RGB signals, and the vector is in the format of equation (69) when calibration was carried out using the standard test chart.

Equation (70) was applied when calibration was carried out using the camouflage samples, in which the average was subtracted to avoid the ill conditioning of the matrices.

When the calibration was based on the camouflage samples, three  $[M]_{8 \times n}$  were trained for three colors.

During the testing,  $\|Conv_1([XYZ]_{N \times 3}) - Conv_1([f]_{N \times 8}[M]_{8 \times 3})\|_{inf}$  was used to acquire the maximal  $\Delta L^*$ ,  $\Delta a^*$  and  $\Delta b^*$ ;  $\|Conv_1([XYZ]_{N \times 3}) - Conv_1([f]_{N \times 8}[M]_{8 \times 3})\|_2$  was used to acquire the  $\Delta E$  in CIEDE76.

## 2.4 Two Illuminants

Another option to improve the color accuracy of the calibration process is to employ an extra illuminant when capturing the image. When the second illumination is applied to the PCA method, for a given color, equations (66-70) are used for calculations.

Here  $[f]_{m \times 15}$  is the matrix of the vectors developed from the  $RGBR'G'B'$  signals and  $R'G'B'$  is the camera response under the second illumination – U30. Equation (75) shows the calibration via the standard test chart and equation (76) the calibration via the camouflage samples.

$$f = (rgb \quad gb \quad rb \quad rg \quad r \quad g \quad b \quad r'g'b' \quad g'b' \quad r'b' \quad r'g' \quad r' \quad g' \quad b' \quad 1) \quad (75)$$

$$f = \begin{pmatrix} (r - \bar{r})(g - \bar{g})(b - \bar{b}) & (g - \bar{g})(b - \bar{b}) & (r - \bar{r})(b - \bar{b}) \\ (r - \bar{r})(g - \bar{g}) & r - \bar{r} & g - \bar{g} \\ b - \bar{b} & (r' - \bar{r}')(g' - \bar{g}')(b' - \bar{b}') & (g' - \bar{g}')(b' - \bar{b}') \\ (r' - \bar{r}')(b' - \bar{b}') & (r' - \bar{r}')(g' - \bar{g}') & r' - \bar{r}' \\ g' - \bar{g}' & b' - \bar{b}' & 1 \end{pmatrix} \quad (76)$$

Here  $\bar{r}, \bar{g}, \bar{b}, \bar{r}', \bar{g}', \bar{b}'$  are the average values of  $RGBR'G'B'$  for one color for all the samples in the training set.

The testing method is the same as that used for the PCA, as shown in equation (72).

In the Multi-Illuminant-Regression method, the regression is carried out under two illuminations. For one color, equations (72-74) are used for the computations. In this case,  $[f]_{m \times 15}$  is the matrix of the vectors developed from the  $RGBR'G'B'$  signals, which is shown in equation (75) when calibration was done via the standard test chart and equation (76) when calibration was carried out using the samples.

The testing method for multi-illumination-regression was the same to that used in regression.

## 2.5 Calibration based on the Camouflage Samples

A different option to improve the accuracy of the calibration is to use the camouflage samples in the training process. If the calibration is done via the camouflage samples, some camouflage samples are required to construct a training data set.

The criteria for the selection of the training data from the camouflage samples were that the training data had to span the region of all the color samples and they should be distributed evenly. The method is described below. Given  $(r_i, g_i, b_i)$  and a required distance  $\mu$ , the data set was divided into a training set  $T$  and the test set  $R$ .

$$\forall i, j \in T, \|(r_i \ g_i \ b_i) - (r_j \ g_j \ b_j)\|_2 > \mu \quad (77)$$

$$\forall i \in T, \exists j \in R, \|(r_i \ g_i \ b_i) - (r_j \ g_j \ b_j)\|_2 < \mu$$

It was ensured that the training set was as large as possible. The simulation was then run such

that the data with the largest  $\Delta L^*$ ,  $\Delta a^*$  and  $\Delta b^*$  values were selected into  $T$ .

This process was repeated several times until the magnitude of the largest  $\Delta L^*$ ,  $\Delta a^*$  and  $\Delta b^*$  values did not decrease further.

There are 106 camouflage samples. For one illumination, 22 samples were used in the training data set. For two illuminations, 20 samples were used for training.

## 2.6 Data Analysis

Table 33 shows the  $\Delta L^*$ ,  $\Delta a^*$  and  $\Delta b^*$  between the actual CIELAB values and the converted CIELAB values from the camouflage samples when the Verivide Digitizer was used for the camera calibration.

Table 33.  $\Delta L^*$ ,  $\Delta a^*$  and  $\Delta b^*$  of Samples when Calibrated using the Digitizer Chart

		Foliage Green			Urban Gray			Desert Sand		
		$\Delta L^*$	$\Delta a^*$	$\Delta b^*$	$\Delta L^*$	$\Delta a^*$	$\Delta b^*$	$\Delta L^*$	$\Delta a^*$	$\Delta b^*$
Regression	Max	0.19	0.96	0.98	0.09	0.95	0.90	0.07	0.81	0.92
	Min	-0.03	-0.79	-0.84	-0.06	-0.77	-1.04	-0.10	-0.81	-0.91
	Avg	0.11	0.47	-0.06	0.01	0.21	-0.11	-0.02	0.08	-0.03
PCA (6 Eigen)	Max	0.03	0.63	0.94	0.06	0.65	1.11	0.10	0.76	0.87
	Min	-0.19	-1.12	-0.87	-0.09	-1.07	-0.84	-0.07	-0.87	-0.95
	Avg	-0.11	-0.64	0.17	-0.02	-0.33	0.18	0.02	-0.12	0.00
2 Illumination PCA	Max	0.01	0.88	0.55	-0.03	1.09	0.52	-0.12	1.36	0.04
	Min	-0.14	-0.64	-0.69	-0.16	-0.53	-0.94	-0.21	-0.16	-1.65
	Avg	-0.07	-0.12	0.00	-0.10	0.22	-0.21	-0.15	0.51	-0.76
2 Illumination Regression	Max	0.14	0.82	1.15	0.17	0.79	1.48	0.22	0.44	2.18
	Min	0.00	-0.93	-0.47	0.05	-0.95	-0.39	0.13	-1.00	0.07
	Avg	0.07	0.08	0.22	0.11	-0.03	0.52	0.16	-0.21	1.06

Table 34 shows the  $\Delta L^*$ ,  $\Delta a^*$  and  $\Delta b^*$  between the actual values and the converted values from the camouflage samples when the Gretag Colorchecker was used for the camera

calibration.

Table 34.  $\Delta L^*$ ,  $\Delta a^*$  and  $\Delta b^*$  of Samples when Calibrated using the Colorchecker Chart

		Foliage Green			Urban Gray			Desert Sand		
		$\Delta L^*$	$\Delta a^*$	$\Delta b^*$	$\Delta L^*$	$\Delta a^*$	$\Delta b^*$	$\Delta L^*$	$\Delta a^*$	$\Delta b^*$
Regression	Max	0.34	1.97	0.37	0.24	1.86	0.37	0.19	1.51	0.51
	Min	0.13	0.24	-1.40	0.09	0.16	-1.53	0.02	-0.10	-1.31
	Avg	0.26	1.48	-0.65	0.17	1.13	-0.64	0.10	0.78	-0.45
PCA (6 Eigen)	Max	-0.12	-0.20	1.49	-0.09	-0.15	1.63	-0.02	0.11	1.33
	Min	-0.34	-1.94	-0.27	-0.23	-1.85	-0.27	-0.19	-1.51	-0.47
	Avg	-0.26	-1.44	0.74	-0.16	-1.12	0.73	-0.10	-0.77	0.48
2 Illumination PCA	Max	-0.05	0.64	0.50	-0.04	1.05	0.30	0.03	1.89	-0.24
	Min	-0.19	-0.94	-0.87	-0.21	-0.79	-1.44	-0.16	-0.27	-2.60
	Avg	-0.15	-0.43	0.02	-0.13	0.05	-0.53	-0.07	0.73	-1.37
2 Illumination Regression	Max	0.19	1.00	0.95	0.21	0.83	1.51	0.16	0.28	2.56
	Min	0.06	-0.56	-0.53	0.05	-0.98	-0.34	-0.01	-1.82	0.19
	Avg	0.15	0.47	0.04	0.14	0.00	0.55	0.08	-0.69	1.32

From Tables 34 and 35, when the biggest max and smallest min  $\Delta L^*$ ,  $\Delta a^*$  and  $\Delta b^*$  were compared, it can be seen that regression performs better than PCA under one illumination. This might be related with the error in the spectral reconstruction. Also, the calibration based on the Verivide Digitizer is more accurate for samples than the calibration via Gretag Colorchecker. Using two illuminations causes bigger max and smaller min  $\Delta L^*$ ,  $\Delta a^*$  and  $\Delta b^*$  than applying only one illumination. This might be explained by the over-fitting from a more complex polynomial regression.

Table 35 shows the maximal, the minimal and the average of the absolute values of the  $\Delta L^*$ ,  $\Delta a^*$  and  $\Delta b^*$  between the actual values and the converted values from the color patches in the two test charts, which demonstrates that two illuminations can reduce the errors in the data mapping from the device space to the color space for the colors in the training set.

Table 35.  $\Delta L^*$ ,  $\Delta a^*$  and  $\Delta b^*$  of the color patches in the two test charts

		Gretag ColorChecker			Verivide Digitizer		
		$\Delta L^*$	$\Delta a^*$	$\Delta b^*$	$\Delta L^*$	$\Delta a^*$	$\Delta b^*$
Regression	Max	0.84	6.59	5.02	0.93	6.01	3.99
	Min	-1.73	-12.35	-9.23	-1.73	-9.04	-13.91
	Avg	0.34	1.90	1.55	0.22	1.22	1.02
PCA (6 Eigen)	Max	0.83	6.70	4.90	0.93	6.02	3.84
	Min	-1.73	-12.49	-9.44	-1.72	-8.92	-13.02
	Avg	0.33	1.89	1.57	0.22	1.24	1.03
2 Illumination PCA	Max	0.57	2.07	4.96	0.62	2.24	1.73
	Min	-1.17	-8.08	-4.67	-0.57	-3.96	-4.35
	Avg	0.16	0.69	0.71	0.09	0.44	0.52
2 Illumination Regression	Max	0.53	2.26	5.41	0.60	1.44	2.40
	Min	-1.13	-7.90	-4.62	-0.50	-2.88	-3.23
	Avg	0.16	0.68	0.66	0.09	0.40	0.42

Table 36 shows the  $\Delta L^*$ ,  $\Delta a^*$  and  $\Delta b^*$  between the actual values and the converted values from the camouflage samples when the camera calibration is done using the camouflage samples. It can be noted that regression still performs slightly better than PCA. When a second illumination is used, the error is reduced, which is different from the results of the calibration based on the standard test charts. Furthermore, the ranges of  $\Delta L^*$ ,  $\Delta a^*$  and  $\Delta b^*$  in Table 36 are smaller than those in Table 33 and Table 34 for all the 106 camouflage samples. Table 37 presents the max, min and average  $\Delta E$  from various methods for calibrations using the camouflage samples. In the best case – two-illumination-regression, most of  $\Delta E_{00}^*$  can be ignored. The maximum  $\Delta E_{00}^*$  in each method is marked in red.

Thus, regression under two illuminations using a calibration based on the camouflage samples gives the best performance. Since the illuminations in the DigiEye chamber are

based on the fluorescent lamps which have similar spectra, regression under one illumination using the camouflage samples was employed in the experiment to compute the tristimuli values of samples.

Table 36.  $\Delta L^*$ ,  $\Delta a^*$  and  $\Delta b^*$  of Samples for Calibration based on the Camouflage Samples

		Foliage Green			Urban Gray			Desert Sand		
		$\Delta L^*$	$\Delta a^*$	$\Delta b^*$	$\Delta L^*$	$\Delta a^*$	$\Delta b^*$	$\Delta L^*$	$\Delta a^*$	$\Delta b^*$
Regression	Max	0.09	0.40	0.31	0.03	0.45	0.39	0.08	0.52	0.66
	Min	-0.11	-0.30	-0.41	-0.04	-0.40	-0.55	-0.07	-0.64	-0.55
	Avg	0.00	0.00	-0.01	0.00	0.04	-0.02	0.01	0.10	-0.09
PCA (6 Eigen)	Max	0.06	0.41	0.26	0.04	0.49	0.35	0.07	0.44	0.68
	Min	-0.09	-0.42	-0.47	-0.04	-0.38	-0.54	-0.08	-0.65	-0.55
	Avg	-0.01	0.00	-0.05	0.00	0.05	-0.04	0.01	0.08	-0.07
2 Illumination PCA	Max	0.02	0.12	0.19	0.01	0.14	0.10	0.03	0.11	0.09
	Min	-0.01	-0.16	-0.19	-0.01	-0.24	-0.07	-0.15	-0.15	-0.15
	Avg	0.00	0.00	0.00	0.00	0.00	0.00	0.00	-0.02	0.01
2 Illumination Regression	Max	0.00	0.06	0.09	0.01	0.07	0.09	0.01	0.07	0.09
	Min	0.00	-0.05	-0.09	-0.01	-0.08	-0.06	-0.01	-0.08	-0.05
	Avg	0.00	0.00	0.01	0.00	0.00	0.01	0.00	-0.01	0.01

Table 37  $\Delta E_{00}^*$  from Various Methods for Calibrations using the Camouflage Samples

	Foliage Green			Urban Gray			Desert Sand		
	Max	Min	Avg	Max	Min	Avg	Max	Min	Avg
Regression	0.59	0.02	0.18	0.75	0.02	0.22	1.02	0.03	0.38
PCA (6 Eigen)	0.61	0.03	0.18	0.78	0.01	0.24	1.04	0.02	0.38
2 Illumination PCA	0.23	0.00	0.06	0.34	0.00	0.08	0.21	0.00	0.06
2 Illumination Regression	0.10	0.00	0.03	0.12	0.00	0.04	0.12	0.00	0.03

## 2.7 Calibration Tool Using Camouflage Samples

Based on the results discussed in the previous section, the regression method using one illumination was used to set up the data mapping from the device space to the color space, with one data mapping for each of the colors in the sample. 22 samples were chosen for the training with the method discussed above for sample selection. A rectangular patch of 43×48 mm was cut off from the training samples. In each patch, the three colors occupy approximately the same proportion of the overall area. These patches were spliced together to generate a calibration tool, which is shown in Figure 74.

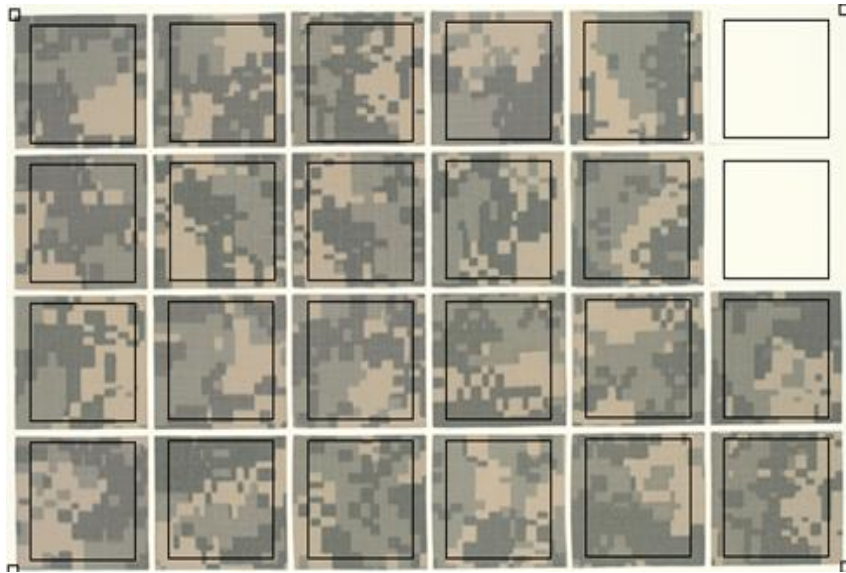


Figure 74. Image of the Calibration Tool based on the Camouflage Samples

The position, index, tristimulus values for each color were recorded into the XML data file.

After the image of the calibration tool was captured, the data mappings were set up from the RGB values to the tristimulus values.

Likewise, the thresholds in the CIELAB color space between the ‘pass’ and the ‘fail’ samples were also stored in the XML data file. If any of the converted tristimulus values was not within the thresholds, the sample failed.

Table D in Appendix shows the color conversion for the samples used in the calibration tool.

$L^*_1, a^*_1, b^*_1$  are the original CIELAB values;  $L^*_2, a^*_2, b^*_2$  are the converted CIELAB values.

Figure 75 shows the distribution of the absolute  $\Delta L^*$ ,  $\Delta a^*$  and  $\Delta b^*$  in Appendix Table D.

Only one third of the absolute values are lower than 0.1. When these CIELAB values are used for the pass / fail judgment, most of the 22 samples are failed, which is not satisfactory.

However, this result is better than that based on the ICC profiles, as shown in Table 30.

The  $\Delta L^*$ ,  $\Delta a^*$  and  $\Delta b^*$  in Appendix Table D are larger than those in the simulation. One possible explanation might be related to the polynomial regression that is applied.

Polynomial regression is sensitive to the input. The selection of the training samples was based on the simulation results. The device values used in the simulation were computed from the spectra of the sample colors, which were not identical to the actual output from the camera.

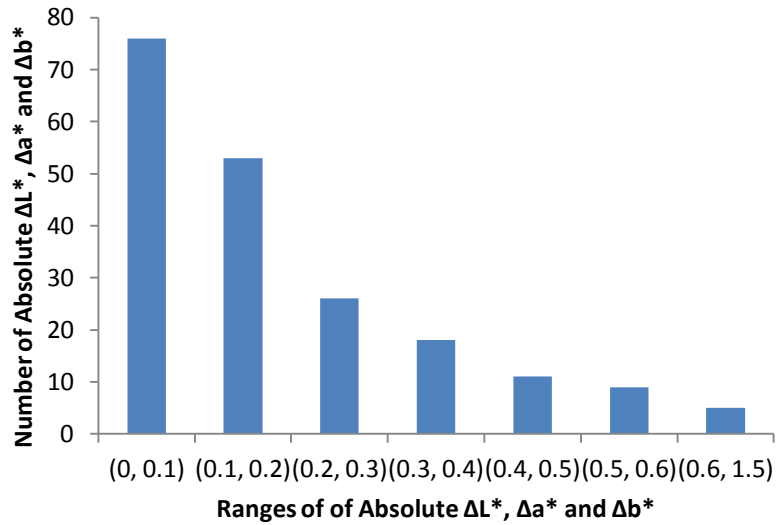


Figure 75. Distribution of Absolute  $\Delta L^*$ ,  $\Delta a^*$  and  $\Delta b^*$  for the Calibration Tool

Similarly, the effect of the camera output variation was also evaluated. Noise error  $\delta$  was added to the camera output of the standard sample.  $\delta$  can be one of (-1, 0, 1). The RGB values with noise signal were then converted into the CIELAB values, as shown in Table 38. When compared with the CIELAB values when there is no noise, the difference is roughly in the range of (-0.7, 0.7). When the range in Table 38 is compared with that in Table 31, it can be noted that regression based the camouflage samples was relatively more stable than the conversion based on the ICC profile.

Thus, tristimulus values might not be suitable for determination of pass / fail ratings. Some other techniques should therefore be examined.

### **3. Pass/Fail Judgments**

In the previous section, based on the calibration of digital camera and surroundings issues, it was concluded that arriving at repeatable pass/fail judgments in the color space is a major challenge. Thus, another method was examined to determine whether the device space can be used to obtain such judgments.

#### **3.1 Pass/Fail Judgments in the Device Space**

In Figure 35 of Chapter III, it was shown that three convex hulls can be formed based on the ‘pass’ samples in the CIEXYZ space, to completely separate the ‘pass’ samples from the ‘fail’ samples. As both CIEXYZ and RGB values are developed from the integration of the color spectra, such convex hulls may be generated in the device space. Figure 76 shows three convex hulls developed from the simulated RGB values of the sample colors, in which the ‘pass’ samples are separated from the ‘fail’ samples completely. The simulation of the RGB values of the sample colors is shown in equations (61-63).

Table 38. Converted CIELAB of the Standard Sample with Noise

Noise $\delta$	Foliage Green			Urban Gray			Desert Sand		
	L*	a*	b*	L*	a*	b*	L*	a*	b*
(1,1,1)	44.49	-1.99	3.30	53.66	-1.11	6.02	65.92	1.82	11.13
(1,0,1)	44.73	-1.81	3.23	53.74	-0.96	5.80	66.03	1.88	10.94
(1,-1,1)	44.96	-1.63	3.16	53.83	-0.82	5.58	66.15	1.95	10.76
(1,1,0)	44.33	-2.34	3.52	53.52	-1.41	6.08	65.86	1.59	11.26
(1,0,0)	44.62	-2.14	3.43	53.63	-1.26	5.87	65.98	1.67	11.08
(1,-1,0)	44.90	-1.94	3.35	53.73	-1.11	5.66	66.09	1.75	10.89
(1,1,-1)	44.18	-2.69	3.74	53.39	-1.72	6.14	65.80	1.37	11.40
(1,0,-1)	44.51	-2.47	3.64	53.51	-1.57	5.93	65.92	1.46	11.21
(1,-1,-1)	44.84	-2.26	3.55	53.64	-1.42	5.73	66.04	1.55	11.02
(0,1,1)	44.63	-1.78	3.15	53.79	-0.88	6.16	65.87	2.02	11.10
(0,0,1)	44.81	-1.60	3.08	53.85	-0.73	5.93	65.98	2.08	10.93
(0,-1,1)	44.98	-1.42	3.01	53.90	-0.58	5.70	66.09	2.13	10.76
(0,1,0)	44.46	-2.12	3.37	53.66	-1.19	6.23	65.81	1.80	11.22
(0,0,0)	44.69	-1.93	3.29	53.74	-1.04	6.00	65.92	1.86	11.05
(0,-1,0)	44.91	-1.74	3.21	53.82	-0.89	5.78	66.03	1.93	10.87
(0,1,-1)	44.30	-2.47	3.59	53.53	-1.50	6.29	65.75	1.57	11.34
(0,0,-1)	44.57	-2.27	3.50	53.63	-1.35	6.07	65.87	1.65	11.16
(0,-1,-1)	44.84	-2.06	3.41	53.73	-1.19	5.85	65.98	1.73	10.99
(-1,1,1)	44.77	-1.56	3.00	53.92	-0.66	6.31	65.82	2.23	11.07
(-1,0,1)	44.88	-1.39	2.93	53.95	-0.51	6.06	65.92	2.27	10.91
(-1,-1,1)	45.00	-1.22	2.86	53.98	-0.35	5.82	66.02	2.32	10.75
(-1,1,0)	44.59	-1.91	3.22	53.80	-0.97	6.38	65.76	2.00	11.18
(-1,0,0)	44.76	-1.73	3.15	53.85	-0.82	6.14	65.87	2.06	11.01
(-1,-1,0)	44.92	-1.55	3.07	53.90	-0.66	5.90	65.97	2.12	10.86
(-1,1,-1)	44.42	-2.26	3.45	53.68	-1.29	6.45	65.70	1.77	11.28
(-1,0,-1)	44.63	-2.06	3.36	53.75	-1.13	6.21	65.81	1.84	11.12
(-1,-1,-1)	44.84	-1.87	3.27	53.82	-0.97	5.98	65.92	1.91	10.96
max	45.00	-1.22	3.74	53.98	-0.35	6.45	66.15	2.32	11.40
min	44.18	-2.69	2.86	53.39	-1.72	5.58	65.70	1.37	10.75
range	0.31	0.71	0.45	0.24	0.69	0.44	0.23	0.46	0.35
	-0.51	-0.75	-0.43	-0.35	-0.68	-0.42	-0.22	-0.50	-0.30

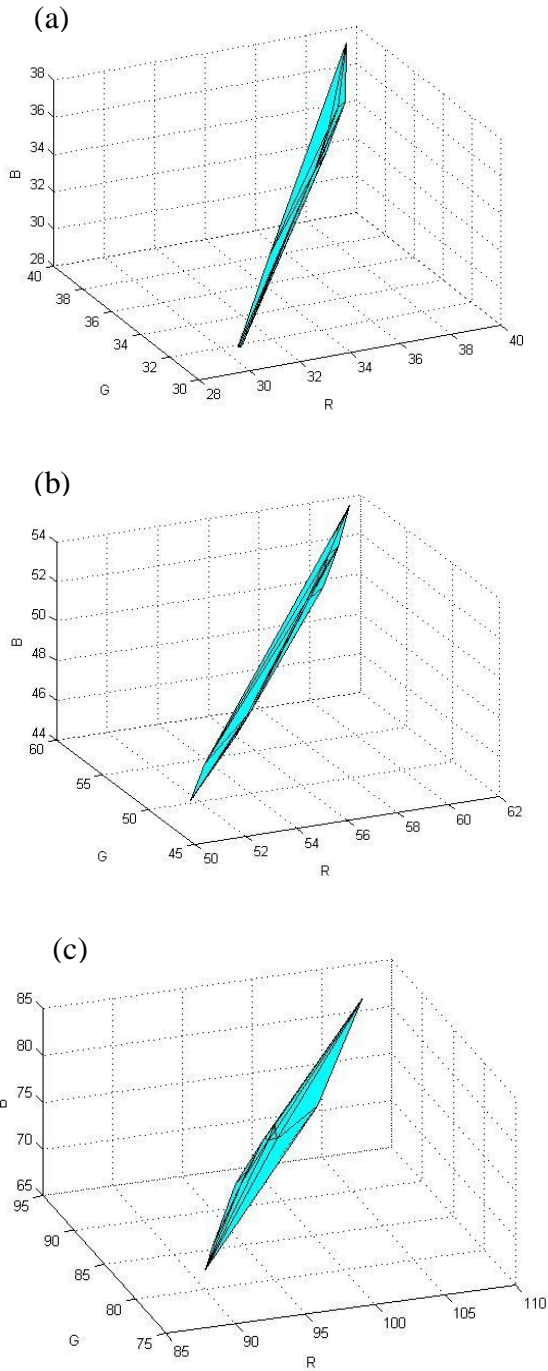


Figure 76. Convex Hulls from the Simulated RGB Values of the 'Pass' Samples Foliage Green (a), Urban Gray (b), Desert Sand (c)

In the development of this camouflage based calibration tool, 24 samples are used, which were chosen from 41 ‘pass’ samples and the standard sample. As the simulated RGB values from equations (61-63) are not actual RGB values and since the actual RGB values depend on the device and camera settings, the selection was done based on the CIEXYZ color space. The selection algorithm is described below:

1. All the ‘pass’ samples and the standard sample are placed in an array. Thus in this case 41 ‘pass’ samples and one standard sample were present in the array;
2. Using 42 samples in the array, 3 convex hulls based on three colors are generated for three colors separately. When all three colors of a given sample are completely within the three convex hulls, the sample is removed. 10 samples are removed and only 32 samples remained;
3. All the samples are enumerated and the following product is computed:

$$\|XYZ_{i,1} - XYZ_{j,1}\|_2 \times \|XYZ_{i,2} - XYZ_{j,2}\|_2 \times \|XYZ_{i,3} - XYZ_{j,3}\|_2$$

Here  $i, j$  are indices of the samples in the array, between 1 and 32;

$XYZ_{i,1}$ ,  $XYZ_{i,2}$  and  $XYZ_{i,3}$  are the CIEXYZ for Desert Sand, Urban Gray and Foliage Green of the  $i$ th sample in the array respectively;

4. When all these possible pairs were computed, the results were put together and the smallest 16 values as well as the associated 16 pairs of indices were determined;
5. From the two indices related with the smallest value, one index which appears more in the associated 16 pairs of indices in step 4 is removed;

6. Steps 3, 4, 5 are repeated until there are only 24 indices left and those are the samples for the creation of the calibration tool.

Figure 77 shows an image of the calibration tool, similar to the calibration tool shown in Figure 74. A rectangular patch with a size of 43×48 mm was cut off from appropriate samples. In each patch, the three colors occupied approximately a similar portion of patch area. All patches were spliced together to generate the calibration tool based on the device space.

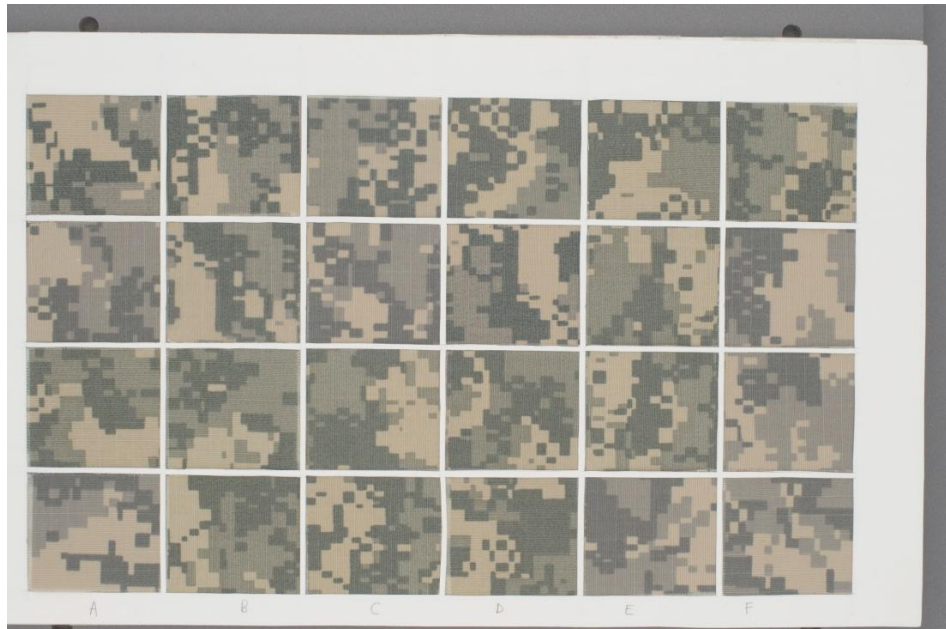


Figure 77. Image of the Calibration Tool used for P/F Ratings based on the Device Space

After capturing the image of the calibration tool, image segmentation algorithms were applied on the sample patches. From each patch, the average RGB values for Desert Sand, Urban Gray and Foliage Green were acquired. The RGB values of each color were put

together as 24 points in the device space to develop a convex hull. The formation of the convex hull is described below:

1. Enumerate all the points and determine four points which are not in a plane. Use these four points to develop a tetrahedron, which is also a convex hull. Put all its four triangle surfaces into an array  $N$  for future computation;
2. Compute the gravity center  $g$  of the convex hull via  $\frac{1}{n} \sum R_i G_i B_i$ . Here  $n$  is the number of the convex hull vertices,  $R_i G_i B_i$  are the coordinates of the  $i$ th vertex;
3. Compute the normal vector  $\vec{n}_i$  of each triangle surface  $tr_i$  of the convex hull and ensure the normal vector  $\vec{n}_i$  points to the inside of the convex, using the condition  $\vec{n}_i \cdot \overrightarrow{tr_i(0)g} > 0$ . If the condition is not met, change the direction of  $\vec{n}_i$ . Here  $tr_i(0)$ ,  $tr_i(1)$ ,  $tr_i(2)$  are three corners of the triangle  $tr_i$ ;
4. Given a new point  $p_j$ , determine if  $p_j$  is within the convex hull. If  $p_j$  is outside of the convex hull, there will be a new convex hull with one vertex being  $p_j$ . Some of the original triangle surfaces might be within this new convex hull and thus should be removed. One method to achieve this is to enumerate all the triangle surfaces in  $N$ . For each triangle surface  $tr_i$ , if  $\vec{n}_i \cdot \overrightarrow{tr_i(0)p_j} < 0$ ,  $tr_i$  should be removed from  $N$ . If no  $tr_i$  is removed from  $N$ ,  $p_j$  is within the convex hull. If  $p_j$  is outside the convex hull, enumerate all the  $tr_i$  in  $N$ . For each  $tr_i$ , construct three new triangle surfaces  $\Delta p_j tr_i(0) tr_i(1)$ ,  $\Delta p_j tr_i(0) tr_i(2)$ ,  $\Delta p_j tr_i(1) tr_i(2)$ . Then compare three new constructed triangles with the triangle surfaces in  $N$ . If one of the three surfaces does not exist in  $N$ , push it into  $N$ ; otherwise, remove the

associated existing item from  $N$ .

5. Repeat from step 2 until all the points are used.

Now a convex hull is developed and all its triangle surfaces are in the array of  $N$ .

Given a point  $p$ , the method below is used to check whether  $p$  is within the convex hull.

Enumerate all the triangle surfaces in  $N$ . For each triangle surface  $tr_i$ , if  $\vec{n}_i \cdot \overrightarrow{tr_i(0)p} < 0$ ,

check if  $\|\overrightarrow{tr_i(0)p}\|_2 < \frac{\sqrt{3}}{2}$ ,  $\|\overrightarrow{tr_i(1)p}\|_2 < \frac{\sqrt{3}}{2}$  or  $\|\overrightarrow{tr_i(2)p}\|_2 < \frac{\sqrt{3}}{2}$ , and then check whether the

distance from  $p$  to  $tr_i$  or the distance from  $p$  to one of the three borders of  $tr_i$  is smaller than

$\frac{\sqrt{3}}{2}$ . If one of the expressions above is true, move to the next  $tr_i$  in  $N$ . Otherwise, stop the

enumeration since the point  $p$  is outside of the convex hull. Here the computation of the

distance between  $p$  and any corner, border of  $tr_i$  and even  $tr_i$  surface itself is used to add a

tolerance of  $\frac{\sqrt{3}}{2}$  in the device space. The tolerance is similar to a layer outside of the convex

hull.  $\frac{\sqrt{3}}{2}$  is an empirical value determined based on Table 43 in Chapter VIII.

### 3.2 Data Analysis and Discussion

The calibration tool shown in Figure 74, was used to check the accuracy of judgments. For

the purpose of accuracy, the output from the raw image was used for computations. Table 39

shows the results, where RGB values of three colors from each sample are shown. The

column ‘Soft Result’ shows the P/F rating based on the software; the column ‘Within Layer’

shows whether at least one of the three colors of a sample is within the  $\frac{\sqrt{3}}{2}$  layer of the convex

hulls when this sample is judged ‘pass’ by the software; the column ‘Natick Result’ is the visual rating based on the Natick Soldier Center assessor. It can be seen that most of the samples that are rated ‘pass’ by the software contain at least one color within the  $\frac{\sqrt{3}}{2}$  layer. In other words, these samples are very close to the three convex hulls in the device space.

Table 39. Results of the Pass / Fail Judgments in the Device Space

Index	Foliage Green			Urban Grey			Desert Sand			Soft Result	Within Layer	Natick Result
	R	G	B	R	G	B	R	G	B			
R1C1	11	18	16	14	22	20	20	28	24	pass	yes	fail
R2C1	11	18	16	14	22	20	19	28	24	pass	yes	fail
R3C1	11	18	16	14	22	20	20	28	25	fail	---	fail
R4C1	11	18	16	15	22	20	20	28	25	pass	yes	pass
R1C2	11	18	16	15	22	20	19	27	24	pass	yes	fail
R2C2	10	17	15	14	22	19	19	28	24	pass	yes	pass
R3C2	11	18	16	14	22	20	19	28	24	pass	yes	fail
R4C2	10	17	15	14	22	20	20	28	24	fail	---	pass
R1C3	10	17	15	14	22	19	19	27	24	pass	yes	fail
R2C3	10	17	15	14	22	19	19	27	24	fail	---	fail
R3C3	11	18	16	14	22	20	19	27	24	pass	yes	fail
R4C3	10	17	15	14	21	19	19	27	24	fail	---	fail
R1C4	11	18	17	15	22	20	20	28	25	pass	yes	pass
R2C4	10	17	15	14	21	19	19	28	24	fail	---	fail
R3C4	11	17	16	14	22	19	19	27	24	pass	yes	pass
R4C4	11	18	17	15	23	20	20	29	25	fail	---	fail
R1C5	11	18	17	15	23	20	21	29	25	fail	---	fail
R2C5	11	18	16	14	22	19	19	28	24	fail	---	fail
R3C5	11	18	16	14	22	19	19	28	24	fail	---	pass
R4C5	11	18	16	14	22	19	20	28	24	fail	---	pass
R3C6	10	17	15	13	21	19	19	27	23	fail	---	fail
R4C6	11	18	16	14	21	19	19	27	24	pass	yes	pass

One method to enlarge the differences among the samples is to change the camera parameters so that more light can enter the CCD. In the above experiment, the shutter speed was set at 1/3 sec and the aperture used was F13. The shutter speed was changed to 1/2 sec and the aperture was set to F9. The calibration tool in Figure 77 was used in both conditions. When the new condition was applied, the volumes of the convex hulls became larger, as shown in Table 40, which means that the differences among the samples become larger as well. On the other hand, with the change of the camera parameters and more lights entering the CCD, the variation among the average RGB in the different regions is also enlarged. Figure 78 shows the snapshot of a camouflage sample where 24 regions were compared. Among these regions, 10 regions containing areas where the proportions of three colors were approximately equal were chosen. In each region, the segmentation algorithm was applied to compute the average RGB values of the three colors. Then the mean and variation of these average RGB values were computed and listed in Table 41. It can be seen that with the application of the new camera parameters, the mean values as well as the variations become larger. So, when the calibration tool in Figure 74 was used to check the performance of the new camera parameters, all sample patches were judged as ‘fail’. In other words, when these camera parameters are used, the area of the sample should be bigger to reduce the variations in the different regions of the sample.

Table 40. Comparison of the Convex Hull Volume

Camera Setting	Foliage Green	Urban Grey	Desert Sand
1/3 – F13	55.91	58.29	41.71
1/2 – F9	158.44	161.68	197.15



Figure 78. Snapshot of the Sample used in the Computation of Variation

Table 41. Comparison of the Average and Standard Deviation

Camera Setting		Foliage Green			Urban Grey			Desert Sand		
		R	G	B	R	G	B	R	G	B
1/3 – F13	Mean	94	155	137	123	193	170	172	247	212
	Var	20.92	27.22	20.42	9.04	15.74	16.36	5.41	8.41	9.95
1/2 – F9	Mean	201	305	277	253	371	332	332	461	404
	Var	39.64	71.51	63.03	22.94	41.27	39.82	11.88	20.73	28.40

In order to reduce sample variability due to creases and shadows, all universal camouflage samples were ironed and held tightly and smoothly inside the DigiEye illumination chamber for image capturing. In each image the selected region comprised the majority of the image to increase sample size, similar to that shown in Figure 78. After the images of all the

samples were captured, the segmentation algorithm was applied on all sample images and the average RGB values of each color were computed, which are listed in Appendix Table E. It was determined that three convex hulls could be constructed based on the average RGB values of the three colors from all the ‘pass’ samples. For each ‘fail’ sample, at least one of its three average RGB values was outside of the associated convex hull.

In order to improve the stability of the system, the convex hulls were expanded according to the method shown below:

1. Compute the center of each convex hull by  $x_{center} = avg(x_i)$ ,  $y_{center} = avg(y_i)$ ,  $z_{center} = avg(z_i)$ . Here  $x_i, y_i, z_i$  are the coordinates of the vertices of the convex hull;
2. Given an expanded ratio  $\alpha$ ,  $x_i' = (x_i - x_{center})\alpha + x_{center}$ ,  $y_i' = (y_i - y_{center})\alpha + y_{center}$ ,  $z_i' = (z_i - z_{center})\alpha + z_{center}$ ,  $\alpha$  is between 1 and 2;

It is clear that after expansion, the center of the convex hull does not change. When  $\alpha$  changes from 1 to 2, with the expansion of the convex hull, more and more ‘fail’ samples will be recognized as ‘pass’, Table 42 shows the relation between  $\alpha$  and the number of the mistakenly judged ‘fail’ samples. Based on the results the value  $\alpha$  was set at 1.5.

Table 42. Relation between  $\alpha$  and Number of the Mistakenly Judged ‘Fail’ Samples

$\alpha$	1.1	1.2	1.3	1.4	1.5	1.6	1.7	1.8	1.9	2
Number of Mistakes	1	4	4	5	8	10	11	14	18	19

Figure 79 shows the convex hull of Urban Gray before and after expansion when  $\alpha$  is 1.5. It can be noted that the volume of the convex hull becomes larger but the shape is still slim. Thus, the variation of the average RGB values might affect the judgment.

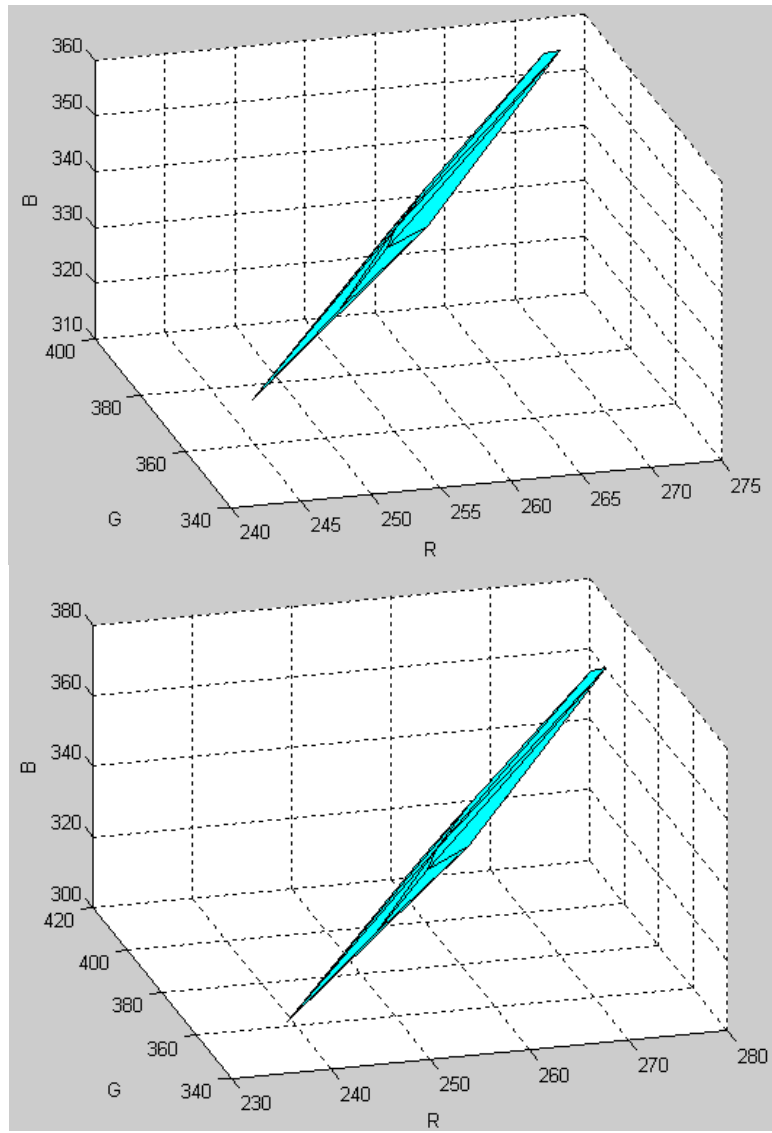


Figure 79. Convex Hull of Urban Gray before (Top) and after (Bottom) Expansion

Furthermore, these convex hulls are based on the average RGB values of all the samples. In order to construct these convex hulls, at least the images of all the 'pass' samples should be taken, which would be lengthy and the results might be affected by the temporal variation of

the system. Therefore other methods for the construction of the convex hulls should be considered.

### **3.3 Comparison of Judgments**

Based on the visual assessment from Natick Soldier Center and the discussions in Chapter III and this Chapter, several methods can be used to separate the ‘pass’ samples from the ‘fail’ samples.

If the tristimulus values from the spectrophotometers are used to separate the ‘pass’ from the ‘fail’, all but one ‘fail’ samples can be distinguished from the ‘pass’ with the max and min CIELAB and CIELCH values from the ‘pass’ samples, with a correct ratio of 99%. When the convex hulls in the CIEXYZ and CIELAB spaces are used, all ‘fail’ samples can be separate from the ‘pass’ samples.

The raw values from the digital camera can be converted into the tristimulus values and these tristimulus values can also be used in the judgment based on the borders from Chapter III. Unfortunately, all the ‘pass’ samples and all the ‘fail’ samples were failed because of the errors in the conversion from the raw values to the color values.

When the raw values from all the ‘pass’ samples are used to construct three convex hulls and these convex hulls can also be used to separate all the ‘pass’ samples from all the ‘fail’ samples. If the convex hulls are expanded to avoid the variation in the raw values, the correct ratio for all the samples is 92.2%.

Thus, currently, the camera based method to separate the ‘pass’ samples from the ‘fail’

samples is through the convex hulls from the raw values of all the ‘pass’ samples.

## 4. Conclusion

- Camera Calibration via the ICC profile fails to provide sufficient accuracy in the sample ratings;
- An extra illumination will decrease the maximal absolute tristimulus values of the samples for calibration using the camouflage samples; but it will increase the maximal absolute tristimulus values of samples when the calibration is carried out using a standard test chart;
- Regression method gives a better performance than the PCA method;
- In all the simulations, the highest accuracy is from the regression method under two illuminations using the camouflage samples;
- For this study, estimated tristimulus values might not be suitable for the determination of pass / fail ratings;
- It is possible to determine P/F ratings based on the DigiEye and Nikon D90 system in the device space, but this judgment might be affected by the variation of the system as the distribution of all colors are in a slim region in the device space;
- As the current method is based on the images of all the camouflage samples, a new method for the construction of the convex hulls should be considered.

## **Chapter VII. Software Design**

### **1. Introduction**

One of the objectives of this study was to develop and implement stand-alone user-friendly software for the assessment of Universal Camouflage Pattern fabric in conjunction with industrial verification and validation of the product. Accordingly a software, denoted as IMACS, “Imaging Methodology for Assessment of Camouflage Substrates”, was developed. The software was developed in the Microsoft Visual Studio 2005 environment, and was drafted in Visual C# and Visual C++.

Visual C# is an object oriented language, simple and efficient. In C#, the software engineering principles such as strong type checking, array bounds checking, detection of attempts to use uninitialized variables, and automatic garbage collection, are well supported. The language is intended for use in developing software components suitable for deployment in distributed environments and only executed under the "management" of a Common Language Runtime Virtual Machine. Thus Visual C# is a good tool in the User-Interface development [101]. Figure 80 shows how C# code is compiled and executed. Unlike traditional programming languages, the compilation of the C# code generates the managed assembly, which contains the intermediate language (IL) code and the related resources as well as a manifest which stores the assembly's type, version, culture and security requirement. When C# code is to be executed, the managed assembly is loaded into the Common Language Runtime (CLR) under the .Net Framework. The loading is based on the

manifest. If the security requirements are met, the CLR performs the Just-In-Time (JIT) compilation on the IL code and generates the native machine instructions for execution [102].

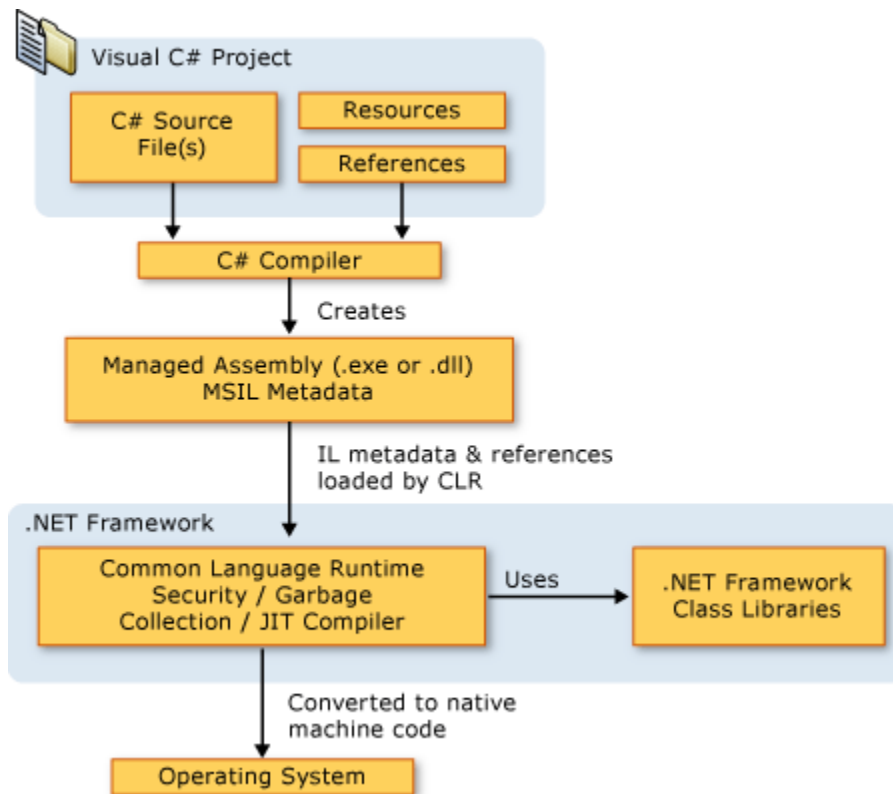


Figure 80. C# and .Net Framework [102]

C++ is also an object-oriented programming language, which was invented by Bjarne Stroustrup in 1979 at Bell Labs. Based on the C language, C++ is equipped with the features such as operators, templates, objects and polymorphism. There are two major parts in C++, the core language and the C++ standard library. C++ can be used in different operating systems, such as Windows and Linux. Currently, C++ is one of the most popular programming tools in the world and has various applications, such as the application

software, system software and device drivers [103].

Visual C++ in Visual Studio 2005 includes MFC 8.0 and .Net 2.0 and can also be executed as the management code. In this project, Visual C++ was used to implement the algorithm. In order to improve the implementation efficiency of the software, no management code was used in this project [104]. Thus, the compilation of the C++ code generated the executable binary file instead of the IL code for the compilation of the CLR.

For the data management of various data, such as the user preference, the tristimulus values of the standard test chart, the device values, tristimulus values and other information of the camouflage samples. A relational database such as Microsoft Access, or the Extensible Markable Language (XML) file may be used.

In this software, two standard test charts are used, each containing 240 color patches. Tens of input and output profiles, hundreds of samples and a set of customer preference settings may be needed in this study. A relational database can be a good option. But if a relational database is used, a thread should be initiated in the operating system, which occupies extra system resources. Since a limited amount of data is expected to be managed, XML was considered sufficient for the purpose of this project. Another consideration for the use XML is that all the data management is in the C# code. The C# code has good support for the processing of XML files when using the “System.Xml” namespace.

## 2. User Interface

The design of the User Interface (UI) was according to the Microsoft Windows user interface style. The menu items are on the top left, and the status bar is on the bottom, as shown in Figure 81. The main UI can be used to show any images captured from Nikon D90 or from an image file, and these images can be zoomed in or out and scrolled to a section of interest. The operators can even choose a region from the image and view information of the region, such as the average tristimulus values.



Figure 81. Snapshot of the Main UI

There are four pixel selection tools in this software, circle, rectangle, user drawn rectangle and point. The size of the circle and rectangle pixel selection tools are fixed values and preset by the user.

When the pixel selection is completed, the software automatically computes the average RGB values in the selected area, and converts the average RGB values to the CIELAB via the device link. Then the position of the selection, the average RGB values and the CIELAB are displayed in the status bar.

Currently, the Nikon D90 is the only camera supported in this software. Figure 82 shows the UI that is used to set the required parameters before capturing an image with Nikon D90. In the dialog the operator can set all the required parameters such as the exposure mode, the shutter speed, white balance, etc. When all the parameters are set, the operator can click “Apply” button to save all the settings for future use. If the operator does not click “Apply” but clicks “Restore”, the originally saved parameters are retrieved and applied. When setting the parameter is completed, the operator can click “Release” to capture the image, at which point the image is synchronized with the computer via the USB cable connection.

Calibration is an important component of this software, and currently four calibrations are used, namely: camera, monitor, camouflage and uniformity of camera. The calibration of the uniformity of camera via the uniformity board is discussed in Chapter V. The calibration of monitor is described in Chapter VI. The calibration of the camera is mentioned in Chapter VII and the calibration of the camouflage is discussed in this chapter.

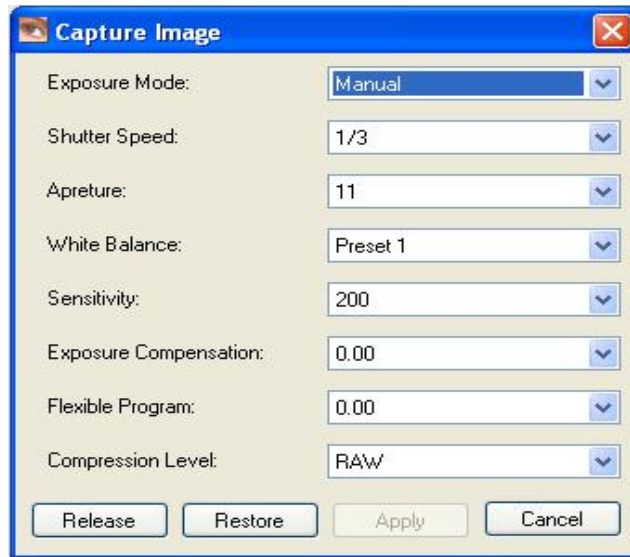


Figure 82. Snapshot of the Camera Setup UI

Figure 83 is a snapshot of the UI used to calibrate the digital camera when the test chart is used. After the image of the test chart is captured, the user is prompted to select four corners in the test chart with the left mouse button and the software can automatically determine the position and size of all the color patches inside the test chart and initiate the computation. The user can remove the selection with the right mouse button. A progress bar can show the progress of the computation, the duration of which depends on the type of computer and processor used.

Figure 84 shows the dialog for the setting options, where the customer can set the preferred input and output profiles, image storage directory, and other useful information. All information is saved in an XML file.

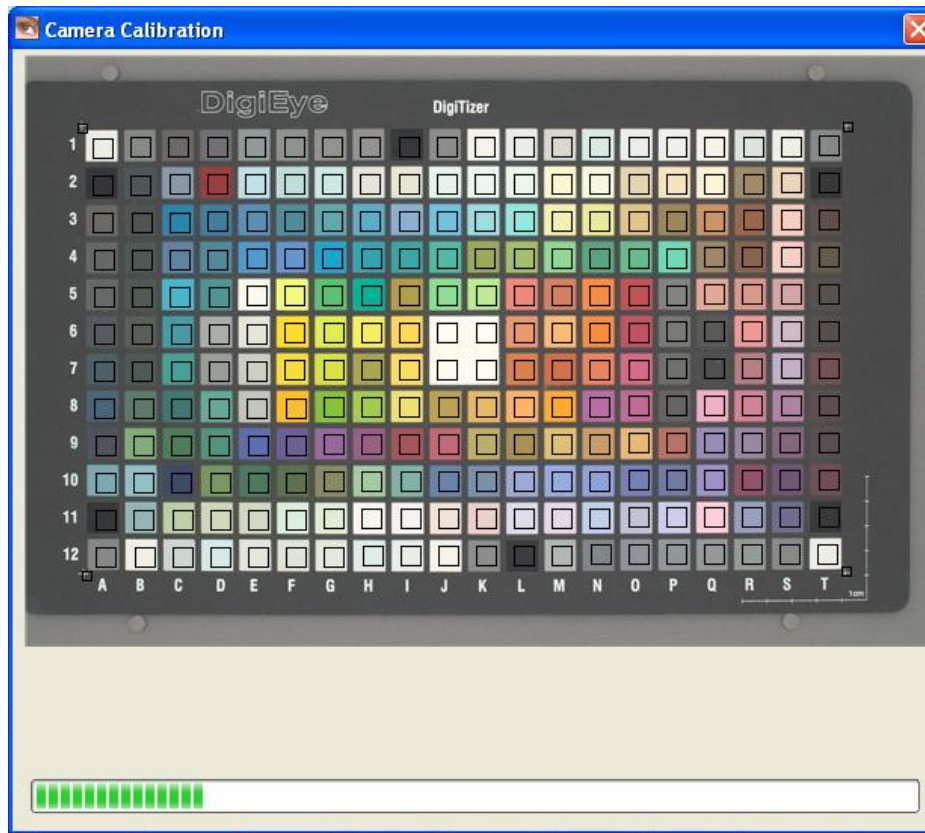


Figure 83. Snapshot of the Camera Calibration UI

Figure 85 shows a snapshot of the UI to capture the image of the sample. The user can select the region of interest with the mouse. The software then divides the selected region into three segmentations based on the color. The average RGB values of each segmentation are computed and then converted to the CIELAB values. In this dialog, the user can enter the basic information of the batch sample such as the producer, batch number and roll number. The software can automatically determine a pass or fail rating to the sample based on the color values.

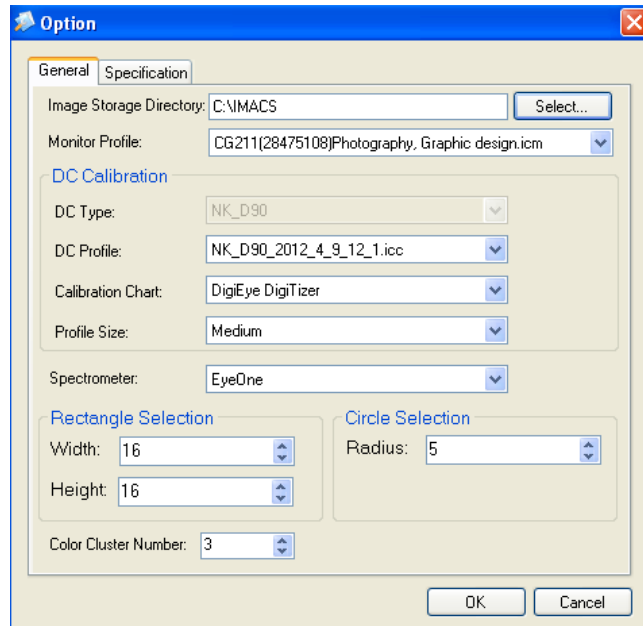


Figure 84. Snapshot of the UI to Setup the Options

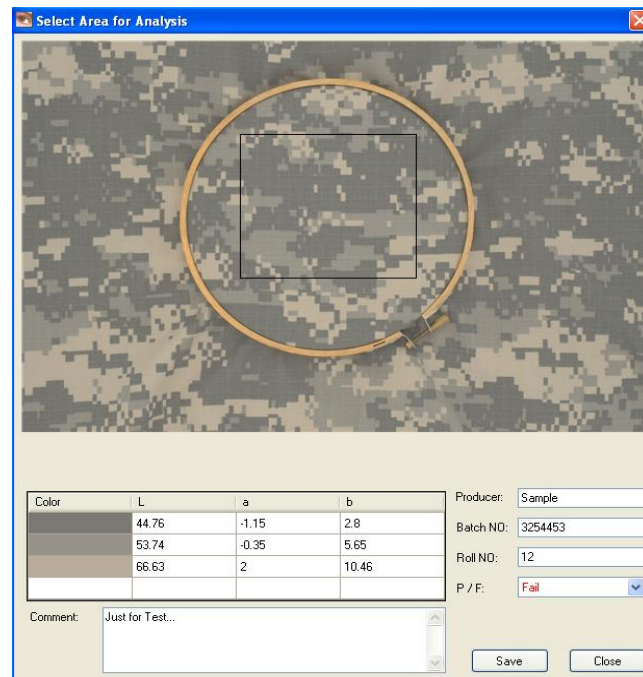


Figure 85. Snapshot of the Sample Capturing UI

## **3. Introduction of the Modules**

### **3.1 Control of Gretag Eye One**

Gretag Eye One is supported in this software for the calibration of the display. Before using this device, its driver must be installed. There are two files in the driver – i1.sys and i1.inf. The communication with the Eye One through the device driver is via a dynamic library – EyeOne.dll. Gretag provides the Software Development Kits (SDK) to call the functions inside EyeOne.dll.

In the visual studio, two “.h” files and a static library should be included, i.e., EyeOne.h, MeasurementConditions.h and EyeOne.lib, which contain the parameter and function definitions necessary for the usage of the dynamic library and the linkage with EyeOne.dll.

In the beginning, I1\_IsConnected() is applied to determine whether Eye One is connected to the computer. If it is connected, I1\_IsConnected() will return 0; otherwise it will return the error code.

In the calibration of Eye One, I1\_SetOption is used to set the measurement mode to the single emission and the illumination mode to the emission and then I1\_Calibrate() is called to carry out the calibration. If the calibration is successful, it will return 0.

In the emission measurement, I1\_SetOption is used to set the measurement mode to the single emission and the color space to the CIEXYZ. After setting the mode, I1\_TriggerMeasurement() is called to start the measurement. When the measurement is finished, I1\_GetTristimulus is employed to read back the tristimulus values [105].

## 3.2 Control of the Nikon D90

Figure 86 shows the flowchart to link and control the camera with a computer. The USB connection is checked first, and if the connection is established, the USB driver is initiated and the communication between the camera and the PC is set up. The camera information is then sent back to the computer. Two protocols are used in this process – Picture Transfer Protocol (PTP) and Media Transfer Protocol (MTP), which depend on the USB setup used in the camera. The PTP mode is the default mode used in this software [106].

When the USB connection is set up, two PC modes can be used for the control of the camera – PC camera mode and PC host mode. The PC camera mode is the default PC mode. Under this mode, the operation of the camera is manual and the PC can only access the camera status. Under the PC host mode, the operation of the camera is fully controlled with the PC and is disabled on the camera. In this study, the PC host mode was used [106].

Nikon provides SDK for the control of the digital camera. In the SDK, MAID module from Nikon is used in the communication between the software application and the device driver, as shown in Figure 87. In the MAID module, the device communication is abstracted into several layers, as shown in Figure 88 [107].

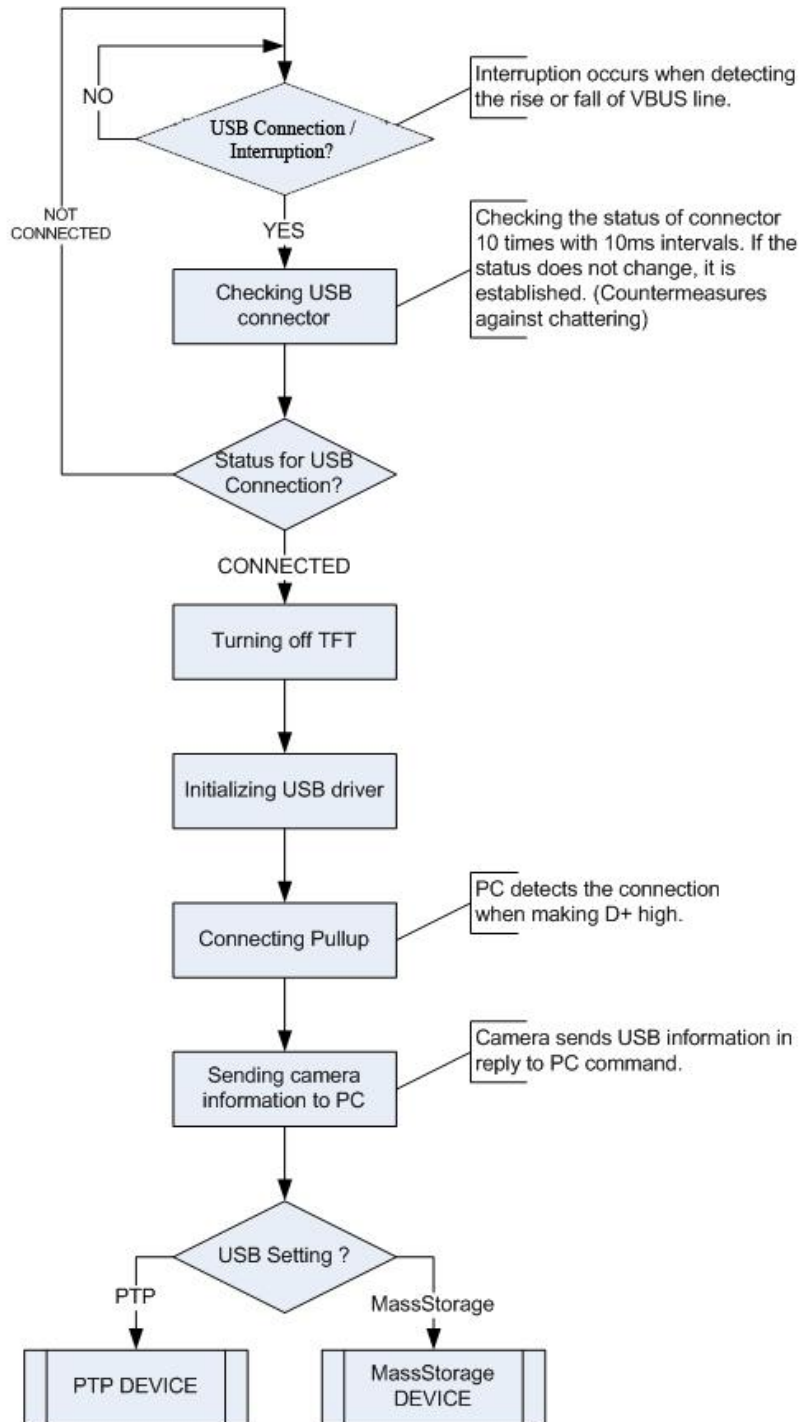


Figure 86. Flowchart of the Process on Nikon D90 [106]

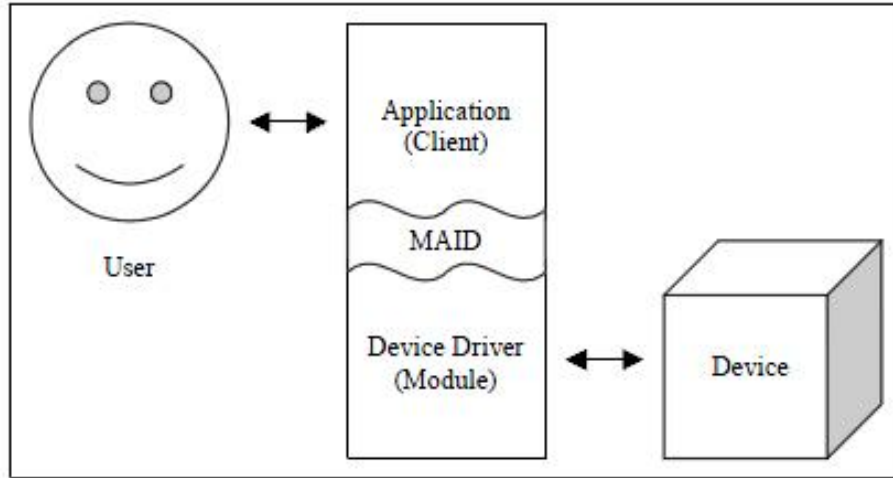


Figure 87. Schematic Representation of MAID [107]

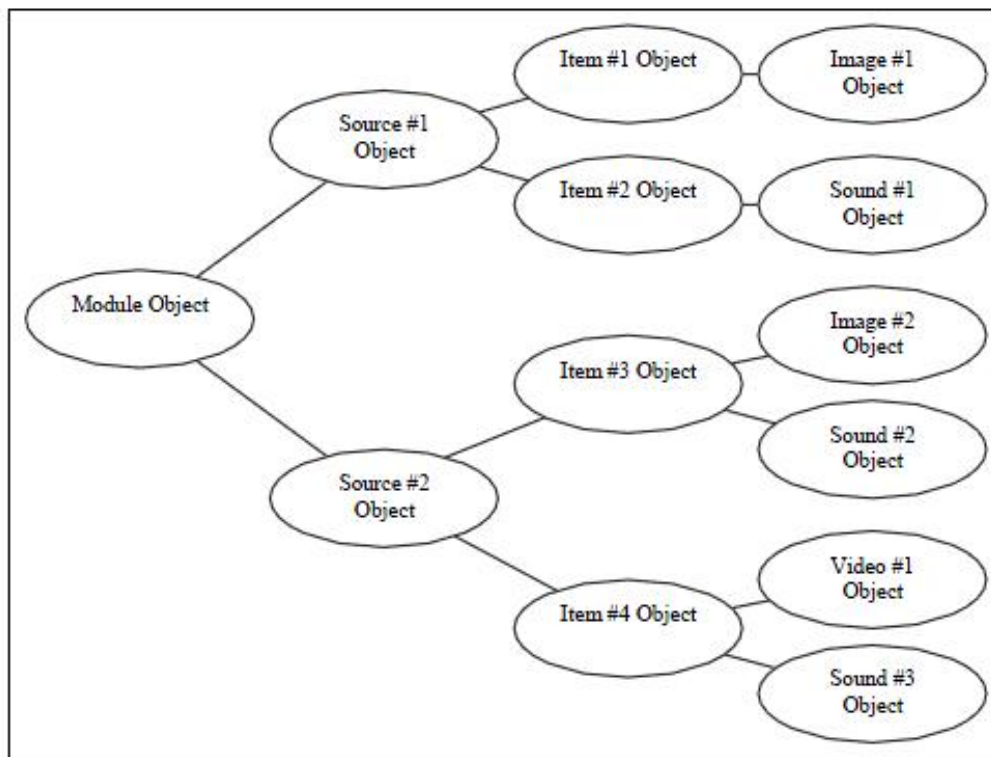


Figure 88. Layers inside MAID [107]

A given computer contains only one MAID module which can access several source objects, such as the digital cameras. In each source object, the computer can access the item objects within the source object. The item object is a combination of several media sources.

An object is alive when the parent object opens it, and it is dead when the parent object closes it. An object can only be accessed by the parent object. The capacities, i.e., the settings of the parent object are passed to all the child objects.

Before using the Nikon D90, the USB driver should be installed. The communication between the computer and D90 depends on two files, Type0003.md3 and NkdPTP.dll, which are usually copied into the folder containing the execution files.

In the initialization of the MAID module, Search\_Module() is called to locate the position of Type0003.md3. When it is found, Load\_Module() is called to load the library into the memory. Then the memory is allocated for the module reference and Command\_Open() is applied to initialize the module. Here the first parameter should be NULL, as the module object does not have a parent object. EnumCapabilities() is called to determine all the settings of the module and SetProc() is called to determine the event and UI request callback functions. Finally SelectSource() is called to determine the device source object. There could be multiple source objects. However in this work, the program always uses the first D90 that it enumerates. So only one Nikon D90 must be connected to prevent system confusion [107]. The program currently supports various camera parameters such as exposure mode, shutter speed, aperture, white balance, sensitivity, exposure compensation, flexible program and compression level [108]. The data types of these parameters are different. In the exposure

mode, there are four options – program, aperture priority, shutter priority and manual. For shutter speed, aperture, white balance, sensitivity and compression level, which are of the array type, a string of 512 characters is allocated and the characters for all the items are placed inside the string with the space character as the interval, and then the index of the selected item is given. For exposure compensation and flexible program, which are of range type, the minimal value, maximal value and the interval is given so that an array can be constructed, and then the index of the selected item is given [108].

A structure NKHDCParam is predefined in the program for the communication between the MAID module and the UI. When retrieving the parameters, all the retrieved parameters are filled in the structure and the structure is sent to the UI for UI display. In setting the parameters, the parameters inside the structure can be changed in the UI setup and then the structure is sent back to the MAID module.

In the retrieval of the parameters, Command\_CapGet() is used to obtain the parameter. If the parameter is of the array data type, Command\_CapGetArray() is used to retrieve the entire string. It should be noted that in this study the exposure mode should be set to only one of the four options. Otherwise, it will be set to its default option – manual exposure mode.

In the setting of the parameters, Command\_CapGet() is used to get the parameter structure. Then the index inside the structure is changed and the parameter structure is reset via Command\_CapSet(). It should be noted here that the setting of the flexible program can only be done when the exposure mode is switched to ‘program’. Therefore, the exposure mode is switched to ‘program’ first, then the flexible program parameters are set and finally the

exposure mode is set to the value selected by the user [107].

For image capturing, IssueProcess() is used to send the capture command to the device, and then Command\_Async() is called to delay the process until the operation is completed. An extra one second is needed here which is obtained via Sleep(1000) to provide sufficient time to complete the operation of the camera. Next, the data source is selected. Firstly the item number is selected using SelectItem(), then under that item the index of the image object is retrieved. IssueAcquire() is used to obtain the image data and write the image data into a temporary file designated in the MAID module. If the file writing is successful, the temporary file is copied to the destination file. Finally, the image file is deleted from the memory of the camera via Command\_CapStart() with the second parameter as kNkMAIDCapability\_DeleteDramImage [107].

### **3.3 Accessing the Raw Image of Nikon D90**

Figure 89 shows the Bayer pattern of the color filter array for D90 image sensor [109], which is stated to be RGGB. Figure 90 shows the CCD output of the top left corner. It can be noted that the output at (1, 2) is identical to those in (3, 2), (1, 4) and (3, 4). This indicates the pattern is GBRG or GRBG. In order to investigate this further, the average values of D2 and D10 in Gretag Colorchecker were analyzed. For the GRBG pattern, the RGB values for D2 should be (45, 128, 165) and those for D10 (171, 91, 78) after demosaicing. But D2 is red, so the R value should be greater than the B value; similarly D10 is blue, the B value should be greater than the R value. Thus, the Bayer pattern for Nikon D90 should be GBRG. The RGB

values of D2 after demosaicing would be (165, 128, 45) and the RGB values after demosaicing for D10 would be (78, 91, 171). These agree with the expected results.

In each pixel, the output is ranged from 0 to 768 (9.5bits). In one image, there are 2868 lines and the compression algorithm is used in each line [109].

The raw file structure for Nikon D90 is based on Tiff Revision 6.0, as shown in Figure 91.

The private tag reserved in TIFF as the Exif-specific additional information is also used.

From Figure 91, it can be noted that there are two image parts in the raw file structure, one is the jpeg image for the preview and the other is the raw image data. In this study, only the raw image data is used [109, 110].

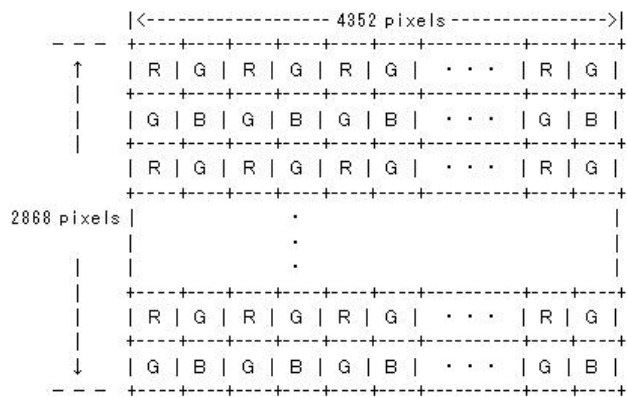


Figure 89. Bayer Pattern of the CFA of D90 Image Sensor from Nikon Document [109]

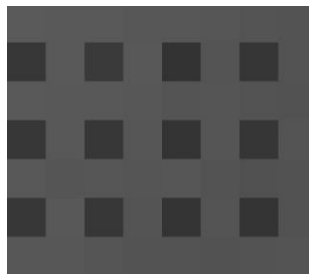


Figure 90. CCD output of the Top Left Corner

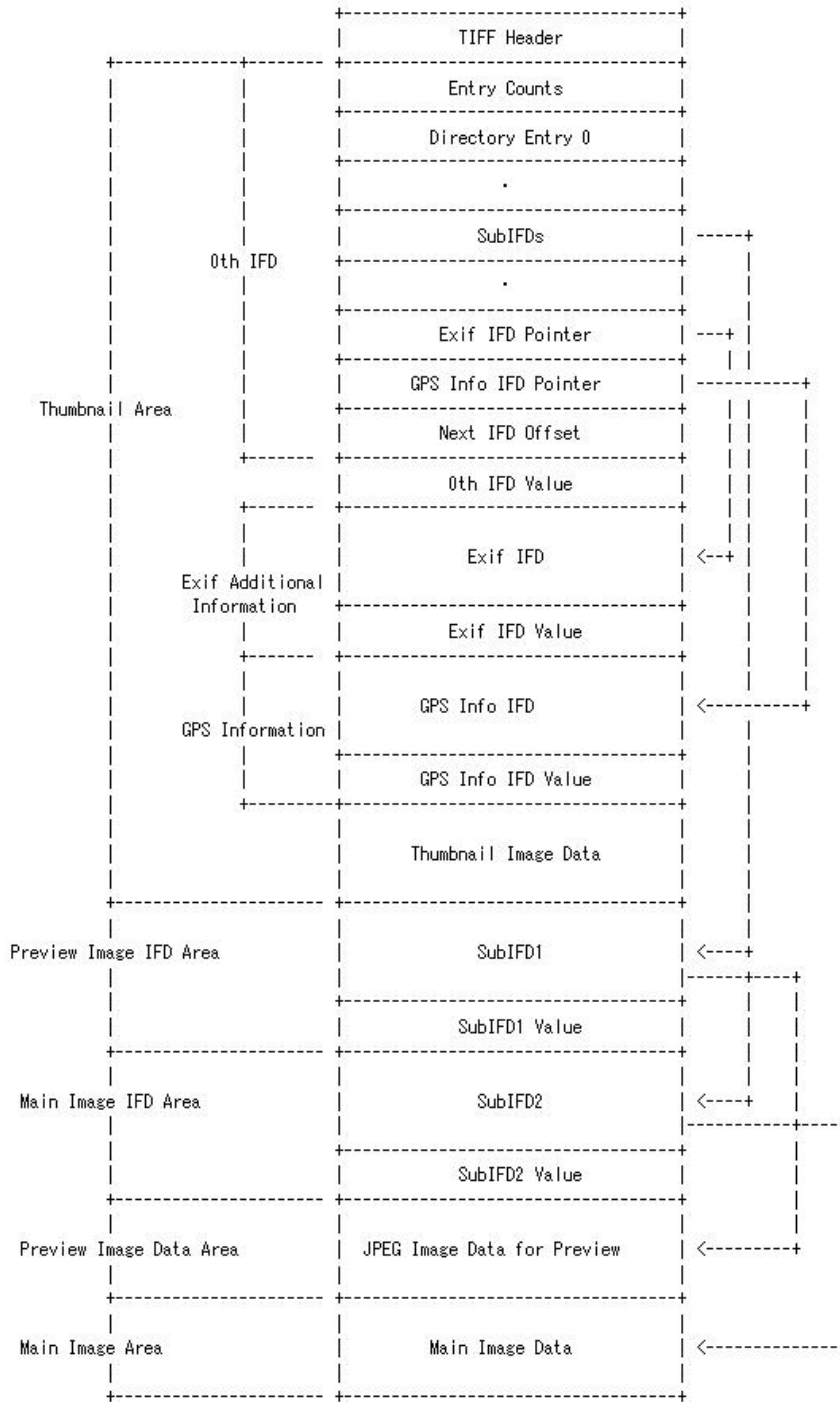


Figure 91. Structure of D90 Raw File [109]

As there is no official document on the compression algorithm employed, it is impossible to read the data out of raw image directly. As mentioned in Chapter VI, there are two methods to access the Nikon raw image, Nikon Image SDK and LibRaw.

Before using the Nikon Image SDK, `OpenLibrary()` should be called to initiate an instance of the Nikon Image SDK library, and this instance should be closed via `CloseLibrary()` when exiting the program. Every time when a file is to be accessed, `OpenSession(filename)` should be called to create a session, and this session should be closed via `CloseSession()` when the file is no longer required.

`GetImageInfo()` can be used to retrieve the image info such as the height, width, color channels and `GetImageData()` is employed to retrieve the RGB values for all the pixels [111].

In the application of LibRaw, all the data and operations regarding a raw image are encapsulated into a class LibRaw. `open_file(filename)` under class LibRaw is called to open a file and the related parameters can be found from the structure `LibRaw.imgdata`. When the `unpack()` is called, the pointer of the data buffer can be retrieved via `get_internal_data_pointer()` [112].

As the output of LibRaw is the Bayer pattern of CFA instead of the RGB values, the demosaicing method should be employed to convert the Bayer pattern encoded image to the true color image. There are various demosaicing algorithms, and here a bilinear interpolation is employed [113, 114].

It should be pointed out that in every line, the values for the 42 pixels on right are not correct. When the uniformity board is used, it can be noted that these values are less than half of

other values. The reason of this phenomenon is unknown. Although this error is not significant in this work, a mirroring technique is applied to modify these values, as shown in equation (78).

$$\begin{cases} r(x, y) = r(4310 \times 2 - x, y) \\ g(x, y) = g(4310 \times 2 - x, y) \\ b(x, y) = b(4310 \times 2 - x, y) \end{cases} \quad (78)$$

Here  $x, y$  are the coordinates of the pixel and  $x$  is between 4311 and 4352.

When the outputs from both methods are compared, it can be noted that the size of the output from Nikon Image SDK is  $4288 \times 2848$ , while the size of the output from LibRaw is  $4352 \times 2868$ , which is the actual size of the image sensor, though the values of the 42 columns of pixels on the right are based on data from other sections of the image. The output data from Nikon Image SDK is 8 bits, while the output data from LibRaw is 9.5 bits.

The Eizo monitor, ColorEdge CG211, which is used in this study, only supports 8 bits. In the computation of the ICC profile, 8 bits is applied. Thus the 9.5 bits from the LibRaw should be converted to 8 bits for use in the display and the for the ICC calculation. Two methods were examined for this conversion, and the relations between the raw pixel value and the pixel value after conversion is shown in Figure 92. Here the transfer curve is stored in the raw data file which can convert the 9.5 bits data into the 12 bits data. After the conversion, the right 4 bits of the 12 bits data are removed so that the 8 bits data can be acquired. From Figure 92, it can be seen that the transfer curve is below the linear curve, so the conversion from the transfer curve would be darker than that from the linear conversion, as shown in Figure 93. In this study, linear conversion was used.

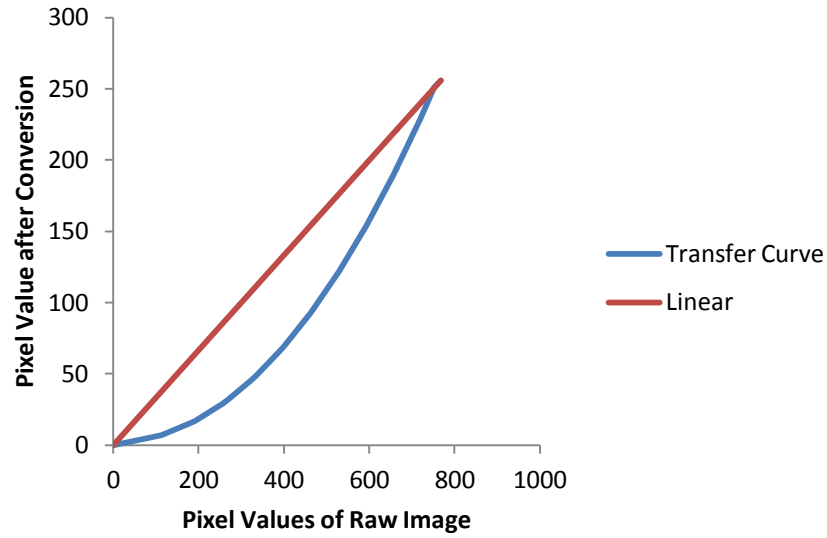


Figure 92. Relation between the Raw Pixel Value and the Pixel Value after Conversion

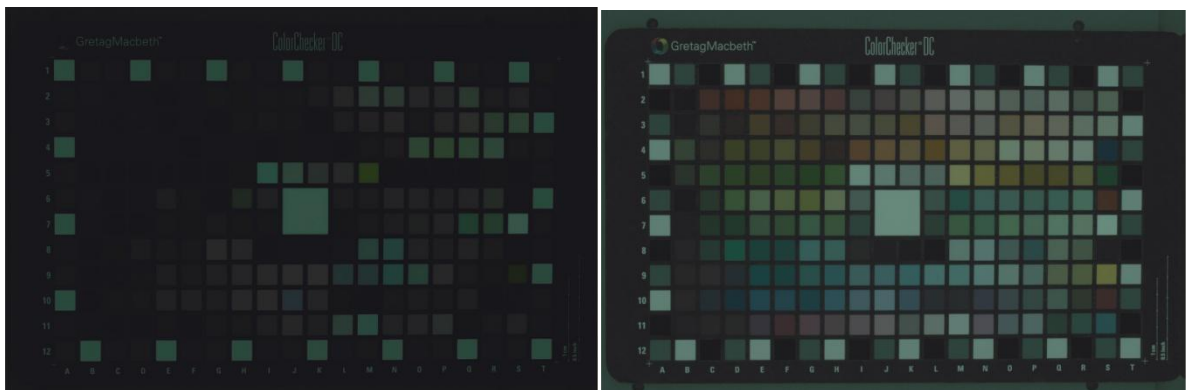


Figure 93. Output from Transfer Curve (Left) vs. that from the Linear Conversion (Right)

### 3.4 Image Segmentation for Camouflage Pattern

In this project, image segmentation is used to divide the image into sections based on the colors in the substrate. The image segmentation is alternation of the K-Means clustering [115], with the procedure described below.

1. Divide the image into the combinations of macro-blocks with a size of  $8 \times 8$  pixels;
2. Compute the average green values of each macro-block;
3. Initialize an array with 256 entries or 768 entries, dependent on whether 8 bits RGB values or 9.5 bits raw values are used. In the array, each entry is the total number of the macro-blocks with the average green values equaling the index of the entry. For example, the data in the 138<sup>th</sup> entry of the array is the total number of the macro-blocks with the average green value being 138;
4. Determine the maximal and the minimal average green values  $G_{max}$  and  $G_{min}$  of these macro-blocks;
5. Compute if  $\sum_{i=G_{max}-16}^{G_{max}} Count_i > 16$ , if not, decrease  $G_{max}$  until this condition is met. This is to avoid the  $G_{max}$  outliers. Here  $Count_i$  is the value of the  $i$ th entry in the array;
6. Similarly, compute if  $\sum_{i=G_{min}}^{G_{min}+16} Count_i > 16$ , if not, increase  $G_{min}$  until this condition is met. This is to avoid the  $G_{min}$  outliers. Here  $Count_i$  is the value of the  $i$ th entry in the array;
7. As there are three colors in the pattern used, three centers from these green values should be determined. The initial centers were set to the  $\frac{1}{6}G_{max} + \frac{5}{6}G_{min}$ ,  $\frac{1}{2}G_{max} + \frac{1}{2}G_{min}$  and  $\frac{5}{6}G_{max} + \frac{1}{6}G_{min}$ ;
8. Enumerate all the entries in the array. For each entry, compute the distance between the index of this entry and the three centers. Assign the entry to the center which is closest to the entry index. Thus all the macro-blocks are divided into three segmentations. Figure 94

shows the histogram of the average green values of all the macro-blocks with the initial and final positions of the three colors in the camouflage pattern;

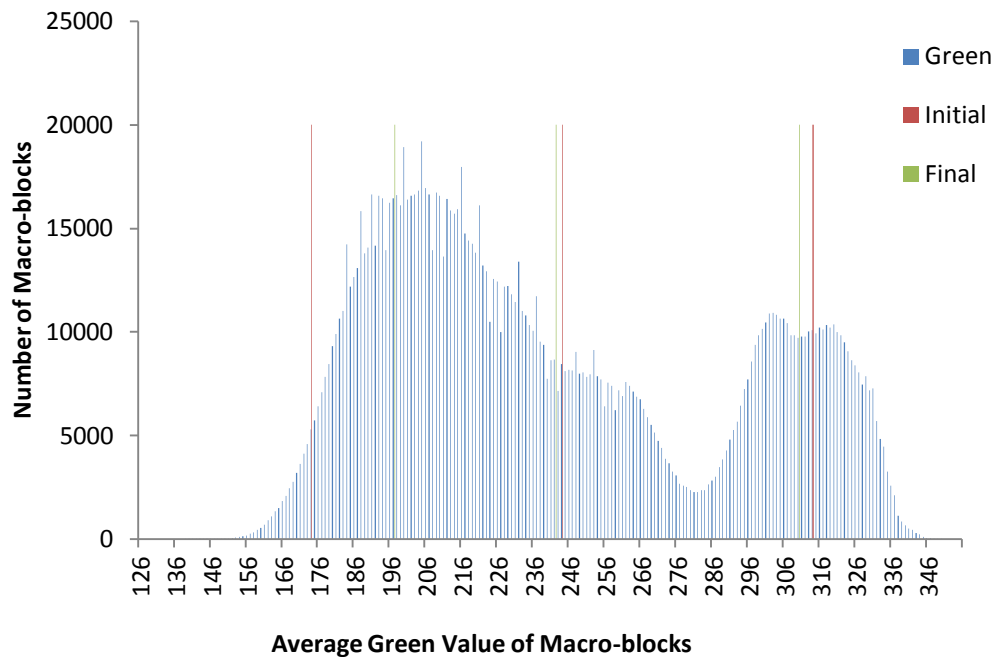


Figure 94. Histogram of Average Green Values of Macroblocks with Initial and Final Positions of Three Colors

9. Compute the average green values in the three segmentations and set these average values as the new centers;
10. Compute the difference between the new centers and the old centers. If the difference is smaller than  $\frac{3}{8}$ , stop; otherwise repeat step 8 and step 9 above;
11. Enumerate all the macro-blocks. Remove any macro-block if its segmentation is different from its 8 surrounding macro-blocks' segmentation. For example, in Figure 95, the macro-block at the center should be removed from the first segmentation as two of its

12. neighboring macro-blocks are in the second segmentation. This step is necessary as the macro-blocks at the boundary between two segmentations are always composed of the color pixels from both segmentations;

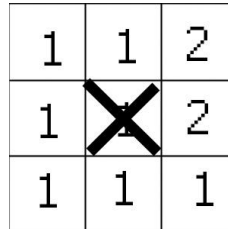


Figure 95. Macro-block to be Removed

13. Compute the average RGB values of the three segmentations;

Figure 96 shows the original image and its reconstruction without step 11. All the pixels in the original image were used to compute the average of the three colors, resulting in some error at the boundary between two neighboring color blocks. Figure 97 shows the original image and its reconstruction after step 11. Only half of the pixels in the original image were used in the computation, because the boundary between two neighboring color blocks was removed no error was obtained. The shortcoming of this method is that some information is lost in the computation.

The material used in this study is textile woven substrates composed of threads. The fabric contains a weave pattern, and dyeing and printing process does not always result in uniform application of color on the substrate. This non-uniformity can affect the visual assessment of the substrate. It would be appropriate to account such non-uniformities in the image segmentation.



Figure 96. Original Image and its Reconstruction without Step 11



Figure 97. Original Image and its Reconstruction with Step 11

In the software developed, the image segmentation is done in a rectangle. As the position and the size of the rectangle is variable, the average RGB values of each color are also variable.

Figure 77 shows the image of the camouflage based calibration tool containing 24 camouflage samples.

The software operator is required to select the four corners of the tool using a mouse and the software then automatically calculates 24 rectangles. In order to determine the variation of the image segmentation, the corner selection above was repeated 10 times. The difference between the maximal and the minimal values of the 10 procedures are computed, as shown in Table 43. It was found that the maximal value was 1.27 and 95% of these values were below 0.5, and as such, 0.5 was used as the threshold for judgments. The raw values were used and all values were ranged between 0 and 768.

### **3.5 Digital Color Management**

Color management is used to set up the device link between the monitor profile and the camera profile. The device link can be used to convert the RGB values from the camera to the RGB values in the display. Little CMS is employed as the color management module, which is an open source project and can be downloaded from the Internet. Little CMS is a small foot-print color engine fully supporting to the ICC profile. It was first released in 1998 and is currently one of the most popular open source color management libraries. Little CMS is widely used in a large number of production projects [116].

When the software is initiated, `cmsOpenProfileFromFile()` is used to open the profile and return the handle of the profile; when exiting the software, `cmsCloseProfile()` must be called to close the profile handle and release the associated resource.

When the handles from the monitor profile and the camera profile are available, `cmsCreateTransform()` is used to set up the profile link and return its handle. Here the first

parameter is the camera profile handle and the third parameter is the monitor profile handle. The second and the fourth parameters are the profile format. As both profiles are 8 bits RGB profiles, these two parameters are TYPE\_RGB\_8, i.e., 0X40019. The fifth parameter is the profile intent. Since the color accuracy is of major consideration in this study, the relative intent was used, and this parameter was set to 1. When exiting the software, cmsDeleteTransform() should be applied to delete the device link handle and release the allocated resources, and the cmsDeleteTransform() must be called before the execution of cmsCloseProfile().

cmsDoTransform() is the function that converts the pixels from camera to the pixels of the monitor. The first parameter is the device link handle. The second parameter is the pointer which points to the input buffer. The third parameter is the pointer which points to the output buffer. The fourth parameter is the pixel number. In Little CMS, there is no hardware acceleration. So, the execution time of cmsDoTransform() is almost proportional to the number of pixels. In the software, each time when cmsDoTransform() is called, a whole line of pixels from the image is sent to the cmsDoTransform() for conversion. As the image size from Nikon Image SDK is 4288×2848, 2848 calls of cmsDoTransform() are made to convert each image.

### **3. Conclusion**

From the description above, the following conclusions can be drawn:

- A software was developed to support the DigiEye system using visual C# / visual C++;

- This software can perform the calibration of the hardware, such as the monitor and the digital camera;
- ICC based color management is supported in this software;
- XML is used for the data management in this software;
- Nikon D90 is supported in this software and two methods are employed to access the raw data output.

Table 43. Difference between Max and Min after Image Segmentation

Patch NO	Foliage Green			Urban Gray			Desert Sand		
	R	G	B	R	G	B	R	G	B
R1S1	0.10	0.12	0.12	0.47	0.61	0.50	0.10	0.15	0.15
R1S2	0.08	0.12	0.12	0.16	0.19	0.14	0.29	0.29	0.22
R1S3	0.15	0.26	0.26	0.08	0.12	0.09	0.12	0.28	0.27
R1S4	0.18	0.25	0.27	0.23	0.39	0.28	0.26	0.36	0.28
R1S5	0.10	0.19	0.24	0.21	0.26	0.19	0.28	0.46	0.45
R1S6	0.03	0.08	0.08	0.26	0.29	0.25	0.16	0.18	0.13
R2S1	0.12	0.22	0.19	0.23	0.39	0.38	0.06	0.10	0.14
R2S2	0.23	0.28	0.29	0.08	0.20	0.17	0.45	0.67	0.62
R2S3	0.24	0.29	0.27	0.18	0.18	0.14	0.27	0.42	0.42
R2S4	0.14	0.16	0.16	0.10	0.06	0.05	0.22	0.30	0.23
R2S5	0.16	0.26	0.28	0.20	0.35	0.32	0.10	0.12	0.14
R2S6	0.27	0.37	0.29	0.44	0.52	0.44	0.16	0.24	0.20
R3S1	0.40	0.61	0.55	0.27	0.31	0.25	0.13	0.16	0.13
R3S2	0.21	0.30	0.25	0.15	0.20	0.16	0.12	0.14	0.14
R3S3	0.03	0.05	0.07	0.31	0.44	0.42	0.28	0.37	0.32
R3S4	0.03	0.03	0.04	0.32	0.50	0.48	0.19	0.30	0.26
R3S5	0.30	0.42	0.47	0.10	0.18	0.17	0.29	0.44	0.35
R3S6	0.24	0.38	0.36	0.27	0.34	0.32	0.18	0.21	0.18
R4S1	0.05	0.08	0.07	0.40	0.53	0.46	0.31	0.35	0.29
R4S2	0.12	0.19	0.18	0.16	0.28	0.25	0.33	0.29	0.35
R4S3	0.34	0.41	0.32	0.21	0.32	0.29	0.49	0.71	0.67
R4S4	0.20	0.29	0.28	0.91	1.27	1.06	0.13	0.19	0.18
R4S5	0.14	0.20	0.19	0.28	0.35	0.29	0.32	0.40	0.40
R4S6	0.16	0.39	0.36	0.13	0.18	0.15	0.16	0.22	0.22

## **Chapter VIII. Conclusions and Future Work**

The Universal Camouflage Pattern is produced for general use in the US Department of Defense and contains three colors, commonly known as: Urban Gray, Foliage Green and Desert Sand. Currently, there is no standard measurement-based system for the quality control of colors produced in this pattern. At the Natick Soldier Division Center, the control of quality was commonly ensured by an expert color assessor using a visual assessment technique. The procedure involved the visual assessor comparing a full width roll of the batch sample against the standard and providing a 'Pass', 'Fail' or "Warn" rating. This procedure is currently outsourced. Due to the use of a perceptual assessment procedure the ratings are subjective and might be affected by several parameters, including but not limited to the assessor's mood, age, and experience. The process is therefore not completely repeatable, nor can it be fully reproduced in different laboratories by other expert assessors. This warranted the US Army to determine whether it would be possible to develop a device based quality control methodology as a supplementary objective technique for use within the supply chain.

The objectives of this work were to examine various solutions to overcome this issue, recommend a methodology together with any required hardware and software to accomplish this task.

From a spectrophotometric point of view, the individual colors on the camouflage pattern can be measured with a reflectance spectrophotometer. However, colors in a sample may slightly

vary in different regions of the sample due to variations in production, coloration and printing. Due to the number of colors present, and the complexity of the patterns the selected region for measurement must be carefully controlled to ensure the aperture port is fully covered with the color of interest while considering the likely effect of the background color (e.g. sample holder), and variability in the structure of the substrate on measurements. Thus, such measurements can be tedious and time consuming. Measurements using different devices or variations in settings can also result in different ratings. These assumptions are known to be inaccurate.

Another complicating factor is that the visual assessment of multicolored printed material, such as camouflage substrates, are affected by several perceptual phenomena including simultaneous contrast, crispening effect, Hunt's effect, etc. Therefore, colorimetric methods would not provide a full picture of the overall pattern that is considered by the visual assessor. The process may thus be better suited to "color appearance models".

Using ratings obtained from a single expert assessor at Natick Soldier Division and based on the spectrophotometric measurement of rated camouflage samples, the boundaries between samples rated as 'Pass' and those rated as 'Fail' were set up using several methods in the color space. It was found that the differences between the colorimetric attributes of samples rated as Pass and those rated as 'Fail' were very small. Therefore, inter- and intra-variances in readings obtained from spectrophotometers could affect quality control ratings and were determined. A method, using calibrations via BCRA tiles, was developed in this study which successfully reduced the magnitude of variations for readings obtained from Datacolor SF

series spectrophotometers and those from a Datacolor SF500 Master spectrophotometer. While this process resulted in improved repeatability and increased accuracy of measured values, it did not address the question of color ‘appearance’. Furthermore, the process was still lengthy and required several careful measurements from each batch sample, usually taking 30 minutes per sample.

In order to overcome the shortcomings associated with spectrophotometric techniques, a camera based system was developed. This included a DigiEye® illumination chamber to diffusely illuminate samples inside a controlled lighting environment, a calibrated Nikon D90 camera to capture the images of the camouflage samples, and a calibrated Eizo ColorEdge monitor for the display of images.

Proprietary software was developed that included a user interface, hardware drivers for the camera and the spectrophotometer, a calibration methodology for the digital camera as well as the monitor used, and data management and image segmentation algorithms.

The Eizo ColorEdge monitor used in this study was successfully calibrated using the ICC profile. The spatial and temporal variations of the Eizo monitor were investigated and taken into account when displaying samples. The spatial and temporal variances of the DigiEye® system were investigated and an algorithm was developed to correct the spatial variance inside the chamber. Such variations could be due to the fluorescent and LED light sources used, the shape and geometry of the illumination system as well as other issues. Several methods were also examined to calibrate the camera and setup a data mapping algorithm from the device space to the color space. The software analyzed the RGB values of each

color from the image of a batch sample. It was found that regression based on the use of camouflage samples for the calibration process gave the best performance, although the level of accuracy attained could be further improved. It was found that when the device space was used to obtain ratings, three convex hulls could be generated based on the images of all samples rated as 'Pass'. These convex hulls were used to rate samples and ratings agreed with the set criteria based on the Natick visual assessor ratings. The overall level of agreement between camera based ratings and those from the expert assessor was approximately 87.5% when the convex hulls were extended 50%.

### **Recommendations for Future Work**

The methodology developed does not currently provide a complete solution to address this challenging issue and several issues remain unresolved. These could be considered in future to improve the repeatability, reproducibility and practicality of non-contact measurement systems for the quality control of complex multicolored patterns. Some issues requiring additional investigation include:

1. The analysis of data in Chapter III confirmed that camouflage samples contain variability within their structure and that such variations affect the tolerance. The exact nature of variability within and among various camouflage patterns should be determined to obtain required production tolerances.
2. In order to improve the accuracy of an acceptability tolerance for camouflage samples, based on their colorimetric attributes, inter- and intra-instrument variability of readings obtained from various spectrophotometers should also be considered. For

- samples close to the boundary, a P/F likelihood score rather than a simple rating could be provided;
3. Visual ratings from a single assessor were used to determine an acceptability boundary. The determination of criteria based on perceptual assessments requires repeated assessments of material by several subjects. Thus additional work is required to determine the minimum degree of variability in perceptual assessment of camouflage substrates among a statistically acceptable pool of subjects.
  4. The Universal Camouflage Pattern included a 'key' section. This section was used for visual assessments by the expert assessor. Some of the batch samples (production submits) did not contain the key region. In a pilot study, it was found that visual assessments were less variable when the key region was included. The role of pattern structure on visual assessments and the likely effects of simultaneous contrast and other perceptual phenomena on ratings were not considered in this study due to time limitations. These should be examined in detail in future studies.
  5. In camera based systems it would be interesting to determine the role of selected patterns on associated Pass / Fail ratings. Thus a pattern recognition algorithm may be developed to determine any patterns such as the 'key' pattern in camouflage samples;
  6. Due to the complexity of the appearance of camouflage substrates, measurements of colors around the 'key' pattern with a spectrophotometer may still not correlate well with their perceived ratings. Alternative methods, such as a hyperspectral camera may be examined to determine their value for the assessment of colors in complex patterns;

7. The image segmentation algorithm can be improved. While the current algorithm can separate colors well, it uses a limited area, as shown in Figure 97 in Chapter VIII. The use of a larger area in the algorithm is expected to result in improved performance of the system;
8. The uniformity of the illumination inside the DigiEye chamber can improve the accuracy of the image capturing process. Figure 79 in Chapter VII shows that the convex hulls of the 'pass' camouflage samples were slim. Thus any variations in the image might affect the ratings. In order to reduce variations in surface characteristics of the camouflage substrates, samples were ironed and held smoothly inside the illumination chamber to obtain images. However, variations, as large as 10 units, in captured data after image segmentation were observed. This may also be related to noise and variability due to the camera. Another possible cause might be due to variations in the reflected light. The exact cause of such variability should be established.
9. It is not easy or practical to capture images of all samples visually rated as 'Pass' to set up the convex hulls. Alternative calibration techniques should be developed and examined;
10. According to Table 23 in Chapter IV, the application of spatial corrections does not fully remove variance from the DigiEye® system. Thus it would be recommended to examine other devices such as scanners or alternative camera models to capture the image. Multi-illumination image capture systems could also be examined.

## References

1. Wyszecki, G., Stiles, W.S., Color science : concepts and methods, quantitative data, and formulae, in: Wiley classics library, John Wiley & Sons, New York, 2000, pp. 7; 26-28; 144-148.
2. R. McDonald, Colour physics for industry, in: , Society of Dyers and Colourists, Bradford, 1997, pp. 427-430; 58-60;.
3. Stanley, C., Lawrence W.M., James T.E., Sensation and perception, in: , J. Wiley & Sons, Hoboken, NJ, 2004, pp. 44-57.
4. Billmeyer, F.W., Saltzman, M., Principles of color technology, in: , Wiley, New York, 1981, pp. 240-137-138.
5. R.S. Berns, Billmeyer and Saltzman's principles of color technology, in: , Wiley, New York, 2000, pp. 51-55, 67-68.
6. P.A. Tipler, Physics for scientists and engineers, in: , W.H. Freeman, New York, 2008, pp. 1056-1089.
7. W.D. Wright, A re-determination of the trichromatic coefficients of the spectral colours, Transactions of the Optical Society 30 (1929) 141-164.
8. S. Jânos, Colorimetry: understanding the CIE system, in: , CIE/Commission internationale de l'eclairage; Wiley-Interscience, Vienna, Austria; Hoboken, N.J., 2007, pp. 459-28.
9. R.G. Kuehni, Color space and its divisions: color order from antiquity to the present, in: 228 (Ed.), , J. Wiley, Hoboken, N.J., 2003, pp. 204-208.
10. Burns, P.D., Berns, R.S., Quantization in Multispectral Color Image Acquisition (1999) 32-35.
11. Green, P., MacDonald, L.W., Colour engineering: achieving device independent colour, in: Wiley SID series in display technology, Wiley, Chichester, 2002, pp. 134-138; 251.
12. M.R. Luo, Development of Colour - Difference Formulae 32 (2002) 28-39.

13. DIN Deutsche Institute für Normung, DIN6176: Farbmessung Bestimmung von Farbabweichungen bei Körperfarben nach der DIN99-Formel (1999).
14. Cui, G., Luo, M.R., Rigg, B., Roesler, G., Witt, K., Uniform Colour Spaces Based on the DIN99 colour-difference Formula, *Color Research and Application* 27 (2002) 282-290.
15. Luo, M.R., Cui, G., Rigg, B., The development of the CIE 2000 colour-difference formula: CIEDE2000, *Color Research and Application* 26 (2001) 340-350.
16. Sharma, G., Wu, W.C., Daa, E.N., The CIEDE2000 color-difference formula: Implementation notes, supplementary test data, and mathematical observations, *Color Research and Application* 30 (2005) 21-30.
17. Luo, M.R., Cui, G., Li, C.J., Uniform Colour Spaces Based on CIECAM02 Colour Appearance Model, *Color Research and Application* 31 (2006) 320-330.
18. Gibert, J.M., Daga, J.M., Gilabert, E.J., Valdeperas, J., Evaluation of Colour Difference Formulae, *Coloration Technology* 121 (2005) 147-152.
19. Mangine, H., Jakes K., Noel, C., A Preliminary Comparison of CIE Color Differences to Textile Color Acceptability Using Average Observers, *Color Research and Application* 30 (2005) 288-294.
20. Shen, S.Z., Berns, R.S., Color-Difference formula performance for several data sets of small color differences based on visual uncertainty, *Color Research and Application* 36 (2010) 15-26.
21. Melgosa, M., Huertas, R., Berns, R.S., Performance of recent advanced color-difference formulas using the standardized residual sum of squares index, *Journal of Optical Society* 25 (2008) 1828-1834.
22. Shamey, R., Hinks, D., Melgosa, M., Luo, M.R., Cui, G., Huertas, R., Cardenas, L., Lee, S.G., Evaluation of Performance of Twelve Color-Difference Formulae Using Two NCSU Experimental Datasets (2010) 423-428.
23. M.D. Fairchild, Color appearance models, in: *Wiley-IS&T series in imaging science and technology*, J. Wiley, Chichester, West Sussex, England ; Hoboken, NJ, 2005, pp. 111-132; 168-170; 265-277.
24. W. Abney, On the Change in Hue of Spectrum Colours by Dilution with White Light 83 (1909) 120-127.

25. R.W.G. Hunt, Light and Dark Adaptation and the Perception of Color, *Journal of Optical Society* 42 (1952) 190-199.
26. Stevens, J.C., Stevens, S.S., Brightness functions: Effects of Adaptation, *Journal of Optical Society* 53 (1963) 375-385.
27. Bartleson, C.J., Breneman, E.J., Brightness perception in complex fields, *Journal of Optical Society* 57 (1967) 953-957.
28. International Color Consortium, Specification ICC.1:2001-04 (2004).
29. M.D. Fairchild, A revision of CIECAM97s for practical applications, *Color Research and Application* 26 (2001) 418-427.
30. Moroney, N., Fairchild, M.D., Hunt, R.W.G., Li, C.J., Luo, M.R., Newman, T., The CIECAM02 Color Appearance Model (2002) 23-27.
31. Li, C.J., Luo, M.R., Hunt, R.W.G., The CIECAM97s2 Model 7 (1999) 262-263.
32. Hunt, R.W.G., Pointer, M.R., A Color-Appearance Transform for 1931 standard colorimetric observer, *Color Research and Application* 10 (1985) 165-179.
33. International Color Consortium, ICC Specification.1:2004-10 (2006).
34. Trussell, H.J., Vrhel, M.M., *Fundamentals of digital imaging*, Cambridge University Press, Cambridge ; New York, 2008.
35. Farell, J., Sherman, D., Wandel, B., How to turn your scanner into a colorimeter (1994) 579-581.
36. Shahin, M.A., Symons, S.J., Color Calibration of Scanners for Scanner-Independent Grain Grading, *Cereal Chemistry* 80 (2003) 285-289.
37. Malmqvist, K., Bergman, L., Buck, H., Malmqvist, L., The 3-colour CCD camera as a densitometer for measuring density of cyan, magenta and yellow in printed solid areas and in screen areas (1993) 342-351.
38. Sodergard, C., Lehtonen, T., Launonen, R., Aikas, J., A System for Inspecting Colour Printing Quality (1995) 620-634.
39. Brydges D., Deppner F., Künzli H., Hersch, R.D., Application of a 3-CCD color camera for colorimetric and densitometric measurements 3300 (1998) 292-301.

40. Marguier, J., Bhatti, N., Baker, H., S üsstrunk, S., A Home D écor expert in your camera 1 (2009) 85-90.
41. Wu, W.C., Allebach, J.P., Analoui, M., Imaging colorimetry using a digital camera, *Journal of Imaging Science and Technology* 44 (2000) 268-279.
42. Ng, D.Y., Allebach, J.P., Analoui, M., Pizlo, Z., Non-contact imaging colorimeter for human tooth color assessment using a digital camera, *Journal of Imaging Science and Technology* 47 (2003) 531-542.
43. Kim, C.S., Kim, M.K., Jung, B., Choi, B., Verkruysse, W., Jeong, M.Y., Nelson, J.S., Determination of An Optimized Conversion Matrix for Device Independent Skin Colour Image Analysis, *Lasers in Surgery and Medicine* 37 (2005) 138-143.
44. Grana, C., Pellacani, G., Seidenari, S., Cuchiarra, R., Color Calibration for a Dermatological Video Camera System 3 (2004) 798-801.
45. Poucke S.V., Haeghen, Y.V., Vissers, K., Meert T., Jorens P., Automatic colorimetric calibration of human wounds, *BMC Medical Imaging* 10 (2010).
46. Cupitt, J., Saunders, D., Martinez, K., Digital Imaging in European Museums 3025 (1997) 144-151.
47. Berns, R.S., Imai, F.H., Burns, P.D., Tzeng, D.Y., Mutli-spectral-based color reproduction research at the Munsell Color Science Laboratory 3409 (1998) 14-25.
48. Brosnan, T., Sun, D.W., Inspection and grading of agricultural and food products by computer vision systems—a review, *Computers and Electronics in Agriculture* 36 (2002) 193-213.
49. Yam, K.L., Papadakis, S.E., A simple digital imaging method for measuring and analyzing color of food surfaces, *Journal of Food Engineering* 61 (2004) 137-142.
50. L. Kleiman, Hyperspectral imaging: the colorimetric high ground, *Proceedings of the SPIE, Color Imaging VIII: Processing, Hardcopy, and Applications* 5008 (2003) 249-259.
51. Brelstaff, G., P áraga, A., Troscianko, T., Carr, D., Hyper-spectral camera system:- acquisition and analysis, *Proceeding of SPIE Conference on Geographic Information Systems, Photogrammetry, and Geological/Geophysical Remote Sensing* 2587 (1995) 150-159.

52. M. Aikio, Hyperspectral prism-grating-prism imaging spectrograph, VTT Publications (2001).
53. Poger, S., Angelopoulou, E., Multispectral Sensors in Computer Vision, Stevens Institute of Technology Technical Report CS-2001-3 (2001).
54. Specim, Color Applications of Specim System.
55. Dinh, T.V., Strokes, D.L., Wabuyele, M.B., Martin, M.E., Song, J.M., Jagannathan, R., Michaud, E., Lee, R.J., Pan, X.G., A Hyperspectral Imaging System for In Vivo Optical Diagnostics, IEEE Engineering in Medicine and Biology Magazine 23 (2004) 40-49.
56. Fischer, C., Kakoulli, I., Multispectral and hyperspectral imaging technologies in conservation: current research and potential applications, Reviews in Conservation 7 (2006) 3-16.
57. Tristimulus colorimeter (2011).
58. Hunter Lab, Insight on Color: Double vs. Single Beam Spectrophotometers 9 (2008).
59. Hunter Lab, Reflectance Measurements: Specular Included versus Specular Excluded 13 (2009).
60. I. Nimeroff, Propagation of errors in spectrophotometric colorimetry, Journal of Optical Society of America 43 (1953) 531-533.
61. Shipley, T., Walker, G. L., Chromatic significance of spectrophotometric errors, Journal of Optical Society of America 46 (1956) 1052-1060.
62. Berns, R.S., Petersen, K.H., Empirical modeling of systematic spectrophotometric errors, Color Research and Applications 13 (1988) 243-256.
63. FairChild, M.D., Reniff, L., Propagation of random errors in spectrophotometric Colorimetry, Color Research and Applications 16 (1991) 361-367.
64. F. Dolezalek, Correction of Colour Measurement Device Errors 52.034 (2005).
65. X-Rite, NetProfiler [http://www.xrite.com/product\\_overview.aspx?ID=775](http://www.xrite.com/product_overview.aspx?ID=775).
66. Berns, R.S., Motta, R.J., Colorimetric Calibration of soft-copy devices to aid in hard-copy reproduction (1988) 266-269.

67. R.J. Motta, An Analytical Model for the Colorimetric Characterization of Color CRTs (1991).
68. Berns, R.S., Motta, R.J., Gorzynski, M.E., CRT Colorimetry. Part I: Theory and Practice, Color Research and Application 18 (1993) 299-314.
69. Berns, R.S., Gorzynski, M.E., Motta, R.J., CRT Colorimetry, part II: methodology, Color Research and Application 18 (1993) 315-325.
70. R.S. Berns, Methods for Characterizing CRT Displays, Displays 16 (1996) 173-182.
71. Cazes, A., Braudaway, G., Christensen, J., Cordes, M., Decain, D., Lien, A., Mintzer, F., Wright, S.L., On the color calibration of liquid crystal displays, IS&T/SPIE Conference on Display Metrology 3636 (1999) 154-161.
72. G. Sharma, LCDs Versus CRTs—Color-Calibration and Gamut Considerations, Proceedings of the IEEE 90 (2002) 605-622.
73. J. Nakamura, Image sensors and signal processing for digital still cameras, Taylor & Francis, Boca Raton, FL, 2006.
74. Pointer, M.R., Attridge, G.G., Jacobson, R.E., Practical camera characterization for colour measurement, Imaging Science Journal 49 (2001) 63.
75. Hong, G.W., Luo, M.R., Rhodes, P.A., A study of digital camera colorimetric characterization based on polynomial modeling, Color Research and Application 26 (2000) 76-84.
76. P.C. Hung, Colorimetric Calibration for Scanners and Media 1448 (1991) 164-174.
77. Trussell, H. J., Vrhel, M.M., Color Correction Using Principal Components, Color Research and Application 17 (1992) 328-338.
78. H.R. Kang, Color scanner calibration of reflected samples, SPIE Vol. 1670 Color Hard Copy and Graphic Arts 1670 (1992) 468-477.
79. Shen, H.L., Xin, J.H., Colorimetric and spectral characterization of a color scanner using local statistics, Journal of Imaging Science and Technology 48 (2004) 342-346.
80. Vrhel, M.M., Trussell, H.J., Color Scanner Calibration via a Neural Network 6 (1999).

81. H.R. Kang, Color technology for electronic imaging devices, SPIE Optical Engineering Press, Bellingham, Wash., USA, 1997.
82. Kasson, J.M., Plouffe, W., Nin, S.I., A tetrahedral interpolation technique for color space conversion 1909 (1993) 127-138.
83. Chatfield, C., Collins, A.J., Introduction to multivariate analysis, CRC Press, 1980.
84. Lasarte, M.D., Arjona, M., Vilaseca, M., Pujol, J., Influence of the Number of Samples of the Training Set on Accuracy of Color Measurement and Spectral Reconstruction, Journal of Imaging Science and Technology 54 (2010) 1-10.
85. Vrhel, M.M., Trussell, H.J., Filter Considerations in Color Correction 1657 (1992) 304-313.
86. Vrhel, M.M., Trussell, H.J., Optimal Nonnegative Color Scanning Filters, IEEE Transactions on Image Processing 7 (1998) 129-133.
87. Sharma, G., Trussell, H. J., Set theoretic estimation in color scanner characterization, Journal of Electronic Imaging 5 (1996) 479-489.
88. Imai, F.H., Quan, S., Rosen, M.R., Berns, R.S., Digital camera filter design for colorimetric and spectral accuracy (2001) 13-16.
89. Hunter, A., DiCarlo, J., Pollard, S., Six Color Scanning (2008) 570-574.
90. Jacobson, R.E., Ray, S.F., Attridge, G.G., Axford, N.R., The manual of photography, in: , Focal Press, 2000, pp. 62-65.
91. Dugas, A., Zupkofska, K. J., DiChiara, A., Kramer, F. M., Universal Camouflage For the Future Warrior (2004).
92. Universal Camouflage Pattern (2011).
93. NCSU, Lina Cardenas (2008).
94. Catmull, E., Rom, R., A class of local interpolating splines, in: Barnhill, R. E., Reisenfeld, R. F. (Ed.), Computer Aided Geometric Design, Academic Press, New York, 1974, pp. 317-326.
95. Verivide, Verivide | DigiEye - Food & Drink.

96. Verivide., Lamp Options (2012).
97. Photo Research, PR670.
98. Photo Research, PR-655/670 SpectraScan User Manual (2009).
99. TIPA, TIPA Awards 2007 (2007).
100. Nikon D90 (2012).
101. K. Hoffman, Microsoft Visual C# 2005 unleashed, in: Visual C# 2005 unleashed, Sams, Indianapolis, Ind., 2006, pp. 5-13.
102. Microsoft, The introduction to the C# Language and .Net Framework (2010).
103. J. Adams, C++ : an introduction to computing, in: S. Leestma, L.R. Nyhoff (Eds.), , Prentice Hall, Upper Saddle River, NJ, 1998, pp. 5-15.
104. G. Hogenson, Foundations of C++/CLI : the visual C++ language for .Net 3.5, in: C++/CLI, Apress; Distributed to the book trade worldwide by Springer-Verlag, Berkeley, CA; New York, 2008, pp. 1-29.
105. Gretagmacbeth, Eye-One C SDK Manual (2003).
106. Nikon Corporation, Digital Camera D90PC Mode Specifications (2008).
107. Nikon Corporation, MAID 3.1 (2001).
108. Nikon Corporation, Type0003 Vender Unique Capabilities (2009).
109. Nikon Corporation, Raw Data Format for Digital Camera (2009).
110. Adobe Developer's Association, Tiff Revisions 6.0 (1992).
111. Nikon Corporation, Specifications for Nikon Image SDK Library Interface (2008).
112. libraw, Raw decoding / processing library | Libraw (2011).
113. Ramanath, R., Snyder, W.E., Bilbro, G.L., Demosaicking methods for Bayer color arrays, Journal of Electronic Imaging 11 (2002) 306-315.

114. Gunturk, B.K., Glotzbach, J., Altunbasak, Y., Schafer, R.W., Mersereau, R.M., Demosaicking: Color Filter Array Interpolation, IEEE Signal Processing Magazine (2005) 44-54.

115. S.S. Haykin 1931-, Neural networks and learning machines, Prentice Hall, New York, 2009.

116. Marti Maria, Little CMS 2011 (2011).

# Appendices

Appendix Table A. CIELAB\* Values of All Samples

Sample ID	P/F	Desert Sand			Urban Gray			Foliage Green		
		L*	a*	b*	L*	a*	b*	L*	a*	b*
236942582	P	42.64	-1.89	2.88	53.26	-0.68	5.82	63.71	2.38	10.16
236942899	P	43.84	-1.69	3.23	52.91	-0.67	5.86	65.16	2.12	9.61
236945484	P	43.83	-1.77	3.27	52.03	-0.67	5.87	64.66	2.32	10.35
236945712	P	43.66	-1.62	3.36	52.70	-0.53	5.98	64.11	2.26	10.01
90018231	P	43.11	-1.62	2.83	54.03	-0.70	6.13	65.17	1.90	10.18
1314355	P	44.55	-1.74	3.06	54.25	-0.51	5.23	65.79	1.97	9.78
1314775	P	45.17	-1.58	3.18	54.10	-0.34	5.46	65.78	2.27	10.14
236942432	P	43.54	-1.59	3.38	52.66	-0.69	5.87	65.53	2.16	10.01
236942413	P	43.28	-1.70	3.19	52.11	-0.70	5.92	64.40	2.36	10.10
236942391	P	43.30	-1.65	3.13	51.63	-0.74	5.78	64.82	2.30	10.02
236942268	P	44.50	-1.97	3.15	53.77	-0.72	5.87	65.14	2.18	10.04
236942298	P	44.45	-1.94	3.39	52.32	-0.72	5.84	65.02	2.22	10.06
236942359	P	44.14	-1.66	3.28	52.72	-0.71	5.82	65.34	2.24	9.82
236942338	P	43.63	-1.90	2.92	52.13	-0.81	5.57	64.38	2.31	10.14
236942321	P	44.25	-1.95	3.22	53.14	-0.73	5.80	64.56	2.31	10.15
236942230	P	44.07	-1.66	3.16	52.80	-0.67	5.93	65.05	2.23	10.07
236942848	P	43.82	-1.77	3.19	52.71	-0.75	5.70	65.08	2.12	9.76
236942377	P	44.44	-1.67	3.23	53.45	-0.72	5.77	65.50	2.27	9.99
236942454	P	43.44	-1.68	3.25	52.37	-0.70	5.96	64.24	2.39	10.17
90018247	P	42.93	-1.62	2.69	54.02	-0.78	5.94	65.11	1.96	10.03
90018273	P	42.45	-1.62	2.74	53.96	-0.74	5.88	65.17	1.95	9.96
90017885	P	41.26	-1.81	2.79	53.26	-0.96	6.12	65.73	1.97	11.05
1314266	P	44.58	-1.73	3.11	54.42	-0.52	5.38	66.04	2.07	10.17
1314261	P	44.65	-1.71	3.11	53.84	-0.51	5.23	65.82	2.15	9.83
1314263	P	44.74	-1.68	3.23	54.31	-0.50	5.40	65.94	2.01	10.12
1314413	P	44.42	-1.83	3.12	53.64	-0.50	5.47	65.94	2.11	9.96
90017910	P	41.28	-1.72	2.79	52.43	-0.90	6.25	65.46	2.01	11.09
1314762	P	44.33	-1.77	3.27	53.84	-0.56	5.47	65.82	1.98	10.00
1314081	P	44.70	-1.90	3.09	54.46	-0.72	5.29	65.54	1.91	9.92
1314623	P	44.36	-1.77	3.04	54.28	-0.48	5.29	65.62	1.92	9.66
1314774	P	44.36	-1.79	3.22	53.97	-0.53	5.51	65.61	1.93	9.98
1314763	P	44.26	-1.79	3.26	54.01	-0.52	5.57	65.67	1.90	9.96
1314075	P	43.94	-1.81	2.96	54.33	-0.56	5.38	65.61	2.09	10.11
1314372	P	44.72	-1.71	3.21	54.13	-0.45	5.37	65.76	2.23	10.09
90017872	P	41.89	-1.83	2.90	53.58	-0.93	6.25	65.87	1.92	10.95
90017935	P	41.27	-1.74	2.82	52.50	-0.87	6.27	65.19	2.00	10.85

Appendix Table A. Continued

Sample ID	P/F	Desert Sand			Urban Gray			Foliage Green		
		L*	a*	b*	L*	a*	b*	L*	a*	b*
1314713	P	44.35	-1.69	3.01	53.87	-0.45	5.24	65.63	2.14	9.68
90018329	P	42.91	-1.62	2.76	54.06	-0.76	5.97	65.00	1.95	10.04
90017860	P	42.37	-1.78	2.90	53.67	-1.00	6.27	66.13	1.85	11.03
1314466	P	45.02	-1.74	3.01	54.60	-0.50	5.26	65.91	2.02	9.77
90018336	P	43.28	-1.60	2.81	54.12	-0.70	6.07	65.23	1.92	10.02
standard	P	43.91	-1.79	3.24	52.69	-0.73	5.86	63.85	2.08	9.81
1280906	F	45.05	-1.79	3.40	53.71	-1.23	6.26	65.87	1.83	11.20
1279788	F	45.54	-1.94	3.42	54.03	-1.28	6.26	65.72	1.43	11.04
1280905	F	44.56	-1.88	3.28	53.73	-1.31	6.10	65.72	1.68	11.31
1281053	F	45.06	-1.78	3.43	53.66	-1.23	6.37	65.46	1.75	11.16
1280817	F	45.92	-1.62	3.44	54.38	-1.00	6.22	65.37	1.72	10.77
1280931	F	44.58	-1.73	3.41	53.51	-1.18	6.30	65.15	1.74	10.99
1280901	F	44.47	-1.74	3.39	53.40	-1.11	6.25	65.39	1.85	11.05
1280796	F	45.67	-1.72	3.45	54.05	-1.15	6.26	65.82	1.67	11.09
12800854	F	44.69	-1.97	3.41	53.41	-1.28	6.37	65.15	1.57	11.27
479690	F	42.24	-1.51	3.27	52.42	-0.71	5.32	64.57	2.64	10.19
478480	F	42.28	-1.54	3.10	52.26	-0.87	5.34	64.63	2.59	10.47
479044	F	42.55	-1.56	3.00	52.80	-0.94	5.28	64.82	2.45	10.21
479354	F	46.02	-1.46	3.33	52.84	-0.93	5.17	65.90	2.55	10.33
479127	F	42.15	-1.63	2.87	52.21	-1.08	4.98	64.91	2.38	10.13
479353	F	44.47	-1.45	3.55	52.15	-0.87	5.43	64.80	2.58	10.79
478644	F	42.90	-1.51	3.13	52.60	-0.82	5.28	65.29	2.54	10.24
478742	F	42.22	-1.50	3.08	52.22	-0.76	5.22	64.79	2.75	10.23
478920	F	43.03	-1.60	2.97	53.53	-0.85	5.37	65.95	2.55	10.34
479115	F	41.99	-1.63	3.02	53.84	-0.97	5.14	64.04	2.18	10.16
460170	F	45.80	-1.21	3.09	55.59	-0.45	5.74	67.03	3.11	10.26
459958	F	46.21	-1.30	2.84	54.80	-0.83	5.19	68.43	3.15	10.30
459983	F	45.74	-1.28	3.00	55.50	-0.48	5.76	67.67	3.16	10.44
460025	F	46.14	-1.21	3.14	55.93	-0.47	5.89	67.06	3.05	10.44
460003	F	46.35	-1.20	3.13	55.65	-0.48	5.84	67.26	3.18	10.47
459906	F	45.78	-1.30	2.96	55.87	-0.60	5.56	67.83	3.00	10.11
460078	F	46.23	-1.22	3.15	55.13	-0.61	5.71	67.97	3.23	10.75
460505	F	46.35	-1.21	3.22	54.69	-0.71	5.59	67.52	3.26	10.71
460202	F	44.92	-1.32	3.07	54.68	-0.55	5.73	66.74	3.02	10.31
460034	F	46.18	-1.33	2.98	55.65	-0.66	5.58	67.79	3.02	10.25
459852	F	45.60	-1.36	2.87	55.61	-0.65	5.51	67.86	3.01	10.19
459769	F	45.60	-1.34	2.95	54.61	-0.81	5.34	68.25	3.10	10.39

Appendix Table A. Continued

Sample ID	P/F	Desert Sand			Urban Gray			Foliage Green		
		L*	a*	b*	L*	a*	b*	L*	a*	b*
478559	F	42.93	-1.53	3.27	52.11	-1.00	5.30	64.89	2.54	10.48
478538	F	42.97	-1.56	3.15	52.21	-1.08	5.15	65.10	2.39	10.30
478524	F	42.25	-1.59	3.07	52.55	-0.93	5.28	65.12	2.49	10.40
478496	F	42.49	-1.50	3.12	52.71	-0.83	5.29	65.11	2.65	10.54
478466	F	42.70	-1.52	3.08	52.55	-0.82	5.38	65.09	2.55	10.38
478950	F	43.66	-1.57	3.14	52.95	-0.92	5.20	65.83	2.53	10.40
479091	F	42.10	-1.58	3.08	52.39	-1.04	5.29	64.27	2.33	10.37
80152360	F	43.24	-1.62	3.18	53.70	-0.72	6.67	65.67	2.50	10.92
80152358	F	43.71	-1.64	3.21	53.96	-0.69	6.73	65.67	2.50	10.86
80152356	F	43.30	-1.62	3.21	53.89	-0.73	6.68	65.45	2.56	10.78
80152405	F	42.86	-1.69	2.96	53.66	-0.74	6.64	65.14	2.77	10.67
80152374	F	42.75	-1.59	3.09	54.05	-0.60	6.80	65.87	2.67	10.90
80156080	F	43.09	-1.71	3.18	54.36	-1.03	6.56	65.62	2.41	10.84
80152862	F	43.48	-1.59	3.27	54.40	-0.78	6.71	65.30	2.41	10.86
80152826	F	43.83	-1.77	3.32	54.09	-1.02	6.38	65.23	2.87	10.95
80152806	F	43.39	-1.73	3.22	54.07	-0.97	6.30	65.25	2.88	10.84
80154096	F	42.89	-1.66	3.21	53.86	-0.79	6.58	65.39	2.64	10.84
80154059	F	42.92	-1.63	3.24	53.85	-0.77	6.49	65.48	2.72	10.97
80154010	F	42.73	-1.64	3.21	53.33	-0.75	6.52	65.48	2.71	10.90
479100	F	42.50	-1.60	3.20	54.24	-0.82	5.33	63.99	2.27	10.28
478682	F	43.05	-1.60	3.02	52.38	-1.00	4.99	65.59	2.51	10.29
478659	F	42.46	-1.63	3.05	52.63	-0.91	5.07	65.12	2.43	9.95
478734	F	42.45	-1.63	3.24	52.13	-1.01	5.19	65.42	2.49	10.54
479023	F	42.29	-1.63	3.05	52.28	-0.99	5.14	64.91	2.46	10.17
1280888	F	44.63	-1.87	3.39	53.75	-1.31	6.25	65.58	1.71	11.18
80152376	F	43.25	-1.59	3.12	54.39	-0.74	6.60	65.98	2.55	10.73
80152375	F	43.43	-1.61	3.20	54.31	-0.80	6.67	65.97	2.52	10.79
478613	F	42.78	-1.65	2.94	52.74	-1.01	4.95	65.00	2.33	9.96
478582	F	42.41	-1.45	3.33	52.41	-0.71	5.34	64.53	2.75	10.24
80156087	F	44.03	-1.62	3.28	54.48	-0.88	6.59	66.01	2.42	10.95
80156077	F	43.05	-1.70	3.18	53.84	-0.95	6.43	65.31	2.44	10.87
462399	F	46.65	-1.14	3.21	55.61	-0.64	5.72	68.11	3.03	10.49
460526	F	46.00	-1.23	3.00	55.40	-0.51	5.69	66.97	3.11	10.46
459792	F	45.70	-1.13	3.23	54.68	-0.57	5.80	66.94	3.22	10.59
459808	F	46.57	-1.28	2.97	55.76	-0.70	5.42	68.66	3.04	10.19

Appendix Table B. CIELAB\* based on the Wrong von – Kries Adaptation

Sample ID	P/F	Urban Gray / Foliage Green			Desert Sand / Foliage Green			Desert Sand / Urban Gray		
		L*	a*	b*	L*	a*	b*	L*	a*	b*
236945712	P	84.68	-2.14	-3.35	70.29	-5.11	-6.51	83.42	-3.79	-4.11
1314763	P	83.79	-2.30	-2.77	69.49	-4.69	-6.45	83.38	-3.18	-4.66
90017872	P	80.48	-2.21	-4.00	65.93	-4.97	-7.54	82.51	-3.74	-4.86
90017935	P	80.94	-2.16	-4.28	65.72	-4.96	-7.57	81.78	-3.77	-4.62
236942432	P	84.54	-1.84	-3.10	68.62	-4.81	-6.13	81.63	-3.78	-3.99
1314261	P	84.69	-2.18	-2.61	69.87	-4.86	-6.60	82.93	-3.47	-4.96
1314413	P	83.98	-2.39	-2.92	69.42	-4.96	-6.67	83.11	-3.41	-4.76
236942338	P	85.47	-2.20	-3.57	69.93	-5.56	-7.29	82.23	-4.24	-4.78
236942321	P	85.01	-2.37	-3.33	70.64	-5.63	-6.93	83.49	-4.15	-4.60
90018231	P	81.86	-2.15	-4.05	68.35	-4.75	-7.16	83.99	-3.44	-4.24
90017885	P	79.77	-2.16	-3.98	65.08	-5.00	-7.72	82.22	-3.86	-5.14
236942230	P	85.22	-2.01	-3.66	69.87	-5.08	-6.75	82.41	-3.88	-4.10
1314355	P	83.93	-2.22	-2.60	69.77	-4.71	-6.59	83.57	-3.28	-4.98
1314623	P	83.57	-2.31	-2.72	69.68	-4.70	-6.48	83.82	-3.18	-4.75
90017910	P	81.04	-2.12	-4.32	65.46	-4.94	-7.83	81.37	-3.79	-4.90
1314466	P	84.22	-2.24	-2.74	70.31	-4.79	-6.72	83.91	-3.33	-4.96
90018336	P	82.02	-2.11	-4.01	68.56	-4.72	-7.01	84.07	-3.44	-4.11
1314762	P	84.15	-2.20	-2.65	69.43	-4.74	-6.49	82.95	-3.32	-4.82
236942359	P	85.48	-1.94	-3.30	69.68	-5.05	-6.22	81.94	-3.92	-3.85
1314372	P	84.39	-2.27	-2.60	70.05	-4.95	-6.77	83.42	-3.49	-5.17
236942298	P	86.58	-2.39	-3.24	70.45	-5.46	-6.48	81.76	-3.92	-4.16
90018273	P	80.88	-2.08	-3.74	67.44	-4.75	-6.92	83.90	-3.56	-4.33
236945484	P	86.18	-2.19	-3.48	70.12	-5.36	-6.98	81.76	-4.01	-4.51
236942391	P	85.66	-1.92	-3.58	69.02	-5.13	-6.64	81.01	-4.04	-4.08
90018329	P	81.50	-2.06	-3.89	68.27	-4.79	-7.11	84.26	-3.61	-4.36
1314263	P	84.17	-2.15	-2.58	69.88	-4.69	-6.72	83.45	-3.31	-5.14
1314081	P	83.88	-2.19	-2.63	70.25	-4.90	-6.80	84.17	-3.52	-5.18
236942413	P	84.89	-2.04	-3.60	69.42	-5.28	-6.74	82.21	-4.10	-4.16
1314075	P	82.82	-2.29	-2.93	69.09	-4.93	-7.06	83.88	-3.49	-5.24
236942454	P	84.81	-2.00	-3.53	69.83	-5.30	-6.80	82.76	-4.16	-4.28
236942377	P	84.91	-1.91	-3.21	69.93	-5.09	-6.52	82.77	-4.00	-4.27
236942848	P	84.94	-2.07	-3.19	69.49	-5.08	-6.28	82.24	-3.84	-4.04
90018247	P	81.59	-2.03	-3.97	68.18	-4.79	-7.15	84.06	-3.63	-4.33

Appendix Table B. Continued

Sample ID	P/F	Urban Gray / Foliage Green			Desert Sand / Foliage Green			Desert Sand / Urban Gray		
		L*	a*	b*	L*	a*	b*	L*	a*	b*
236942582	P	82.16	-2.41	-3.68	69.23	-5.65	-7.36	84.72	-4.23	-4.82
90017860	P	81.15	-2.04	-4.07	66.35	-4.85	-7.65	82.33	-3.75	-4.89
236942899	P	84.68	-2.05	-3.37	69.43	-4.94	-6.03	82.43	-3.71	-3.59
1314775	P	84.95	-2.23	-2.85	70.47	-4.85	-6.94	83.36	-3.39	-5.09
1314266	P	83.74	-2.20	-2.74	69.56	-4.80	-6.93	83.51	-3.41	-5.24
1314774	P	84.01	-2.28	-2.77	69.69	-4.74	-6.59	83.39	-3.26	-4.81
Standard	P	84.92	-2.08	-3.05	68.77	-5.25	-7.17	81.44	-4.05	-5.20
1314713	P	84.11	-2.24	-2.66	69.72	-4.82	-6.53	83.32	-3.38	-4.85
236942268	P	84.55	-2.42	-3.45	70.39	-5.47	-6.79	83.67	-3.94	-4.33
479044	F	82.68	-1.45	-2.73	67.94	-5.08	-7.03	82.67	-4.54	-5.44
460170	F	84.09	-1.52	-3.24	70.23	-5.23	-7.04	83.94	-4.56	-4.83
460034	F	84.63	-1.42	-3.25	69.98	-5.26	-7.10	83.11	-4.68	-4.89
478496	F	82.71	-1.51	-2.53	67.54	-5.18	-7.14	82.18	-4.60	-5.79
479127	F	82.84	-1.38	-2.54	67.26	-5.10	-7.03	81.72	-4.63	-5.66
460078	F	85.45	-1.31	-3.25	69.86	-5.31	-7.41	82.18	-4.81	-5.22
1280931	F	85.07	-1.34	-3.74	70.50	-4.56	-7.64	83.27	-3.94	-4.98
80156080	F	81.38	-1.86	-3.98	67.89	-5.35	-7.28	83.92	-4.48	-4.48
478466	F	83.31	-1.55	-2.82	67.87	-5.12	-7.07	81.96	-4.46	-5.38
80152405	F	81.96	-2.24	-4.63	68.02	-5.71	-7.51	83.49	-4.52	-4.07
80152358	F	82.97	-2.19	-4.37	68.69	-5.37	-7.36	83.27	-4.12	-4.14
459852	F	83.75	-1.47	-3.25	69.10	-5.25	-7.07	82.97	-4.66	-4.91
1280905	F	84.70	-1.40	-3.59	69.85	-4.70	-8.07	82.89	-4.05	-5.65
478920	F	82.46	-1.65	-2.87	67.46	-5.18	-7.04	82.33	-4.47	-5.34
80152374	F	81.30	-2.26	-4.50	67.19	-5.39	-7.34	83.18	-4.14	-4.06
80152375	F	81.98	-2.00	-4.19	67.99	-5.29	-7.17	83.44	-4.25	-4.14
479091	F	82.52	-1.35	-2.59	67.87	-5.02	-7.12	82.74	-4.57	-5.69
80156077	F	83.04	-1.82	-4.01	69.00	-5.31	-7.54	83.56	-4.41	-4.69
1280796	F	86.08	-1.31	-3.67	71.33	-4.46	-7.75	83.24	-3.81	-5.13
478734	F	83.58	-1.42	-2.24	67.27	-5.16	-6.86	80.99	-4.63	-5.74
479115	F	80.27	-1.53	-2.26	67.93	-4.94	-7.00	85.14	-4.37	-5.98
80154010	F	82.21	-2.14	-4.02	67.51	-5.54	-7.27	82.63	-4.41	-4.44
1281053	F	85.50	-1.37	-3.88	70.72	-4.67	-7.87	83.11	-4.01	-5.09
460505	F	86.27	-1.14	-3.01	70.48	-5.38	-7.37	82.09	-5.02	-5.38

Appendix Table B. Continued

Sample ID	P/F	Urban Gray / Foliage Green			Desert Sand / Foliage Green			Desert Sand / Urban Gray		
		L*	a*	b*	L*	a*	b*	L*	a*	b*
80154059	F	81.80	-2.09	-3.87	67.78	-5.54	-7.36	83.37	-4.47	-4.69
478559	F	84.33	-1.34	-2.48	68.40	-5.15	-6.97	81.59	-4.67	-5.57
80152826	F	82.98	-1.94	-3.63	69.31	-5.97	-7.46	83.98	-5.07	-4.97
460202	F	83.94	-1.58	-3.31	69.30	-5.28	-7.03	83.01	-4.58	-4.78
478480	F	83.02	-1.51	-2.65	67.75	-5.21	-7.15	82.12	-4.63	-5.67
459906	F	83.68	-1.45	-3.17	69.38	-5.16	-6.89	83.37	-4.57	-4.77
478659	F	82.77	-1.62	-2.36	67.49	-5.12	-6.55	82.05	-4.43	-5.28
460025	F	84.18	-1.48	-3.39	70.69	-5.19	-7.23	84.38	-4.53	-4.88
12800854	F	85.34	-1.54	-3.85	70.60	-4.70	-7.96	83.13	-3.88	-5.23
478538	F	84.25	-1.22	-2.38	68.25	-5.00	-6.89	81.49	-4.61	-5.58
1280888	F	84.79	-1.36	-3.66	70.10	-4.70	-7.79	83.09	-4.09	-5.26
478742	F	82.97	-1.62	-2.55	67.50	-5.30	-6.85	81.86	-4.63	-5.43
479690	F	82.72	-1.69	-2.35	67.75	-5.20	-6.58	82.42	-4.45	-5.32
1280906	F	85.55	-1.32	-3.71	70.39	-4.71	-7.83	82.68	-4.10	-5.22
478950	F	84.31	-1.46	-2.47	68.46	-5.12	-6.95	81.67	-4.52	-5.55
80152376	F	81.61	-2.05	-4.19	67.73	-5.28	-7.19	83.51	-4.21	-4.16
479353	F	86.90	-1.32	-2.35	70.70	-5.16	-7.24	81.74	-4.58	-5.85
478644	F	83.56	-1.53	-2.58	67.94	-5.07	-6.79	81.81	-4.42	-5.30
80152862	F	81.96	-2.00	-4.12	68.76	-5.23	-7.32	84.37	-4.16	-4.35
459808	F	85.11	-1.26	-3.05	69.63	-5.14	-6.92	82.24	-4.69	-4.90
478613	F	83.17	-1.48	-2.36	68.08	-5.08	-6.82	82.35	-4.48	-5.56
459983	F	84.13	-1.59	-3.48	69.48	-5.31	-7.25	83.03	-4.60	-4.85
479023	F	83.00	-1.49	-2.48	67.46	-5.16	-6.82	81.79	-4.59	-5.46
45769	F	85.14	-1.21	-3.03	68.70	-5.26	-7.11	81.14	-4.88	-5.15
478682	F	84.15	-1.41	-2.37	67.85	-5.16	-6.98	81.12	-4.63	-5.71
80156087	F	82.76	-1.89	-3.99	68.80	-5.23	-7.35	83.60	-4.26	-4.50
80152806	F	82.28	-1.95	-3.64	68.68	-5.89	-7.38	83.95	-5.00	-4.91
479100	F	80.58	-1.66	-2.22	68.74	-5.02	-6.96	85.78	-4.31	-5.95
1280901	F	84.88	-1.48	-3.76	70.06	-4.71	-7.70	82.95	-3.98	-5.05
1280817	F	86.01	-1.36	-3.60	72.17	-4.41	-7.53	84.25	-3.69	-4.92
459792	F	85.22	-1.23	-3.24	70.18	-5.25	-7.23	82.76	-4.83	-5.03
478524	F	82.53	-1.52	-2.61	67.19	-5.13	-7.01	81.94	-4.54	-5.57
459958	F	85.89	-1.11	-3.01	69.37	-5.28	-7.23	81.19	-4.97	-5.27
80154096	F	81.73	-2.09	-4.03	67.83	-5.49	-7.26	83.49	-4.42	-4.40

Appendix Table B. Continued

Sample ID	P/F	Urban Gray / Foliage Green			Desert Sand / Foliage Green			Desert Sand / Urban Gray		
		L*	a*	b*	L*	a*	b*	L*	a*	b*
479354	F	88.47	-1.20	-2.43	71.74	-5.11	-7.06	81.43	-4.57	-5.51
460526	F	84.69	-1.47	-3.42	70.56	-5.30	-7.47	83.73	-4.66	-5.13
462399	F	85.33	-1.15	-3.15	70.20	-5.01	-7.05	82.68	-4.63	-4.92
478582	F	83.00	-1.58	-2.30	68.03	-5.24	-6.59	82.45	-4.58	-5.36
1279788	F	85.90	-1.49	-3.71	71.24	-4.52	-7.74	83.32	-3.71	-5.08
80152356	F	82.39	-2.14	-4.28	68.35	-5.39	-7.27	83.45	-4.22	-4.14

Appendix Table C. Variances in the Repeated Color Measurement of UCP Samples

Sample ID	Desert sand			Foliage Green			Urban Gray		
	Var(L*)	Var(a*)	Var(b*)	Var(L*)	Var(a*)	Var(b*)	Var(L*)	Var(a*)	Var(b*)
1280906	0.15	0.00	0.01	0.08	0.00	0.00	0.01	0.00	0.01
1279788	0.20	0.01	0.02	0.18	0.00	0.01	0.18	0.01	0.05
1280905	0.12	0.00	0.01	0.10	0.00	0.00	0.08	0.02	0.01
1281053	0.03	0.00	0.01	0.06	0.01	0.01	0.09	0.00	0.02
1280817	0.16	0.00	0.01	0.18	0.01	0.00	0.10	0.01	0.03
1280931	0.17	0.00	0.00	0.15	0.02	0.01	0.03	0.01	0.01
1280901	0.14	0.00	0.01	0.13	0.01	0.01	0.04	0.01	0.01
1280796	0.24	0.00	0.02	0.10	0.00	0.00	0.06	0.01	0.01
12800854	0.02	0.01	0.01	0.03	0.01	0.01	0.08	0.01	0.02
479690	0.03	0.00	0.01	0.07	0.00	0.01	0.01	0.01	0.02
478480	0.22	0.00	0.00	0.06	0.00	0.01	0.08	0.00	0.06
479044	0.24	0.00	0.01	0.10	0.00	0.02	0.18	0.02	0.06
479354	0.15	0.00	0.01	0.09	0.01	0.03	0.14	0.02	0.14
479127	0.16	0.00	0.01	0.13	0.01	0.03	0.11	0.03	0.07
479353	0.11	0.00	0.01	0.12	0.01	0.03	0.19	0.03	0.10
478644	0.05	0.00	0.01	0.06	0.00	0.02	0.12	0.01	0.03
478742	0.34	0.00	0.01	0.03	0.00	0.02	0.06	0.03	0.11
478920	0.02	0.00	0.01	0.16	0.01	0.03	0.16	0.02	0.06
479115	0.07	0.00	0.01	0.02	0.00	0.01	0.12	0.01	0.06
460170	0.08	0.00	0.01	0.12	0.00	0.01	0.08	0.03	0.05
459983	0.23	0.00	0.01	0.04	0.01	0.01	0.09	0.06	0.20
459958	0.13	0.00	0.02	0.34	0.02	0.05	0.18	0.04	0.14
460025	0.15	0.00	0.01	0.19	0.00	0.02	0.03	0.02	0.07
460003	0.38	0.01	0.01	0.10	0.00	0.01	0.09	0.04	0.12
459906	0.23	0.00	0.01	0.35	0.02	0.05	0.06	0.00	0.01
460078	0.12	0.00	0.02	0.16	0.01	0.01	0.12	0.03	0.15
460505	0.27	0.00	0.01	0.05	0.00	0.00	0.05	0.03	0.13
460202	0.26	0.00	0.03	0.29	0.01	0.03	0.05	0.00	0.02
460034	0.17	0.00	0.01	0.14	0.00	0.03	0.21	0.02	0.10
459852	0.09	0.00	0.00	0.10	0.01	0.04	0.14	0.02	0.05
459769	0.05	0.00	0.01	0.11	0.00	0.01	0.04	0.04	0.14
478559	0.11	0.00	0.01	0.04	0.00	0.00	0.06	0.02	0.06
478538	0.19	0.00	0.00	0.06	0.01	0.03	0.16	0.01	0.03
478524	0.24	0.00	0.02	0.05	0.01	0.02	0.08	0.01	0.08
478496	0.02	0.00	0.01	0.18	0.00	0.03	0.07	0.02	0.10
478466	0.27	0.00	0.01	0.08	0.01	0.04	0.08	0.02	0.07

Appendix Table C. Continued

Sample ID	Desert sand			Foliage Green			Urban Gray		
	Var(L*)	Var(a*)	Var(b*)	Var(L*)	Var(a*)	Var(b*)	Var(L*)	Var(a*)	Var(b*)
478950	0.68	0.01	0.01	0.19	0.00	0.02	0.13	0.02	0.06
479091	0.18	0.00	0.00	0.03	0.00	0.01	0.09	0.03	0.10
80152360	0.17	0.00	0.00	0.03	0.01	0.00	0.05	0.00	0.01
80152358	0.16	0.00	0.00	0.07	0.00	0.01	0.06	0.01	0.02
80152356	0.29	0.00	0.00	0.09	0.00	0.03	0.05	0.00	0.00
80152405	0.45	0.00	0.01	0.06	0.00	0.02	0.19	0.01	0.03
80152374	0.14	0.00	0.01	0.23	0.01	0.03	0.08	0.02	0.01
80156080	0.52	0.00	0.01	0.04	0.00	0.00	0.04	0.01	0.00
80152862	0.09	0.00	0.01	0.13	0.00	0.01	0.07	0.01	0.02
80152826	0.11	0.00	0.00	0.07	0.00	0.01	0.09	0.01	0.03
80152806	0.17	0.00	0.00	0.03	0.00	0.01	0.07	0.04	0.03
80154096	0.40	0.00	0.02	0.13	0.01	0.01	0.07	0.00	0.02
80154059	0.12	0.00	0.01	0.23	0.00	0.01	0.08	0.02	0.03
80154010	0.36	0.00	0.01	0.06	0.00	0.03	0.10	0.01	0.01
479100	0.12	0.00	0.00	0.07	0.00	0.02	0.06	0.01	0.08
478682	0.17	0.00	0.01	0.05	0.00	0.01	0.08	0.04	0.14
478659	0.18	0.00	0.03	0.14	0.00	0.02	0.03	0.00	0.01
478734	0.17	0.00	0.01	0.03	0.00	0.01	0.06	0.02	0.08
479023	0.30	0.00	0.00	0.14	0.01	0.03	0.03	0.01	0.02
1280888	0.19	0.00	0.01	0.08	0.00	0.00	0.08	0.01	0.02
80152376	0.19	0.00	0.01	0.06	0.01	0.02	0.02	0.03	0.01
80152375	0.13	0.00	0.01	0.02	0.01	0.01	0.07	0.02	0.01
478582	0.16	0.00	0.00	0.08	0.01	0.02	0.14	0.02	0.08
478613	0.16	0.00	0.01	0.02	0.00	0.00	0.08	0.00	0.03
80156087	0.24	0.00	0.02	0.07	0.01	0.01	0.07	0.00	0.04
80156077	0.95	0.00	0.01	0.23	0.00	0.02	0.15	0.01	0.03
462399	0.28	0.01	0.02	0.27	0.01	0.02	0.18	0.03	0.09
460526	0.14	0.00	0.01	0.16	0.01	0.04	0.08	0.03	0.09
459792	0.46	0.00	0.01	0.07	0.00	0.02	0.02	0.04	0.08
459808	0.06	0.00	0.01	0.02	0.00	0.01	0.17	0.04	0.12
236942582	0.12	0.00	0.01	0.11	0.00	0.00	0.10	0.00	0.02
236942899	0.05	0.00	0.00	0.18	0.00	0.01	0.19	0.00	0.02
236945484	0.42	0.00	0.01	0.18	0.00	0.01	0.21	0.00	0.01
236945712	0.27	0.00	0.01	0.11	0.00	0.02	0.16	0.01	0.02
90018231	0.03	0.00	0.01	0.15	0.00	0.02	0.07	0.00	0.02
1314355	0.10	0.00	0.01	0.13	0.00	0.01	0.04	0.01	0.02

Appendix Table C. Continued

Sample ID	Desert sand			Foliage Green			Urban Gray		
	Var(L*)	Var(a*)	Var(b*)	Var(L*)	Var(a*)	Var(b*)	Var(L*)	Var(a*)	Var(b*)
1314775	0.11	0.00	0.01	0.04	0.00	0.00	0.02	0.00	0.00
236942432	0.06	0.00	0.01	0.27	0.00	0.00	0.26	0.01	0.02
236942413	0.07	0.00	0.03	0.47	0.00	0.01	0.15	0.00	0.01
236942391	0.06	0.00	0.01	0.08	0.00	0.00	0.06	0.00	0.01
236942268	0.06	0.00	0.00	0.19	0.00	0.01	0.01	0.01	0.03
236942298	0.02	0.00	0.00	0.09	0.00	0.01	0.02	0.00	0.01
236942359	0.11	0.00	0.01	0.09	0.00	0.01	0.46	0.01	0.02
236942338	0.26	0.00	0.00	0.29	0.00	0.01	0.27	0.00	0.01
236942321	0.18	0.00	0.00	0.14	0.00	0.01	0.11	0.01	0.05
236942230	0.20	0.00	0.00	0.19	0.00	0.01	0.08	0.01	0.01
236942848	0.10	0.00	0.00	0.05	0.00	0.01	0.31	0.00	0.03
236942377	0.08	0.00	0.00	0.05	0.00	0.00	1.12	0.01	0.06
236942454	0.04	0.00	0.01	0.14	0.02	0.05	0.28	0.01	0.01
90018247	0.24	0.00	0.01	0.09	0.00	0.02	0.12	0.01	0.03
90018273	0.20	0.00	0.01	0.40	0.00	0.01	0.12	0.00	0.01
90017885	0.06	0.00	0.01	0.12	0.00	0.01	0.06	0.01	0.01
1314266	0.07	0.00	0.00	0.04	0.01	0.01	0.02	0.02	0.02
1314261	0.27	0.00	0.01	0.07	0.00	0.01	0.04	0.02	0.01
1314263	0.12	0.00	0.06	0.13	0.00	0.00	0.03	0.01	0.00
1314413	0.26	0.00	0.02	0.95	0.01	0.03	0.02	0.01	0.01
90017910	0.06	0.00	0.01	0.31	0.01	0.01	0.06	0.00	0.02
1314762	0.02	0.00	0.01	0.08	0.00	0.00	0.03	0.01	0.03
1314081	0.08	0.00	0.01	0.13	0.01	0.00	0.01	0.00	0.02
1314623	0.09	0.00	0.01	0.10	0.00	0.00	0.02	0.01	0.01
1314763	0.10	0.00	0.00	0.07	0.00	0.02	0.03	0.01	0.03
1314774	0.04	0.00	0.01	0.10	0.00	0.01	0.01	0.00	0.01
1314075	0.06	0.00	0.00	0.14	0.00	0.01	0.00	0.01	0.03
1314372	0.09	0.00	0.01	0.05	0.00	0.01	0.06	0.02	0.01
90017872	0.22	0.00	0.01	0.17	0.00	0.01	0.07	0.00	0.02
90017935	0.29	0.00	0.02	0.14	0.00	0.01	0.02	0.00	0.01
1314713	0.03	0.00	0.01	0.16	0.00	0.01	0.03	0.01	0.02
90018329	0.07	0.00	0.01	0.09	0.00	0.01	0.07	0.01	0.01
90017860	0.10	0.00	0.00	0.07	0.00	0.01	0.03	0.01	0.01
1314466	0.04	0.00	0.01	0.04	0.00	0.00	0.01	0.00	0.01
90018336	0.24	0.00	0.01	0.42	0.00	0.02	0.10	0.01	0.02

Appendix Table D. Original and Converted Tristimulus of the 22 Training Samples Colors in the Calibration Tool

Color	ID	$L_1^*$	$a_1^*$	$b_1^*$	$L_2^*$	$a_2^*$	$b_2^*$	$\Delta L^*$	$\Delta a^*$	$\Delta b^*$
Foliage Green	1279788	45.07	-1.35	2.95	45.59	-1.40	2.96	<b>-0.52</b>	<b>0.05</b>	<b>-0.01</b>
	1280906	44.86	-1.26	2.91	45.10	-1.28	2.97	<b>-0.24</b>	<b>0.02</b>	<b>-0.06</b>
	460202	44.51	-2.29	3.45	45.07	-1.90	3.31	<b>-0.56</b>	<b>-0.39</b>	<b>0.14</b>
	1314713	44.98	-1.22	2.88	44.39	-1.16	2.57	<b>0.60</b>	<b>-0.07</b>	<b>0.31</b>
	1280931	45.04	-1.38	2.97	44.64	-1.21	2.98	<b>0.41</b>	<b>-0.17</b>	<b>-0.01</b>
	90017885	41.40	-2.21	2.88	41.37	-2.23	2.84	<b>0.03</b>	<b>0.02</b>	<b>0.04</b>
	1280817	45.01	-1.38	2.91	45.97	-1.11	3.03	<b>-0.97</b>	<b>-0.27</b>	<b>-0.12</b>
	90017860	42.39	-2.21	3.08	42.49	-2.19	2.95	<b>-0.10</b>	<b>-0.02</b>	<b>0.13</b>
	80152360	43.50	-2.11	3.21	43.37	-2.04	3.27	<b>0.12</b>	<b>-0.07</b>	<b>-0.06</b>
	80152405	42.85	-1.93	3.02	42.98	-2.11	3.03	<b>-0.14</b>	<b>0.18</b>	<b>-0.01</b>
	1280854	45.04	-1.24	2.84	44.73	-1.42	2.95	<b>0.31</b>	<b>0.18</b>	<b>-0.11</b>
	478466	42.97	-2.20	3.15	42.85	-2.12	3.27	<b>0.13</b>	<b>-0.08</b>	<b>-0.12</b>
	1314466	45.28	-1.04	2.58	45.06	-1.19	2.56	<b>0.22</b>	<b>0.15</b>	<b>0.02</b>
	478682	43.33	-2.13	3.25	43.19	-2.21	3.21	<b>0.15</b>	<b>0.07</b>	<b>0.04</b>
	236942321	44.11	-2.35	3.45	44.39	-2.55	3.56	<b>-0.28</b>	<b>0.20</b>	<b>-0.11</b>
	459852	45.92	-1.96	3.19	45.74	-1.93	3.11	<b>0.18</b>	<b>-0.03</b>	<b>0.08</b>
	459958	46.42	-1.87	3.14	46.35	-1.85	3.07	<b>0.07</b>	<b>-0.01</b>	<b>0.07</b>
	479354	45.83	-2.08	3.33	46.18	-2.08	3.55	<b>-0.35</b>	<b>-0.01</b>	<b>-0.22</b>
	standard	44.58	-2.20	3.42	44.06	-2.39	3.59	<b>0.51</b>	<b>0.20</b>	<b>-0.17</b>
	236942268	45.00	-2.39	3.58	44.64	-2.57	3.50	<b>0.35</b>	<b>0.18</b>	<b>0.08</b>
478480	42.43	-2.28	3.15	42.43	-2.15	3.30	<b>0.00</b>	<b>-0.13</b>	<b>-0.14</b>	
236942338	43.90	-2.46	3.48	43.77	-2.48	3.25	<b>0.13</b>	<b>0.02</b>	<b>0.23</b>	
Urban Gray	1279788	53.81	-0.81	5.66	54.22	-0.90	5.97	<b>-0.41</b>	<b>0.09</b>	<b>-0.32</b>
	1280906	53.72	-0.62	6.07	53.90	-0.86	5.98	<b>-0.18</b>	<b>0.24</b>	<b>0.10</b>
	460202	53.64	-1.40	6.02	54.97	-1.24	6.27	<b>-1.32</b>	<b>-0.17</b>	<b>-0.24</b>
	1314713	53.95	-0.32	5.38	54.05	-0.07	5.03	<b>-0.10</b>	<b>-0.25</b>	<b>0.35</b>
	1280931	54.19	-0.75	5.81	53.70	-0.79	6.02	<b>0.49</b>	<b>0.04</b>	<b>-0.21</b>
	90017885	53.66	-0.78	6.14	53.46	-0.63	5.87	<b>0.20</b>	<b>-0.15</b>	<b>0.27</b>
	1280817	54.20	-0.68	5.98	54.57	-0.63	5.97	<b>-0.37</b>	<b>-0.05</b>	<b>0.01</b>
	90017860	53.96	-0.72	6.16	53.87	-0.68	6.02	<b>0.09</b>	<b>-0.04</b>	<b>0.14</b>
	80152360	53.83	-0.59	6.30	53.92	-0.44	6.47	<b>-0.09</b>	<b>-0.15</b>	<b>-0.17</b>
	80152405	53.82	-0.47	6.37	53.89	-0.47	6.43	<b>-0.07</b>	<b>0.01</b>	<b>-0.07</b>
	1280854	54.18	-0.60	5.91	53.60	-0.90	6.08	<b>0.58</b>	<b>0.30</b>	<b>-0.17</b>
	478466	52.82	-1.57	5.90	52.81	-1.51	5.87	<b>0.00</b>	<b>-0.07</b>	<b>0.03</b>
	1314466	54.77	-0.08	5.03	54.77	-0.12	5.05	<b>0.00</b>	<b>0.03</b>	<b>-0.02</b>
	478682	53.11	-1.57	5.61	52.63	-1.67	5.45	<b>0.48</b>	<b>0.10</b>	<b>0.16</b>
	236942321	53.85	-1.39	6.53	53.43	-1.44	6.37	<b>0.42</b>	<b>0.05</b>	<b>0.16</b>

Appendix Table D. Continued

Color	ID	L <sub>1</sub> *	a <sub>1</sub> *	b <sub>1</sub> *	L <sub>2</sub> *	a <sub>2</sub> *	b <sub>2</sub> *	ΔL*	Δa*	Δb*
Urban Gray	459852	55.76	-1.37	6.03	55.89	-1.33	6.03	<b>-0.13</b>	<b>-0.05</b>	<b>0.00</b>
	459958	55.18	-1.47	5.74	55.06	-1.48	5.67	<b>0.12</b>	<b>0.01</b>	<b>0.06</b>
	479354	53.37	-1.57	5.68	53.10	-1.60	5.64	<b>0.27</b>	<b>0.03</b>	<b>0.04</b>
	standard	53.35	-1.36	6.23	52.98	-1.44	6.42	<b>0.37</b>	<b>0.08</b>	<b>-0.19</b>
	236942268	53.95	-1.49	6.53	54.06	-1.45	6.44	<b>-0.12</b>	<b>-0.04</b>	<b>0.09</b>
	478480	52.33	-1.60	5.70	52.52	-1.56	5.82	<b>-0.20</b>	<b>-0.04</b>	<b>-0.12</b>
	236942338	52.42	-1.49	6.22	52.41	-1.52	6.14	<b>0.01</b>	<b>0.03</b>	<b>0.09</b>
Desert Sand	1279788	65.77	2.05	11.05	66.34	1.95	11.40	<b>-0.57</b>	<b>0.10</b>	<b>-0.35</b>
	1280906	66.09	1.91	11.04	67.29	2.29	11.31	<b>-1.20</b>	<b>-0.37</b>	<b>-0.28</b>
	460202	66.34	2.06	10.49	66.07	2.28	9.90	<b>0.28</b>	<b>-0.22</b>	<b>0.60</b>
	1314713	65.86	1.87	11.02	65.61	1.88	11.16	<b>0.25</b>	<b>-0.01</b>	<b>-0.14</b>
	1280931	65.81	1.87	11.15	66.22	2.01	11.27	<b>-0.41</b>	<b>-0.14</b>	<b>-0.12</b>
	90017885	65.89	2.04	11.03	65.82	1.87	10.95	<b>0.07</b>	<b>0.18</b>	<b>0.08</b>
	1280817	66.08	1.86	10.91	66.61	1.88	11.24	<b>-0.53</b>	<b>-0.03</b>	<b>-0.33</b>
	90017860	65.93	2.26	10.89	66.16	2.51	11.21	<b>-0.24</b>	<b>-0.25</b>	<b>-0.32</b>
	80152360	65.56	2.60	11.12	65.64	2.76	10.99	<b>-0.08</b>	<b>-0.15</b>	<b>0.13</b>
	80152405	65.96	2.04	10.92	65.62	1.71	11.43	<b>0.34</b>	<b>0.33</b>	<b>-0.50</b>
	1280854	65.37	1.49	11.50	65.64	1.71	11.33	<b>-0.27</b>	<b>-0.22</b>	<b>0.17</b>
	478466	66.82	2.26	10.33	66.34	2.17	9.98	<b>0.48</b>	<b>0.09</b>	<b>0.36</b>
	1314466	66.00	1.55	11.05	66.14	1.64	11.24	<b>-0.14</b>	<b>-0.09</b>	<b>-0.19</b>
	478682	65.63	1.89	11.33	65.07	1.73	10.92	<b>0.56</b>	<b>0.16</b>	<b>0.41</b>
	236942321	68.31	2.27	11.14	68.41	2.28	11.21	<b>-0.10</b>	<b>-0.01</b>	<b>-0.06</b>
	459852	69.01	2.43	11.33	68.99	2.43	11.33	<b>0.02</b>	<b>0.00</b>	<b>0.00</b>
	459958	66.04	1.54	11.04	66.44	1.71	11.26	<b>-0.40</b>	<b>-0.17</b>	<b>-0.23</b>
	479354	65.79	1.73	11.35	64.34	1.49	10.56	<b>1.45</b>	<b>0.24</b>	<b>0.79</b>
	standard	66.13	1.78	10.97	65.64	1.59	10.80	<b>0.49</b>	<b>0.19</b>	<b>0.17</b>
	236942268	65.00	1.74	11.26	65.18	1.73	11.44	<b>-0.19</b>	<b>0.01</b>	<b>-0.18</b>
478480	65.39	1.77	11.21	64.90	1.73	10.91	<b>0.50</b>	<b>0.04</b>	<b>0.30</b>	
236942338	65.96	1.92	10.93	66.18	1.57	11.18	<b>-0.23</b>	<b>0.35</b>	<b>-0.25</b>	

Appendix Table E. Average RGB values of the Samples after Image Segmentation

Sample ID	P/F	Foliage Green			Urban Gray			Desert Sand		
		R	G	B	R	G	B	R	G	B
1314075	p	207	312	288	268	388	352	343	476	421
1314081	p	201	305	281	260	379	343	331	462	408
1314261	p	213	320	296	270	392	356	348	483	428
1314263	p	202	305	281	259	375	341	334	464	411
1314266	p	203	307	283	260	378	343	336	467	413
1314372	p	216	323	298	272	393	357	348	482	427
1314413	p	201	305	281	259	376	341	332	463	409
1314466	p	213	321	296	271	393	357	348	483	429
1314623	p	203	306	282	260	378	343	332	463	410
1314713	p	201	303	280	257	373	339	332	461	409
1314762	p	210	316	291	268	388	352	345	479	424
1314763	p	200	301	278	256	371	337	330	459	406
1314774	p	206	310	285	262	380	344	336	467	413
1314775	p	206	310	285	262	379	343	336	467	412
90017860	p	196	303	275	267	388	349	350	485	427
90017872	p	182	282	256	252	366	329	331	461	404
90017885	p	183	283	257	252	366	329	331	461	404
90017910	p	190	293	266	260	376	337	342	474	416
90017935	p	189	292	266	259	375	337	341	473	415
90018231	p	197	304	277	267	387	349	339	472	417
90018247	p	199	307	280	269	390	352	342	477	421
90018273	p	188	290	265	254	369	334	326	454	401
90018329	p	196	302	276	266	386	349	338	471	416
90018336	p	199	306	279	266	386	348	339	472	417
236942230	p	205	313	281	256	375	332	338	471	412
236942268	p	209	319	287	262	384	340	341	476	416
236942298	p	207	316	284	255	373	331	338	472	412
236942321	p	203	312	280	259	380	337	337	471	411
236942338	p	195	300	269	245	360	318	323	452	394
236942359	p	204	311	280	254	373	331	336	469	410
236942377	p	201	306	275	253	371	329	329	460	403
236942391	p	201	308	276	252	369	327	338	471	411
236942413	p	202	308	276	254	372	329	335	467	407
236942432	p	204	311	279	258	378	335	341	477	417
236942454	p	203	309	278	255	373	330	336	468	409

Appendix Table E. Continued

Sample ID	P/F	Foliage Green			Urban Gray			Desert Sand		
		R	G	B	R	G	B	R	G	B
236942582	p	200	307	276	260	381	338	331	461	401
236942848	p	203	310	279	257	377	335	339	474	416
236942899	p	205	313	282	260	381	338	342	478	420
236945484	p	205	314	282	254	372	329	338	471	410
236945712	p	202	308	277	257	376	333	332	463	404
standard	p	204	312	281	257	378	335	342	475	411
459769	f	203	312	284	257	379	339	346	480	421
459792	f	205	313	285	258	378	339	342	473	414
459808	f	215	328	299	271	399	357	360	500	439
459852	f	203	312	283	262	385	343	343	476	416
459906	f	203	310	282	263	385	344	343	477	417
459958	f	212	324	295	266	393	351	357	495	433
459983	f	205	314	286	263	386	346	343	476	416
460025	f	205	313	284	264	386	344	339	469	409
460034	f	211	322	293	271	397	355	354	491	430
460078	f	214	325	295	268	393	351	357	493	430
460170	f	210	319	290	270	394	352	349	483	422
460202	f	199	305	277	256	376	335	338	469	409
460505	f	215	327	297	267	392	350	356	492	430
460526	f	204	312	284	261	382	342	337	467	409
462399	f	206	314	285	262	385	343	345	477	417
478466	f	193	299	270	251	372	332	333	465	405
478480	f	185	287	259	242	358	319	322	450	391
478496	f	193	298	270	254	375	335	335	469	409
478524	f	191	296	269	252	373	334	334	468	409
478538	f	185	287	260	240	356	319	322	452	393
478559	f	193	298	270	250	369	330	333	466	405
478582	f	185	286	259	244	361	323	322	450	393
478613	f	191	296	268	251	372	333	329	462	403
478644	f	193	298	270	253	374	333	335	468	408
478659	f	192	297	269	251	372	333	334	468	409
478682	f	194	301	272	251	373	333	337	472	412
478734	f	185	287	260	241	357	320	325	456	397
478742	f	184	285	259	242	358	321	321	449	393
478950	f	198	306	278	256	379	339	341	478	418

Appendix Table E. Continued

Sample ID	P/F	Foliage Green			Urban Gray			Desert Sand		
		R	G	B	R	G	B	R	G	B
479023	f	186	288	262	243	361	324	324	455	397
479044	f	186	287	261	245	362	324	322	451	394
479091	f	185	287	260	244	361	323	319	448	391
479100	f	193	298	270	264	389	348	328	461	401
479115	f	191	295	268	260	384	344	327	460	401
479127	f	189	294	266	249	370	330	331	465	405
479353	f	196	302	273	243	359	321	324	453	395
479354	f	209	321	290	252	373	333	338	473	412
479690	f	192	296	268	253	372	332	333	464	404
1279788	f	206	310	285	259	377	340	333	463	406
1280796	f	216	323	297	268	389	350	346	479	421
1280817	f	215	321	296	267	387	350	343	475	418
1280854	f	201	303	279	254	369	332	328	456	399
1280888	f	209	314	289	264	384	346	344	476	418
1280901	f	201	304	280	254	369	334	330	458	403
1280905	f	210	315	290	264	384	346	343	475	417
1280906	f	211	317	292	265	385	348	344	476	419
1280931	f	200	302	277	254	368	332	329	455	400
80152356	f	198	303	276	265	383	344	343	474	417
80152358	f	197	303	275	265	383	344	343	474	417
80152374	f	197	302	275	266	384	346	345	477	420
80152375	f	198	304	276	268	388	349	346	478	421
80152376	f	191	293	266	259	375	337	334	461	405
80152405	f	189	291	265	255	369	331	328	453	399
80152806	f	197	303	275	267	386	348	342	470	413
80152826	f	198	304	276	265	384	346	343	472	414
80152862	f	200	307	278	267	386	346	343	473	415
80154010	f	195	300	273	266	384	345	344	474	417
80154059	f	195	300	272	264	381	343	342	471	414
80154096	f	191	293	266	258	373	335	333	459	403
80156077	f	197	302	274	264	381	342	342	472	414
80156080	f	199	305	277	267	386	347	343	474	417
80156087	f	202	310	281	269	389	350	346	478	421

## **Appendix F. Data Analysis of Visual Assessment Results at NCSU**

A pilot study involving visual assessment of military camouflage samples was carried out at NCSU. Sixty batch samples were used in the pilot study, which included 24 pass samples and 36 fail samples. From the 24 pass samples 16 samples included the key pattern, while from the 36 fail samples 24 samples included the key pattern.

Twenty five observers participated in the pilot study in three separate trials. In each trial, every observer was asked to compare the batch sample against the standard sample and then give a pass / fail judgment based on the difference between the colors in the standard and in the batch.

Two methods were used. The first method is called the “Pass/Fail Judgment with Distance Observation” (PFJDO). The standard and the batch samples were placed at a distance and did not touch each other. For the samples including the key pattern, the observer determined the key pattern in both the standard sample and the batch sample and then gave a judgment of the overall difference around the key pattern as well as the difference for each of the colors. In the second method, called the “Pass/Fail Judgment with No Distance” (PFJND), the standard and the batch sample were placed adjacent to each other and compared.

Based on the visual judgment, a sample was passed only when its overall pass ratio was larger than 50%. For the PFJDO method, the maximal and minimal CIELAB values for ‘pass’ samples were determined to form definite borders separating the ‘pass’ samples from the ‘fail’ samples and only 2 fail samples were recognized as ‘pass’. This is shown in Appendix Table

1. When all data are converted to CIELCH, similar boundaries were determined to divide the ‘pass’ samples from the ‘fail’ samples with the exception of one ‘fail’ sample as shown in Appendix Table 2, where 1 ‘fail’ sample was mistakenly passed. Appendix Table 3 and Table 4 show boundaries in the CIELAB and CIELCH spaces based on the results from the PFJND method, where 10 and 7 ‘fail’ samples are mistakenly judged in each space respectively.

Appendix Table 1. Boundaries between the Samples Rated as ‘Pass’ and ‘Fail’ in the CIELAB Space from the results of the PFJDO method

	Desert Sand			Urban Gray			Foliage Green		
	L*	a*	b*	L*	a*	b*	L*	a*	b*
Max	68.66	3.11	10.49	55.76	-0.51	5.87	46.65	-1.14	3.39
Min	63.85	2.08	9.76	52.03	-0.94	5.28	42.24	-1.97	2.87

Appendix Table 2. Boundaries between the Samples Rated as ‘Pass’ and ‘Fail’ in the CIELCH Space from the results of the PFJDO method

	Desert Sand			Urban Gray			Foliage Green		
	L*	C*	h°	L*	C*	h°	L*	C*	h°
Max	68.66	10.92	78.03	55.76	5.91	100.06	46.65	3.91	122.95
Min	63.71	9.84	76.79	52.03	5.36	95.12	42.24	3.18	109.58

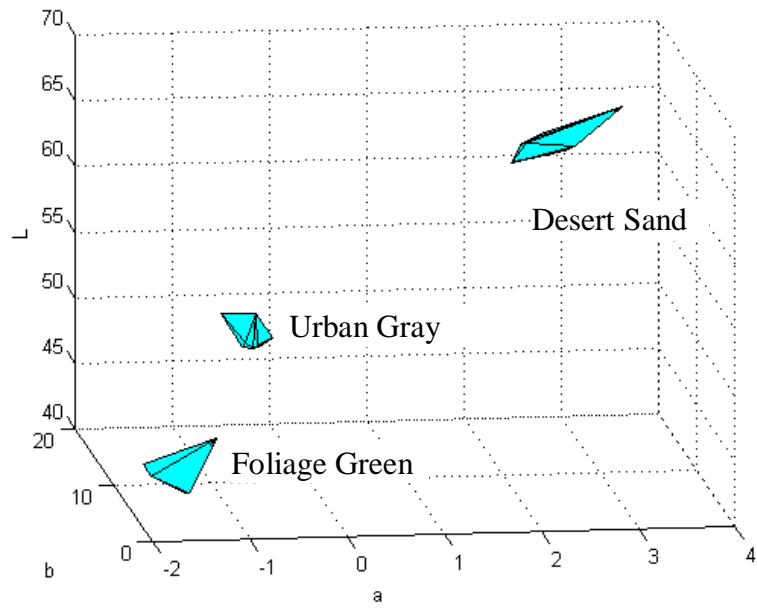
Appendix Table 3. Boundaries between the Samples Rated as ‘Pass’ and ‘Fail’ in the CIELAB Space from the results of the PFJND method

	Desert Sand			Urban Gray			Foliage Green		
	L*	a*	b*	L*	a*	b*	L*	a*	b*
Max	67.52	3.26	10.84	54.69	-0.53	6.56	46.35	-1.21	3.39
Min	63.85	2.08	9.81	52.03	-1.03	5.22	42.22	-1.97	2.92

Appendix Table 4. Boundaries between the Samples Rated as ‘Pass’ and ‘Fail’ in the CIELCH Space from the results of the PFJND method

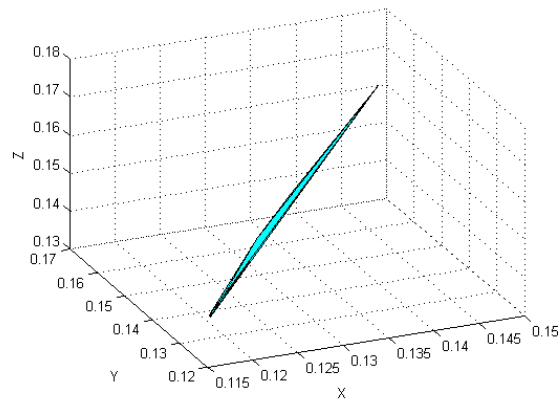
	Desert Sand			Urban Gray			Foliage Green		
	L*	C*	h°	L*	C*	h°	L*	C*	h°
Max	67.52	11.20	78.03	54.69	6.64	99.27	46.35	3.91	122.95
Min	63.85	10.02	73.07	52.03	5.27	95.08	42.22	3.43	110.59

Similarly, convex hulls in the CIELAB and CIEXYZ color spaces based on the ‘pass’ samples were examined to separate the ‘pass’ samples from the ‘fail’. Appendix Figure 1 shows convex hulls in the CIELAB space based on the PFJND method results, where only 1 ‘fail’ sample was mistaken as ‘pass’. Appendix Figure 2 shows convex hulls in the CIEXYZ space based on the PFJND method results, where only 4 ‘fail’ samples were mistaken as ‘pass’. Appendix Figure 3 shows convex hulls in the CIELAB space based on the PFJDO method results, which can separate all ‘pass’ samples from all ‘fail’. Appendix Figure 4 shows convex hulls in the CIEXYZ based on the PFJDO results, where only 1 ‘fail’ sample was mistaken as ‘pass’. Thus, it can be seen that there are less errors in the results from PFJDO than those from PFJND.

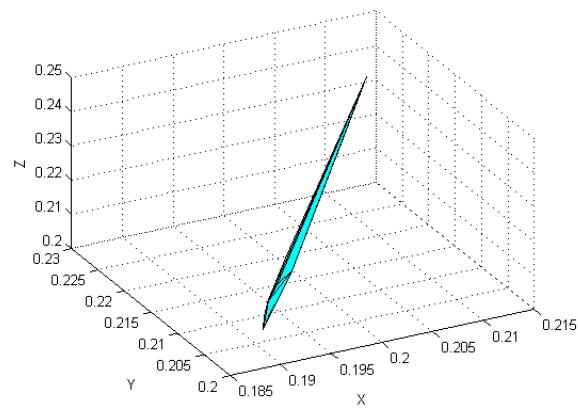


Appendix Figure 1. Convex Hulls from the “Pass” Samples of Three Colors in the CIELAB space based on the PFJND method

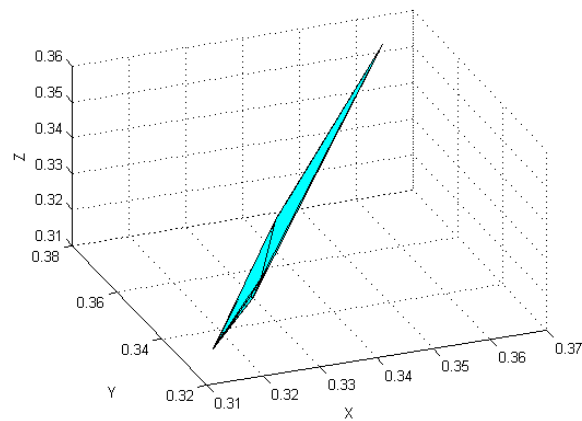
(a)



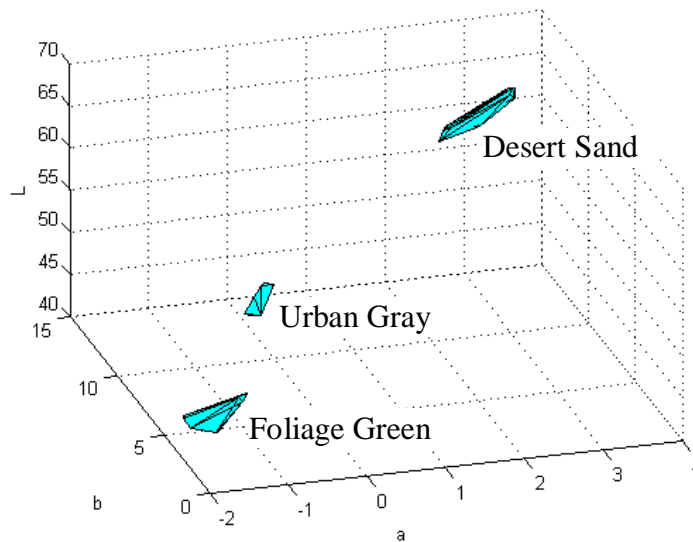
(b)



(c)



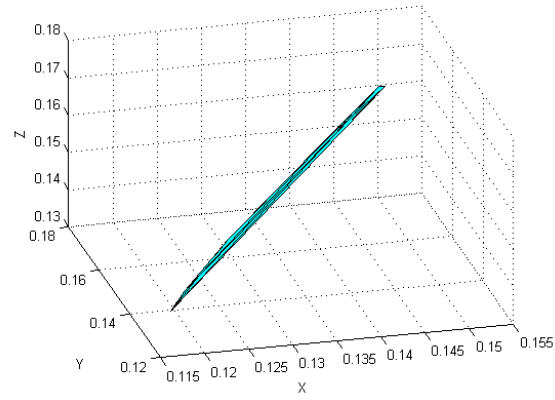
Appendix Figure 2(a-c). Convex Hulls from the Samples Rated as “Pass” of Three Colors in the CIEXYZ Space based on the PFJND method- Foliage Green (a), Urban Gray (b), Desert Sand (c)



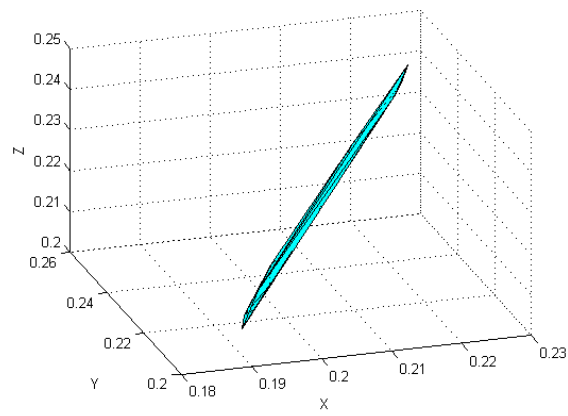
Appendix Figure 3. Convex Hulls from the “Pass” Samples of Three Colors in the CIELAB space based on the PFJDO method.

When the images from the camera output were used for judgments, the ‘pass’/‘fail’ judgment methods shown in Chapter VI, both in the color space and in the device space, were examined for the results obtained from both PFJND and PFJDO methods. For the judgment in the color space, all the ‘pass’ samples and all the ‘fail’ samples were failed because of the error in the conversion from the device space to the color space. With the judgment based on the convex hulls developed from the ‘pass’ samples, all the ‘pass’ samples can be separated from all the ‘fail’ samples. Similarly, the convex hulls can be expanded to avoid the variation in the image output. Appendix Table 5 shows the relation between  $\alpha$  and Number of the Mistakes from PFJDO and PFJND methods. From this table, it can be noted that the PFJND method still performs better than the PFJDO method.

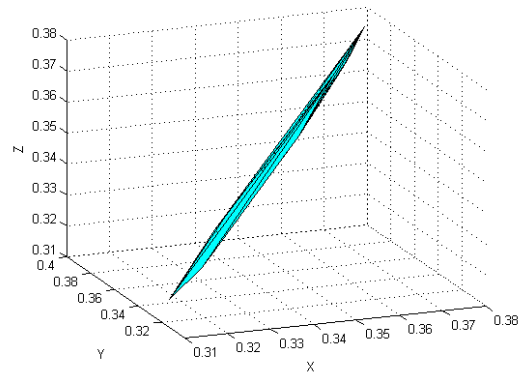
(a)



(b)



(c)



Appendix Figure 4(a-c). Convex Hulls from the Samples Rated as “Pass” of Three Colors in the CIEXYZ Space based on the PFJDO method- Foliage Green (a), Urban Gray (b), Desert Sand (c)

Appendix Table 5. Relation between  $\alpha$  and Number of the Mistakes from the PFJDO and PFJND methods

	$\alpha$	1.0	1.1	1.2	1.3	1.4	1.5	1.6	1.7	1.8	1.9	2
Number of Mistakes	PFJDO	0	0	0	0	0	2	2	2	3	3	3
	PFJND	0	1	2	2	2	3	4	5	5	6	7

Appendix Table 6 shows the comparison of the correct ratio based on different methods. AS shown the PFJDO method performs better than the PFJND method.

Appendix Table 6. Comparison of the Correct Ratio using Different Methods

Correct Ratio	PFJDO	PFJND
CIELAB Boundaries	95%	83.33%
CIELCH Boundaries	97.5%	88.33%
CIELAB Convex Hulls	100%	98.33%
CIEXYZ Convex Hulls	97.5%	92.86%
RGB Convex Hulls	100%	100%
RGB Convex Hulls with $\alpha$ of 1.5	95%	95%